WIRE-ACTUATED PARALLEL ROBOTS FOR COCHLEAR IMPLANTATION WITH IN-VIVO SENSORY FEEDBACK

By

Jason Pile

Dissertation

Submitted to the Faculty of the

Graduate School of Vanderbilt University

in partial fulfillment of the requirements

for the degree of

DOCTOR OF PHILOSOPHY

in

Mechanical Engineering

August 2015

Nashville, Tennessee

Approved:

Nabil Simaan, Ph.D.

Michael Goldfarb, Ph.D.

George B. Wanna, M.D.

Mario Svirsky, Ph,D.

MECHANICAL ENGINEERING

Dissertation under the direction of Professor Nabil Simaan

Robot-assisted cochlear implant (CI) surgery is a new research area that emerged in the last decade. The goal of robotic assistance is to improve patient hearing outcomes through improved surgical access and the minimization of intracochlear trauma during implantation. This thesis presents several research efforts converging on a system for robotic atraumatic CI insertion. The work begins with the characterization of fundamental aspects of CI implantation. This leads to the synthesis of a robot design for the implantation task. Lastly, intelligent control through in-vivo sensory feedback is investigated for improvement in CI insertion and final placement.

The motivation behind this research stems from fundamental knowledge gaps in both characterization of the CI surgical domain and in robot design and control. Current solutions for robot-assisted CI surgery do not exhibit adaptability to changes from nominal CI insertion plans. This lead to exploration of a new domain of in-vivo sensory guided robotic insertion of CI electrode arrays.

The contributions of this work include a system architecture derived from the clinical specifications of CI surgery while simultaneously exploring theoretical gaps in the areas of mechanism design and static balancing of serial and parallel mechanisms. Methodical derivation of specifications for surgical access during CI implantation are presented and include available workspace, kinematic behavior of under-actuated implants, and baseline expectations of insertion forces. From this, the synthesis of a robotic wire-driven insertion platform for CI is presented. Lastly, both force and intra-cochlear impedance data collected by the proposed robot are used to add intelligent correction to the implantation procedure. These corrections include physical

misalignment of the robotic system to the patient anatomy and incorrect models of the non-visible intra-cochlear geometry. Novel algorithms utilizing in-vivo sensory feedback for robot-assisted CI insertion guidance and fault detection are proposed and experimentally demonstrated using several robotic platforms. The implications of this research extend to providing new methods of CI insertion and also design of compact parallel robots with remote actuation.

Approved: Nabil Simaan Date: 5/29/2015

ACKNOWLEDGEMENTS

I would like to thank my advisor, Dr. Nabil Simaan, for his support and guidance throughout my graduate education. Over the last five years he has been a mentor and friend for myself and my fellow lab mates. I will always be grateful for the opportunities he and his lab have provided for me.

From my lab mates I have had the wonderful experience of being a student, teacher and friend. I would like to thank Dr Andrea Bajo, Dr Roger Goldman, Dr Jian Zhang, Haoran Yu, Sam Bhattacharyya, Long Wang, Giuseppe Del Giudice, Aditya Bhowmick, Dr. Rajarshi Roy, Nima Sarli, Zhangshi Liu, and Rashid Yasin for their friendship, help, and patience.

The work presented in this dissertation is motivated by gaps in clinical technology and it has provided me an opportunity to work directly with the clinical researchers at Vanderbilt University. Dr George Wanna and Dr Alex Sweeney have been wonderful collaborators who have volunteered their time and expertise in the clinical aspects of the work and helping me to better understand the clinical procedure and motivations. I would also like to thank Dr Robert Labadie, Dr Ramya Balachandran, Pooyan Rohani and the members of the CAOS lab at Vanderbilt for there assistance in my research and for providing me the opportunity to work with their group.

During the course of my graduate studies my research in robotic-assisted cochlear implantation has been supported by Cochlear Ltd. In addition to funding and material support for experiments, members of the staff at Cochlear have been gracious with their time to share expertise on technical and clinical aspects of the CI procedure. I would like to thank Claudiu Treaba, Ann Tsay, James Dalton, Jonathon Kirk, and Shaun Kumar for their insights and direction during the course of my research.

I would also like to thank the members of my defense committee; Dr Michael Goldfarb, Dr. Pietro Valdastri, Dr George Wanna, and Dr Mario Svirsky for taking the time to serve on the committee. In addition to their review and feedback on my dissertation they have been each been either teachers or research colleagues that I have enriched my graduate experience.

Completing my graduate studies would not have been possible without the love and support of my family. My mother and brother have always helped me keep perspective and balance in my life. My wife Tran has been the pillar of strength for our growing family. Her encouragement and faith in me has been a blessing I cannot put into words. She has and always will have my love and I dedicate this work to her.

Contents

List of Tables

List of Figures

Chapter I

INTRODUCTION

Surgical robotic systems have been entering clinical use throughout the past two decades starting with automated bone drilling for knee replacement surgery and progressing to minimally invasive laproscopic surgery. Although not yet clinically available, there is a large body of work moving robotic surgery research to micro-level manipulation and intervention with applications to opthalmic surgery. In otology, there has been preliminary work in developing robotic solutions to cochlear implant (CI) surgery. This is a new area of research which has gained attention over the last decade.

Cochlear implants are designed to provide some level of auditory perception in patients with total or profound hearing loss. CI surgery, from an implantation task standpoint, can be broken into three phases; gaining access to the cochlea, the insertion of the electrode array, and closing of the surgical site. The task of insertion has a demand for high precision and the desire to mitigate the degree of trauma imparted on the intracochlear anatomy. Robots are well suited to this task as they are capable of position and force control on scales below the human threshold of quantitative perception.

In the application of robotic technology to surgical tasks, devices in clinical uses (such as the MAKOplasty [67] and Da Vinci [45]) are large systems taking significant footprint in the OR. While acceptable for procedures on the knee or abdominal area there is a practical need for device miniaturization for ophthalmic or otological procedures due to significantly smaller workspaces. Existing mechanism paradigms in

clinically available robotic systems do not scale well for this requirement and there is an opportunity for new mechanisms to be tested in these applications.

This work is focused on the design and implementation of a robotic system to insert CI electrode arrays while minimizing trauma to the intra-cochlear anatomy. The mechanism presented is a kinematically parallel architecture using constant length wire loops to transmit force to prismatic links. Analysis and synthesis methods for this type of mechanism are presented along with the mathematical models used in the calibration and evaluation of the device.

The research presented in this dissertation also explores new approaches to electrode array insertion into the cochlea. One part of this approach is the quantitative characterization of electrode array kinematics and experimentally derived insertion force models. The other part of the presented work in insertion control is the demonstration of the utility of in-vivo sensory feedback to intelligently adjust the pre-planned insertion trajectory. This feedback takes the form of real time insertion force monitoring and the use of bi-polar electrical impedance signals measured by the implant itself during insertion. The end result is a set of control algorithms which can lead to a rapidly deployable implantation tool that may facilitate safer CI insertions.

In this chapter, a brief overview of CI surgery is presented along with considerations specific to implantation. An overview of robotic applications in this surgical field is presented along with considerations specific to surgical robots. Lastly, a review of scientific needs not yet addressed is presented as the motivation for this research.

I.1 Related Work

There are two collections of work which must be reviewed to present new methods for the robotic insertion of cochlear implants. The first is the CI procedure itself, including the basic steps of the procedure, the current tools, and the surgical

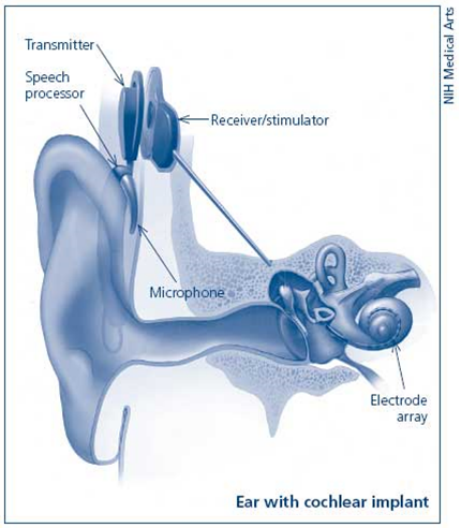

Figure I.1: Cochlear Implant System. A typical CI system includes the implant with a subdermal transceiver. The CI recipient wears an external audio receiver which processes signals for transmission to the implant via short range wireless (RF) communication. The implant's electronics fire electrical charges into the electrode array to produce auditory sensation [72]

considerations. The second area of background is in robotic surgical systems. This includes the current types of clinically deployable systems and those in the literature addressing the various facets of CI surgery.

Cochlear Implant Surgery

As of 2010 there are approximately 71,200 CI recipients (42,600 adults and 28,400 children) in the United States and 219,000 worldwide [72]. A thorough review of cochlear implants history and clinical considerations can be found in a review by Waltzman [116].

CI surgery aims to restore auditory perception to the deaf or those with profound hearing loss. This restoration is achieved by delivering direct electrical stimulation to the auditory nerve through an electrode array implanted inside the cochlea. Control of the electrical signal to produce distinguishable auditory sensations is accomplished by an audio receiver and processor worn externally by the CI recipient (Figure I.1).

The cochlea is a helical structure (Figure I.2) in the inner ear which converts mechanical energy from sound waves into electrical signals in the auditory nerve. The cochlea is separated into three chambers, the scala vestibuli, scala media, and the scala tympani with the thin basilar membrane separating the scala tympani and vestibuli. Each chamber runs through the entire length of the cochlea spiral. The oval and round windows are membrane layers sealing the vestibuli and tympani chambers respectively. In the hearing process, sound wave are propagated through the ear canal to the ear drum. These acoustic waves cause vibrations in the ossicles and the stapes' vibration delivers mechanical energy to the oval and round windows. The chambers of the cochlea are filled with perilymph and vibrations at the external membranes propagate acoustic waves through the fluid-filled cochlea. Inside a normal healthy cochlea, there are hair cells attached to the organ of Cortii and through vibrations in the chambers the hair cells make contact with the tectorial membrane. An electric charge is created and transmitted to the auditory nerve and the signal is sent to the brain to process as sound.

Damage or absence of these hair cells will prevent the transmission of acoustic energy to electrical stimulation but CI's substitute this mechanism through direct electrical excitation. Traditionally, the surgeon performs a mastoidectomy to gain access to the cochlea. A small opening must be drilled into the scala tympani chamber of the cochlea through either the round window, modified round window or cochleostomy approach (Figure I.3). Different electrode manufacturers have varying preferences to the opening type depending on the design of a particular electrode. Current clinical practice then has the surgeon manually insert the electrode using a pair of forceps or other electrode-specific manually operated tools.

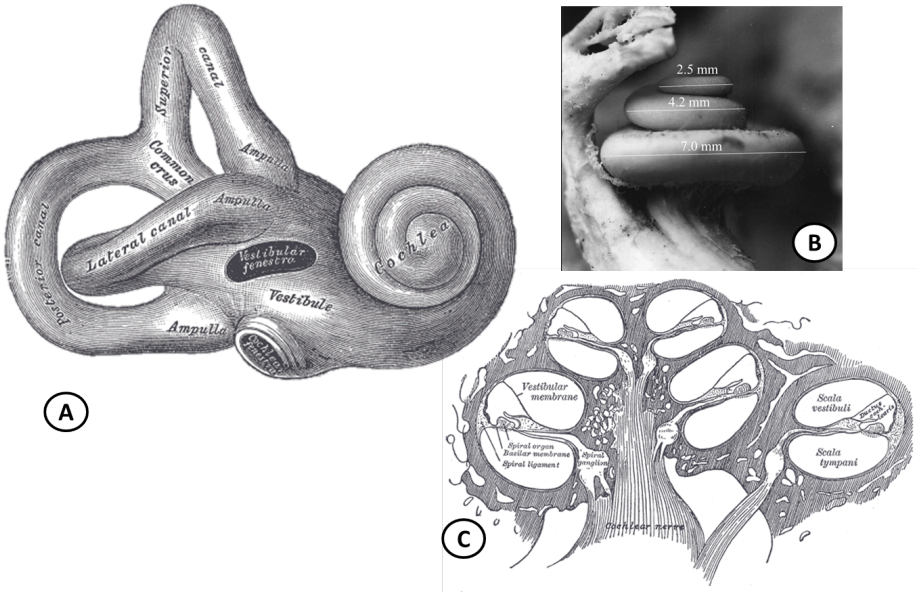

Figure I.2: Anatomy of the cochlea. (A) Classic drawing of the isolated cochlea. (B) A reconstructed cochlea from a human cadaveric specimen presented by Erixon [31]. (C) Classic cross section view of the cochlea interior. Shown are the scala tympani, vestibuli, and media chambers.

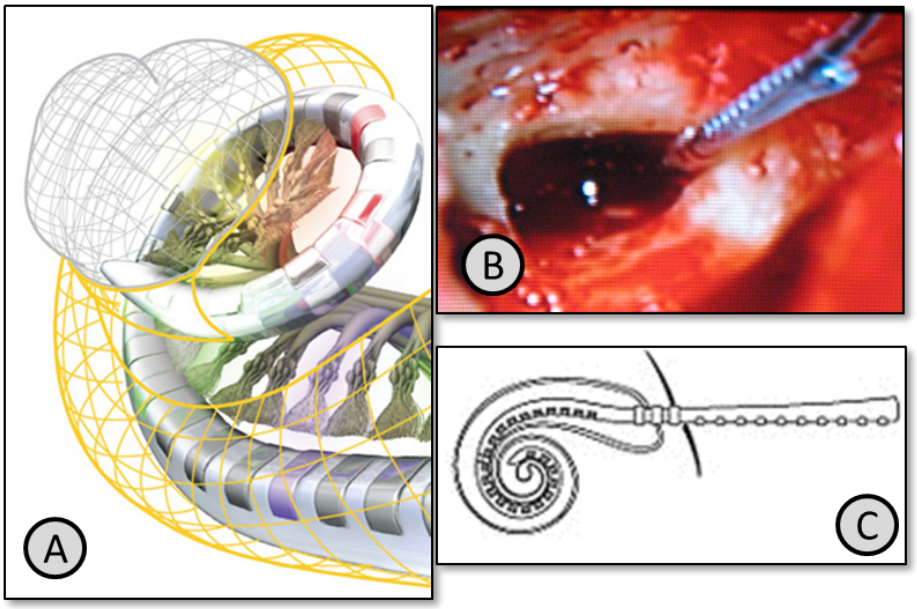

Figure I.3: Cochlear Implantation. (A) A rendering of a PEA within the scala tympani volume showing the proximity of electrode contacts to the auditory nerve. (B) A surgical view of electrode implantation in a live patient with the PEA passing through the facial recess access. (C) The schematic view of final PEA placement within the cochlea.

Figure I.4: Advance off stylet. The PEA is inserted normally into the cochlea until reaching the basal turn. At this point the stylet is retracted at approximately the same rate as the PEA is inserted. Using this technique, the PEA should maintain contact with the modiolar wall. Diagram from Todd [110]

There are several types of electrodes clinically available but they can be separated into two general groups. The first are straight lateral-wall electrode arrays. Their name comes from the fact that they slide along the lateral (outer) wall of the cochlea during insertion. The second group are actuated perimodiolar electrode arrays (PEA). In the case of perimodiolar electrodes there is an additional component to the electrode, a thin metal stylet embedded in its silicone body. During the insertion of this type of electrode the stylet must be held fixed in space after the first stage of insertion as the electrode is guided deeper into the cochlea, a technique referred to as advance off stylet (AoS). The ideal AoS technique is shown in Figure I.4. While their designs differ, all electrode arrays share the characteristic of being thin and delicate structures.

A new method of accessing the cochlea through a minimally invasive percutaneous approach was proposed by Labadie et al [60] in 2005 through the use of a stereotactic frame attached to the patient's skull. Placement of the frame [59] was accomplished through CT image registration to anatomical landmarks [74, 73, 75].

There is a tremendous body of research on CI surgery ranging from surgical technique and planning to post operative evaluation, signal processing, and histological

studies. The following sections review these works with the aim of highlighting knowledge gaps and opportunities for new research.

Robot-Assisted Cochlear Implant Surgery

This section reviews applications of robotic systems to the CI procedure. Included in this review are devices related to gaining surgical access to the cochlea, insertion electrode arrays, and systems facilitating basic research in CI implantation.

The first work presented on applying robotic systems to CI surgery came from Zhang et al. [130] in 2006. This work looked at the application of underacted steerable electrodes with robotic controlled insertion as a method to reduce contact between the cochlea and the electrode and hence reduce the likelihood of trauma. A mathematical model for the optimization of these steerable electrodes was later presented by Zhang in [126]. Figure I.5 shows the process of inserting a steerable electrode into a cochlea. The mechanics of this type of electrode also led to the exploration of required workspace for a robotic system [127].

Since the characterization of insertion force as a metric of evaluation of electrode insertion by Roland [86] there have been numerous studies [66, 125, 85, 54, 53, 70, 99] reporting insertion forces as a quantitative evaluation of insertion. The relationship between insertion speed and insertion force was first explored using plastic models and straight outer wall electrodes by Zhang et al in [125] using a robotic insertion system and later using perimodiolar electrode arrays by Kontorinis et al. [53]. Results presented by Zhang showed an inverse correlation between insertion force and speed at rates up to 8mm/s for lateral wall electrode arrays. This reduction was attributed to viscous friction effects dominating contact loads at higher speeds. The study by Kontorinis showed less correlation between forces and speed in perimodiolar electrodes

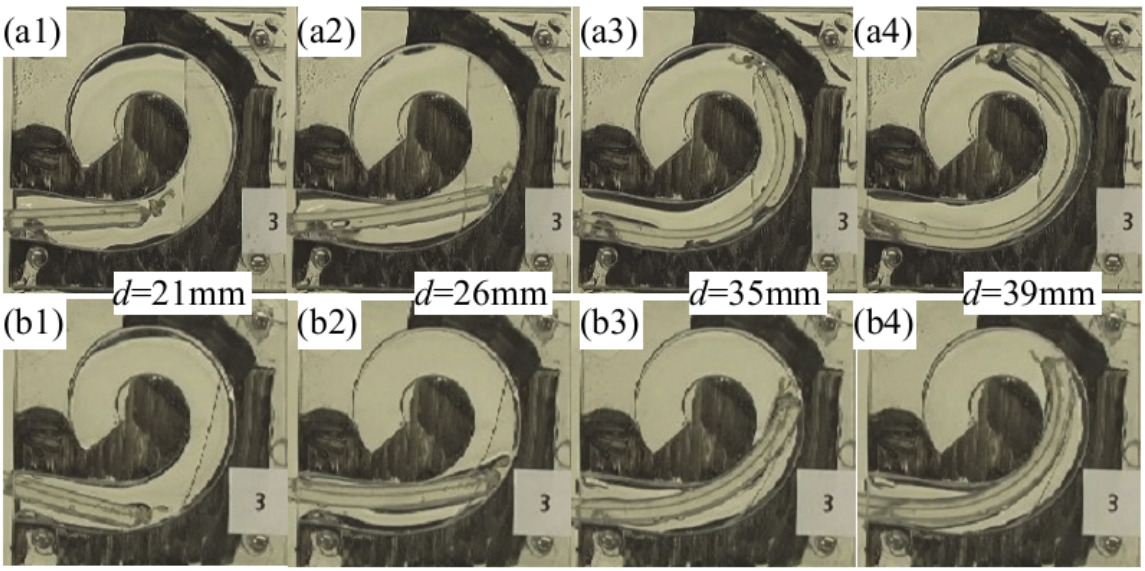

Figure I.5: Prototype steerable electrode used in scaled plastic cochlea model. The orientation of the electrode is manipulated by applying tension to an embedded wire.

and work presented in Chapter V confirms this finding with insertions in human cadaveric specimens.

There have been several automated systems proposed in the literature specifically designed to insert electrode arrays. A graphical review of these robotic systems is shown in Figure I.6. In 2010 Zhang et al proposed using a custom designed 6 DoF Stewart-Gough platform to control the insertion of electrode arrays into the cochlea with observation of insertion forces and moments [128].

Building on the percutaneous insertion approach proposed by Labadie et al. [60], a single degree of freedom robotic insertion tool was presented by Majdani et al. [66] in 2010 for use in percutaneous insertion. Schurzig et el incorporated custom single-axis force sensing into the device evaluated the insertion performance of the tool in phantom models in [92, 93]. Similar evaluations were performed by Rau et al. [85] on the same robot.

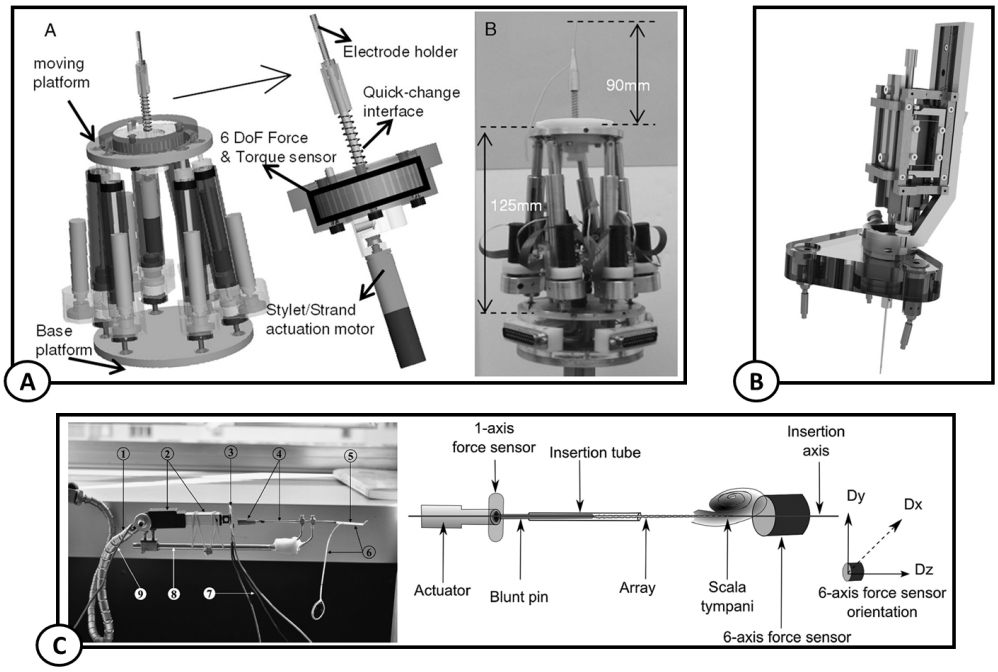

Figure I.6: Prior robotic CI insertion systems. (A) A 6 dof CI insertion system with 6 axis force sensing proposed by Zhang et al. in 2006. (B) a single axis insertion system with 1 dof force sensing presented by Schurzig et al in 2010. (C) A bench top 1 dof insertion system for force sensing experiments performed by Miroir et al. in 2012.

Force laboratory testing of insertion forces Miroir et al. [70] presented in 2012 a single axis electrode insertion tool. This device was not designed with consideration for clinical deployment but only for work with phantom models. Their experimental setup included a single axis force sensor on the insertion tool and a 6 dof force/torque sensor on the cochlea phantom. Reported reaction forces were large compared to prior studies and there appeared to be sensitivity problems in the apparatus however it is one of few studies to incorporate dual force transducers as a way to verify measurements.

Robotics have been applied to other parts of CI surgery, most notably in performing the mastoidectomy. In 2010 Baron et al. proposed using an optically tracked industrial manipulator for performing mastoidectomy [9]. Work presented by Lim et al. [64] demonstrated a cooperative parallel robot which allowed to the user to guide a surgical drill through the mastoidectomy while preventing motion of the drill to pass safety boundaries determined from image guidance. Kratchman et al. presented a parallel robot for drill positioning in percutaneous insertion [56] compatible with the prior percutaneous insertion method presented by Labadie [60, 59].

Other tools proposed in the literature related to CI surgery are shown in Figure I.8. Kratchman et al. [57] demonstrated a manually operated insertion tool for periomodiolar electrodes in 2012 that was compatible with the percutaneous insertion approach. Work from Maier in 2010 presented a simple teleoperated system for high precision manipulation in inner ear surgery [65]. This device was designed to work with existing clinical instruments and use the robotic system for position control.

The tools presented in this section vary significantly both in aims and complexity but share a common assumption. Each device executes pre-programmed motion, either mechanically or through software, without adaptation. Such a paradigm relies

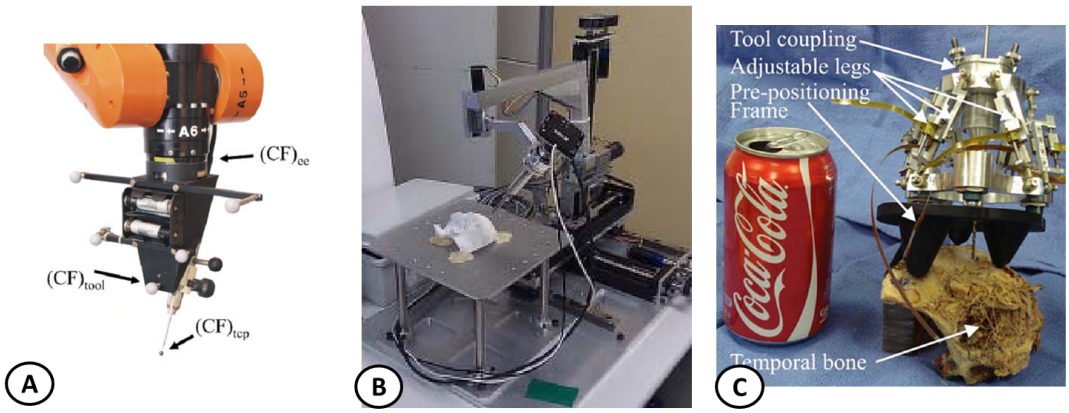

Figure I.7: Robots used in performing mastoidectomy / percutaneous drilling. (A) Optically tracked drilling tool by Baron et al. [9]. (B) Cooperative mastoidectomy drilling presented by Lim et al. [64]. (C) Percutaneous drilling platform presented by Kratchman et al. [56]

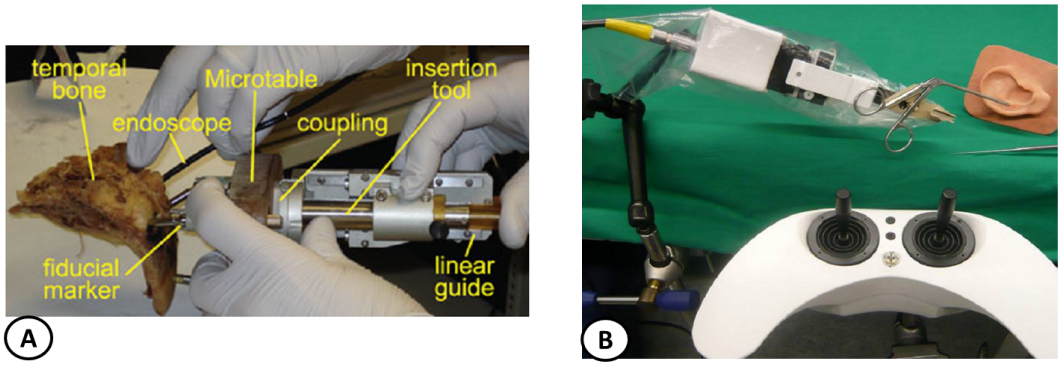

Figure I.8: Other tools for CI surgery. (A) Manual insertion tool by Kratchman et al. [57]. (B) Teleoperation system concept for middle ear surgery by Maier [65]

heavily on pre-registration and as such can introduce single point failures. There is an opportunity to incorporate sensory feedback into robotic systems so that they automatically adjust to deviations from pre-planned models.

Design Considerations of Clinically Deployable Robots

The existing prototype surgical systems related to CI procedures not only vary in both their kinematic designs and limitations but also in their intended role within the entirety of the CI surgery. However, all these devices share a set of design considerations given their nature as surgical tools. A review by Taylor [107] in 2003 covered surgical robot requirements within the context of the greater computer integrated surgical system. Among the requirements were a focus on safety, workspace, dexterity, sterilization, and accuracy. While most of these attributes are important to any robotic system, sterilization is a special concern of medical instruments. Any tools which may make contact with the patient must be sterilized between procedures. This process usually involves submersion or high temperature treatments that restrict material and actuator options in the mechanism design.

There are two general methods to solve the sterilization problem. In the case of the ROBODOC system [49, 48], the serial robot arm is entirely draped with a sterile barrier with only the end effector drill requiring full sterilization. The fully draped robot is an attractive choice since far fewer restrictions are placed on the robotic manipulator design. In some applications however, a fully draped system may not be viable due to the need to exchange tools connected to the manipulator. To address this particular requirement, a robot design has its sterilizable end effectors separated from the actuators through a transmission system. The tools and connection interface must be fully sterilizable but the sensitive actuators and control electronics can be isolated from the surgical site. A famous implementation of this design scheme is the

DaVinci system from Intuitive Surgical [40]. The *DaVinci* uses a closed loop wire transmission scheme to connect the actuators to the end effector.

Removing the actuators from the surgical site has been an important consideration for several surgical systems including the *DaVinci* and the *neuroArm*[105]. In the case of the *neuroArm*, hydraulics were used for MR compatibility while the *DaVinci* is one of many proposed robot designs to use wire actuation and isolate motors from the manipulator mechanism. The MIT WAM [88] was an early example to use wires to drive a 7 DoF articulated arm. While the articulated arm is generally a serial structure, the routing of wires to distal links introduces kinematic coupling [123] between the actuators and the configuration of the arm links. The solution to decoupling joint/actuator kinematics proposed by Tsai [111] uses a structural matrix based on pulley ratios and wire routing directions.

These early surgical robot applications have been geared toward large workspace procedures in the abdomen and knee. With increasing numbers of surgical procedure in small surgical fields such as the head and neck, there is an increased need for less obtrusive tools in the operating room. Technological solutions addressing intrusiveness and rapid deployability are needed in addition to considerations of safety and sterilization. Parallel robotic structures have the potential to provide high-accuracy, compact tools in the operating room.

In regards to stiffness, payload capacity, and theoretical accuracy, parallel kinematic structures such as the Stewart-Gough [100] or DELTA [78] manipulators have significant advantage to serial structures [96]. The trade off to these advantages are comparatively smaller workspaces and more difficult singularity analysis [20]. So far in the literature, wire actuation for parallel structures has largely focused on suspended platforms like the RoboCrane [11]. These parallel robots rely on an "N+1"

wire suspension scheme to insure force closure [58, 10, 38, 71] and a stable pose. Wire actuation is also used in linkage assemblies with applications in haptic devices [69, 36, 68]. So far in the literature there was been little work to incorporate wire or cable routing to drive prismatic links in parallel kinematic architectures.

Safety is a key concern with robotic surgical systems and must be incorporated into several facets of the overall system design. Undesirable motion of robotic links is prevented through several layers of redundancy and cross checking. At the software level, error handling logic with redundant multi-sensory feedback [49] can mitigate potential problems. At the mechanical level, there are several methods of improving device safety. The first is to minimize the number of single point failures in the design and the second is through designing systems with actuator capacity limited to intrinsically safe levels. Static balancing involves using passive energy storage within a mechanism to reduce the effect of gravitational loading on actuator requirements. By reducing this load effect, actuators may be reduced in capacity to a magnitude which is safe for interaction with a patient [115]. In the event of power failure, statically balanced mechanisms also do not change position and during use are more energy efficient. The trade to this reduction in actuator capacity is slower end effector motion.

Solutions to the static balancing (sometimes referred to as gravity compensation) problem have been explored by numerous researchers and a brief review of the type of solutions in the literature is presented here. The uses of counter weights to balance mechanism links is the most simple approach to the problem but faces the problem of significantly increased mass. Some theoretical on balancing parallel mechanisms with counter masses has been presented [87] but has not been demonstrated in a feasible prototype.

The most common method of static method involves using linear springs strategically placed in the structure. Determination of the spring connection points satisfies the condition that the gravitational potential energy of the mechanism remains constant through its workspace [33, 98, 98, 7]. The application of this method has been used in numerous parallel kinematic architectures [37, 37, 89, 61, 63, 18] while some groups prefer to explicitly solve reaction forces during the synthesis phase of design [30, 55]. Medical applications of static balancing have included uses in leg orthosis [2] and patient side manipulators [63, 115].

Earlier static balancing designs [3, 2, 37, 37, 89, 61] often incorporated parallelogram linkages as a means of generating the proper energy functions to cancel out gravity load. These designs generally occupy large volumes to accommodate the linkages. More recent applications have moved toward specialize drive trains to generate the energy functions. Kim and Song [51] achieved 80% balancing in a three link serial manipulator by embedding the springs and tendons inside the individual links and rely on the tendon routing to decouple the links. Carricato [18] proposed using masses and springs within prismatic jacks to balance a particular configuration of the Stewart-Gough design. Kilic [50] demonstrated using cams wrapped by the actuation wire to balance single links.

It was a combination of these works that inspired the use of wire actuation for the parallel robotic system presented in this dissertation. Wire actuation lends itself to sterilization since the actuators can be isolated from the mechanism links and therefore not required to endure sterilization procedures. The second factor in selecting wire actuation is its increasing use in static balancing solutions due to its compactness compared to previous linkage based designs.

Grade	Description
0	No detectable trauma
1	Elevation of basilar membrane
2	Rupture of the basilar membrane
3	Electrode entry into the scala vestibuli
4	Severe trauma (i.e fracturing of rigid structures)

Table I.1: Trauma scale proposed by Eshraghi [32]

I.2 Summary of scientific and clinical needs

Development of surgical tools is motivated by the application's needs. In CI surgery there exists a desire in the clinical community to both reduce the trauma of CI insertion and to preserve residual hearing in patients with partial acoustic hearing. Summarized below is the work in the areas of CI trauma and post-operative outcomes. Both are important quality of life considerations for CI recipients and are areas where improved tools have opportunities to improve results clinically and in basic research.

CI Trauma

Intra-cochlear trauma receives considerable attention in the literature. In 2003, Eshraghi [32] presented a qualitative scale to assess the severity of intra-cochlear trauma from one of five grades. Table I.1 reviews this scale with examples from two studies [32, 119] shown in Figure I.9. In a series of 2 papers [119, 118] Wardrop presented histological examinations of temporal bone specimens implanted with a representative set of commercially available electrodes. Results showed that atraumatic insertion of electrodes is possible across the range of electrodes but not guaranteed. Other trauma studies have included those performed in animals [24] and in the evaluation of new electrodes and surgical technique [43, 14, 1, 27, 95, 112, 109, 101].

Intraoperative indication of trauma or incorrect positioning of an electrode array is possible through flouroscopy as demonstrated by Fishman in [34] although care

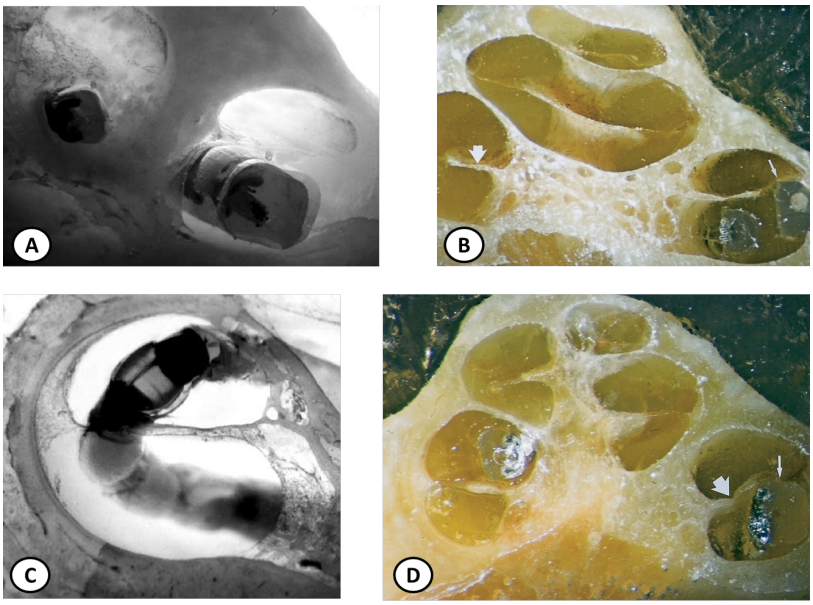

Figure I.9: Categories of trauma to intra-cochlear anatomy with histological images.

must taken to safely manage radiation applied to the patient. X-ray computed tomography (CT) has also been used in examining electrode array placement [109]. Currently, there has been no presented cases of intraoperative CT scanning and its use is restricted to pre operative planning and post operative evaluation. So far in the literature there have been no methods presented which provide feedback on the likelihood of trauma intraoperatively without the uses of carefully managed radiological imaging. Also, such imaging systems are expensive to operate and not available at institutions across the world. Solutions that can access risks of trauma without the overhead of state of the art imaging is still relatively unexplored in CI applications.

Post Operative Outcomes

In 2006 a study by Fraysse et al. [35] examined the effects of residual hearing preservation (HP) with electroacoustic stimulation on speech perception in CI patients. The electrode used in the study was the Nucleus 24 Contour Advance from Cochlear Ltd and a "soft-surgery" protocol was followed. Patients were separated

into two groups; those with little to no residual hearing and those whose residual hearing was sufficiently high enough to gain some benefit from an ipsilateral hearing aid. Review of speech perception scores showed that up to 5dB SNR, the electroacoustic group had statistically significant benefit from combined CI stimulation with residual hearing through a hearing aid. When SNR levels had reached 10dB there was no longer any statistically significant benefit to speech perception in this group.

A study on post operative outcomes of 31 pediatric CI recipients was presented by Brown et al. [16] in 2010. While it did not compare the benefits of HP to pure electrical stimulation it showed that HP is possible for the intermediate term (up to 30 months in the study) for children with CI. The nature of the onset of hearing loss would be a major factor in determining if acoustic hearing perception would continue to deteriorate with age.

Carlson el al. [17] reported a tentative link between preservation of residual hearing through atraumatic technique and speech perception scores in 2011. Only approximately 50% of the CI recipients retained any acoustic hearing and there was less decrease in pure tone perception in the residual hearing group.

Recently, a study published by Cosetti et al. [29] also examined the role of residual hearing in speech perception. Like in [35] a "soft-surgery" technique was used for patient implantation although unlike this prior study a hearing aid was not used in the evaluation of residual hearing. Their results showed no benefit from residual hearing in regards to speech perception scores. This work also questions the validity of conclusions drawn by Carlson in [17] do to inherent speech recognition advantages in his residual hearing sample group. Regardless, several of these studies [35, 17, 29] encourage maintaining hearing preservation as a goal during CI surgery.

Identification of Scientific Needs

From the available literature, there is a noticeable trend in emphasizing "soft" surgical techniques [32, 35, 29] and an assumption that minimizing insertion forces helps in minimizing trauma [86, 110]. From a mechanical perspective this is a valid assumption since negligible force acting on the electrode means it is not physically interacting with anatomical structures. However, it does not imply the converse is true and additional experiments will be needed to definitively link force and trauma.

While forces have been reported in the literature below 50 mN for perimodiolar insertions [86, 110, 93] they have all been performed in ideal set-up not entirely reflective of a surgical scenario. Other studies have reported higher insertion forces [125, 70, 53] despite following similar experimental protocols. The difference in these forces could be due to subtle differences in lubrication, the geometry of the cochlea model, or the execution of the AoS technique. To date, there have been no proposed solutions to using measured forces in feedback control to attempt to minimize the magnitude of forces imparted on the cochlea.

There still exists a gap in the clinical knowledge to understand how implantation trauma associates with hearing outcome. The most obvious reason for this gap is that histological analysis can only be performed on cadaveric specimens while hearing outcome can only be assessed in live patients. Imaging modalities do not have the resolution to discern fine details in the cochlea without significant amounts of radiation. Force sensing tools with fine position control may not only help in producing more atraumatic insertions but also be used as a powerful research tool. Surgical systems record a large array of data which may be analyzed for correlations to patient outcomes not currently available in the CI field.

I.3 Contribution of this Dissertation

The work presented in this thesis bases its utility on proposing a robotic tool with accuracy and measuring capabilities useful both in clinical application and research. The contribution of this dissertation consists of three main elements. The first is the identification of task parameters for robotic multi-degree of freedom insertion not present in the current literature. The second is the development of a compact and rapidly deployable robotic system for CI implantation using wire actuation. Lastly, a set of control and fault detection methods are integrated into the robot control so that the insertion system may respond to unexpected conditions and reduce the risk of inducing trauma on the anatomy.

The sum of these contributions aims to move robotic insertion away from restrictive registration and pre-imaging/planning constraints and demonstrate that smaller dexterous tools can be applied to the CI procedure. Such a system has patient benefits both as a research device for use with new electrodes but also as a path toward clinically deployable tools that will provide greater information to the surgeon.

I.4 Outline

The remainder of this dissertation is organized as follows:

Chapter II presents a technical formulation of the insertion task and the requirements imposed on a robotic tool. These specifications begin with the characterization of the working environment, followed by modelling of the electrode array itself. This analysis concludes with the determination of required workspace, precision, and sensory capability for a robotic insertion tool.

Chapter III uses the requirements presented in the previous chapter in the synthesis of a parallel robot insertion platform actuated by constant length wire loops. A

model for the general case of this class of robot is presented with an analysis of a planar mechanism subcase presented as a physical embodiment of the concept. A review of the physical implementation of the robotic insertion system including the mechanical design, control architecture, calibration, and performance evaluation concludes the chapter.

Chapter IV presents the analysis and validation of a method for incorporating static balancing into a wire actuated mechanism. Static balancing of surgical manipulators reduce actuator requirements and introduce an additional level of safety into the mechanism.

Chapter V presents a set of experimentally derived models for the expected insertion forces in CI surgery. From this experimental data it is shown that predictions on the expected insertion force can be made in-vivo and in real time as an insertion progresses.

Chapter VI demonstrates that force and telemetry information from a robotic insertion tool can be used to identify several complications including electrode tip folding and extra-cochlear buckling of the implant. This chapter also demonstrates the effectiveness of using force/ position admittance control to actively reduce insertion forces.

Chapter VII proposes using CI electrode electrical impedance signals intra-operatively to assist in the placement of electrode arrays. An automated algorithm for electrode insertion using this method is demonstrated.

Chapter II

DERIVED SPECIFICATIONS FOR CI INSERTION

In order to design a robot for CI electrode array insertion, it is first necessary to derive a set of specifications for the surgical task. This chapter begins by reviewing prior quantification of the intra cochlear geometry. Based on this review, the work presents a model for the shape of the scala tympani chamber. Access to the cochlea is restricted by the facial recess. Previous literature did not quantify this constraint in terms of available access directions. To address this gap, a series of experiments are presented to identify the constraints on possible insertion vectors. The third part of this chapter presents a kinematic model of the PEA, an instantaneous kinematic model, a method for identifying the model coefficients, and how to estimate the kinematic behavior when an exact model is not available. From the information gathered in the preceding three points, the chapter concludes with the simulation of optimal insertion paths. These simulations create the workspace definition used for the design of a robotic insertion system presented in subsequent chapters. Lastly, a review of prior works quantifying characteristics of nominal CI insertion are presented to complete a set of specifications for the robot design.

Part of the work presented in this chapter has been previously published in [79, 81].

II.1 Geometry of the Cochlea

To perform robotic insertion of cochlear implants a set of frames must be defined to describe the spatial relationship between the robot, electrode, and the cochlea itself. Recently, a panel of clinicians have proposed a standardized coordinate frame model for the cochlea [114], which is adopted here to define the cochlea frame $\{\mathbf{C}\}$.

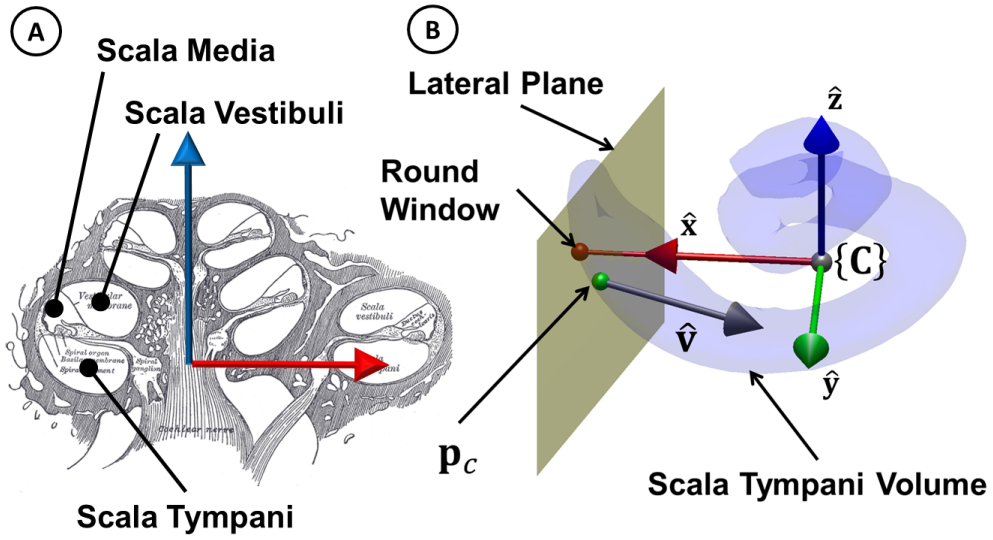

Figure II.1: Cochlea coordinate frame. (A) Internal cross section of the cochlea; the top chamber is the scala vestibuli and lower chamber is the scala tympani. (B) The frame C is define with $\hat{\mathbf{z}}$ colinear with the cochlea's helical axis and $\hat{\mathbf{x}}$ passing through the center of the round window. The point $\mathbf{p}_c$ is the location of the surgeon-created entrance into the cochlea. In the case of a round window insertion $\mathbf{p}_c$ lies along $\hat{\mathbf{x}}$.

Figure II.1(B) depicts frame $\{\mathbf{C}\}$ with respect to cochlea features. The axis of the cochlea's helix defines $\hat{\mathbf{z}}_C$ with the axis $\hat{\mathbf{x}}_C$ passing through the center of round window and $\hat{\mathbf{y}}_C$ completing a right-handed orientation frame. Access into the cochlea is achieve by either drilling a cochleostomy inferior to the round window or through opening the round window [14]. Regardless of the technique used, the access location for electrode insertion will be referred to as the *insertion point* and is denoted by the vector ${}^C\mathbf{p}_c$[1] in the cochlea's local frame. At the point ${}^C\mathbf{p}_c$, the unit vector $\hat{\mathbf{v}}$ denotes the expected direction of insertion into the scala tympani.

The shape of the chambers within the cochlea have been modelled using several techniques but a commonly referenced representation of the scala tympani shape was proposed by Cohen et al. [26] in 1996. This model defines the lateral (outer) wall of

[1] ${}^C\mathbf{p}_c$ is interpreted as vector $\mathbf{p}_c$ expressed in frame $\{\mathbf{C}\}$

A	3.84 mm
B	0.001317
D	0.12869
θ_0	5.0°
$\theta_{cochleostomy}$	23°

Table II.1: Cohen Template Parameters

the scala tympani as a piecewise continuous function in 2D polar coordinates. The shape is a projected onto the $\hat{\mathbf{x}}_C\hat{\mathbf{y}}_C$ plane with a point defined by the angle θ and radius $r(\theta)$. The magnitude of θ is defined as the rotation about $\hat{\mathbf{z}}_C$ starting from $\hat{\mathbf{x}}_C$ with an offset of 10.3°. This offset is a throwback from prior representations of the cochlea and the line defined by $\theta = 10.3°$ is collinear with $\hat{\mathbf{x}}_C$.

$$r(\theta) = \begin{cases} \mathrm{A}e^{-\mathrm{B}\theta} & \theta \geq 100^o \\ \mathrm{C}\left[1 - \mathrm{D}\ln(\theta - \theta_0)\right] & \theta < 100^o \end{cases} \quad \theta \in \left[\ 10.3^o, \quad 910^o\ \right] \tag{II.1}$$

The parameter values are specified in the results of Cohen [26] and shown in Table II.1. It should be noted that the value for A used in this model is an average value, with male cochleas being larger than female ones [26]. Also the value of C is constrained to make the two sections of the curve continuous. Because the tested electrode arrays are models based on their interior edge, a model for the interior wall of the scala tympani is required.

A study by Zrunek et al. [133] found the average interior width and height dimensions of the scala tympani through measuring negative space molds of bone specimens. Width refers to the maximum cross section dimension in the space $\{\hat{\mathbf{x}}_C, \hat{\mathbf{y}}_C\}$ and normal to the lateral wall while height is the maximum section thickness in the space $\{\hat{\mathbf{z}}_C\}$. A linear interpolation of the results as a function of angle θ in [26] was used to

θ (deg)	0	10.3	90.0	180	270	360	450	585	675	1000
width (mm)	1.66	1.66	1.60	1.41	1.31	1.21	1.20	1.30	1.29	1
height (mm)	1.25	1.25	1.22	1.03	0.96	0.82	0.87	0.78	0.65	0.65

Table II.2: Scala Tympani Width as a Function of Depth Angle

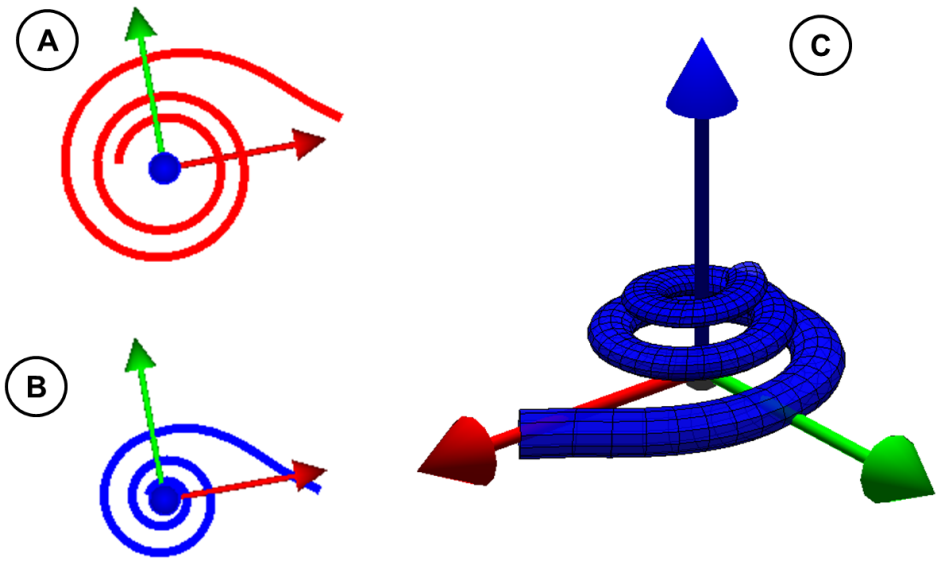

Figure II.2: Nominal cochlea shape. (A) 2D View of lateral (outer) wall helical pattern from Cohen model. (B) 2D View of modiolar (inner) wall helical pattern extrapolated from Cohen model and Zrunek data. (C) A 3D rendering of the scala tympani volume based on these parameters.

construct the inner wall of the scala tympani. The control points used in the interpolation are shown in Table II.2. The height of the cochlea through three turns has been measured by Erixon et al. [31] as approximately 4mm with a resulting helical pitch of roughly 1 mm/turn. The results from Whiting et al. [121], based of CT scans of implanted electrodes, also supports this estimated helical pitch. A digital rendering of the cochlea model based on data these works is shown in Figure II.2.

II.2 Surgical Access to the Cochlea

Access to the cochlea lies past the facial recess which poses two restrictions on any tool used for CI implantation. A study by Teszler et al. [108] examined the shape of the facial recess through measurements of imaged cross sections of the temporal bone in 200 patients. These results indicated a minimum clearance of 2 mm through the facial recess at its narrowest point which suggests that tools designed to pass through this anatomical constraint should be below this diameter. While Teszler's study examined the dimensions of the facial recess, it did not characterize the allowable electrode insertion approach angles. The anatomy of the facial recess limits the orientation workspace of a robot gripper. This information about the orientation workspace is an important design specification that has not been characterized in the literature.

An experiment was designed to obtain an accurate specification for the allowable orientation workspace for cochlear implant surgery. For this experiment, a tool with a diameter of 1.8mm was used to test the available angular workspace on 10 human cadaveric temporal bone specimens. An NDI Polaris Vicra optical tracker was used to collect position and orientation information on the tool. The tool tip was placed at the cochleostomy and measurements were taken as the tool was pivoted about the cochleostomy to trace the angular limitations of the facial recess. For each bone, 10 trials were conducted with roughly 600 data points taken per trial. A convex hull method [8] was used to reconstruct the continuous curve enclosing the allowable angular straight line access to the cochlea. Figure II.3 shows a polar plot of the available tool tilting workspace for all temporal bones. The radial distance of each point on a given closed curve provides the maximal tilt angle at a given tilt direction, designated in the plot by the polar coordinate. The figure shows a high variability of

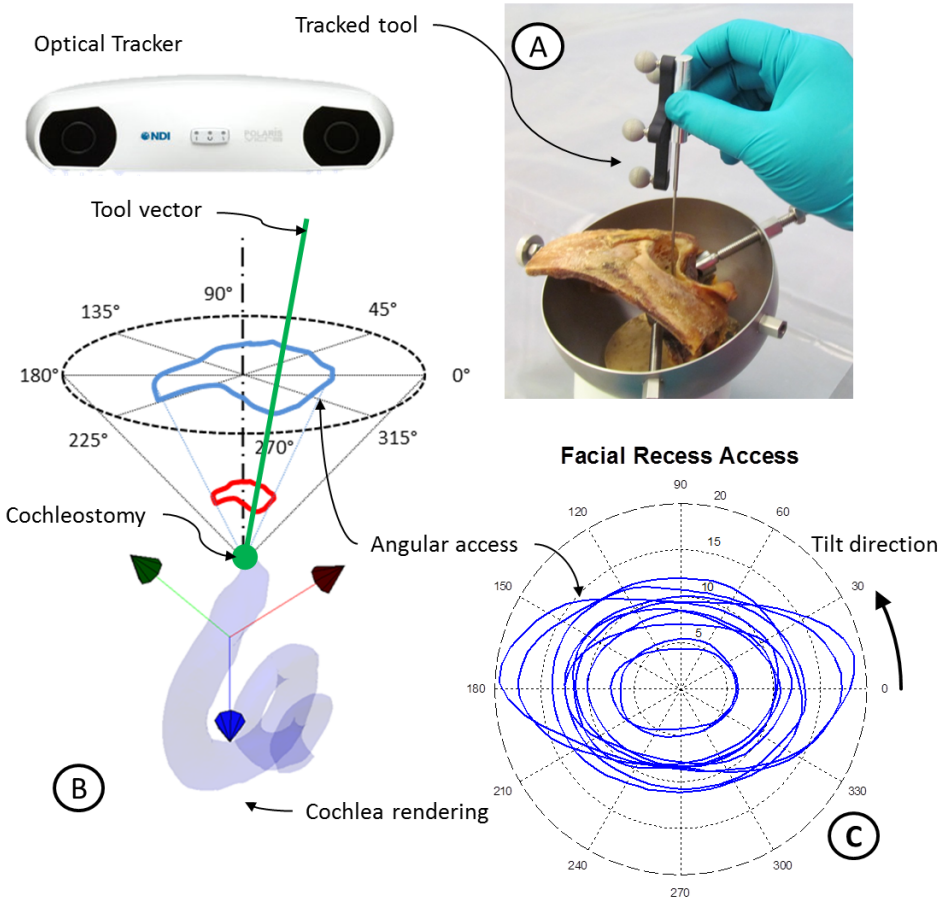

Figure II.3: (A) A tracked tool with diameter comparable to the proposed insertion robot's gripper pivots about cochleostomy of 10 human temporal bones. (B) For each temporal bone an angular access perimeter is defined by tracing the limits imposed by the facial recess. (C) The results show average access of approximately $\pm 10°$

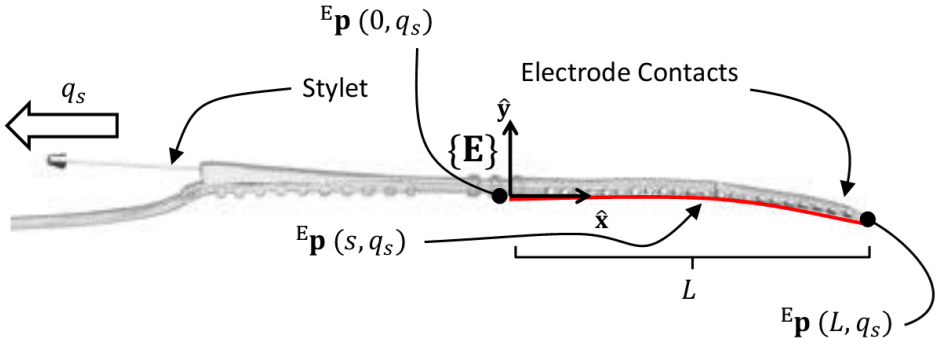

Figure II.4: *Contour Advance* perimodiolar electrode array.

maximal tilting range. Note that all curves have been plotted such that their major axes align along the 0° tilt direction. The major axis aligned with our proposed 2D insertion plane. The results show that the minimal angular tilting workspace was 6° and the maximal range was 17°. This data is used to define workspace requirements for the design of the robot for CI insertion described in Chapter III.

II.3 Perimodiolar Electrode Array Shape Modeling

The PEA is an underactuated elastic beam comprising of 22 electrode contacts embedded into an elastomer body. A stylet is also placed in the *Contour Advance* PEA from Cochlear Ltd. as shown in Figure II.4. This section covers the modelling of the PEA kinematics and a method to estimate the shape of new PEA's based on measurements from a representative sample set.

Frame $\{\mathbf{E}\}$ defines the local coordinate frame of the PEA and is centered on the manufacturer-specified point to grip the PEA. This can be seen as a set of three toroidal ribs in the midsection of the PEA. The frame axis $\hat{\mathbf{x}}_E$ is aligned with the length of the stylet and axis $\hat{\mathbf{z}}_E$ is normal to the plane in which the PEA curls. The shape of the electrode array as a planar representation can be written as a function $\theta(s, q_s)$ where θ is the tangent of the curve, s represents arc length, and q_s is the

length of removed stylet. The curvature modeled is on the modiolar edge of the PEA which is the side of the PEA touching the modiolus (inner wall) during insertion. Using a modal representation [22] and following the approach of Zhang et al. [130], the shape function can be given as:

$$\theta(s, q_s) = \boldsymbol{\psi}(s)^T \mathbf{a}(q_s) \tag{II.2}$$

where $\mathbf{a}(q_s)$ is the vector of modal function coefficients for a given amount of pull on the stylet q_s and $\boldsymbol{\psi}(s)$ is a vector containing the modal basis as a function of arc length $s \in [0, L]$. The vector $\mathbf{a}(q_s)$ is given as a function of a characteristic matrix $\mathbf{A}$ that maps modal basis functions $\boldsymbol{\eta}(q_s)$ to describe the change in electrode shape as a function of stylet pull.

$$\mathbf{a}(q_s) = \mathbf{A}\boldsymbol{\eta}(q_s) \tag{II.3}$$

This characteristic matrix $\mathbf{A}$ is an unknown *calibration matrix* that is sought to model an individual PEA. It is an application of Zhang's method [130] to the modelling of clinically available electrode rather than to the design of custom steerable electrodes. First, this section will detail how the calibration matrix is used to reproduce PEA kinematics and the following section will detail the identification of the calibration matrix elements from physical data. The modal basis functions $\boldsymbol{\psi}(s)$ and $\boldsymbol{\eta}(q_s)$ are polynomial sets of degree n and m respectively:

$$\boldsymbol{\psi}(s) = [s^0, s^1, s^2, ..., s^{n-1}]^T,\ \boldsymbol{\psi}(s) \in \mathbb{R}^{n\times 1} \tag{II.4}$$

$$\boldsymbol{\eta}(q_s) = [q_s^0, q_s^1, q_s^2, ..., q_s^{m-1}]^T,\ \boldsymbol{\eta}(q_s) \in \mathbb{R}^{m\times 1} \tag{II.5}$$

It must be noted that numerical stability becomes an issue with high order polynomial

basis functions [6] and in general it is better to use basis functions such as Chebychev polynomials or Fourier series if a high number of terms in the basis is required. For this application, third order polynomials (i.e. $m = n = 4$) were sufficient to accurately capture the kinematics of PEA's.

Given matrix $\mathbf{A}$, the tangent angles along the electrode are:

$$\theta(s, q_s) = \boldsymbol{\psi}(s)^T \mathbf{A} \boldsymbol{\eta}(q_s) \quad \mathbf{A} \in \mathbb{R}^{m \times n},\ \boldsymbol{\psi}(s) \in \mathbb{R}^m,\ \boldsymbol{\eta}(q_s) \in \mathbb{R}^n \tag{II.6}$$

The points along the curve are given in the PEA by vector $\mathbf{p}_e(s, q_s)$ and can be found by integrating the tangent function along the arc length:

$$\mathbf{p}_e(s, q_s) = \begin{bmatrix} \int_0^s cos\left(\theta(\tau, q_s)\right) d\tau \\ \int_0^s sin\left(\theta(\tau, q_s)\right) d\tau \\ 0 \end{bmatrix} \tag{II.7}$$

The shape jacobian for a position s along the electrode array's length becomes:

$$\frac{d\mathbf{p}_e}{dt}(s, q_s) = \begin{bmatrix} -\int_0^s \left(sin\left(\theta(\tau, q_s)\right) \frac{d\theta}{dt}\right) d\tau \\ \int_0^s \left(cos\left(\theta(\tau, q_s)\right) \frac{d\theta}{dt}\right) d\tau \\ 0 \end{bmatrix} \tag{II.8}$$

where:

$$\frac{d\theta}{dt} = \frac{d}{dt}\left(\boldsymbol{\psi}(s)^T \mathbf{A} \boldsymbol{\eta}(q_s)\right) = \left[\boldsymbol{\psi}(s)^T \mathbf{A} \left(\frac{d\boldsymbol{\eta}(\boldsymbol{s})}{dq_s}\right)\right] \frac{dq_s}{dt} \tag{II.9}$$

To determine whether robotic insertion of PEA's is possible there is a need to determine the bounds on shape variability and the variations in the calibration matrix $\mathbf{A}$. This information will inform whether individual PEA calibration is necessary. To test shape variability a series of seven electrode arrays were tested to record their shape

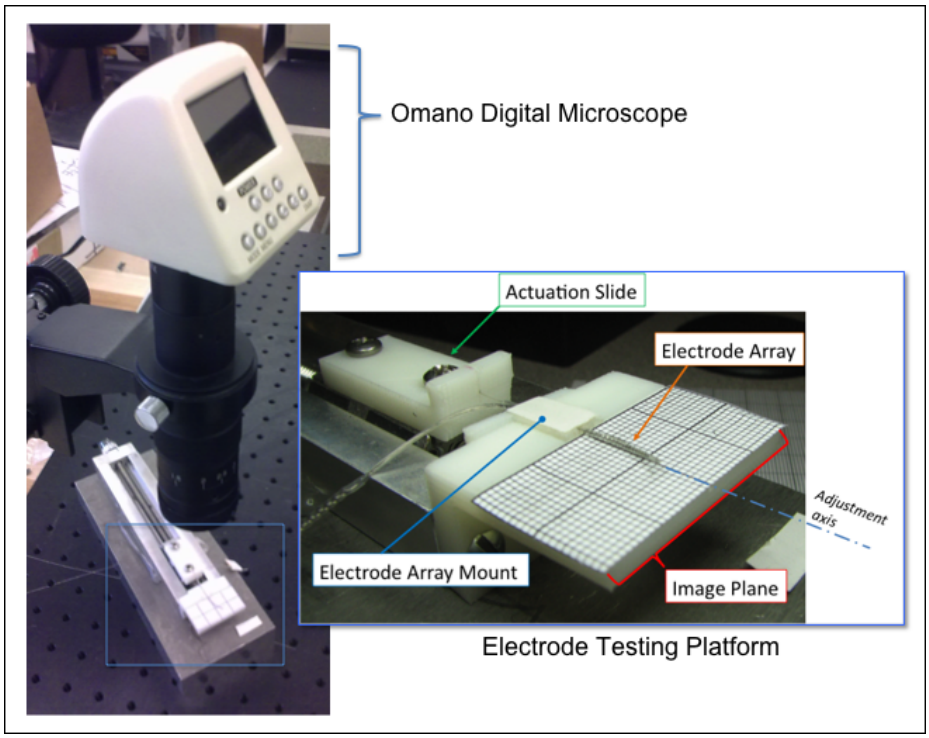

Figure II.5: Electrode array calibration test fixture

under actuation. A set of Contour Advance PEA's were supplied by Cochlear Ltd. for experimental evaluation.

The test setup cantilevered a single PEA from its base over an imaging plane with a separation of approximately 1 mm. Grid paper was adhered to the imaging plane to provide orientation and scale for the captured images. A high definition digital microscope was placed over the imaging plane to photograph the electrode array. The section of the fixture constraining the base of the array was rotated about its longitudinal axis so that the array curled in the imaging plane. The electrode arrays' stylet was removed by manual turning of a linear slide with an accuracy of 0.05 mm.

A single trial of an electrode array involved capturing an image of the array in its initial state and subsequent images as the stylet was removed in 1.27 mm increments

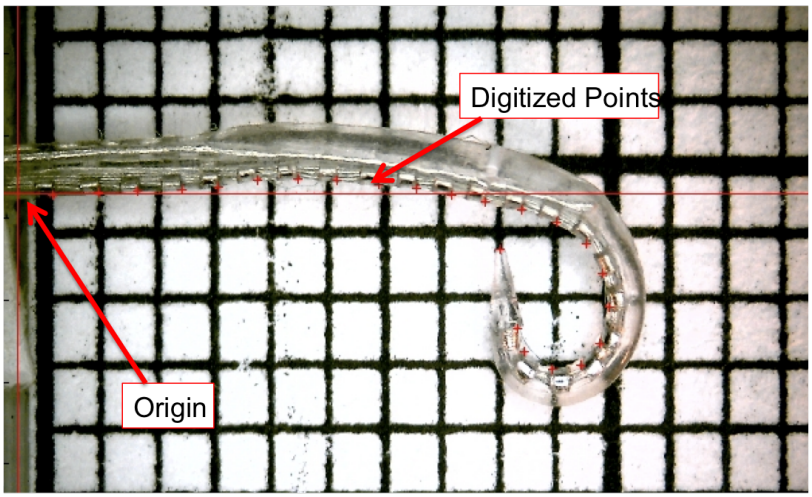

Figure II.6: Digitized image of Contour Advance electrode array.

as determined by the pitch of the lead screw. After each step of actuation, an image was taken after any transient deformation had passed. A minimum of 14 steps were required before further stylet removal had no impact on the final shape. The first trial of a new electrode array was considered the reference trial and three additional trials per array were made. This reference trial was considered the baseline shape for comparison with repeated trials on an array and was used for shape repeatability for a given PEA and for comparison of shape variations among different arrays. Between each trial on a single array, the stylet was reinserted using a custom tool provided by Cochlear Ltd.

After a series of images were taken, points along the array were manually digitized. Within each array, there are 23 distinct electrode sections and a marker was digitally added to a corner of each of these segments and to the tip of the implant for a total of 24 markers, Figure II.6. The corners of the electrodes could be located within 0.01mm of their true location in the image.

For calibrating the shape kinematics of the PEA's, points along a given PEA are segmented for arc length values $s = s_0, s_1, ..., s_{max}$ where $s_{max} = L$ is the length

of the electrode from some base position s_0. These points are segmented from a collection of images that correspond with a given known amount of pull on the stylet $q_s = q_{s,0}, ..., q_{s,max}$ where $q_{s,max}$ is the length required to remove the stylet from the electrode array. By taking w measurements of the shape (the tangent angle at a segmentation point) for z steps of stylet actuation, all experimental data can be captured in an experimental data matrix $\mathbf{\Phi}$ such that:

$$\mathbf{\Phi} = \mathbf{\Omega A \Gamma} \tag{II.10}$$

where:

$$\mathbf{\Gamma} = [\boldsymbol{\eta}(q_{1,0}), ..., \boldsymbol{\eta}(q_{s,max})] = \begin{bmatrix} 1 & \cdots & \cdots & 1 \\ q_{s,min} & \ddots & & q_{s,max} \\ \vdots & & \ddots & \vdots \\ q_{s,min}^{m-1} & \cdots & \cdots & q_{s,max}^{m-1} \end{bmatrix} \in \mathbb{R}^{m \times z} \tag{II.11}$$

$$\mathbf{\Omega} = \begin{bmatrix} \boldsymbol{\psi}(s = s_0)^T \\ \vdots \\ \boldsymbol{\psi}(s = s_{max})^T \end{bmatrix} = \begin{bmatrix} 1 & \cdots & (s = 0)^{n-1} \\ \vdots & \ddots & \vdots \\ 1 & \cdots & (s = s_{max})^{n-1} \end{bmatrix} \in \mathbb{R}^{n \times w} \tag{II.12}$$

$$\mathbf{\Phi} = \begin{bmatrix} \theta(s_0, q_{1,0}) & \cdots & \theta(s_0, q_{1,max}) \\ \vdots & \ddots & \vdots \\ \theta(s_{max}, q_{1,0}) & \cdots & \theta(s_{max}, q_{1,max}) \end{bmatrix} \in \mathbb{R}^{w \times z} \tag{II.13}$$

The matrix system of equations from (II.10) can be solved for the calibration matrix $\mathbf{A}$ by using Kronecker product $\otimes$ algebra [39]:

$$\left(\mathbf{\Gamma}^T \otimes \mathbf{\Omega}\right) Vec(\mathbf{A}) = Vec(\mathbf{\Phi}) \tag{II.14}$$

From the digitized images, the experimental matrices Ω, Γ, and Φ were constructed and the calibration matrix $\mathbf{A}$ was calculated for each PEA. To verify the model, calculated PEA shape was overlaid over the experimental image. The results showed a good agreement with the experimental results as shown Fig. II.7.

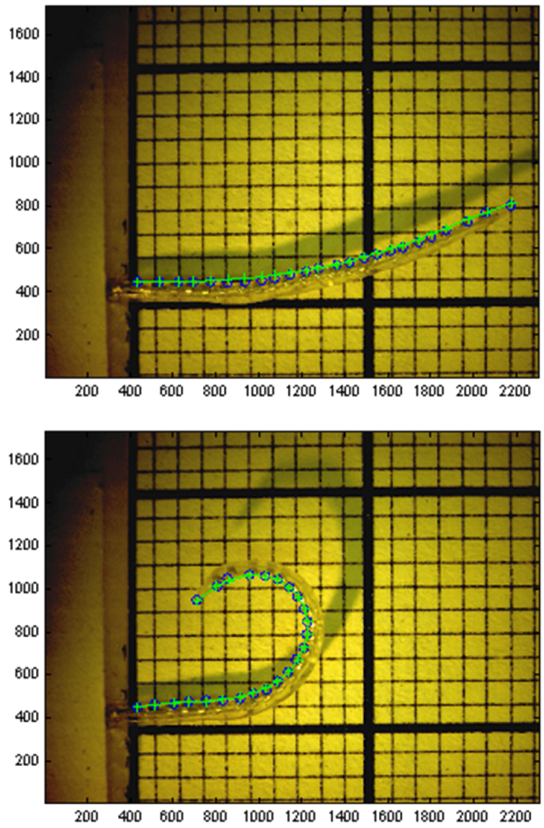

Figure II.7: Tested electrode arrays with shape reconstruction overlay, axes are in pixels. The reconstructed shape of the PEA's modiolar side is shown in green. The calibration matrix accurately captures the shape seen in the original image.

Variability Upon Stylet Reinsertion

Two forms of repeatability are important to consider when evaluating the PEA's. During manufacturing, PEA's require the stylet to be loaded inside the silicone carrier and its final shape checked for suitability for surgical insertion. After this check, the stylet position may need modification. In this case, the stylet must be reinserted

into the silicone encapsulant surrounding the electrode array. By examining shape variability in each electrode array for each stylet reinsertion, a new calibration matrix can be implemented should a second insertion attempt be necessary.

Shown below in Figure II.8 is a representative result of shape variability upon stylet reinsertion. In each column of plots, the left figure is the shape of the electrode array in the four trials and the listed stage of actuation (q_s = 1.27mm, 3.81mm, etc.). The blue curve is the reference trial used as a basis of comparison. The right plots are the mean errors along the segmentation points with the error bars spanning 3 standard deviations. On the onset of stylet removal, the mean error from the reference trial at the electrode tip is smaller than 1 mm. As can be expected, the position error increases along the length of the electrode array since small variations in θ accumulate as position variations.

Variability Between Electrode Arrays

The second form of repeatability to be examined is the shape variation between fresh electrode arrays. Since the arrays are not actuated before use, development of a single model with an understanding of error bounds was considered as a potential method for developing an insertion path plan. In comparing different electrode arrays, segmentation was reinterpolated at fixed length intervals. This was necessitated by slight manufacturing variations in the spacing of electrodes. An initial comparison of different arrays resulted in large variations. Securing the base of the electrode array resulted in large variations of the tangent angle in the first segment.

Variation in tangent angle and position of the PEA's with the stylet fully inserted were calculated and plotted below in Figure II.9. The position variation is considerably larger between the electrode arrays than within one electrode with multiple stylet reinsertions. The position standard deviation is upwards of four times greater

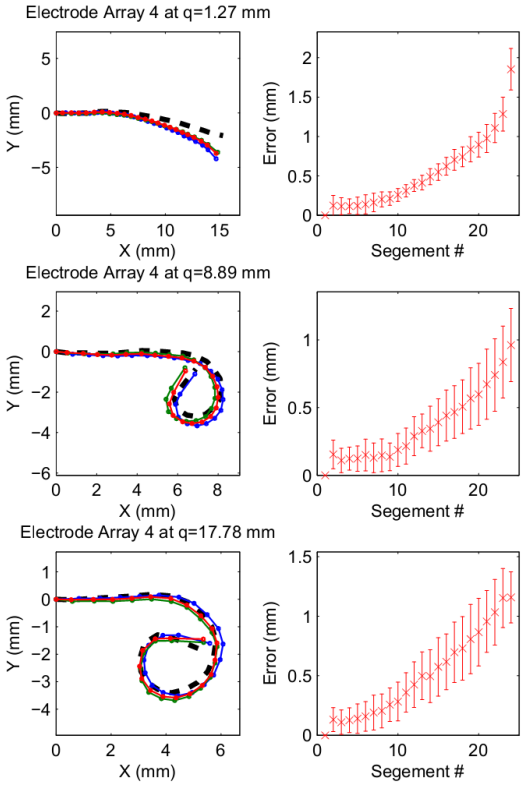

Figure II.8: Shape variation in electrode array 4 (thick dashed line represents reference trial, dotted lines represent repeated trials)

than the comparisons of the previous section. This suggested that the electrode arrays should not be modeled using a single calibration matrix but should instead be inserted using their specific calibration matrix. *This conclusion justifies the use of a insertion robotic tool as opposed to designing a mechanical linkage for insertion of a "nominal" electrode with an average calibration matrix* **A**.

PEA Shape Estimation

This section presents a method of estimating the kinematic parameters of a new PEA based on knowledge gained from the set of calibrated PEA's. The goal of this algorithm is to find a reasonable approximation of **A** without performing detailed measurements.

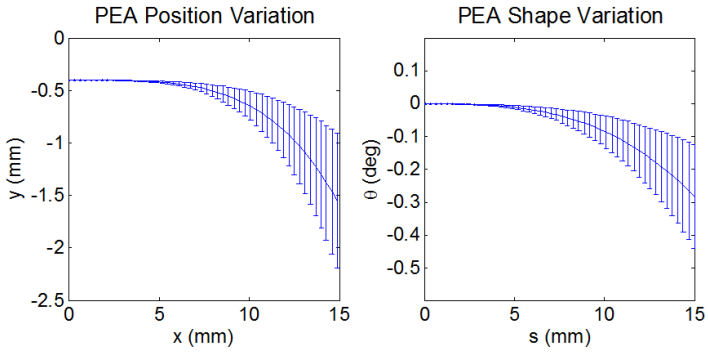

Figure II.9: Electrode array standard deviation as a function of arc length. Left: Average position and standard deviation of PEA curve along $\hat{\mathbf{y}}_E$ as a function of length along $\hat{\mathbf{x}}_E$. Right: Tangent angle θ average and standard deviation as a function of arc length s.

Calibration of individual PEA's prior to insertion is not clinically viable since reinsertion of the stylet into an array is not allowed prior to insertion in a patient. This is due to the risk of puncturing the PEA silicone body and increasing the risk of infection. However, the measured data may be used to construct a likely PEA matrix $\mathbf{A}_{est}$ which may be used for path planning.

One assumption in the estimation of a PEA's shape is that there is a known point that the PEA passes through. This point is called the *insertion constraint* and is expressed in the PEA frame $\{\mathbf{E}\}$. Figure II.10 is used to describe the insertion constraint. When the PEA tip is brought to the insertion point it must pass through $\mathbf{p}_c$. We define the point ${}^E\mathbf{p}_m$ as a measured point along the PEA length in frame $\{E\}$ with[2] $\mathbf{p}_m = {}^E\mathbf{T}_C\mathbf{p}_e$.

Creating an estimate of the calibration matrix $\mathbf{A}$ is a two step process: first the initial shape is defined and then the relationship between stylet actuation and change in shape is applied. Data from previously calibrated PEA's is used to generate an estimation for the current PEA. The calibration matrix defined in (II.3) can be split

[2]Notation ${}^B\mathbf{T}_A$ is the homogeneous transformation from $\{A\}$ to frame$\{B\}$

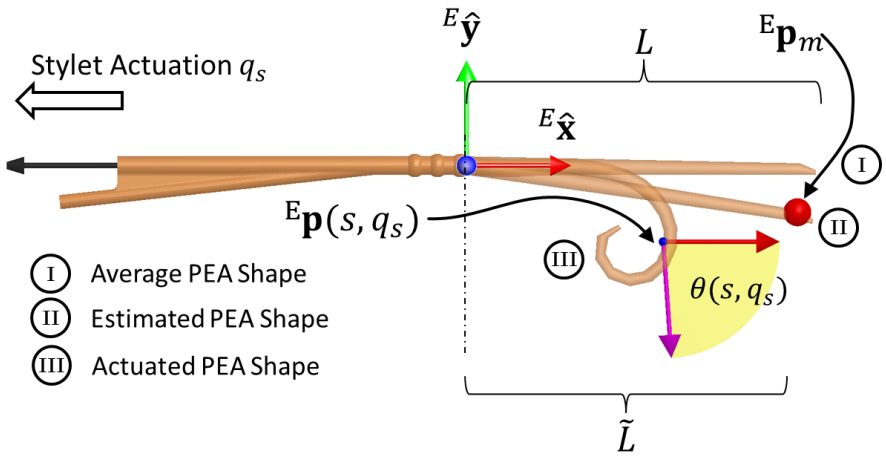

Figure II.10: PEA shape estimation. The shape is defined by the tangent $\theta(s, q_s)$ of the PEA's modiolar edge. A nominal PEA shape $\bar{\theta}(s, q_s)$ (I) is modified to pass through the known point of insertion, ${}^E\mathbf{p}_m$ (II). The distance along the PEA curve to the insertion point is denoted as $\tilde{L}$. An estimate of the relationship between $\dot{\theta}$ and stylet actuation $\dot{q}_s$ completes the kinematic model of the PEA with a example of an actuated PEA shown with (III).

into a column vector and a 4×3 matrix:

$$\mathbf{A} = \begin{bmatrix} \mathbf{a}_{0_{[4\times1]}}, & \tilde{\mathbf{A}}_{[4\times3]} \end{bmatrix} \tag{II.15}$$

When $q_s = 0$, (II.10) can be written as:

$$\theta(s, 0) = \boldsymbol{\psi}(s)^T \mathbf{a}_0 \tag{II.16}$$

The average initial PEA shape is defined as $\bar{\theta}(s, 0)$ and discretize the PEA into z evenly distributed points to create the vector $\bar{\boldsymbol{\theta}} \in \mathbb{R}^{z\times1}$. This average shape comes from the experimentally measured PEA's. For a given $\mathbf{a}_0$, a set of discretized points of the estimated shape creates the vector $\tilde{\boldsymbol{\theta}} \in \mathbb{R}^{z\times1}$. The difference between the average

and estimated shape is then defined as:

$$\Delta\boldsymbol{\theta} = \tilde{\boldsymbol{\theta}} - \bar{\boldsymbol{\theta}}\,(s, 0) \tag{II.17}$$

The scalar value $\tilde{L} \in [0, L]$ defines a point along the PEA which intersects with the insertion point ${}^{E}\mathbf{p}_m$. Using these definitions, the initial shape of the PEA is estimated by numerically solving the following constrained optimization problem:

$$\begin{aligned} &\underset{\mathbf{a}_0, \tilde{L}}{\text{minimize}} \quad \Delta\boldsymbol{\theta}^T \Delta\boldsymbol{\theta} \\ &\text{subject to} \quad \mathbf{p}(\tilde{L}, 0) = \mathbf{p}_m, \quad \tilde{L} \in [0, L] \end{aligned} \tag{II.18}$$

The solution set of coefficients are denoted as $\tilde{\mathbf{a}}_{0,est}$. Once the estimate of the initial shape ($\theta(s, 0) \forall s \in [0, L]$) is made, an estimate of the average rate of change of PEA shape to stylet actuation ($\frac{d\bar{\theta}}{dq_s}$) is based on the average of rates of change of previously calibrated PEA's. These rates are computed from the sub-matrices $\tilde{\mathbf{A}}$. It can be shown that the average of the h known calibration matrices $\tilde{\mathbf{A}}_i, i = 1, ..., h$ describes the average rate of shape change per stylet pull $\frac{d\bar{\theta}}{dq_s}$ and the estimated calibration matrix becomes:

$$\mathbf{A}_{est} = \begin{bmatrix} \mathbf{a}_{0,est} & \sum_{i=1}^{h} \frac{1}{h} \tilde{\mathbf{A}}_i \end{bmatrix} \tag{II.19}$$

II.4 Insertion path planning

Insertion path planning is separated into two tasks: finding optimal positions and orientations for the electrode array through the range of insertion depths into the cochlea and smoothing those optimal points into a trajectory a robotic insertion tool may follow. Assuming that the PEA bending plane has been aligned with the plane approximating the basal turn, the path planning DoF can be described as the length

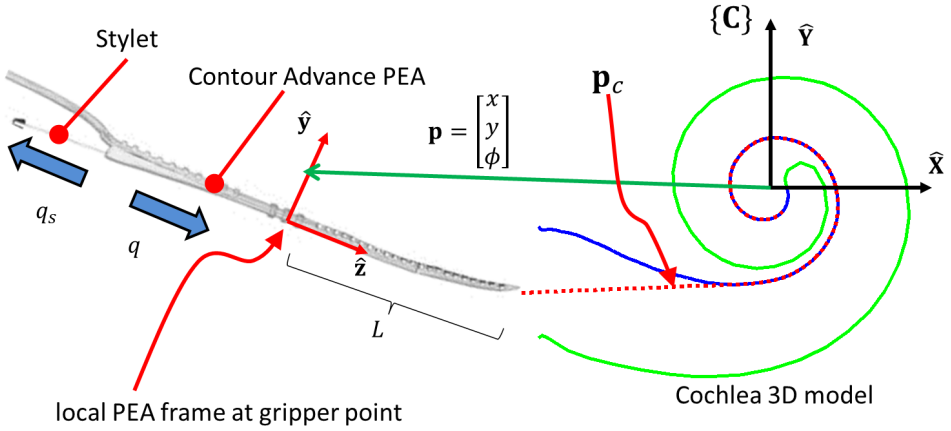

Figure II.11: 2D Robot insertion concept with four dof

of stylet removed from the perimodiolar electrode array q_s, rotation of the electrode in the 2D plane ϕ, and two translation components in the plane (Fig. II.11). Finding a trajectory requires a 2D model of the scala tympani while smoothing of discrete path points can be done by fitting a cubic spline.

For optimal insertion, the PEA should fit the shape of the scala tympani by approximating the modiolar (inner) wall as much as possible while avoiding contact with the lateral (outer) wall. The desired path for the PEA tip begins as a straight line from the insertion point into the scala tympani toward the modiolar wall intersecting at the closest point of tangency. Let the points along this path be given by Cartesian coordinates $\mathbf{p}_p(s) \in \mathbb{R}^{2\times 1}$. During insertion, the focus is on the inserted portion of the PEA; hence, we define a weight matrix $\mathbf{W} = diag(0...w, w, w, w) \in \mathbb{R}^{2z\times 2z}$ where the scalar weight w is used for points that are inside the scala tympani and a zero value for points not yet inserted into the scala tympani. We define an objective function for each insertion depth d such that a penalty is applied for deviation from the desired

path and an additional penalty is applied for violating the modiolar wall boundary:

$$\underset{d,\phi}{\operatorname{argmin}} \frac{1}{2} \left(\mathbf{T}^T \mathbf{W} \mathbf{T} + \mathbf{U}^T \mathbf{W} \mathbf{U} \right) \tag{II.20}$$

where the vectors $\mathbf{T}$ and $\mathbf{U}$ are given by:

$$\mathbf{T} = \begin{bmatrix} \mathbf{p}_c(s=0) - \mathbf{p}_e(d,\phi,s=0) \\ \vdots \\ \mathbf{p}_c(s=L) - \mathbf{p}_e(d,\phi,s=L) \end{bmatrix} \in \mathbb{R}^{2z \times 1} \tag{II.21}$$

$$\mathbf{U} = \begin{bmatrix} u_e(s=0), & \cdots, & u_e(s=L) \end{bmatrix}^T \in \mathbb{R}^{2z \times 1} \tag{II.22}$$

The value of $u_e(s)$ indicates the interference distance relative to the modiolar wall for each digitized point along the electrode array (II.23).

The vectors $\mathbf{r}_e(s)$ and $\mathbf{r}_c(s)$ respectively denote the radial distances from the center of the cochlea to a point on the PEA specified by arc length s and the closest corresponding point on the scala tympani inner wall. This wall intersection penalty is a modification of the optimization function proposed in [129] which encourages reducing applying pressure on the modiolar wall.

$$\underset{s \in [0,\, L]}{\mathrm{u_e(s)}} = \begin{cases} \|\mathbf{r}_c(s) - \mathbf{r}_e(s)\| & if \, \|\mathbf{r}_c(s)\| > \|\mathbf{r}_e(s)\| \\ 0 & if \, \|\mathbf{r}_c(s)\| \leq \|\mathbf{r}_e(s)\| \end{cases} \tag{II.23}$$

During the simulation, the insertion depth d was set for 15 mm in 0.5 mm increments. Optimal position and orientation of the electrode array base were determined at each increment using a line search optimization method. The base location and

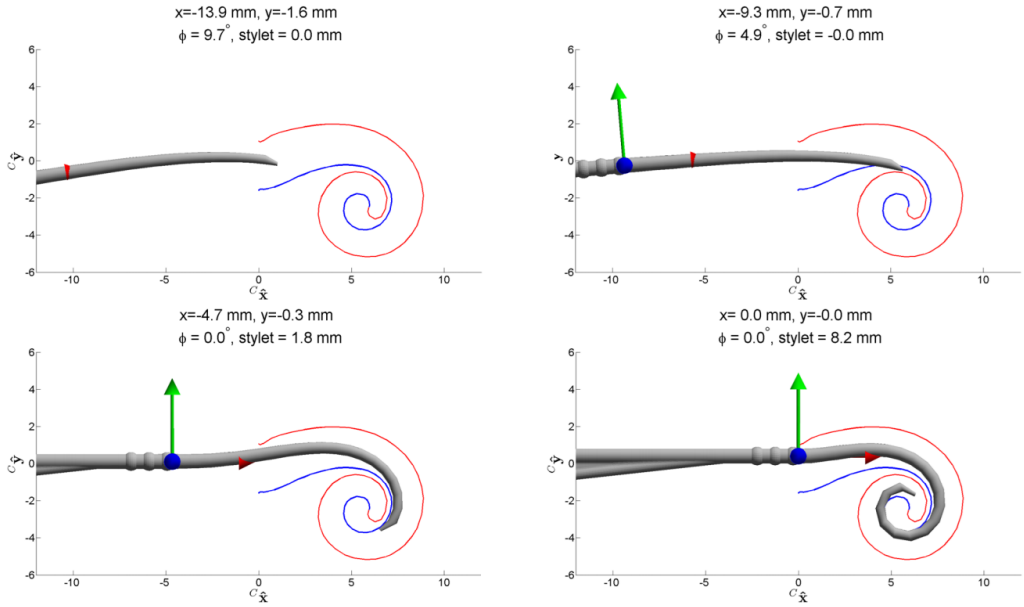

Figure II.12: Insertion simulation with 4 DoF

orientation of the simulated electrode define the end effector path of the robot. Sample snapshots of the insertion stages are shown in Figure II.12. In this figure, the blue curve is the modiolar (inner) wall of the scala tympani and the red curve is the lateral (outer) wall of the scala tympani. A cubic spline interpolation was used for evaluating intermediate positions along the trajectory for all DoF.

Each electrode array examined had a shape function incapable of not interfering to some degree with the inner wall of the scala tympani. Beyond an insertion depth of 9mm a purely kinematic model of the implant can no longer be used with these electrodes and a stiffness and friction model like the one proposed by Zhang et al. [127] is required.

A reduction of the DoF required on the insertion tool could be made by fixing ϕ to a constant value. For each electrode array, the single insertion angle with minimal error was selected. The summed error over each insertion step was used as the basis of comparison between the four and three degree of freedom design options. Using this

metric, the addition of the orientation DoF reduced the total error by an average of 35%. These results suggest that a 4 DoF insertion platform would be advantageous. Chapter III will use these results in the synthesis process.

Insertion Workspace Determination

The workspace for an insertion tool was bounded by the maximal and minimal values for each DoF over the entire insertion path. Figure II.13 shows the unsmoothed bounds for the workspace of the insertion tool based on the information gathered from the tested electrode arrays. The bound encompasses the paths from all electrode trials. In this simulation, most of the translation of the electrode occurs along the x axis. Translation in the orthogonal direction is limited, starting with a variation of approximately 8mm and converging to negligible variation near full insertion. Variation in electrode orientation requires that the insertion tool maintain mobility in this joint at full insertion depth. Although not required by the path planning routine, actuation in q_s must be capable of completely removing the stylet from the implant.

II.5 Summary of Insertion System Requirements

This chapter has presented a modeling framework to derive the workspace requirements for multi-degree of freedom robotic insertion system. In addition to the cochlea shape, access restrictions, and the behavior of the PEA during actuation there are several other important parameters which will be reviewed here and summarized in Table II.3. Work presented in [59] demonstrated that a targeting accuracy of 0.4 mm at the cochleostomy was sufficient for percutaneous electrode array insertion using a tool rigidly attached to the patient's skull without the capability of adjustment during insertion and sets the minimum known accuracy specification for successful CI insertion. Work from Zhang et al. [125] explored the relationship of speed and

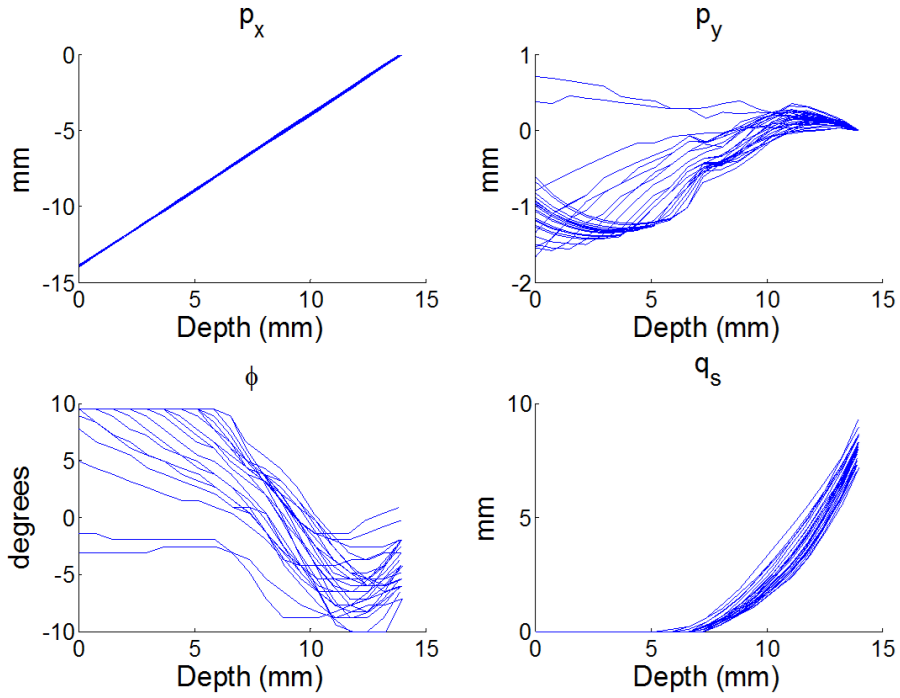

Figure II.13: Workspace bounds for the robot gripper in the cochlea frame $\{\mathbf{C}\}$.

Specification	Target Value	Ref.
Targeting accuracy	≤ 0.4 mm	[59]
Tool Maximum Dia.	2.0 mm	[108]
Insertion speed	0.5 - 5 mm/s	[125, 53]
Insertion force	$\sim$0.05 N	[66, 86, 53]
Angle of approach	$\pm 10^{\circ}$	

Table II.3: Summary of Derived CI Insertion Specifications

friction force using outer wall electrodes and found that insertion forces could be reduced by increase speed with the reduction seen at speeds as high as 5 mm/s. This speed was set as the maximum insertion speed requirement for a robotic CI insertion system. Work from several groups [66, 86, 53] have measured insertion forces in bone specimens and a general concensus is that a laboratory insertion can achieve insertion forces below 0.05N and this sets the force goal for robotic insertion. Lastly, experiments presented in this chapter have bounded the expected range of access a tool can use during CI insertion. Insertion simulations show that PEA insertion within this bound is feasible. The compilation of these various results create the set of design specifications for a robotic CI insertion system used in the next chapter.

In addition to the quantitative measures described in Table II.3 there are several other considerations specific to the CI insertion procedure. The surgical site is small and space above the site must be reserved for microscope vision. This implies that the tool design must be compact and lightweight so as to be as unobtrusive as possible. The design should also be sterilizable without requiring the disposal of expensive components. Since insertion forces are a critical means of assessing insertion quality, integrated force sensing is required. Lastly, the design should make the loading of PEA's into the gripper easy enough to be done during operation.

Chapter III

SYNTHESIS AND EVALUATION OF A WIRE-DRIVEN PARALLEL ROBOT FOR CI INSERTION

This chapter presents the kinematic modelling and task-driven synthesis of a robotic insertion tool for CI surgery. The chapter begins with the conceptualization of the insertion system and its place in the CI procedure. A model of the kinematics of closed loop wire actuation is then presented including analysis of conditioning, compliance, and sources of error specific to wire actuation. From this model and the task requirements presented in the previous chapter, a method of dimensional synthesis is presented.

The motivation for applying wire actuation into the mechanical design arose from several considerations. The first motivating consideration was the desire to isolate the DC motor actuators from the end effector. When this is accomplished with rigid link transmissions there is a penalty in weight added to the design. Wire rope, on the other hand, has negligible weight. This also allows greater flexibility in adjusting the weight distribution of the total device since the repositioning of the actuators does not incur a significant addition of weight. Also, application of wire actuation introduces several considerations not present in rigid transmission actuation schemes that have not been explored in parallel robot design. Wire-actuated links introduce kinematic coupling with implications on the mechanism's stiffness which are derived and discussed in this work.

The final sections of this chapter review the control system and mechanical design. A method of calibration addressing wire actuation backlash is presented in this

chapter. Finally, the chapter ends with a review of the prototype's performance based on requirements derived in Chapter II.

Part of the work presented in this chapter has been previously published in [81].

III.1 System Architecture

A conceptual illustration of robotic CI implantation is shown in Figure III.1. An electrode insertion system is supported on the operating table by a support arm. This arm is passive and may be statically balanced like the surgical microscope typically used in this procedure. The patient's head is expect to be secured in position by a Mayfield frame or similar device. The work presented in this chapter focuses on the insertion robot itself with the support arm considered a commercially available product.

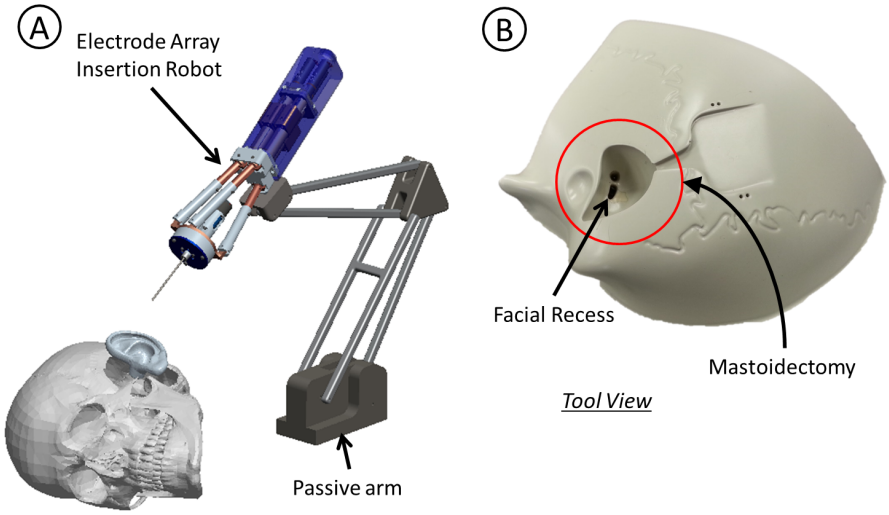

Figure III.1: Robotic insertion concept. (A) After the surgeon has completed the mastoidectomy and gained access to the cochlea, the robotic system is brought to place on a passive arm. Registration to the cochlea can be done with external vision of the cochleostomy or through preoperative image registration [59] (B) The view of the surgical site from the tool's perspective. The mastoidectomy and small opening through the facial recess restrict tool dimensions and angle of approach. Model temporal bone provided by Cochlear Ltd.

The insertion robot uses a planar 3 DoF parallel kinematic structure with a fourth actuator mounted on the end effector for stylet actuation for several reasons. A planar structure matches the kinematic description of the PEA insertion process [28] and the approximate 2D model of the cochlea [26, 114] without added complexity. A parallel mechanism was chosen to control PEA placement due to its advantages in precision, compactness and stiffness [96]. Lastly, forces acting on the PEA must be transmitted completely through the force transducer. This necessitates having a separate actuator on the end effector.

Among various configurations of planar parallel mechanisms a design was chosen based on the 3R$\bar{\text{P}}$R configuration: 3 parallel actuated prismatic links connected to the robot base and end effector with revolute joints. This type of kinematic chain leads to a compact form factor and allows exploration of new wire actuation concepts which, to the best of the author's knowledge, has not been applied to planar, piston driven parallel mechanisms.

The kinematic definition of one of the three chains is shown in Figure III.2(A). Force transmission between the motors and the moving platform is accomplished through a tensioned wire loop for each leg (Fig III.2 (B)). Motor rotation was transferred to wire translation through a lead screw. While this adds length to the device for the screw/nut travel it was incorporated into the initial design for two considerations. 1) The motor assemblies need a right angle connection to minimize the cross sectional footprint of the device. 2) backlash in the motor gearheads (necessary for compact motors) leading to position errors is reduced in proportion to the pitch of the lead screw used. Future designs will remove this intermediate step and connect the wire loop to a capstan coupled to the motor output shafts for further compactness.

Wire actuation was selected over rigid transmission elements to enable motor

isolation and to have greater control over weight distribution. Another significant advantage is that wires have greater potential for miniaturization in comparison to lead screws and other linear motion mechanisms which would be found inside the prismatic links. The concessions made in using wirerope for this application include a reduction in joint stiffness and a smaller load capacity. Internal friction [88] may necessitate nonlinear compensation. Also, fatigue on wire rope can lead to breakage and as a result need more disciplined maintenance. Since cochlea insertion forces generally do not exceed $0.5N$, the stiffness and capacity losses were not expected to significantly disrupt performance.

III.2 Kinematic Modeling

Position control of the parallel robot is accomplished using a closed form inverse position solution. The linearized instantaneous kinematics of the robot is used in performance analysis, calibration and for real time regulation of position based on limitations of the actuators, joints and task space constraints. The derivation of the kinematics and the effects of wire actuation are presented throughout this chapter.

Figure III.2(A) shows the kinematic model of one kinematic chain of the robot. Unless otherwise explicitly stated, all vectors will be described in the robot base frame $\{\mathbf{B}\}$. Motor input is described by a vector $\boldsymbol{\theta} = [\theta_1, \theta_2, \theta_3]^{\mathrm{T}}$. Motor rotations θ_i correspond with linear translations u_i of wire-carriages by using lead screws and nuts. The task space configuration is defined at the tip of the electrode array gripper by $\mathbf{x} = [p_x, p_y, \phi]^{\mathrm{T}}$. The active joint variables $\mathbf{q} = [q_1, q_2, q_3]^T$ designate the piston strokes. The fourth degree of actuation is employed specifically for perimodiolar electrodes which require the coordinated pulling of the embedded stylet during the insertion process. Pulling of the stylet is denoted by q_s.

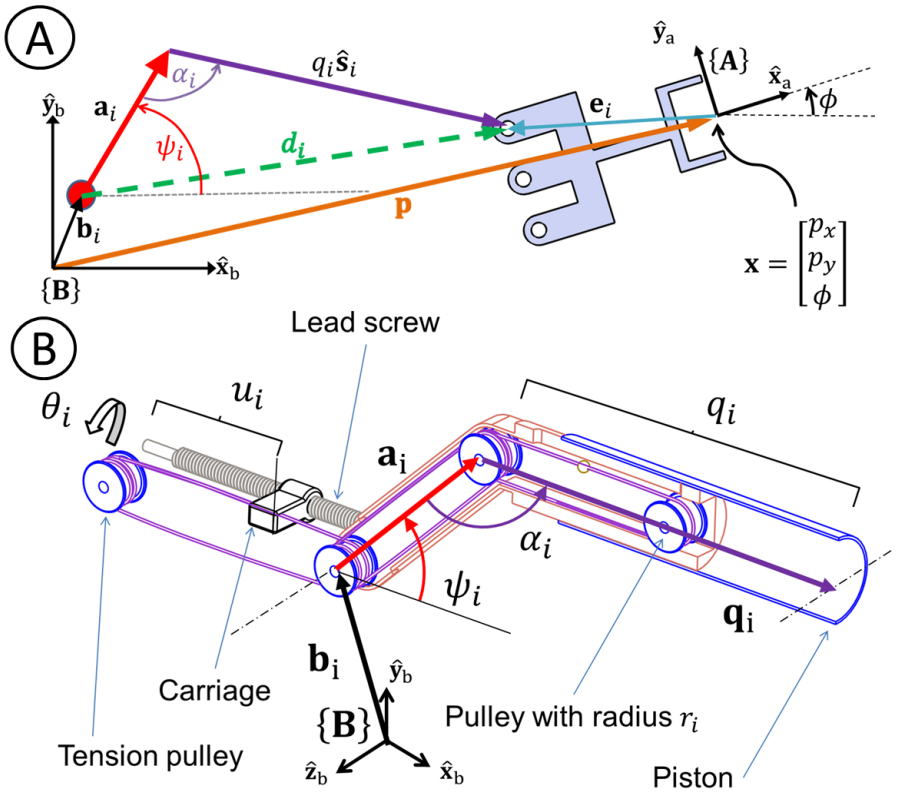

Figure III.2: Kinematic diagram for 3RPR manipulator. (A) One of the three kinematic chains is shown schematically for the 3RPR design. (B) The prismatic link is actuated through a closed loop wire rope. This approach allows the motors to be placed at an arbitrary distance from the link. The motors drive a carriage on a leadscrew which transmits motion to the piston.

Inverse Kinematics

Given the gripper pose $\mathbf{x} = \left[\mathbf{p}^{\mathrm{T}}, \phi\right]^{\mathrm{T}}$ the inverse kinematic solution is found using loop closure of the kinematic chains. Vectors $\mathbf{b}_i$ in Figure III.2 define the location of the i'th fixed revolute joint in the robot base frame. Vectors $\mathbf{a}_i = [\cos(\psi_i), \sin(\psi_i), 0]^T$ define the mechanical offset of the piston axis from the i'th fixed revolute joint and the distances a_i are defined as $a_i = \|\mathbf{a}_i\|$. The piston stroke is defined by $\mathbf{q}_i = q_i\hat{\mathbf{s}}_i$. The angles α_i are the fixed interior angles between the piston axis $\hat{\mathbf{s}}_i$ and $\mathbf{a}_i$. The i'th

revolute joint on the moving platform connects to the piston tip. Vectors $\mathbf{e}_i$ connect the gripper point $\mathbf{p}$ to the i'th revolute joint of the moving platform.

To write loop closure equations, we define vectors $\mathbf{d}_i$ from the i'th fixed revolute joint to the corresponding revolute joint in the moving platform (Fig. III.2). We then solve the following loop closure equation for $\mathbf{d}_i$:

$$\mathbf{p} + \mathbf{e}_i - \mathbf{d}_i - \mathbf{b}_i = \mathbf{0} \tag{III.1}$$

Given $\mathbf{d}_i$, the piston stroke can be found using the cosine triangle identity:

$$q_i = a_i \cos(\alpha_i) \pm \sqrt{a_i^2 \cos^2(\alpha_i) - a_i^2 + d_i^2} \tag{III.2}$$

and through completing the triangle, the vectors $\mathbf{a}_i$ and $\mathbf{q}_i$ are known. Given $\mathbf{d}_i$ and q_i, ψ_i is obtained using the law of sines:

$$\psi_i = \text{atan2}\left(d_{y,i},\ d_{x,i}\right) + \arcsin\left(\frac{q_i}{d_i \sin\left(\alpha_i\right)}\right) \tag{III.3}$$

Due to the wire actuation, the piston strokes q_i are coupled with ψ_i based on the radius of the wire rope pulley r_i and the translation of the wire carriages u_i. A known home configuration is assumed with values $q_{i,\,home}$, $\psi_{i,\,home}$, and $\theta_{i,\,home}$. Given lead screws with a known lead η_i the carriage displacement u_i is given by $u_i = \eta_i\left(\theta_i - \theta_{i,home}\right)$. The matrices $\mathbf{R} = diag^1\left([r_1, r_2, r_3]\right)$ and $\mathbf{G} = diag\left(\left[\frac{1}{\eta_1}, \frac{1}{\eta_2}, \frac{1}{\eta_3}\right]\right)$ are defined as the pulley radius and transmission gain matrices. Using these definitions, the kinematic compatibility of the inextensable wire loop is given by:

$$\mathbf{G}^{-1}\left(\boldsymbol{\theta} - \boldsymbol{\theta}_{home}\right) + \mathbf{R}\left(\boldsymbol{\psi} - \boldsymbol{\psi}_{home}\right) = \mathbf{q} - \mathbf{q}_{home} \tag{III.4}$$

[1] $diag(\mathbf{a})$ is the diagonalization of vector $\mathbf{a}$

Lastly, the motor rotations $\boldsymbol{\theta}$ are found using (III.4).

Instantaneous Kinematics

The instantaneous kinematics is useful for evaluating the quality of the mechanism, for control algorithms and for calibration. Following an approach presented by Tsai [111] and Simaan [97], the solution to the instantaneous kinematics begins by writing the loop closure equations of the kinematic chains:

$$\mathbf{b}_i + \mathbf{a}_i + \mathbf{q}_i = \mathbf{p} + \mathbf{e}_i \tag{III.5}$$

Taking the time derivative of both sides of (III.5) yields:

$$\dot{q}_i \hat{\mathbf{s}}_i + \dot{\psi}_i(\hat{\mathbf{z}}_b \times (\mathbf{a}_i + q_i \hat{\mathbf{s}}_i)) = \dot{\mathbf{p}} + \dot{\phi}(\hat{\mathbf{z}}_b \times \mathbf{e}_i) \tag{III.6}$$

First, the relationship between task space velocity $\boldsymbol{\zeta}$ and piston velocity $\dot{\mathbf{q}}$ is found by eliminating $\dot{\psi}$ from (III.6). This is accomplished by pre-multiplying (III.6) by $(\mathbf{a}_i + q_i \hat{\mathbf{s}}_i)^{\mathrm{T}}$ and simplifying using triple product rules:

$$\mathbf{J}_q \dot{\mathbf{q}} = \mathbf{J}_\zeta \boldsymbol{\zeta} \tag{III.7}$$

where the instantaneous inverse and direct kinematic matrices [97] are denoted as $\mathbf{J}_q$ and $\mathbf{J}_\zeta$ respectively and defined as:

$$\mathbf{J}_q = diag\left(\left[\mathbf{a}_1^{\mathrm{T}} \hat{\mathbf{s}}_1 + q_1, \mathbf{a}_2^{\mathrm{T}} \hat{\mathbf{s}}_2 + q_2, \mathbf{a}_3^{\mathrm{T}} \hat{\mathbf{s}}_3 + q_3\right]\right) \tag{III.8}$$

$$\mathbf{J}_\zeta = \begin{bmatrix} (\mathbf{a}_1 + q_1 \hat{\mathbf{s}}_1)^{\mathrm{T}} & \left[\mathbf{e}_1 \times (\mathbf{a}_1 + q_1 \hat{\mathbf{s}}_1)\right]^{\mathrm{T}} \hat{\mathbf{z}}_b \\ (\mathbf{a}_2 + q_2 \hat{\mathbf{s}}_2)^{\mathrm{T}} & \left[\mathbf{e}_2 \times (\mathbf{a}_2 + q_2 \hat{\mathbf{s}}_2)\right]^{\mathrm{T}} \hat{\mathbf{z}}_b \\ (\mathbf{a}_3 + q_3 \hat{\mathbf{s}}_3)^{\mathrm{T}} & \left[\mathbf{e}_3 \times (\mathbf{a}_3 + q_3 \hat{\mathbf{s}}_3)\right]^{\mathrm{T}} \hat{\mathbf{z}}_b \end{bmatrix} \tag{III.9}$$

The relationship between $\boldsymbol{\zeta}$ and $\dot{\mathbf{q}}$ can be written as:

$$\dot{\mathbf{q}} = \mathbf{J}_q^{-1}\mathbf{J}_\zeta\boldsymbol{\zeta} = \mathbf{J}_{q\zeta}\boldsymbol{\zeta} \tag{III.10}$$

Due to wire routing, the piston strokes are not independent of each other. Decoupling relationships are required to relate $\dot{\boldsymbol{\theta}}$ to $\boldsymbol{\zeta}$. The time derivative of (III.4) is:

$$\dot{\boldsymbol{\theta}} = \mathbf{G}\left(\dot{\mathbf{q}} - \mathbf{R}\,\dot{\boldsymbol{\psi}}\right) \tag{III.11}$$

The relationship between $\dot{\boldsymbol{\psi}}$ and $\boldsymbol{\zeta}$ is obtained by substituting $\mathbf{d}_i = \mathbf{a}_i + q_i\hat{\mathbf{s}}_i$ into (III.6):

$$\dot{\psi}_i\left[\hat{\mathbf{z}}_b \times \mathbf{d}_i\right] + \dot{q}_i\,\hat{\mathbf{s}}_i = \dot{\mathbf{p}} + \dot{\phi}\left[\hat{\mathbf{z}}_b \times \mathbf{e}_i\right] \tag{III.12}$$

pre-multiplying (III.12) by $\left[\hat{\mathbf{z}}_b \times \mathbf{d}_i\right]^{\mathrm{T}}$ and with the simplification $\left[\hat{\mathbf{z}}_b \times \mathbf{d}_i\right]^{\mathrm{T}}\left[\hat{\mathbf{z}}_b \times \mathbf{e}_i\right] = \mathbf{d}_i^{\mathrm{T}}\mathbf{e}_i$ for the planar mechanism the following result is obtained:

$$\dot{\boldsymbol{\psi}} = \left(\mathbf{J}_1\mathbf{J}_{q\zeta} + \mathbf{J}_2\right)\boldsymbol{\zeta} = \mathbf{J}_{\psi\zeta}\boldsymbol{\zeta} \tag{III.13}$$

where

$$\begin{aligned}
\mathbf{J}_1 &= diag\left(\left[\begin{array}{ccc} \frac{[\hat{\mathbf{z}}_b\times\mathbf{d}_1]^{\mathrm{T}}\hat{\mathbf{s}}_1}{\mathbf{d}_1^{\mathrm{T}}\mathbf{d}_1}, & \frac{[\hat{\mathbf{z}}_b\times\mathbf{d}_2]^{\mathrm{T}}\hat{\mathbf{s}}_2}{\mathbf{d}_2^{\mathrm{T}}\mathbf{d}_2}, & \frac{[\hat{\mathbf{z}}_b\times\mathbf{d}_3]^{\mathrm{T}}\hat{\mathbf{s}}_3}{\mathbf{d}_3^{\mathrm{T}}\mathbf{d}_3} \end{array}\right]\right) \\
\mathbf{J}_2 &= \left[\begin{array}{cc} \frac{[\hat{\mathbf{z}}_b\times\mathbf{d}_1]^{\mathrm{T}}}{\mathbf{d}_1^{\mathrm{T}}\mathbf{d}_1} & \frac{\mathbf{d}_1^{\mathrm{T}}\mathbf{e}_1}{\mathbf{d}_1^{\mathrm{T}}\mathbf{d}_1} \\ \frac{[\hat{\mathbf{z}}_b\times\mathbf{d}_2]^{\mathrm{T}}}{\mathbf{d}_2^{\mathrm{T}}\mathbf{d}_2} & \frac{\mathbf{d}_2^{\mathrm{T}}\mathbf{e}_2}{\mathbf{d}_2^{\mathrm{T}}\mathbf{d}_2} \\ \frac{[\hat{\mathbf{z}}_b\times\mathbf{d}_3]^{\mathrm{T}}}{\mathbf{d}_3^{\mathrm{T}}\mathbf{d}_3} & \frac{\mathbf{d}_3^{\mathrm{T}}\mathbf{e}_3}{\mathbf{d}_3^{\mathrm{T}}\mathbf{d}_3} \end{array}\right]
\end{aligned} \tag{III.14}$$

If $\mathbf{d}_i$ and $\hat{\mathbf{s}}_i$ are collinear then $\dot{q}_i\left[\hat{\mathbf{z}}_b \times \mathbf{d}_i\right]^{\mathrm{T}}\hat{\mathbf{s}}_i = 0$ and $\mathbf{J}_1 = \mathbf{0}$. Using (III.11) $\dot{\boldsymbol{\theta}}$ is given by:

$$\dot{\boldsymbol{\theta}} = \mathbf{G}\left(\mathbf{J}_{q\zeta} - \mathbf{R}\,\mathbf{J}_{\psi\zeta}\right)\boldsymbol{\zeta} = \mathbf{J}_{\theta\zeta}\boldsymbol{\zeta} \tag{III.15}$$

III.3 Stiffness Modelling

Mechanism stiffness is an important consideration in device intended to operate with high precision. This section examines the effect of the proposed wire actuation scheme on end effector stiffness.

The analysis starts with determining the static load solution for the mechanism. Using the instantaneous kinematics, a first order approximation of the loads transmitted from the end effector to the motor is made. Figure III.2(B) shows the constant-length wire loop transmitting force between the actuator and the piston. Using the virtual work method [111] and neglecting piston weight the statics of the robot can be written as:

$$\boldsymbol{\tau}_\theta^{\mathrm{T}} \delta\boldsymbol{\theta} = \boldsymbol{\tau}_\theta^{\mathrm{T}} \mathbf{J}_{\theta\zeta} \delta\mathbf{x} = \mathbf{w}^{\mathrm{T}} \delta\mathbf{x} \tag{III.16}$$

where $\mathbf{w}$ represents the wrench acting on the end effector (a two-component force in plane $\hat{\mathbf{x}}_b\hat{\mathbf{y}}_b$ and a moment about $\hat{\mathbf{z}}_b$) and $\boldsymbol{\tau}_\theta$ is the vector of motor torques. Using (III.16) the following is obtained:

$$\boldsymbol{\tau}_\theta = \left(\mathbf{J}_{\theta\zeta}^{\mathrm{T}}\right)^{-1} \mathbf{w} \tag{III.17}$$

Wire carriage stiffness is considered infinite due to the drastic difference in compliance between the wire rope and lead screw transmission (Figure III.3). The linearized stiffness and the length for the j'th wire rope section of the i'th leg are defined as $k_{i,j}$ and $h_{i,j}$ respectively. The stiffness of the wire is in reality a function of the tension in the wire,$\boldsymbol{\tau}_{h,j}$, and should the load applied on the carriage ($\boldsymbol{\tau}_u$) exceed force in a wire segment that wire will become slack. The heaviside function $H(x)$ is used to express

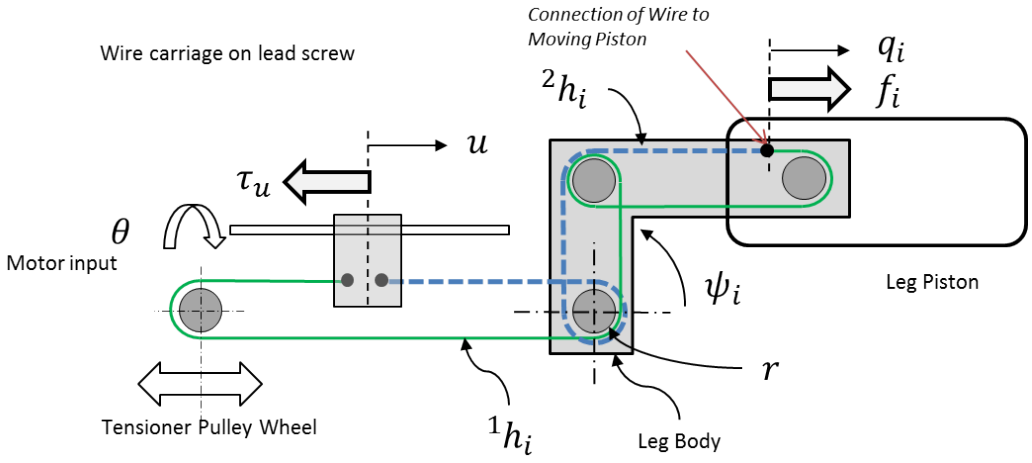

Figure III.3: Force transmission through a single kinematic chain.

the stiffness matrices $\mathbf{K}_1$and $\mathbf{K}_2$ as:

$$\begin{aligned}\mathbf{K}_1 &= diag\left(H\left(\boldsymbol{\tau}_{h1} - \boldsymbol{\tau}_u\right)\right) diag\left(\begin{bmatrix} k_{1,1}, & k_{2,1}, & k_{3,1} \end{bmatrix}\right) \\ \mathbf{K}_2 &= diag\left(H\left(\boldsymbol{\tau}_u - \boldsymbol{\tau}_{h2}\right)\right) diag\left(\begin{bmatrix} k_{1,2}, & k_{2,2}, & k_{3,2} \end{bmatrix}\right)\end{aligned} \tag{III.18}$$

End effector stiffness is defined as:

$$\mathbf{K} = \frac{d\mathbf{w}}{d\mathbf{x}} \tag{III.19}$$

Substituting (III.17) into (III.19) yields:

$$\mathbf{K} = \sum_{i=1}^{3} \frac{\partial \left[\mathbf{J}_{u\zeta}^{\mathrm{T}}\right]^{(i)}}{\partial \mathbf{x}} \tau_{u,i} + \mathbf{J}_{u\zeta}^{\mathrm{T}} \frac{d\boldsymbol{\tau}_u}{d\mathbf{x}} \tag{III.20}$$

Where $\left[\mathbf{J}_{u\zeta}^{\mathrm{T}}\right]^{(i)}$ refers to the i'th column of the matrix $\mathbf{J}_{u\zeta}^{\mathrm{T}}$. From an applied wrench $\mathbf{w}$, the pistons will experience a generalized force $\mathbf{f}$ that will stretch the wires based on their compliance. Let $\bar{\mathbf{h}}$ be the unperturbed length of a wire segment (not the same as its free length since it is under preload). Given $\mathbf{h}_j = \begin{bmatrix} h_{1,j} & h_{2,j} & h_{3,j} \end{bmatrix}^{\mathrm{T}}$,

the new length of the wire segments are described by:

$$\begin{aligned} \mathbf{h}_1 &= \bar{\mathbf{h}}_1 + (\mathbf{q} - \bar{\mathbf{q}}) - \mathbf{R}\left(\boldsymbol{\psi} - \bar{\boldsymbol{\psi}}\right) \\ \mathbf{h}_2 &= \bar{\mathbf{h}}_2 - (\mathbf{q} - \bar{\mathbf{q}}) + \mathbf{R}\left(\boldsymbol{\psi} - \bar{\boldsymbol{\psi}}\right) \end{aligned} \tag{III.21}$$

Where $\bar{\mathbf{q}}$ and $\bar{\boldsymbol{\psi}}$ are the unperturbed piston positions and leg orientations respectively. The force acting on the linear actuator carriage is expressed in the force vector $\boldsymbol{\tau}_u$ and through force balance:

$$\boldsymbol{\tau}_u = \boldsymbol{\tau}_{h1} - \boldsymbol{\tau}_{h2} = \mathbf{K}_1 \left(\mathbf{h}_1 - \bar{\mathbf{h}}_1\right) - \mathbf{K}_2 \left(\mathbf{h}_2 - \bar{\mathbf{h}}_2\right) \tag{III.22}$$

Substituting (III.21) into (III.22) and taking its derivative with respect to $\mathbf{x}$ yields:

$$\frac{d\boldsymbol{\tau}_u}{d\mathbf{x}} = \mathbf{K}_1 \frac{d\mathbf{h}_1}{d\mathbf{x}} - \mathbf{K}_2 \frac{d\mathbf{h}_2}{d\mathbf{x}} \tag{III.23}$$

$$\frac{d\boldsymbol{\tau}_u}{d\mathbf{x}} = (\mathbf{K}_1 + \mathbf{K}_2)\left(\frac{d\mathbf{q}}{d\mathbf{x}} - \mathbf{R}\frac{d\boldsymbol{\psi}}{d\mathbf{x}}\right) \tag{III.24}$$

$$\frac{d\boldsymbol{\tau}_u}{d\mathbf{x}} = \mathbf{K}_{12}\left(\mathbf{J}_{q\zeta} - \mathbf{R}\,\mathbf{J}_{\psi\zeta}\right) = \mathbf{K}_{12}\mathbf{J}_{u\zeta} \tag{III.25}$$

From (III.20) and (III.25) the linearized stiffness therefore becomes:

$$\mathbf{K} = \sum_{i=1}^{3} \frac{\partial \left[\mathbf{J}_{u\zeta}^{\mathrm{T}}\right]^{(i)}}{\partial \mathbf{x}} \tau_{u,i} + \mathbf{J}_{u\zeta}^{\mathrm{T}} \mathbf{K}_{12} \mathbf{J}_{u\zeta} \tag{III.26}$$

The first term is called the active stiffness which is affected by preload and the second term is called the passive stiffness []. It can be seen from (III.3) that the stiffness of the mechanism is a function of the pulley radius r_i. Figure III.4 shows the relative change of the stiffness matrix K as a function of r.

The stiffness curves shown in this figure are based on the manufactured prototype

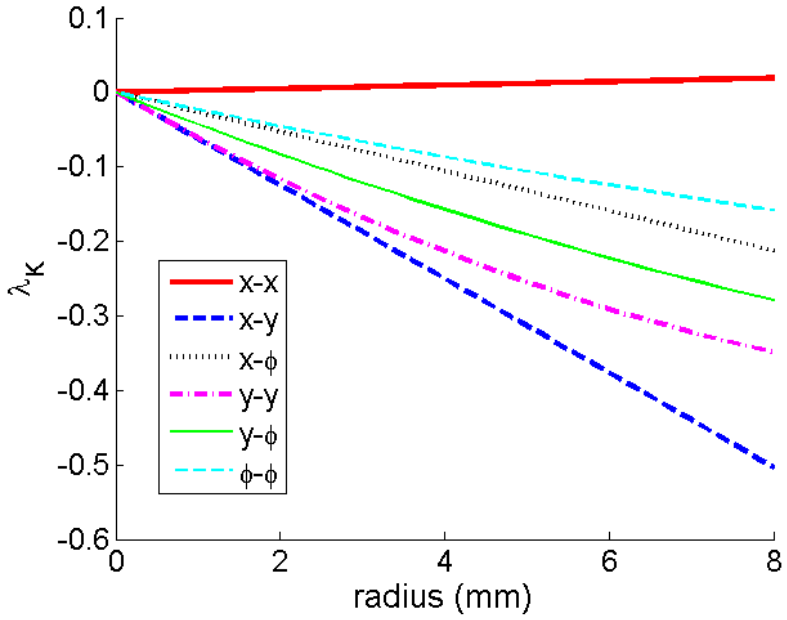

Figure III.4: Relative stiffness change as a function of pulley radius. The curves represent change in force / displacement relationship. For example, 'x-y' is interpreted as change in displacement y for force input in direction x.

presented later in this chapter. The stiffness is computed as an average over the mechanism's entire workspace.

Empirical Testing of Wire Rope Mechanical Properties

The wire rope used in the implementations presented in this dissertation is a multi-strand construction from Asahi Intec (type S model 33). It is a 1x19 + (1x7)x8 construction: the center bundle has 19 strands and is surrounded by 8 bundles of 7 strands each. The elastic properties of the wirerope is not provided by the manufacturer and necessitated physical testing to determine its properties. The goal of the experiments was to determine the wire stiffness as a function of length and tension.

The experimental setup is shown in Figure III.5(A) with the cross-sectional diagram of the wire rope shown in Figure III.5(B). Varying lengths of wire rope were wrapped around 4mm diameter disks and secured in a TTC-102ML tensile testing

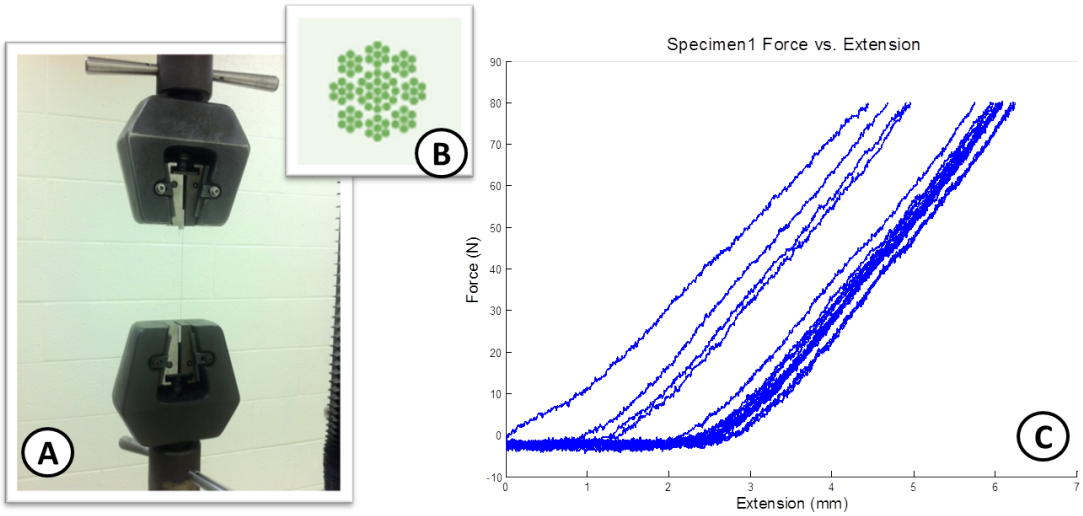

Figure III.5: Asahi wire rope testing. (A) The experimental setup with the wire pulled by the TTC-102ML tensile testing system. (B) The bundle pattern for the Asahi wire rope. (C) Displacement vs. force measurement data.

Table III.1: Tension Test Parameters

Parameter	Value
Displacement Rate	$5mm/min$
Peak Tension	$80N$
Minimum Cycles	10
Maximum Cycles	20
Wire Segment Lengths	52, 65, 95, 125, $180mm$

system (Instru-Met Corp, Union N.J.). The disks were machined to the expected diameter of the idler pulleys used in the robotic system to maintain similar boundary conditions on the wire rope. Each sample underwent at least 11 sequences of fixed rate elongation terminating at a tensile load of 80N. The wire rope was then relaxed, the force displacement curve saved, and the experiment was repeated. The experimental parameters are summarized in Table III.1. The raw measurement results on a single specimen are shown in Figure III.5(C). It can be seen that at least 4 series of experiments are needed before the wire is conditioned and reaches a fixed unloaded

length. Initial loading of a new wire rope realigns the individual strands and several cycles of loading are typically required before a wire rope may be considered conditioned. From this raw information a stiffness model can be determined. Stiffness (κ) is defined as:

$$\kappa = \frac{dt}{dy} \tag{III.27}$$

where t is the tension in the wire segment and y is the elongation of the wire segment. Due to noisy measurements, direct differentiation of the force / elongation curve would produce a noisy stiffness estimation. Instead a locally first order approximation is made of the form:

$$\kappa\left(y,t\right) = \kappa_0\left(t\right) + \kappa_1\left(t\right)\ y \tag{III.28}$$

The tension / elongation curve is discretely sampled into N measurements with the *ith* force and elongation measurement represented by $\mathbf{t} = \left[t_1, ..., t_i, ..., t_N\right]^T$ and $\mathbf{y} = \left[y_1, ..., y_i, ..., y_N\right]^T$ respectively. A weighted least-squares solution was employed to fit (III.28) for any load t_i. At any load t_i the stiffness is the slope of the locally fitted line and equals $\kappa_{1,i}\left(t_i\right)$. Defining the coefficient vector $\boldsymbol{\kappa}_i = \left[\kappa_{0,i},\ \kappa_{1,i}\right]^T$ the linear model becomes:

$$\left(\mathbf{A}^T\mathbf{W}_i\mathbf{A}\right)\boldsymbol{\kappa}_i = \mathbf{A}^T\mathbf{W}_i\mathbf{t} \tag{III.29}$$

where:

$$\mathbf{A} = \left[\mathbf{1}^{n\times 1},\ \mathbf{t}\right] \tag{III.30}$$

and the weight function is an exponential decay centered at the current measurement t_i:

$$\mathbf{W}_i = diag\left(\left[e^{-\alpha(y_1-y_i)^2}, ..., e^{-\alpha(y_N-y_i)^2}\right]\right) \tag{III.31}$$

The final solution for the local linear fit coefficients is:

$$\boldsymbol{\kappa}_i = \left(\mathbf{A}^T\mathbf{W}_i\mathbf{A}\right)^{-1}\mathbf{A}^T\mathbf{W}_i\mathbf{t} \tag{III.32}$$

A series of nine specimens were tested with the stiffness values extracted using this fitting method and an exponential decay rate of $\alpha = 20mm^{-1}$. This value corresponds to a 95% weight reduction at $y = y_i \pm 0.4mm$ of elongation. The results are shown in Figure III.6(A). In linear, pure-tension elements the stiffness is often related to the

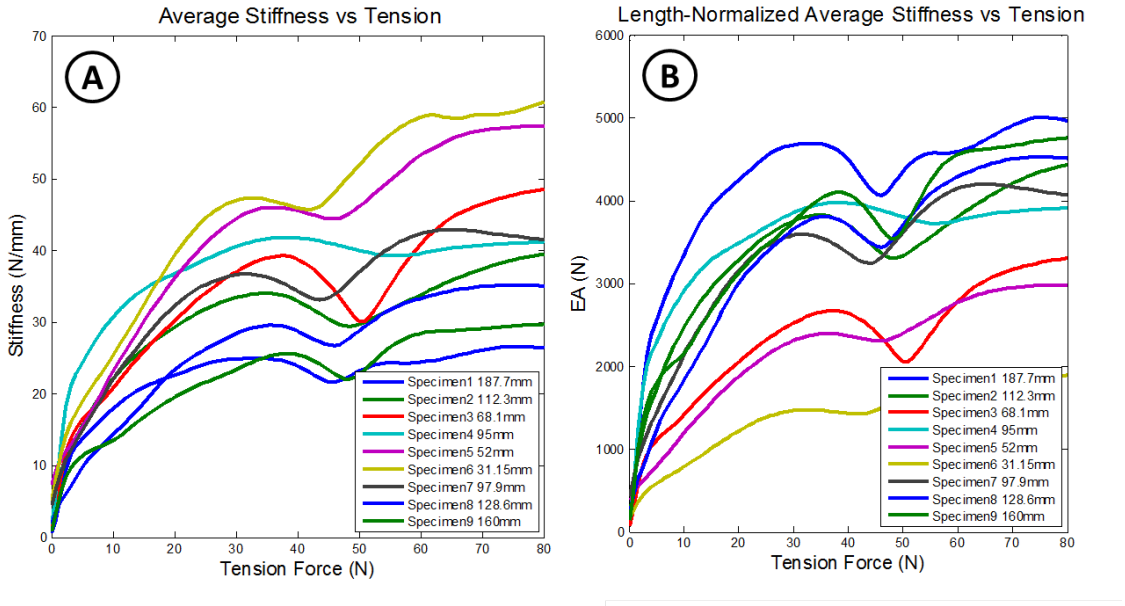

Figure III.6: Asahi wire rope stiffness. (A) Stiffness curves for specimens of different length as a function of applied load. (B) Stiffness curves are normalized by the specimen length to give an effective cross sectional stiffness.

elastic modulus, E, the cross sectional area, A, and the length, L, by the relationship:

$$\kappa = \frac{EA}{L} \tag{III.33}$$

To apply the stiffness model to an arbitrary length of wire rope, the term EA is

required. Figure III.6(B) plots the stiffness curves of Figure III.6(A), correcting for the wire rope length. It can be seen that specimens over $100mm$ in length have a range of $EA \in [3200,\ 5000]\,N$ but the three specimens under $100mm$ in length have a lower elastic modulus. Also, all specimens reach full stiffness with a tension of $30N$ and exhibit a small dip in the stiffness at approximately $50N$. While this data has a relatively large range, it sets bounds for the expected stiffness of the wire rope. For conservative estimation, when compliance is evaluated as the desired metric, the higher stiffness bound ($EA = 5000N$) will be assumed. Conversely, when stiffness is evaluated as the desired metric, the lower bound ($EA = 3200N$) will be assumed for all wire segments greater than $100mm$ in length.

III.4 Wire Actuation Misalignment

So far in this chapter, the kinematic model has assumed that the wire aligned perfectly parallel with the carriage translation vector $\mathbf{u}_i$. The sensitivity to alignment error in the wire path will define the tolerance specifications for a fabricated design. This section addresses this error to assist in the design specifications in Chapter V. Figure III.2 (B) shows how the wire is routed through a single actuation chain. The area of interest in this analysis is the section of wire between the carriage and adjacent pulley wheel and is shown schematically in Figure III.7. The length of the

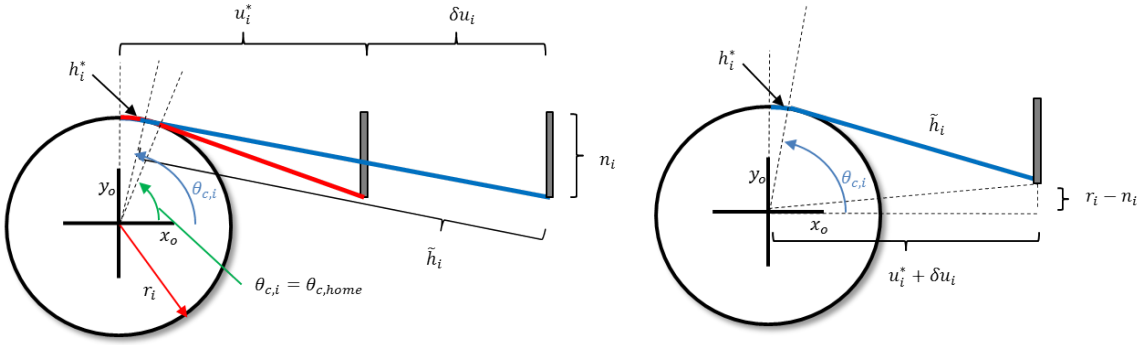

Figure III.7: Wire Misalignment Compensation Diagram

wire segment measured from the top of the routing pulley to the wire carriage in the *ith* actuation chain is defined as h_i. In the case of misalignment, the length of the wire segment h_i will not change at the same rate as the carriage displaces (i.e. $\frac{dh_i}{dt} \neq \frac{du_i}{dt}$). Ideally, the wire is parallel to the direction of travel of the carriage - denoted by the unit vector $\hat{\mathbf{u}}_i$. To simplify analysis, a coordinate frame $\left\{ \begin{array}{ccc} \hat{\mathbf{x}}_o & \hat{\mathbf{y}}_o & \hat{\mathbf{z}}_o \end{array} \right\}$ is assigned at the pulley wheel with the pulley axis co-linear with $\hat{\mathbf{z}}_o$. All vectors and quantities in this section are expressed in this coordinate frame.

The value of u_i expresses the distance from the $\hat{\mathbf{y}}_o$ axis to the wire carriage and is split into two components. The minimum, or home displacement is given by the constant u_i^* and the variable describing the current displacement of the carriage is δu_i. The length of the wire segment is separated into two parts: the section wrapped around the pulley is h_i^* and the straight section leading to the wire carriage is $\tilde{h}_i$. The relationships are then written as:

$$u_i = u_i^* + \delta u_i \tag{III.34}$$

$$h_i = h_i^* + \tilde{h}_i \tag{III.35}$$

The value of $\theta_{c,i}$ locates the point of tangency of the wire rope to the pulley and where the split between h_i^* and $\tilde{h}_i$ occurs. The magnitude of offset from the ideal line of travel for the wire is given as n_i and the radius of the pulley is r_i. Using this notation, the location of the connection between the wire and carriage is given by the vector $\left[\begin{array}{ccc} u_i^* + \delta u_i, & r_i - n_i & 0 \end{array} \right]^T$. Now an expression for the length of the wire from the top of the pulley wheel to the connection point is needed. From completing

triangles the value of $\theta_{c,i}$ may be computed:

$$\theta_{c,i} = \arctan\left(\frac{r_i - n_i}{u_i^* + \delta u_i}\right) - \arctan\left(\frac{\tilde{h}_i}{r_i}\right) \tag{III.36}$$

Also, the length of the wire segments are given by:

$$h_i^* = r_i \left(\frac{\pi}{2} - \theta_{c,i}\right) \tag{III.37}$$

$$\tilde{h}_i = \sqrt{(u_i^* + \delta u_i)^2 + (r_i - n_i)^2 - r_i^2} = \sqrt{(u_i^* + \delta u_i)^2 - 2\, r_i\, n_i + n_i^2} \tag{III.38}$$

Substituting (III.36) into (III.37) yields:

$$h_i^* = r_i \left(\frac{\pi}{2} - \arctan\left(\frac{r_i\ (r_i - n_i) - \tilde{h}_i\ (u_i^* + \delta u_i)}{r_i\ (u_i^* + \delta u_i) - \tilde{h}_i\ (r_i - n_i)}\right)\right) \tag{III.39}$$

Using the trigonometric identity: $\arctan(\alpha) \pm \arctan(\beta) = \arctan\left(\frac{\alpha \pm \beta}{1 \mp \alpha\, \beta}\right)$ and substituting (III.38) and (III.39) into (III.35), the length of the wire segment simplifies to:

$$\begin{aligned} h_i = r_i & \left(\frac{\pi}{2} - \arctan\left(\frac{r_i\ (r_i - n_i) - \tilde{h}_i\ (u_i^* + \delta u_i)}{r_i\ (u_i^* + \delta u_i) - \tilde{h}_i\ (r_i - n_i)}\right)\right) \\ & + \sqrt{(u_i^* + \delta u_i)^2 - 2\, r_i\, n_i + n_i^2} \end{aligned} \tag{III.40}$$

From this model the difference in expected actuation can be calculated. The home position ($\delta u_i = 0$) has a corresponding home value for the wire segment length ($h_{i,\,home}$):

$$h_{i,\,home} = \quad r_i \left(\frac{\pi}{2} - \arctan \left(\frac{r_i \,(r_i - n_i) - u_i^* \sqrt{(u_i^*)^2 - 2\, r_i\, n_i + n_i^2}}{r_i\, u_i^* - (r_i - n_i) \sqrt{(u_i^*)^2 - 2\, r_i\, n_i + n_i^2}} \right) \right) + \sqrt{(u_i^*)^2 - 2\, r_i\, n_i + n_i^2} \quad \text{(III.41)}$$

The variable $\Delta h_i\,(\delta u_i)$, describes the change in length of the wire segment under actuation and in the ideal case:

$$\Delta h_i\,(\delta u_i)_{ideal} = \delta u_i \quad \text{(III.42)}$$

Under non-ideal conditions ($n_i \neq 0$) the change in segment length is:

$$\Delta h_i\,(\delta u_i)_{ideal} = h_i - h_{i,\,ideal} \quad \text{(III.43)}$$

To analyze the effect of misalignment on change in segment length, the following non-dimensional parameters are introduced:

$$\sigma_1 = \frac{u_i^*}{r} \quad \text{(III.44)}$$

$$\sigma_2 = \frac{n_i^*}{r} \quad \text{(III.45)}$$

$$\sigma_3 = \frac{\delta u_i}{r} \quad \text{(III.46)}$$

$$\epsilon = \frac{\Delta h_i}{h_{i,\,ideal}} \quad \text{(III.47)}$$

Figure III.8 plots the strain in nominal wire length, ϵ, as a function of the non-dimensional parameters. Plot III.8(A) shows ϵ as a function of σ_1 and σ_2 while (B)

plots the surfaces of constant strain in relation to the parameters σ_1, σ_2, and σ_3. In both plots a pulley radius of $r = 2mm$ was selected based on available physical parts. It can be seen from the plots that misalignment of the wire carriage only has

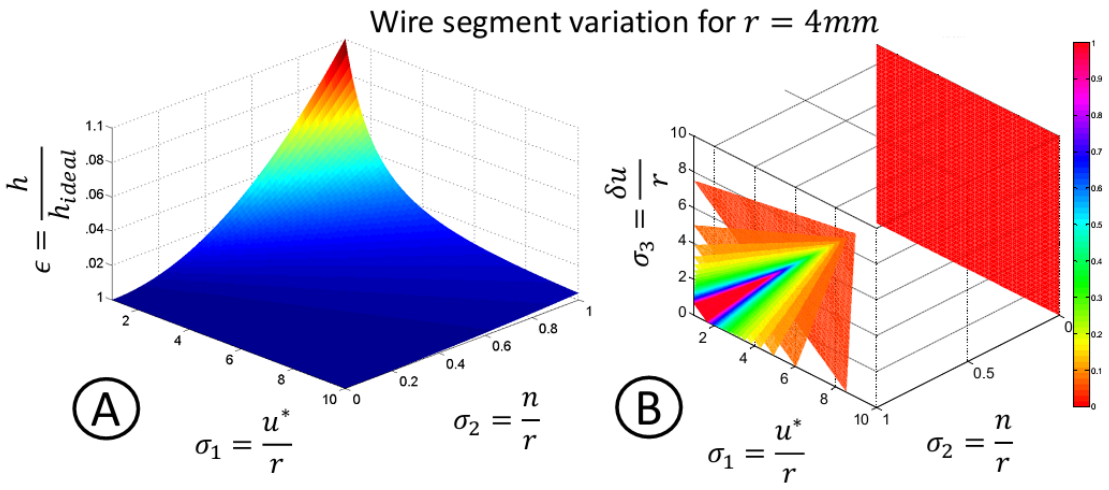

Figure III.8: Misalignment strain in wire segments. (A) Strain (vertical axis) is expressed as a function of σ_1 and σ_2. (B) Isosurfaces of constant strain as a function of σ_1, σ_2, and σ_3.

significant effect on the wire segment ($\epsilon > 1.02$ or 2% strain) when the minimum distance of the carriage is less than 4 times the pulley radius and the magnitude of the misalignment is relatively large ($n_i > 0.4r_i$). Manufacturing and assembly errors are expected to be within 0.5 mm and given a radius of 2mm, the peak strain is expected to be less than 1.002. This also translates to an actuation error bounded within 0.005 mm. This error is two orders of magnitude before the assumed actuation error used in the following sections. This implies that the error contribution from this misalignment effect is not significant in the proposed design.

III.5 Dimensional Synthesis

The dimensional synthesis of the insertion robot was defined with the aim of determining the kinematic parameters that minimize sensitivity to actuation error while

Variable	Units	Range/Value	Variable	Units	Value
a_i	mm	$[10, 80]$	ϵ_x	mm	0.4
e_x	mm	$[-100, -50]$	ϵ_y	mm	0.4
e_y	mm	$[-25, 25]$	ϵ_ϕ	deg	0.3
$\delta\theta$	rad	0.2	p_{max}	mW	75
$\tilde{a}$	mm	20	λ_c	mm^{-1}	0.5

Table III.2: Optimization Parameters

making efficient use of piston stroke and minimizing actuator power. The problem was cast as a constrained minimization problem solving for the leg lengths a_i and ${}^A\mathbf{e}_i = [e_{x,i}, e_{y,i}, 0]^T$ for a total of nine design parameters. Vectors $\mathbf{b}_i$ were predefined due to the size limitations. The final prototype used $\alpha_i = \pi$ for manufacturing cost considerations. The simulated insertion trajectories were discretized into 100 sample poses per insertion path and used to define the workspace $\mathbb{W}$ over which the following cost function was calculated:

$$f\left(a_i,\, {}^A\mathbf{e}_i\right)_{obj} = f_{err} + f_{leg} + f_{power} \tag{III.48}$$

where f_{err}, f_{leg}, and f_{power} are defined in the following sections. The reader should refer to Table III.2 for parameters used in evaluating the optimization function.

Error Sensitivity

The sensitivity analysis determines the maximal end effector pose error $\delta\mathbf{x}$ stemming from a bounded motor input error $\delta\boldsymbol{\theta}$ such that $\delta\theta_i \in [\theta_i - \zeta_\theta, \theta_i + \zeta_\theta]$. Instead of using error ellipsoids assuming norm-bounded error $\delta\boldsymbol{\theta}$, more conservative error polytopes [21] were used where it was assumed that each actuator has a bounded

error. The maximal expected pose error is approximated by:

$$\delta\mathbf{x}\left(\delta\boldsymbol{\theta}\right) = \text{argmax}\left(\mathbf{J}_{\zeta\theta}\delta\boldsymbol{\theta}\right),\ \delta\theta_i \in [-\zeta_\theta, \zeta_\theta] \tag{III.49}$$

A weighted objective function f_{err} quantifying the weighted norm of the end effector error was defined as the following:

$$f_{err} = \delta\mathbf{x}^{\mathrm{T}}\mathbf{W}\delta\mathbf{x} \tag{III.50}$$

The weight matrix $\mathbf{W} = diag\left(\left[\frac{1}{\epsilon_x^2}, \frac{1}{\epsilon_y^2}, \frac{1}{\epsilon_\phi^2}\right]\right)$ addresses dimensionality by scaling the three components of $\delta\mathbf{x}$ by their respective desired accuracy requirements defined in Table III.2.

Power Requirements

The function f_{power} quantifies the average peak power across all insertion runs and discourages design solutions with rapid motion through sections of the insertion trajectory. For i'th leg ($i = 1, 2, 3$) the j'th pose ($j = 1, 2, \ldots, 100$) along a given insertion path we calculate $\tau_{\theta,i,j}$ and $\dot{\theta}_{i,j}$ assuming an insertion rate of $1mm/s$. The instantaneous power is calculated and normalized by the maximal actuator power $p_{w,max}$. The vector $\mathbf{p}_w$ with elements $p_{w,k}$ ($k = 1, 2, \ldots, n$) represents the maximal required normalized power for all insertion paths in $\mathbb{W}$. Using these definitions, the objective function f_{power} is given by:

$$f_{power} = \left(\mathbf{p}_w^{\mathrm{T}}\mathbf{p}_w\right)/n \tag{III.51}$$

where $n = 28$ is the number of insertion paths and $p_{w,j}$ is:

$$p_{w,k} = \text{argmax}\left(\left(\tau_{\theta,i,j}\,\dot{\theta}_{i,j}\right)/p_{w,max}\right) \tag{III.52}$$

It must be noted that the power estimation presented here does not include the effects of friction.

Piston Stroke Utilization

The objective function f_{leg} guides the design to avoid exceeding the feasible piston strokes. Also, an ideal design uses the entire available stroke in each leg. Thus this function is defined as a sum of three positive definite functions:

$$f_{leg} = \mathbf{f}_1^{\mathrm{T}}\mathbf{f}_1 + \mathbf{f}_2^{\mathrm{T}}\mathbf{f}_2 + \mathbf{f}_3^{\mathrm{T}}\mathbf{f}_3 \tag{III.53}$$

Across all simulated insertion trajectories, a minimum and maximum piston position $q_{i,min}$ and $q_{i,max}$ is determined for each leg with their difference defined as $\Delta q_i = q_{i,max} - q_{i,min}$. Let the constant $\tilde{a}_i$ designate a portion of the initial leg length that must be reserved for mechanical assembly and let $\bar{q}_{i,min} = 0$ and $\bar{q}_{i,max} = a_i - \tilde{a}_i$ designate the feasible upper and lower bounds of the piston stroke. Using these definitions, what follows is the rationale behind defining $\mathbf{f}_1, \mathbf{f}_2, \mathbf{f}_3$ used in (III.53).

Stroke utilization was defined as the unused portion of the minimal required leg length. In the constructed prototype, $\mathbf{a}_i$ and $\mathbf{q}_i$ (Fig.III.10) are collinear and the stroke utilization metric $\mathbf{f}_1 \in \mathbb{R}^{3\times 1}$ is defined with it components given by:

$$f_{1,i} = 1 - \Delta q_i/\bar{q}_{i,max} \tag{III.54}$$

In addition to stroke utilization there was a desire to guide the synthesis towards

mechanically feasible designs where the minimal length is zero or positive and the stroke does not exceed feasible limits. This is achieved by demanding that $q_{i,min} \in [0, \bar{q}_{i,max}]$ and $\Delta q_i \in [0, \bar{q}_{i,max} - q_{i,min}]$. Given a stroke interval with a minimum (c_0) and a maximum (c_1), the cost function is defined as:

$$c(x, c_0, c_1) = \lambda_c \left(\sqrt{(x - c_0)^2 + \epsilon} + \sqrt{(x - c_1)^2 + \epsilon} + c_0 - c_1 \right) \tag{III.55}$$

This function is zero within the interval and increases linearly outside the interval. An example of the function is shown in Figure III.9. The small value, ϵ, allows smooth differentiation during numerical optimization. The constant $\lambda_c > 0$ scales the penalty per unit distance.

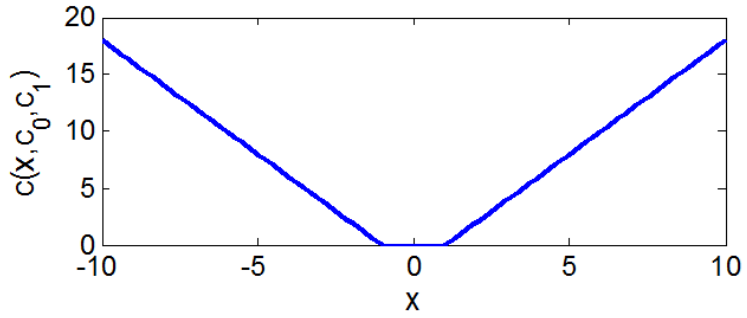

Figure III.9: Constraint function $c(x, c_0, c_1)$ example. The constants for this example are $c_0 = -1$ and $c_1 = 1$.

The functions $\mathbf{f}_2, \mathbf{f}_3 \in \mathbb{R}^{3\times 1}$ are defined with their components given by $f_{2,i} = c(q_{i,min}, 0, \bar{q}_{i,max})$ and $f_{3,i} = c(\Delta q_i, 0, \bar{q}_{i,max} - q_{i,min})$.

Optimization Constraints and Results

Results of this optimization are given in Table III.3. It must be noted that practical limitations for the device geometry, including the dimensions of the available force

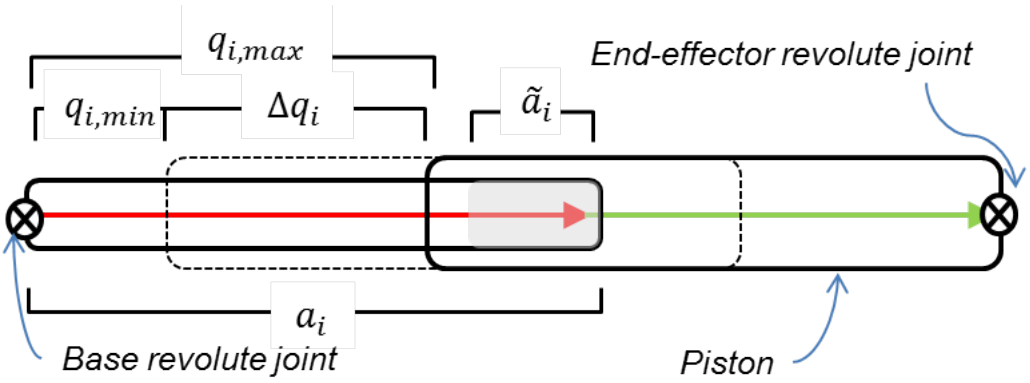

Figure III.10: Stroke utilization and stroke limits. Solid/dashed line designates a fully extended/retracted piston.

sensor, place limits on the available configurations where a local minima in the objective function was not reached. The expected performance measures, also included in Table III.3, are based on the dimensions of the system as built.

Table III.3: Kinematic parameters and expected performance

Parameter	Value as built	Metric	Est. Performance
$[a_1, a_2, a_3]$	$\begin{bmatrix} 63.2 & 63.2 & 64 \end{bmatrix}$	$\delta\mathbf{x}$	$\begin{bmatrix} 0.02mm \\ 0.34mm \\ 0.1^\circ \end{bmatrix}$
$[\mathbf{b}_1, \mathbf{b}_2, \mathbf{b}_3]$	$\begin{bmatrix} 0, 0, 0 \\ 8, -8, 0 \end{bmatrix}$	Max p_w	$< 3mW$
$[\mathbf{e}_1, \mathbf{e}_2, \mathbf{e}_3]$	$\begin{bmatrix} -88, -88, -88 \\ -2, -21, 21 \end{bmatrix}$	Stroke	$[0.61, 0.86, 0.58]$

III.6 Mechanical Design

Based on the kinematic design parameters derived in Chapter III a prototype insertion system was fabricated for validation. A CAD rendering of the prototype is shown in Figure III.11. The robotic tool can be divided into two major components; the 3RPR parallel manipulator and the insertion module responsible for grasping the PEA and actuating the stylet. A 6 axis force / moment transducer from *ATI*

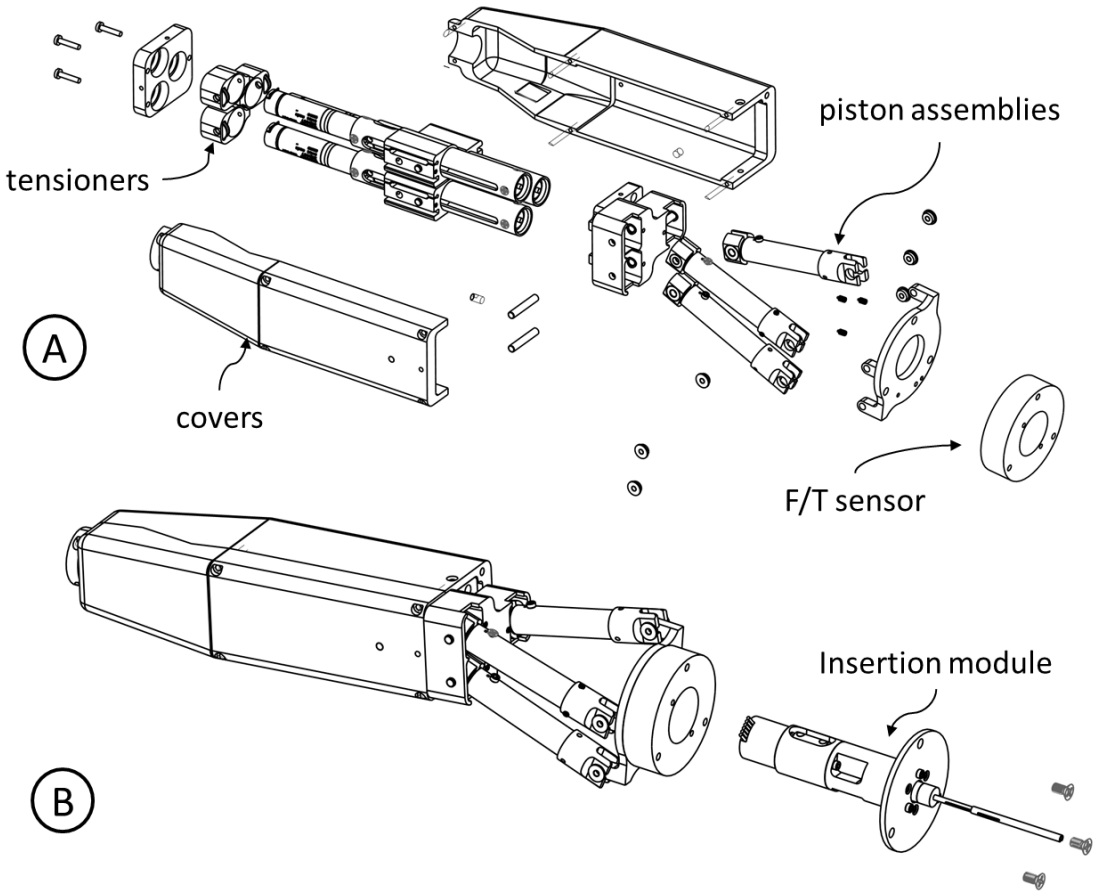

Figure III.11: Prototype Insertion System Rendering. (A) An exploded view of the 3RPR planar manipulator. (B) The insertion module attaches to the robot through a 6 axis force/moment transducer.

Table III.4: Kinematic parameters and expected performance

Parameter	Value as built	Metric	Est. Performance
$[a_1, a_2, a_3]$	$\begin{bmatrix} 63.2 & 63.2 & 64 \end{bmatrix}$	$\delta\mathbf{x}$	$\begin{bmatrix} 0.02mm \\ 0.34mm \\ 0.1^\circ \end{bmatrix}$
$[\mathbf{b}_1, \mathbf{b}_2, \mathbf{b}_3]$	$\begin{bmatrix} 0, 0, 0 \\ 8, -8, 0 \end{bmatrix}$	Max p_w	$< 3mW$
$[\mathbf{e}_1, \mathbf{e}_2, \mathbf{e}_3]$	$\begin{bmatrix} -88, -88, -88 \\ -2, -21, 21 \end{bmatrix}$	Stroke	$[0.61, 0.86, 0.58]$

Industrial (Nano43) acts as the physical link between the insertion module and the robotic manipulator. Loads acting on the PEA are transmitted through the gripper and insertion module and perceived by the F/T transducer as an external wrench.

The insertion module is shown in Figure III.12. The servo (Micromo 1506-SR) uses a lead screw assembly to transmit linear motion to a stylet rod. This rod (stylet stem) has a hook at its distal end to engage the stylet bulb and remove the stylet from the PEA body. The gripper is a long hollow tube slotted at the distal end to engage the PEA. The stylet is aligned with the gripper tube's axis and the stylet stem pulls the stylet through the center of the gripper tube. This actuation is unidirectional and the stylet cannot be reinserted into the PEA while held by the robot.

Several fabrication revisions to the original design have been made and the kinematic parameters were adjusted from the synthesis result out of necessity. Table III.4 shows the resulting kinematic parameters after fabrication. Figure III.13 overlays the kinematic vectors on the fabricated design for reference. The vectors $\mathbf{e}_i$ are shown for all kinematic links to identify each of the kinematic chains. Only one of the piston vectors $\mathbf{a}_1$ is shown for clarity. Photographs of the prototype insertion tool are shown in Figure III.14.

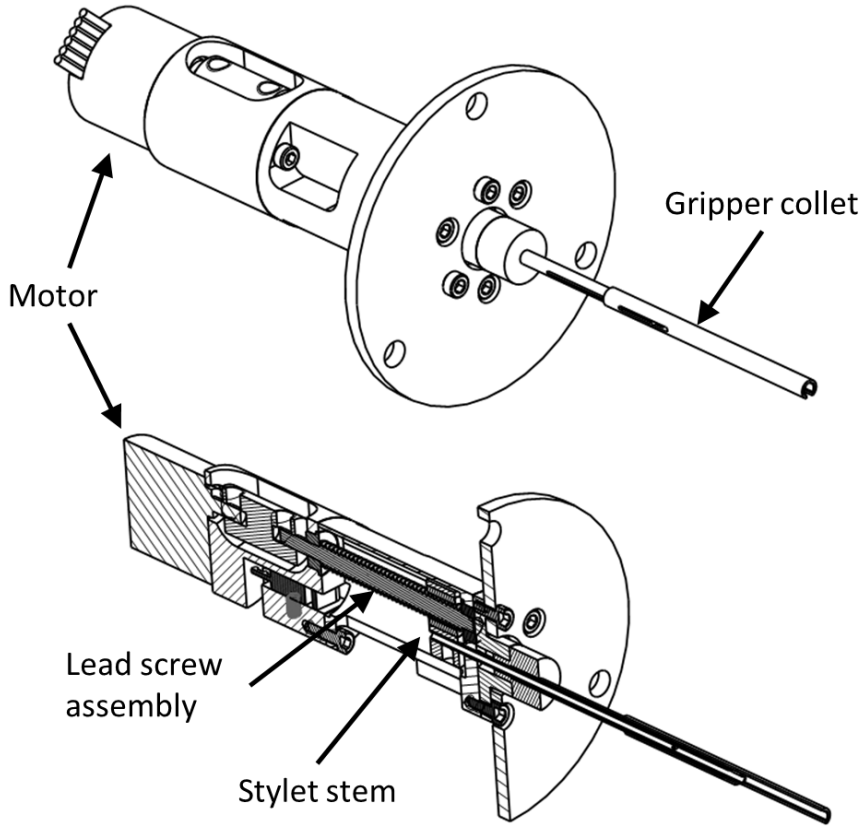

Figure III.12: Insertion Module Rendering. The insertion module uses a single actuator to drive a lead screw transmission. The travelling nut linearly moves a hooked rod through the hollow gripper stem to pull on the PEA stylet. A collet is used to apply compression on the PEA to hold it in the gripper

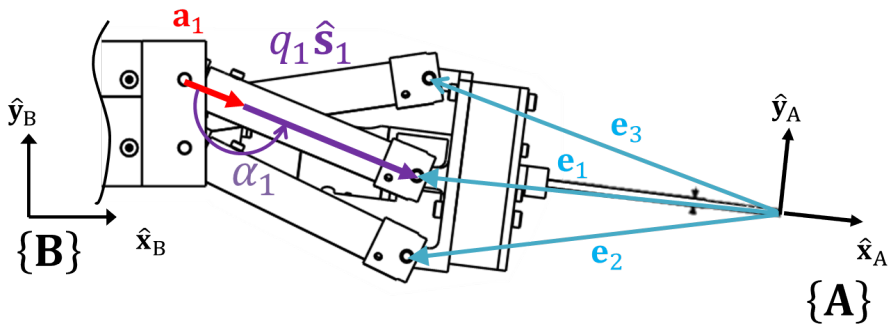

Figure III.13: Kinematic Overlay.

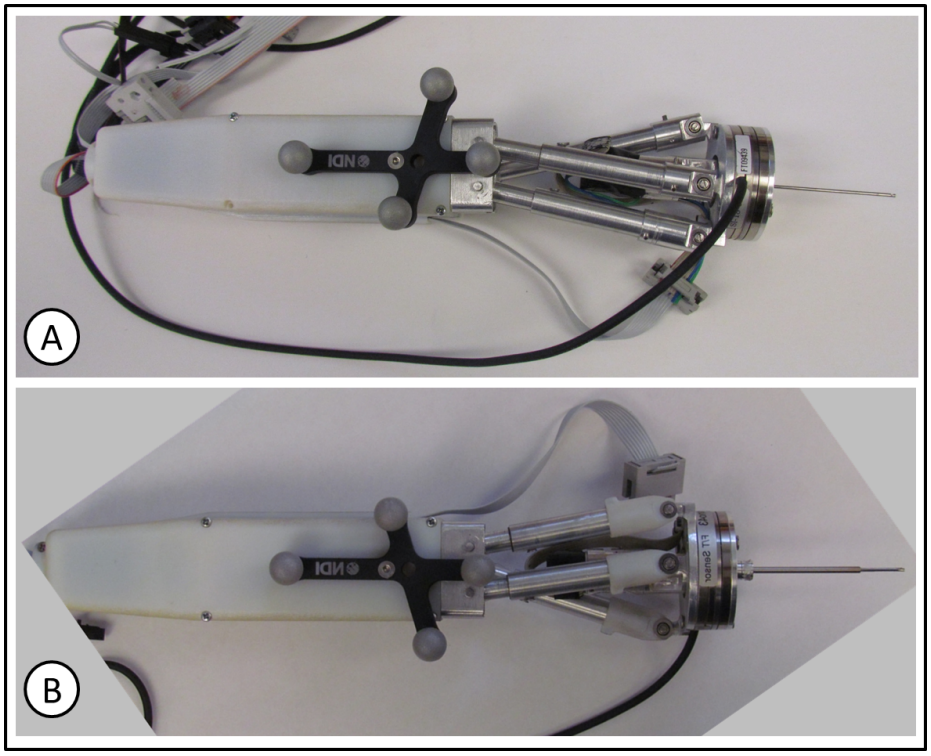

Figure III.14: Prototype system photographs. (A) The original prototype system with coverings and an attached optical tracking frame. (B) Revisions to the distal revolute joint links in each piston introduced slight variation from the original kinematic parameters.

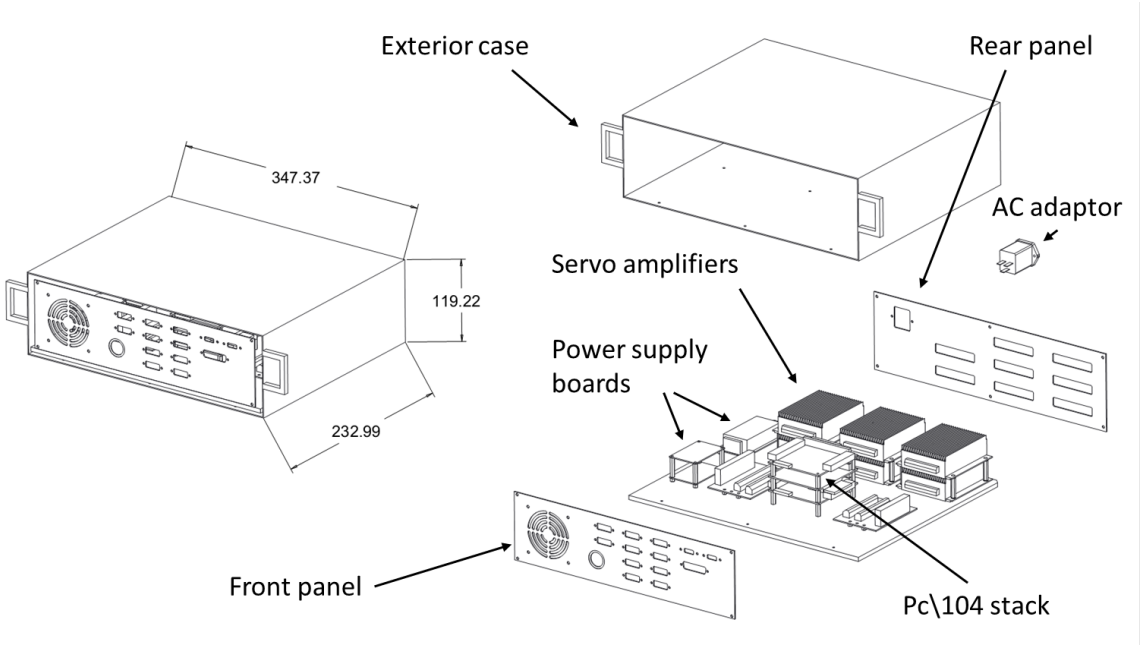

Figure III.15: PC/104 control electronics.

III.7 Control Environment

The control system for the robotic manipulator is a combination of digital and analog data acquisition, transmission electronics, and a real-time software operating system. The electronics hardware centers around a pc/104 single board computer (*Advantech* PCM-3355) running the xPC real-time OS from *Mathworks*. The PC board is supported by two identical control cards (*Sensoray* Model 526) which process digital/analog inputs, read quadrature encoder signals, and provide analog output signals. Analog outputs are used to set control references for a series of 8 servo amplifiers which in turn provide a maximum capacity of 8 individual motor. All components are housed in a single enclosure that is shown in Figure III.15 and a summary of the principle electronic components is presented in Table III.5.

The xPC real-time OS kernel is a part of the MATLAB/Simulink Real Time Workshop. It is designed to translate Simulink models to machine code running at

Component	Parameter	Value
Advantech pc/104 PCM-3350	CPU Speed	500MHz
	RAM	2 GB
	I/O	RS232, Ethernet
Sensoray Model 526 (×2)	DI/O	10 channels
	Analog Input	8 differential / 16 uni (16-bit)
	Analog Output	4 (16-bit)
	Quad. Enc. Counter	4 (32-bit)
Maxon LSC 30/2 Servo Amplifier (×8)	Voltage Output	±10V
	Max Voltage	25V
	Max Current	2 Amps
	Max Power	50W
CUI VMS-160 Power Supply	Input Voltage	90-264 VAC
	Output Voltage	24V
	Max Current	6.7 Amps
	Max Power	160W
	Efficiency	90%
	Output ports	4

Table III.5: PC/104 Electronic Component Specifications

fixed clock cycles. The deployment process is a host/target relationship. The host computer compiles the model and sends it to the target machine via a network connection. The target runs a real-time OS which independently executes the compiled code. A communication protocol is built into the xPC OS so that the host computer may update parameters or retrieve signals. This can be done through either the MATLAB environment or through custom code using the xPC Application Program Interface (API) supplied by *Mathworks*.

The basic control scheme is shown schematically in Figure III.16. A complete computation of the control loop is completed once for each period of the fundamental time step Δt. The High-Level Controller (HLC) translates user inputs into task space motions. This input can be either point-to-point position control, telemanipulation

velocity control or preprogrammed path following control. In all modes of operation a desired task space position vector $\mathbf{x}_{des}$ is output.

The force sensor is a subsystem, converting analog voltage measurements from the force transducer to a wrench in the force sensor frame $\{\mathbf{F}\}$ and is denoted as ${}^{F}\mathbf{f}$. The pose of the force sensor, dependent on the task space pose $\mathbf{x}_{cur}$, affected the wrench measurements due to the effect of gravity loading. A compensation subsystem removes this loading effect and expresses the compensate wrench measurement in the robot base frame $\{\mathbf{B}\}$ as ${}^{F}\tilde{\mathbf{f}}$.

The combination of the current pose $\mathbf{x}_{cur}$, desired pose $\mathbf{x}_{des}$, and perceived wrench ${}^{F}\tilde{\mathbf{f}}$ enter the hybrid force/position admittance control law to produce a modified input trajectory $\mathbf{x}_{admit}$. The strength of the admittance law and the dimensions in which admittance is enable are controlled in this system.

The modified task space input $\mathbf{x}_{admit}$ enters the trajectory planner where inverse kinematics are computed to find reference joint level commands $\mathbf{q}_{ref}$. Safety constraints are imposed in the subsystem to prevent the robot from entering configurations which may damage the mechanical structure of the robot. Also, velocity limits are placement on the allowable task space displacement.

In the Low-Level Controller (LLC) the joint references are converted to actuator references, $\boldsymbol{\theta}_{ref}$, for closed loop position control on the individual servos. The control low at this level is a PID control law. The current actuator feedback, $\boldsymbol{\theta}_{cur}$, is set as an input to a iterative forward kinematic model which computes the estimated current pose $\mathbf{x}_{cur}$. This pose estimation is sent to the pose compensation for the force measurements and completes the outer control loop. The following subsections address the details of the subsystems within the control model.

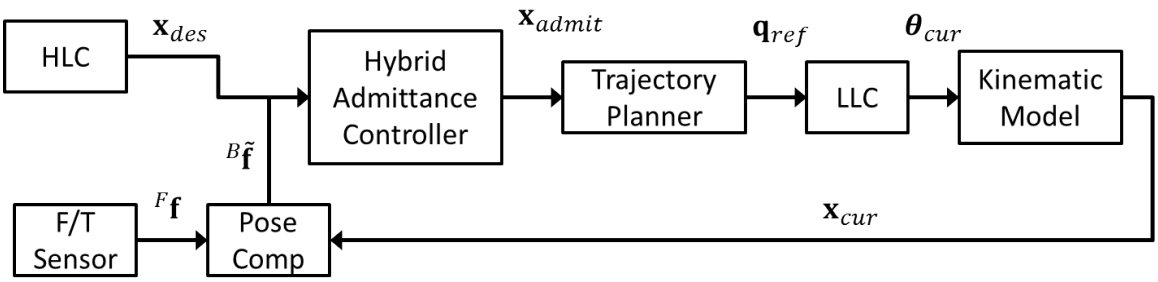

Figure III.16: Control Schematic. The control of the parallel manipulator is separated into a High-Level Controller (HLC), hybrid force/position admittance controller, trajectory planner, and Low-Level Controller (LLC).

High Level Controller

The HLC computes trajectories for the end effector with only kinematic considerations. The system can process inputs from interface devices such as the Geomagic Phantom Omni, Force Dimension Omega series haptic devices, or LEAP motion controller to specify desired motions or direct point to point input through an interface on the host PC. In either case, a resolved rate motion algorithm is used to linearly move the end effector to the desired pose [122]. The maximum rate of motion is specified by the user.

Another mode of operation is the automatic execution of an insertion trajectory as described in Chapter II. The path for insertion can be parameterized by linear depth of insertion ,$d \in [0, L]$, where L is the total length of the PEA to be inserted into the cochlea. The pre-computed trajectory is descretized into N steps along the path with linear interpolation used between the control points.

Force Sensing and Compensation

The ATI Nano43 force/torque transducer signal is processed by the Sensoray DAQ card and when multiplied with a manufacturer-supplied calibration matrix, reports a measured wrench on the sensor. The force/moment sensor frame is denoted as $\{\mathbf{F}\}$

and the wrench applied to the sensor is:

$$^{F}\mathbf{f} = \left[^{F}\mathbf{f}_{s}^{T}, ^{F}\mathbf{m}_{s}^{T}\right]^{T} \tag{III.56}$$

where $^{F}\mathbf{f}_{s}^{T} \in \mathbb{R}^{3}$ is the measured force and $^{F}\mathbf{m}_{s}^{T} \in \mathbb{R}^{3}$ is the measured moment. The perceived wrench ($^{F}\mathbf{f}$) requires a forward feeding compensation term $^{F}\mathbf{f}_{e}$ to account for the forces and moments due to gravity acting on the insertion module:

$$^{F}\mathbf{f}_{e} = \begin{bmatrix} ^{F}\mathbf{R}_{B} & \mathbf{0}_{[3\times3]} \\ \mathbf{0}_{[3\times3]} & ^{F}\mathbf{R}_{B} \end{bmatrix} \mathbf{f}_{g} +^{F} \mathbf{b}_{f} \tag{III.57}$$

where $\mathbf{f}_{g} \in \mathbb{R}^{6}$ is the gravitational wrench, $\mathbf{b}_{f} \in \mathbb{R}^{6}$ is the force sensor bias and $^{F}\mathbf{R}_{B}$ is the rotation matrix describing frame $\{\mathbf{B}\}$ in frame $\{\mathbf{F}\}$. Each time the system is initialized a training routine is performed to determine the direction of gravity and the sensor's static bias. This training requires collecting a set of poses varying in orientation and applying a least squares fitting to $\mathbf{f}_{g}$ and $\mathbf{b}_{f}$ in (III.57).

After applying a $8Hz$ Butterworth filter at $1kHz$ sampling rate and unbiasing, the resulting force projection into the robot base frame is denoted as $^{B}\tilde{\mathbf{f}}_{s}$ where:

$$^{B}\tilde{\mathbf{f}}_{s} = \begin{bmatrix} ^{B}\mathbf{R}_{F} & \mathbf{0}_{[3\times3]} \\ \mathbf{0}_{[3\times3]} & ^{B}\mathbf{R}_{F} \end{bmatrix} \left(^{F}\mathbf{f} -^{F} \mathbf{f}_{e}\right) \tag{III.58}$$

Hybrid Position-Admittance Controller

The goal of the hybrid position-admittance controller is to correct for both registration and kinematic errors in the task space trajectory through active compliance. The clinical motivation comes from the goal of correcting the insertion trajectory due to errors in registration between the robot and patient. This type of controller is

similar to hybrid force controllers that have been applied to many problems and the foundational work can be reviewed in [84]. Given an applied wrench on the robot end effector, $\mathbf{f}$, the admittance control laws can be generalized to a form of:

$$\dot{\mathbf{x}}_{admittance} = g\left(\mathbf{f}\right) \tag{III.59}$$

This admittance velocity is then added to the original desired trajectory $\mathbf{x}_{des}$ to produce a new reference $\mathbf{x}_{admit}$. The parallel robots presented in this work are controlled in position space rather than velocity and this leads to the expression:

$$\mathbf{x}_{admit} = \mathbf{x}_{des} + \int \dot{\mathbf{x}}_{admittance}\, dt \tag{III.60}$$

which is passed as the desired pose to the trajectory planner. The exact definition of the admittance law $g\left(\mathbf{f}\right)$ will be presented in Chapter VI.

III.8 Calibration and Performance Quantification

Before evaluating the accuracy of the robotic manipulator the device had to be calibrated. Typical mechanism calibration looks to adjust geometric parameters and actuator gains so as to minimize the error between the expected pose of the manipulator and the actual pose as measured by some for of external metrology. In the case of this robotic system, the individual joint positions and link dimension were calibrated individually prior to assembly so that geometric calibration would not be mixed with actuator calibration.

The wire actuation lead to a type of backlash resulting from wire extension and internal friction in the pistons. Whenever a piston's direction would change the tension in the wires rapidly switches between the segments and transfers a reverse load to the wire carriage. An unknown amount of load is required to begin moving the

piston in the new direction. During this change of loading the wire carriage is moving and the controller expects that the piston of also moving. A corrective calibration model is required to adjust motor inputs $\boldsymbol{\theta}$ so that the expected piston extensions $\mathbf{q}$ and end effector pose $\mathbf{x}$ were observed.

A new binary state vector $\mathbf{m} = [m_1, m_2, m_3]^T$ is introduced to represent the direction of piston motion. A value $m_i = 0$ indicates that the i'th piston is retracting and a value $m_i = 1$ indicates extension. In the absence of motion the state variable retains its previous value.

Calibration began by returning the system to it's home configuration ($q_i = 0, \psi_i = \psi_0, \theta_i = \theta_0, \mathbf{m} = \mathbf{0}$) and then moving through a sequence of 300 poses $\mathbf{x}_k, k = [1, ..., 300]$. The Polaris Vicra optical tracker was used to measure the relative transformations of the end effector to the robot base. Tracking markers were embedded into the covers of the tool to define the base frame of the robot and to later register the device to the surgical environment. Using (III.5) the value of the measured piston extensions, $\mathbf{q}_k$, was determined. Values recorded from the controller included motor positions $\boldsymbol{\theta}_k$ and the motor direction $\mathbf{m}_k$. The error between measured and the expected piston stroke are written as $\Delta q_{i,k} = q_{i,k} - q_{i,0} = q_{i,k}$. Defining $\Delta\theta_{i,k} = \theta_{i,k} - \theta_{i,0}$ and $\Delta\psi_{i,k} = \psi_{i,k} - \theta_{i,0}$, each kinematic chain has its experimental data separated according to motor direction. A plane is then fitted to the separate data sets for each leg using orthogonal regression satisfying:

$$\Delta\theta_i = \left(\frac{1}{\eta_i}\bigg|_{m_{i,k}} \right) q_i - \left(\frac{r_i}{\eta_i}\bigg|_{m_{i,k}} \right) \Delta\psi_i - \chi_i|_{m_{i,k}}$$

where η_i is the transmission ratio, r_i is the pulley radius, and χ_i is the separation between the forward and backward motion planes caused by backlash.

Figure III.17(B) presents a graphical representation of the fitting process and

shows collected data from the first kinematic chain. Although the fitting in (III.61) allows for different values of r_i and η_i depending on $m_{i,k}$, in practice the coefficients are constant within measurement noise and provide additional validation to the calibration model. The RMS error for the planar fitting was below 0.6 radians in each chain. With a uniform actuator transmission ratio of $\eta_i = 0.097mm/rad$, the fitting error was below the 0.1 mm q_i error assumed during the design synthesis phase. Once χ_i is known, it is applied to the controller to adjust $\boldsymbol{\theta}$ based on $\mathbf{m}$.

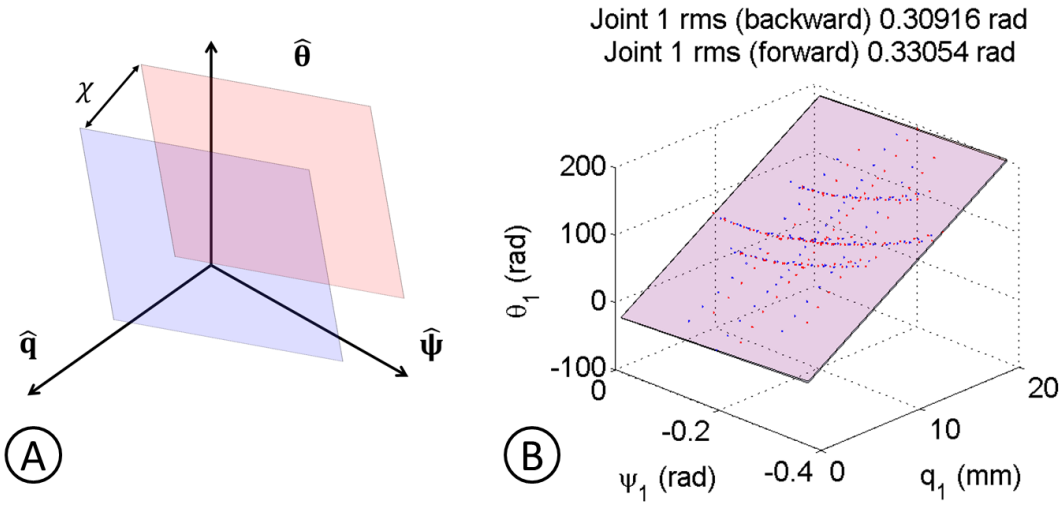

Figure III.17: Joint level kinematics and backlash. Piston extension q_i, arm rotation angle ψ_i, and motor input θ_i are linearly related in the kinematic model. (A) An unknown degree of backlash χ_i crete two planes of motion dependent on the direction of motion in the actuator. (B) Sample calibration results for joint 1.

The task space positioning accuracy and repeatability were tested after calibration. Two experiments were designed to capture the global performance throughout the reachable workspace and along an electrode insertion trajectory. For both types of experiments, trials were repeated 10 times with the robotic system restarted each time to insure that errors in the homing procedure were also included in the evaluation.

A single workspace test involved isolated cyclic movement in each task space

direction (p_x, p_y, ϕ) while the other two positions remained unchanged. Position repeatability is quantified as the RMS error from the average positions at each sample point in the tests. Task space accuracy is presented as the RMS error from the measured end effector position and the desired task space position. Table III.6 presents both the task space position repeatability and accuracy.

Table III.6: System performance quantification

	Positional Repeatability	Positional Accuracy
p_x (mm rms)	$0.02mm$	$0.1mm$
p_y (mm rms)	$0.13mm$	$0.8mm$
ϕ (deg rms)	0.04°	0.25°

The performance of the robot along the electrode insertion path was quantified by following a single electrode insertion trajectory. Figure III.18 shows the insertion trajectory in a solid line, target task-space error bounds of $\pm 0.4mm$ in dashed lines, the error bars for twenty discrete points sampled along the trajectory, and a greyed area showing the uncertainty stemming from the optical tracker error as provided by the manufacturer specifications. The figure shows that the accuracy along the insertion trajectory is better than the global accuracy throughout the entire workspace.

III.9 Conclusions

This chapter has presented a model for the kinematics, statics, and stiffness of a wire actuated 3R$\bar{\text{P}}$R robotic mechanism actuated by closed loop wire rope. The introduction of the wire rope in the actuation scheme couples the prismatic joint actuation in each chain with changes in the orientation of the prismatic link with respect to the robot base frame. From the derivation of the instantaneous kinematics the first order statics and stiffness model were derived. An effect of the coupling between the prismatic actuation and link orientation is a change in the stiffness characteristics of

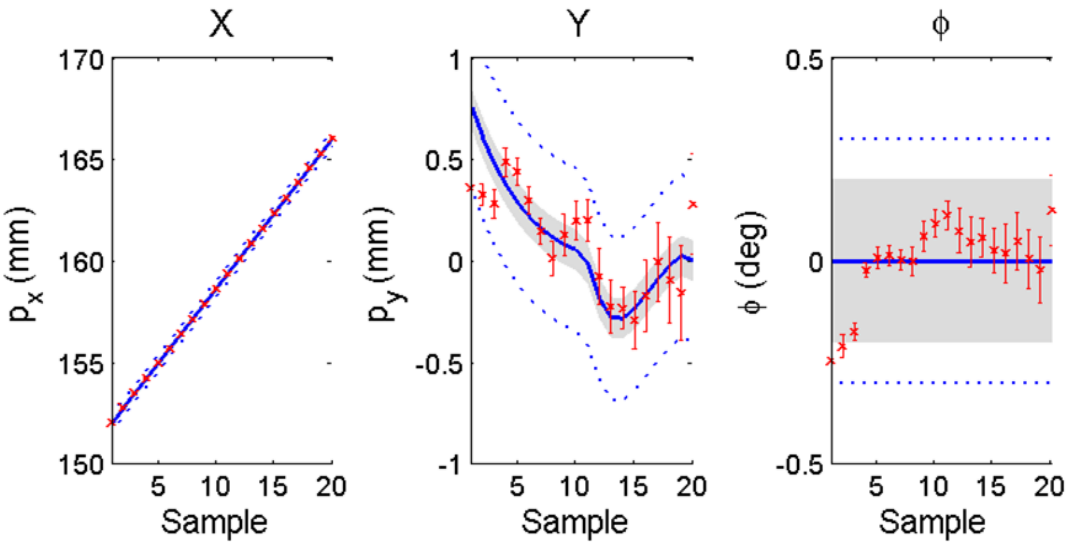

Figure III.18: Position tracking post calibration. Solid line represents desired trajectory, grey area represents tracker uncertainty, and points with error bars show average position and deviation of tracked end effector using 10 trials.

the mechanism. Wire actuation allows a degree of freedom in the design process to introduce intentional compliance into the mechanism.

From this model a synthesis method was presented. The objective was driven from CI task-specific goals presented in the previous chapter. The proposed design emphasizes compactness and accuracy along the preplanned insertion trajectories. The set of kinematic parameters obtained from this optimization are used in the fabrication of the prototype system.

After calibration and task space performance evaluation, the accuracy of the task space position control in the direction $\hat{\mathbf{y}}_B$ was below the desired target specified in Table II.3. While the prototype did not reach the desired specification it will be shown in the following chapter that this did not impede the robot from executing a proper insertion with low insertion force. A major contributor to the error was the friction in the wrapping of the wire rope on the idler pulleys. To address this issue, a design revision will separate the wire paths onto separate pulleys so the the

wire segment coming from the carriage does not rub against the wire rope segment returning to the carriage.

Chapter IV

STATIC BALANCING OF WIRE-DRIVEN MECHANISMS

In the previous chapter it was assumed that the robotic insertion system would be supported by a statically balanced arm as shown in Figure III.1. While there are commercially available support arms that can accomplish this task they typically employ mass and / or spring assemblies as discussed in Chapter I. This chapter addresses the problem of synthesizing mechanisms to solve the static balancing problem. In the previous chapter, the proposed parallel robot used closed loop constant length wire transmissions between the actuators and the prismatic links. While this transmission method introduces kinematic coupling, there were benefits in improving sterilization by isolating the motors from the mechanism's rigid links. The coupling introduced by wire transmission will be exploited in this chapter to present an elegant solution to the static balancing problem. The kinematic coupling will be used to decouple the gravitational torques dependant on a mechanism's configuration.

Prior works [2, 37, 30, 30] have presented balanced mechanisms using a combination of linkage and eleastic elements, usually linear springs, to balance various mechanisms. These proposed devices require complicated synthesis procedures that are specific to the mechanism architecture under study. Also, while the advantage of adding springs and linkage saves mass versus counter weights, it adds more mechanism restrictions and possibilities of linkage interferences. Some works have proposed incorporating cams [55, 50] driving spring elements to generate balancing torques. These designs are compact and elegant but do not easily translate to high dof mechanisms. The embodiment of the balancing solutions derived in this chapter most

closely match the recent results by Kim [51, 52] which used kinematic coupling to decouple torque requirements for balancing a serial arm. The solution proposed in that work depends on solving force balancing equations specific to the serial arm they presented.

The contribution of this chapter is to present an algorithm that will synthesize balancing solutions to a mechanism based on decoupling potential energy between combinations of joint positions. Wire routing provides both a compact and practical physical realization (as seen in [51, 52]) and an efficient means to decouple the required torques for balancing. The first section presents the method proposed to synthesize a static balancing solution to general mechanisms. This is followed by case studies of several mechanism architectures. The chapter closes with discussion of potential further developments for this method.

IV.1 Static Balancing Methodology

The importance of static balancing in medical device applications was discussed in Chapter I and included the benefits of actuator power reduction and improved system safety. In addition to sterilization and miniaturization advantages to wire actuation in parallel mechanisms, there exists the potential to use wire actuation in static balancing of the mechanism. Such a balancing technique would reduce actuator power requirements and provide an added degree of safety in the event of power failure. As discussed in the previous chapter, closed loop wire transmissions can introduce kinematic coupling in the mechanism. This coupling can be exploited to create simple counter balancing mechanisms in high dof kinematic chains.

The basic concept is shown in Figure IV.1. A revolute link is attached to a capstan through a closed loop wire transmission. In turn the capstan is connected to mechanism with an elastic element that produces a counter torque to resist the

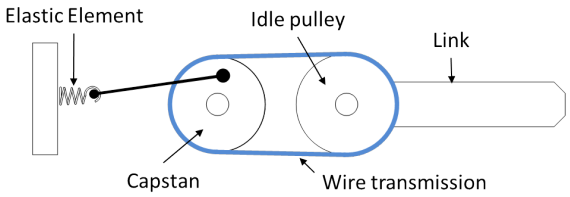

Figure IV.1: Balancing concept.

moment on the joint from the link's mass and gravity. The wire transmission can be routed through multiple links to use the kinematic coupling to alter the capstan's motion as multiple links move.

The algebraic variables discussed here pertain to this chapter only and should not be confused with notation in other chapters of this dissertation. Any mechanism, whether kinematically serial or parallel, has its pose expressed in a vector of joint level generalized coordinates $\boldsymbol{\theta} \in \mathbb{R}^n$. These joints include both active (actuator driven) and passive joints. The task (operational) space coordinates of the mechanism's end effector is expressed by the vector $\mathbf{x} \in \mathbb{R}^w$. When using closed loop wire actuation, the generalized joint coordinates are coupled to new inputs. The *coupled coordinates* are expressed by the vector $\boldsymbol{\psi} \in \mathbb{R}^m$. In general, $m \geq n$ although in cases where some of the joints' rotation axes are parallel to the gravity vector m may be smaller than n. An example of this will be discussed later in the chapter.

Both serial and parallel mechanism are considered in this chapter. A parallel mechanism is considered a collection of serial kinematic chains and thus the focus of the chapter addresses the serial chain balancing. Conversion of the method to parallel architectures is addressed later in the chapter. The general algorithm can be summarized in the following steps with details covered in the subsequent subsections:

1. Calculate the potential energy of the target mechanism throughout its workspace expressed in its generalized joint coordinates $\boldsymbol{\theta}$.

2. Map the generalized coordinates, $\boldsymbol{\theta}$, into a new set of coupled coordinates $\boldsymbol{\psi}$ including all unique combinations of the generalized coordinates.

3. Select a basis function in the new coupled coordinates, $\Phi_i(\psi_i)\,\forall i = 1, \ldots, m$

4. Identify the basis functions that can be summed to best approximate the total potential energy of the system.

5. For each of the selected coupled coordinate, add a torque generating mechanism that cancels out the change in potential energy for the mechanism.

6. Verify actuator torque reduction through virtual work analysis

The work presented in this chapter limits the types of mechanisms considered to those which exclusively have combinations of revolute joints. Actuation of prismatic, continuum and flexural joints are left as possible future directions of research to limit the algorithm to a single basis type in the synthesis process. Universal and spherical joints are included in this discussion since they are simply special sequences of revolute joints with orthogonal intersecting axes at a common point.

Potential Energy Modelling of Generalized Parallel Mechanisms

Satisfying the conditions for a balanced system can be achieved by having the total potential energy of a mechanism remain constant throughout the workspace as shown in [3]. If a mechanism's configuration can be completely defined by a vector of generalized coordinates $\boldsymbol{\theta} \in \mathbb{R}^n$ in a workspace W, then the potential energy of the mechanism due to gravity is defined as $V_g(\boldsymbol{\theta})$. Gravity counter balancing is accomplished through the deflection of elastic elements attached to the mechanism. Letting $V_e(\boldsymbol{\theta})$ be the total elastic energy in the system, the total potential energy of

the combined system, $V(\boldsymbol{\theta})$, is defined as:

$$V(\boldsymbol{\theta}) = V_g(\boldsymbol{\theta}) + V_e(\boldsymbol{\theta}) \tag{IV.1}$$

The procedure for computing the mechanical potential energy is simple. A parallel structure is modelled as a collection of c serial kinematic chains that obey a set of kinematic constraints at their distal end. Each kinematic chain includes $n_{(j)}$, $j = 1, \ldots, c$ links. Figure IV.2 shows a representative link connected by a revolute joint. When more than one kinematic chain exists within a mechanism, any property x associated with the $k'th$ kinematic chain will be designated using $x_{(k)}$ for $k = 1, \ldots, c$.

For the $i'th$ link, the scalar $m_{i,(j)}$ is the mass of the $i'th$ link in the $j'th$ kinematic chain, the vector $\mathbf{a}_{i,(j)} \in \mathbb{R}^3$ defines the location of the of the next link, and the vector $\mathbf{c}_{i,(j)} \in \mathbb{R}^3$ defines the center of mass in the link's local frame. The vector $\mathbf{b}_{(j)}$ denotes the location of the base of the $j'th$ kinematic chain in the world frame $\{0\}$. The joint parameters θ_i are rotations about the axis $\hat{\mathbf{z}}_{i-1}$. Additionally, parameters α_i and β_i are Euler angle rotations about $\hat{\mathbf{x}}_{i-1}$ and $\hat{\mathbf{y}}_{i-1}$ respectively that are part of a link kinematic definition. The homogeneous transform ${}^{i-1}\mathbf{T}_i$ from link $i-1$ to link i is then a function of θ_i, α_i, β_i and $\mathbf{a}_i$ with the details of its calculation presented in Appendix B. Also, the vector $\mathbf{o}_i$ specifies the location of the end of the $i'th$ link.

Defining the vector $\mathbf{g}$ as the gravity acceleration vector then the total potential energy of the mechanism is given by:

$$V_g(\boldsymbol{\theta}) = -\sum_{j=1}^{c} \left(\sum_{i=1}^{n_{(j)}} m_{i,(j)} \left[{}^0\mathbf{c}_{i,(j)} + \mathbf{o}_{i-1} \right] \right)^T \mathbf{g} \tag{IV.2}$$

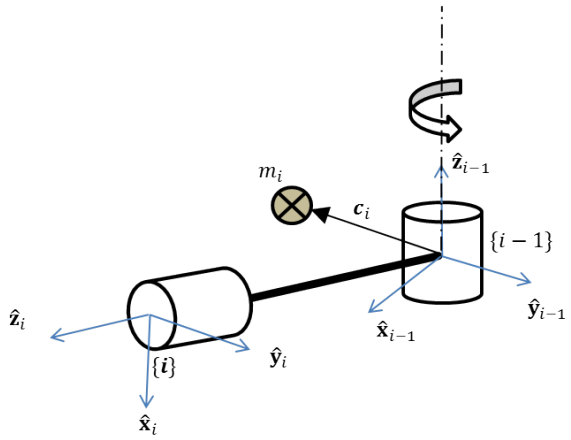

Figure IV.2: A general serial mechanism with revolute links. For the $i'th$ link, the vector $\mathbf{c}_i$ specifies the link's center of mass (magnitude of m_i) with respect to the local frame. The vector $\mathbf{a}_i$ defines the origin of the $i+1$ link in the $i'th$ link frame.

To be statically balanced, the total potential energy must remain constant throughout changes in the mechanism's configuration. This dictates that the following relation for the elastic potential in the mechanism must hold true:

$$\frac{dV_e(\boldsymbol{\theta})}{d\boldsymbol{\theta}} = -\frac{dV_g(\boldsymbol{\theta})}{d\boldsymbol{\theta}} \qquad \forall \boldsymbol{\theta} \in \{W\} \tag{IV.3}$$

The potential energy function is rarely linear with respect to the generalized coordinates $\boldsymbol{\theta}$ but may be expressed in a more convenient form through a linear mapping. Using wire routed actuation, it is possible to map the generalized coordinates $\boldsymbol{\theta}$ to a new space $\boldsymbol{\psi} \in \mathbb{R}^m$ through a structure matrix $\mathbf{S} \in \mathbb{R}^{m \times n}$ such that:

$$\boldsymbol{\psi} = \mathbf{S}\boldsymbol{\theta} \tag{IV.4}$$

This is a common model in coupled tendon mechanisms such as the *daVinci* endowrist [40] and the details of deriving such structural matrices can be reviewed in Tsai's robot analysis text [111]. If the potential energy is then expressed as the sum

of a set of m basis functions $\Phi_i(\psi_i)$ where $i = 1, \ldots, m$, this leads to the expression:

$$V_g(\boldsymbol{\theta}) = \sum_{i=1}^{m} \Phi_i(\psi_i(\boldsymbol{\theta})) \tag{IV.5}$$

The advantage of such a form is that the total gravitational potential energy is the sum of independent terms which can be addressed individually. If a suitable balancing mechanism can be designed to match the general function $\Phi_i(\psi_i)$, then the mechanism can be balanced. In this work only mechanisms with revolute links are considered which leads to the following basis function:

$$\Phi_i = a_i \cos(\psi_i) + b_i \sin(\psi_i) \tag{IV.6}$$

The motivation for this basis function is two fold. The first is that the potential energy, as expressed in equation (IV.2) results in combinations of sine and cosine functions with various combinations of joint angles in the arguments. The true purpose of the coupled generalized coordinates is to reflect the combinations. The second motivation for the basis is an alternative way of expressing a sine wave with a phase shift using a linear combination rather than including the phase inside the sine argument.

The correct coupled coordinates ψ_i to use in the basis in equation (IV.6) for a given mechanism needs to be determined from a collection of all possible unique combinations. We begin with the set of all unique combinations of close loop wire transmissions, $\hat{\mathbf{S}} \in \mathbb{R}^{p \times n}$, from which the final structural matrix $\mathbf{S}$ is a subset (i.e. $\mathbf{S} \subset \hat{\mathbf{S}}$).

Each row of $\hat{\mathbf{S}}$ represents a combination of θ_i that could be a coupled coordinate ψ. It is assumed that any element of $\hat{\mathbf{S}}$ is trinary and can take a value of either 1, 0 or -1. The actual orientation of the link is the important term in relation to gravitational

potential energy and so transmissions must remain 1:1. It was stated that only unique combinations are considered and therefore no row in $\hat{\mathbf{S}}$ can be written as the negative of another row in $\hat{\mathbf{S}}$. The total number of combinations p in $\hat{\mathbf{S}}$ leading to unique basis functions is dependant on dimension of $\boldsymbol{\theta}$ and is:

$$p = \sum_{i=1}^{n} \left(3^{n-i}\right) \tag{IV.7}$$

with $\hat{\mathbf{S}} \in \mathbb{R}^{p \times n}$.

To identify the desired structural matrix $\mathbf{S}$, the workspace W is discretized into u points with index $k = 1, \ldots, u$ for which the generalized coordinates, $\boldsymbol{\theta}^k = \left[\theta_1^k, \ldots, \theta_n^k\right]^T$ and the potential energy V_g^k are calculated. In the notation that follows, a right side superscript indices refers to a discrete pose within the workspace W. The entire set of pose measurements in the workspace W are arranged in a matrix with each configuration represented in a column vector:

$$\boldsymbol{\Theta} = \begin{bmatrix} \theta_1^1 & \ldots & \theta_1^u \\ \vdots & & \vdots \\ \theta_n^1 & \ldots & \theta_n^u \end{bmatrix} \in \mathbf{R}^{n \times u} \tag{IV.8}$$

The structure matrix $\hat{\mathbf{S}}$ is used to remap the configurations to the coupled coordinates across the entire sampled workspace:

$$\boldsymbol{\Psi} = \hat{\mathbf{S}}\boldsymbol{\Theta} = \begin{bmatrix} \Psi_1^1 & \ldots & \Psi_1^u \\ \vdots & & \vdots \\ \Psi_p^1 & \ldots & \Psi_p^u \end{bmatrix} \in \mathbb{R}^{p \times u} \tag{IV.9}$$

The mechanism's gravitational potential energy at each pose is then organized into a

column vector $\mathbf{v}$:

$$\mathbf{v} = \left[V_g^1, \ldots, V_g^k, \ldots, V_g^u\right]^T \in \mathbb{R}^u \tag{IV.10}$$

The next step is to use the set of coupled coordinates Ψ from the matrix $\mathbf{\Psi}$ in the basis functions Φ_i in equations (IV.5) and (IV.6). This results in the linear set of equations:

$$\mathbf{A}\mathbf{o} = \mathbf{v} \tag{IV.11}$$

where matrix $\mathbf{A}$ contains the trigonometric evaluations from equation (IV.6) to be used in determining the potential energy as expressed in equation (IV.5). The vector $\mathbf{o}$ contains the coefficients from (IV.6) and $\mathbf{v}$ is a vector of potential energies. Each row of $\mathbf{A}$ contains all basis terms for a single pose in the workspace and the entire matrix is of the form:

$$\mathbf{A} = \begin{bmatrix} 1, & \cos\Psi_1^1, & \ldots, & \cos\Psi_p^1, & \sin\Psi_1^1, & \ldots, & \sin\Psi_p^1 \\ \vdots & & & & & & \vdots \\ 1, & \cos\Psi_1^u, & \ldots, & \cos\Psi_p^u, & \sin\Psi_1^u, & \ldots, & \sin\Psi_p^u \end{bmatrix} \in \mathbf{R}^{u \times 2p+1} \tag{IV.12}$$

The first column in the matrix $\mathbf{A}$ has a value of 1 for each element and is associated with a constant offset in the potential energy functions based on the elevation of the base of each kinematic chain. The coefficients for the trigonometric functions contained in $\mathbf{o}$ are:

$$\mathbf{o} = [a_0, a_1, \ldots, a_p, b_1, \ldots, b_p]^T = \left[a_0, \mathbf{o}_a^T, \mathbf{o}_b^T\right]^T = \mathbf{A}^\dagger \mathbf{v} \in \mathbb{R}^{2p+1} \tag{IV.13}$$

The coefficient a_0 is the magnitude of the constant potential energy offset and is

ignored in the balancing problem since its contribution disappears when differentiating potential energy in equation (IV.3). The subvectors of $\mathbf{o}$ are $\mathbf{o}_a$, $\mathbf{o}_b \in \mathbb{R}^p$ and are the coefficients of the cosine and sine parts of the basis function respectively.

The non-zero elements of the vector $\mathbf{o}_a$ and $\mathbf{o}_b$ correspond to an identified relevant row of $\hat{\mathbf{S}}$ that is a part of $\mathbf{S}$. Once the columns of $\mathbf{S}$ have been found, $\boldsymbol{\psi}$ is calculated using (IV.4) and the reconstructed potential energy $\tilde{V}_g$ is calculated for each point in the workspace. The error in the reconstruction of the potential field, $\boldsymbol{\epsilon}$ is defined as:

$$\boldsymbol{\epsilon} = \begin{bmatrix} V_g^1 - \tilde{V}_g^1 \\ \vdots \\ V_m^u - \tilde{V}_m^u \end{bmatrix} \in \mathbb{R}^u \tag{IV.14}$$

In addition to the maximum and minimum error, the RMS error is also computed as:

$$\epsilon_{RMS} = \sqrt{\frac{\boldsymbol{\epsilon}^T \boldsymbol{\epsilon}}{u}} \tag{IV.15}$$

Checking the errors in the reconstruction of the potential energy with the identified coupling terms is a critical step in the process. If the RMS or maximum errors are large, one of two conclusions could be inferred. The first is that the identification of the relevant coupled generalized coordinates has an error in implementation. The second is that the basis function may not be suitable for the mechanism under study.

Serial Chain Energy Mapping

To demonstrate this basis function approach, an example case will be presented. Consider a $3R$ planar serial kinematic chain moving in the vertical plane. A schematic representation of the mechanism is shown in Figure IV.1.

The link parameters are summarized in Table IV.1. The workspace was discretized

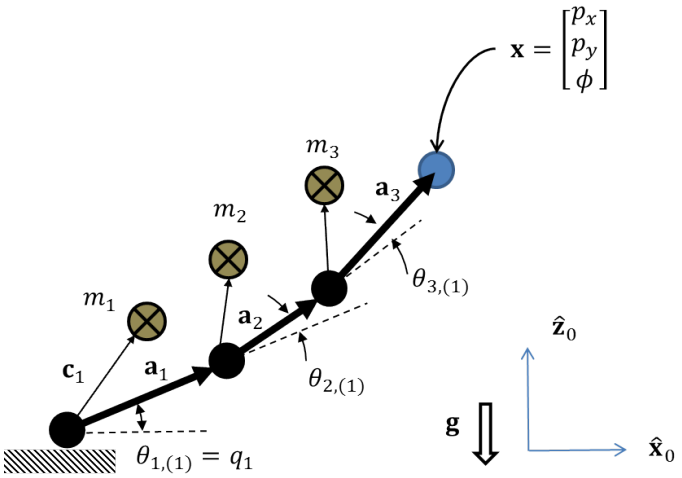

Figure IV.3: $3\bar{R}$ kinematic diagram.

into 40 points per joint with limits set to $\theta_i \in [-120°, 120°]$ for a total of $u = 2400$ poses in W.

Table IV.1: Example Parameters for 3R Serial Planar Robot

Parameter	m_1 (kg)	m_2 (kg)	m_3 (kg)
Value	1	1	1
Parameter	$\mathbf{a}_1$ (m)	$\mathbf{a}_2$ (m)	$\mathbf{a}_3$ (m)
Value	$[10, 0, 0]^T$	$[10, 0, 0]^T$	$[10, 0, 0]^T$
Parameter	$\mathbf{c}_1$ (m)	$\mathbf{c}_2$ (m)	$\mathbf{c}_3$ (m)
Value	$[5, 0, 0]^T$	$[5, 0, 0]^T$	$[5, 0, 0]^T$
Parameter	α_1 (rad)	α_2 (rad)	α_3 (rad)
Value	0	0	0
Parameter	α_1 (rad)	α_2 (rad)	α_3 (rad)
Value	0	0	0
Parameter	$\mathbf{g}$ (m/s^2)		
Value	$[0, -9.81, 0]^T$		

Since the number of generalized coordinates in this example is $n = 3$, the total number of structural matrix combinations from (IV.7) is $p = 13$. The wire routing

permutation matrix is:

$$\hat{\mathbf{S}} = \begin{bmatrix} 1, & 1, & 1, & 1, & 1, & 1, & 1, & 1, & 1, & 0, & 0, & 0, & 0 \\ 0, & 1, & -1, & 0, & 0, & 1, & 1, & -1, & -1, & 1, & 1, & 1, & 0 \\ 0, & 0, & 0, & 1, & -1, & 1, & -1, & 1, & -1, & 0, & 1, & -1, & 1 \end{bmatrix}^T$$

Computing equations (IV.8) through (IV.13) and solving for the vector $\mathbf{o}$ in equation (IV.11) the subvectors $\mathbf{o}_a$ and $\mathbf{o}_b$ are:

$$\mathbf{o}_a = [245, 147.15, 0, 0, 0, 49.05, 0, 0, 0, 0, 0, 0, 0]^T$$
$$\mathbf{o}_b = [0, 0, 0, 0, 0, 0, 0, 0, 0, 0, 0, 0, 0]^T$$

Any component that is non-zero in *either* $\mathbf{o}_a$ or $\mathbf{o}_b$ indicates a relevant basis function. In this case the first, second, and sixth rows are taken from $\hat{\mathbf{S}}$ and the final structural matrix $\mathbf{S}$ is determined to be:

$$\mathbf{S} = \begin{bmatrix} 1, & 0, & 0 \\ 1, & 1, & 0 \\ 1, & 1, & 1 \end{bmatrix}$$

This result for the wire routing pattern based on this structural matrix is shown in Figure IV.1. The balancing system using elastic components is attached to the capstans with degree of freedom ψ_i. The actuators driving the links could either be direct drive on each link (directly control θ_i) or can be attached to the capstans (control ψ_i). It must also be noted that wire routing is only one of several possible ways to realize the coupling structural matrix. The use of timing belts or linkages

could also be used if the design requires it. So long a the kinematic coupling obeys (IV.4) any physical implementation will work in this formulation.

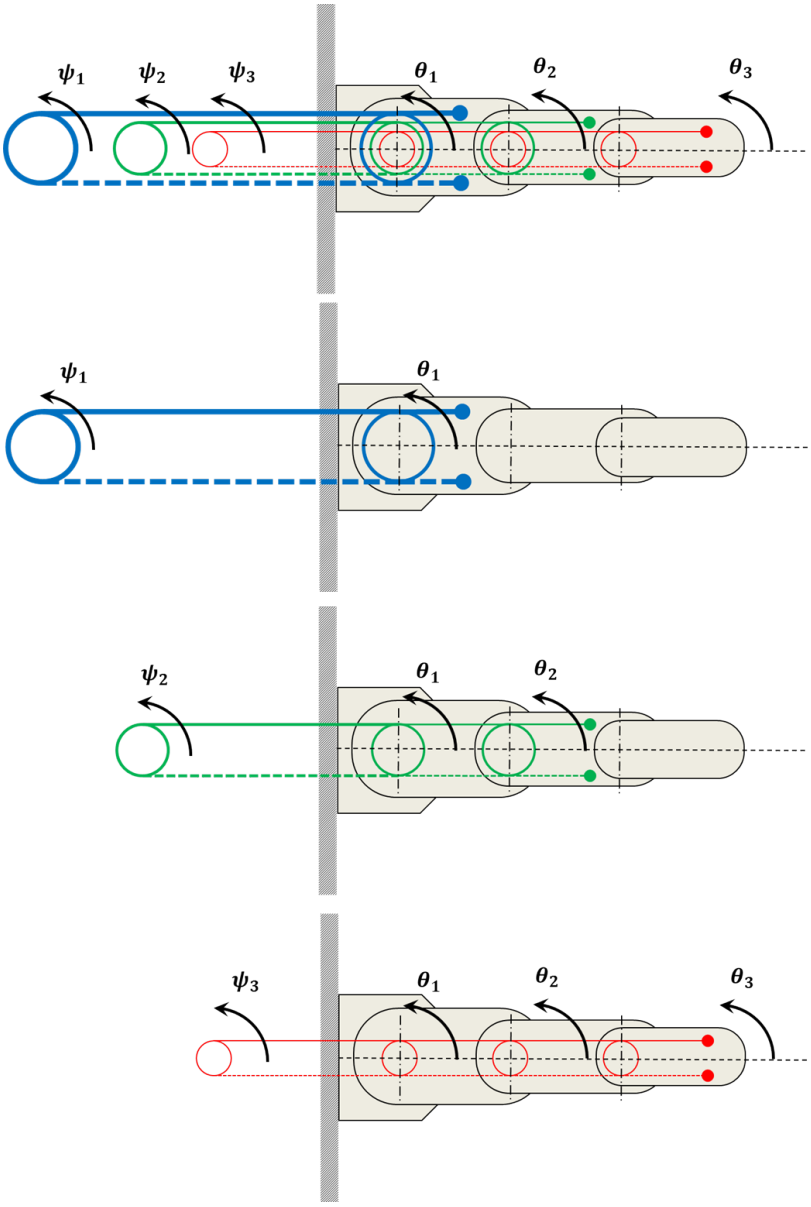

Figure IV.4: Wire actuation in a serial revolute link chain. Dashed lines are used to represent the return path of a wire loop. The top figure shows all three wire routings with lower figure showing a single routing and the associated degrees of freedom.

For this example serial mechanism, the potential energy curves as a function of ψ are shown in Figure IV.5. The required motion range for each degree of freedom

ψ_i grows as more links are coupled. The error in the fitting of the potential function is on the order of $10^{-13}\,J$ which indicates a perfect fitting of the gravitational energy function.

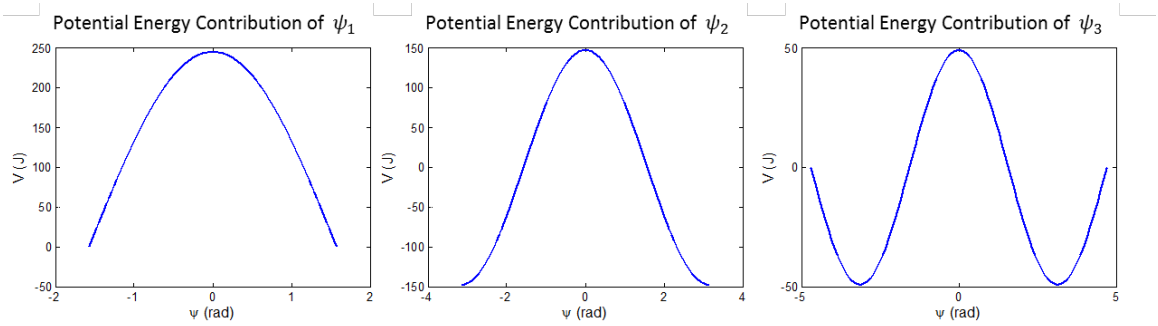

Figure IV.5: Decoupled Potential Energy in $3R$ Mechanism. The total potential energy of the $3R$ serial mechanism is expressed as the sum of potentials in the generalized coordinate space $\boldsymbol{\psi}$.

Once the potential energy is expressed in terms of the generalized coordinates $\boldsymbol{\psi}$, the balancing problem is solved through the synthesis of torque generating mechanisms attached to each degree of freedom ψ_i. This process is covered in the next section.

Counter Balance Mechanism Synthesis

Once the desired potential energy functions $\Phi_i(\psi_i)$ are found, a mechanism must be synthesized to create the required counter-torque. A separate counter-torque mechanism is created for each coupled coordinate, ψ_i. Substituting equation (IV.5) into equation (IV.1) expresses the energy equation as:

$$V(\boldsymbol{\psi}) = \sum_{i=1}^{m} \Phi_i(\psi_i) + V_e(\boldsymbol{\psi}) \tag{IV.16}$$

The energy equations are now completely represented in terms of the coupled

coordinates $\boldsymbol{\psi}$. The total energy must remain constant for static balancing and differentiating (IV.16) with respect to $\boldsymbol{\psi}$ yields:

$$\frac{dV_e(\boldsymbol{\psi})}{d\boldsymbol{\psi}} = -\frac{d}{d\psi}\left(\sum_{i=1}^{m}\Phi_i(\psi_i)\right) \tag{IV.17}$$

Therefore in the coupled coordinates, the required torque function $y_i(\psi_i)$ is:

$$y_i(\psi_i) = -\frac{dV_e(\boldsymbol{\psi})}{d\psi_i} = a_i\sin(\psi_i) - b_i\cos(\psi_i) \tag{IV.18}$$

A simple method of generating this sine wave function is using a spring loaded cable attached to the capstan as shown in Figure IV.1. A similar mechanism has been presented recently by Kim [52] for the balancing of serial arms. The cable passed through idle pulleys and is attached to the capstan at a radius r with an offset angle η when the capstan is at angle $\psi_i = 0$. The distance between the axis of the capstan and the idler pulleys is denoted as d.

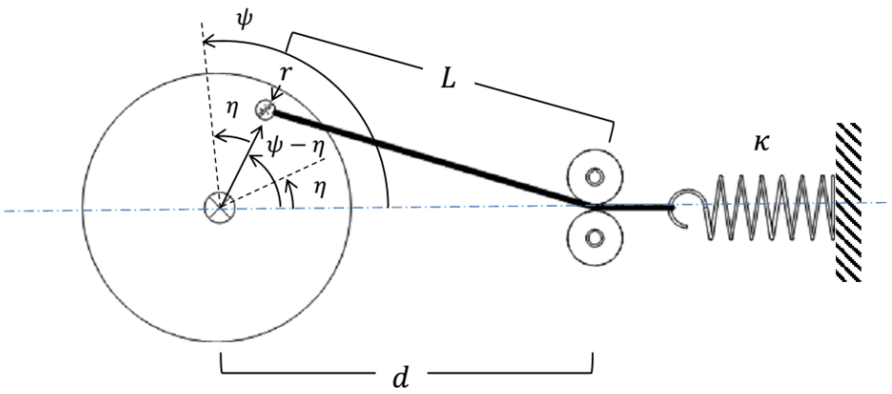

Figure IV.6: Balance mechanism schematic.

Using the identity $\sin(\alpha-\beta) = \sin(\alpha)\cos(\beta) - \cos(\alpha)\sin(\beta)$, it is possible to

rewrite (IV.18) as the following:

$$y_i(\psi_i) = A\sin(\psi_i - \eta) \tag{IV.19}$$

where

$$A = \sqrt{a_i^2 + b_i^2} \tag{IV.20}$$

and

$$\eta = \text{atan2}\,(b_i, a_i) \tag{IV.21}$$

The required torque to counter balance the capstan is a sinusoidal function identical to the form found when balancing a single link with the use of a zero length spring. The first use of this balancing concept is credited to LaCoste and a review of its use in static balancing can be found in work by Deepak [30]. What follows are the calculations proving the balancing condition. The analysis begins with the energy stored in the elastic spring of length l, free length l_0 and a linear spring constant denoted by κ.

$$V_e(\psi_i) = \frac{1}{2}\kappa(l - l_0)^2 \tag{IV.22}$$

The length of the spring is the only term that is a function of ψ_i and can be computed through triangulation:

$$l = \left[(d - r\,\cos(\psi_i - \eta))^2 + r^2\sin^2(\psi_i - \eta)\right]^{\frac{1}{2}} = \left[d^2 - 2rd\cos(\psi_i - \eta) + r^2\right]^{\frac{1}{2}} \tag{IV.23}$$

The torque generated by the mechanism is determined by taking the partial derivative of the energy with respect to the variable ψ_i. This yields:

$$\tau_e(\psi_i) = \frac{\partial V_e}{\partial \psi_i} = \kappa(l - l_0)\frac{dl}{d\psi_i} \tag{IV.24}$$

where

$$\frac{dl}{d\psi_i} = rd\sin(\psi_i - \eta)\left[d^2 - 2rd\cos(\psi_i - \eta) + r^2\right]^{-\frac{1}{2}} = \frac{rd\sin(\psi_i - \eta)}{l} \tag{IV.25}$$

The simplified torque equation then becomes:

$$\tau_e(\psi_i) = \kappa(l - l_0)\frac{2rd\sin(\psi_i + \eta)}{l} \tag{IV.26}$$

For perfect balancing, the sum of equations (IV.19) and (IV.26) must be equal to zero. The resulting equation is:

$$y_i(\psi_i) + \tau_e = A\sin(\psi_i + \eta) + \kappa(l - l_0)\frac{rd\sin(\psi_i + \eta)}{l} = 0 \tag{IV.27}$$

This equation demonstrates the necessity of a zero-length spring for perfect balancing. The length l contains a cosine function and therefore the first and second terms in (IV.27) cannot sum to zero. If $l_0 = 0$ then the length l appears in both the numerator and denominator of the second term and they cancel each other out of the equation. Factoring out $\sin(\psi_i - \eta)$ leaves the following equality:

$$A + 2\kappa rd = 0 \tag{IV.28}$$

Now any two of the three parameters r, d, and κ can be chosen freely. In practice, spring constants are limited to discrete values based on manufacturer availability. The radius of the capstan could be limited by physical considerations and usually adjusting the separation d is the easiest parameter to adjust and is computed from

(IV.28) as:

$$d = -\frac{A}{2\kappa r} \tag{IV.29}$$

This simple mechanism can provide perfect counter balancing for capstans requiring sinusoidal torque functions. The final step of the synthesis process is to verify the torque reduction through virtual work methods and is covered in the next section.

Residual Required Static Actuation Computation

The verification of the torque reduction is calculated through the application of virtual work principles. There are four sources of energy to account for in the entire system. The first is the torque applied by each actuator which is expressed in the vector $\boldsymbol{\tau}_q \in \mathbb{R}^q$. The next is the wrench applied by the end effector on the environment, denoted as $\boldsymbol{\tau}_w \in \mathbb{R}^w$. The torque generated by the counter balancing mechanisms discussed in the previous section are $\boldsymbol{\tau}_e \in \mathbb{R}^m$. Lastly, if the weight of z links in the assembly cannot be considered negligible, then a set of gravitational forces $\boldsymbol{\tau}_{c,i} \in \mathbb{R}^3$ for $i = 1, \ldots, z$ must be calculated.

For the virtual work method the instantaneous velocities at the points of wrench application are also required. The twist of the end effector is denoted as $\dot{\mathbf{x}}$. The joint velocities are expressed in the vector $\dot{\boldsymbol{\theta}}$ from which a subset are the actuated joints with velocities in the vector $\dot{\mathbf{q}}$. The coupled joint velocities $\dot{\boldsymbol{\psi}}$ are related to $\dot{\boldsymbol{\theta}}$ through the structural matrix $\mathbf{S}$. Lastly, the velocities of the rigid links' centers of mass are denoted by the vectors $\dot{\mathbf{c}}_i$ for $i = 1, \ldots, z$. The value of z is equivalent to the sum of $n_{(j)}$ links for c kinematic chains:

$$z = \sum_{j=1}^{c} n_{(j)} \tag{IV.30}$$

With this notation, the complete energy balance equation is given by:

$$\boldsymbol{\tau}_q^T \dot{\mathbf{q}} + \boldsymbol{\tau}_w^T \dot{\mathbf{x}} + \boldsymbol{\tau}_e^T \dot{\boldsymbol{\psi}} + \sum_{i=1}^{z} \left(\boldsymbol{\tau}_{c,(i)}^T \dot{\mathbf{c}}_i \right) = 0 \tag{IV.31}$$

The goal is to compute the actuator torque needed to satisfy (IV.31). This torque is called the *residual torque* and in the case of perfect balancing this quantity would remain zero throughout the workspace. To solve for $\boldsymbol{\tau}_q$, several Jacobians are introduced to map all velocities into a common coordinate system. In this case, all velocities are mapped into the task space based on personal preference. Table IV.2 presents a summary of the required Jacobians, their dimensionality and relationship between parameters. The derivation of mechanism-specific Jacobians are included in Appendix B.

Table IV.2: Summary of Required Jacobians for Static Balancing

Jacobian	Dimensionality	Relationship
$\mathbf{J}_{qx}$	$q \times w$	$\dot{\mathbf{q}} = \mathbf{J}_{qx}\dot{\mathbf{x}}$
$\mathbf{J}_{\theta x}$	$n \times w$	$\dot{\boldsymbol{\theta}} = \mathbf{J}_{\theta x}\dot{\mathbf{x}}$
$\mathbf{J}_{c\theta,i}$	$3 \times n$	$\dot{\mathbf{c}}_i = \mathbf{J}_{c\theta,i}\dot{\boldsymbol{\theta}}$
$\mathbf{S}$	$m \times n$	$\dot{\boldsymbol{\psi}} = \mathbf{S}\dot{\boldsymbol{\theta}}$

Applying the Jacobians in Table IV.2 into equation (IV.31) and factoring the common $\dot{\mathbf{x}}$ results in the following:

$$\left[\boldsymbol{\tau}_q^T \mathbf{J}_{qx} + \boldsymbol{\tau}_w^T + \boldsymbol{\tau}_e^T \mathbf{S}\mathbf{J}_{\theta x} + \sum_{i=1}^{z} \left(\boldsymbol{\tau}_{c,i}^T \mathbf{J}_{c\theta,i}\mathbf{J}_{\theta x} \right) \right] \dot{\mathbf{x}} = 0 \tag{IV.32}$$

The trivial solution is $\dot{\mathbf{x}} = \mathbf{0}$ but the final residual torque solution is the following:

$$\boldsymbol{\tau}_q = -\left(\mathbf{J}_{qx}^T\right)^{-1}\left[\boldsymbol{\tau}_w + \mathbf{J}_{\theta x}^T\mathbf{S}^T\boldsymbol{\tau}_e + \sum_{i=1}^{z}\left(\mathbf{J}_{\theta x}^T\mathbf{J}_{c\theta,i}^T\boldsymbol{\tau}_{c,i}\right)\right] \tag{IV.33}$$

The residual actuator torque $\boldsymbol{\tau}_q$ is calculated throughout the discretized workspace for the evaluation of the static balancing. The key statistics of comparison are the average magnitude of torque per actuator and the maximum magnitude of torque required throughout the workspace. In cases without perfect balancing, reduction of peak magnitudes still allow for reduction in actuator size. Similarly, reductions in the average actuator torque translate into power savings. The next section will present some examples of applying this balancing synthesis method to serial and parallel mechanisms.

IV.2 Balancing of Various Mechanism Architectures

In this section several mechanism types will be presented along with the results of the balancing solutions. These mechanisms include the $3\bar{R}$ planar serial robot, the $3\bar{R}RR$ planar parallel robot, and the $3\bar{R}S\bar{R}R$ spatial parallel robot. A bar over a joint description indicates that the joint is actively actuated. Each of these mechanisms can be perfectly balanced in theory with the approach presented in this chapter but the requirements for wire routing may make the solution unattractive from an implementation point of view.

$3\bar{R}$ Balancing

The $3\bar{R}$ planar serial robot is shown schematically in Figure IV.1. Link parameters and masses are taken from Table IV.1. The details of the kinematic equations and Jacobians used in (IV.33) are found in the Appendices in section B.1.

The average magnitude of torque for the $i'th$ actuator, $\tau_{avg,i}$, is computed as:

$$\tau_{avg,i} = \frac{1}{u} \sum_{k=1}^{u} \left| \tau_{q,i} \left(\theta_{(k)} \right) \right| \tag{IV.34}$$

while the peak torque is define as the largest magnitude of residual torque throughout the workspace.

Figure IV.2 compares the torque reduction under several conditions with both average and peak values plotted. Due to implementation restrictions it may not be possible or undesirable to route coupling wires to distal links. This figure shows how actuator torques are reduced as more of the coupled joint capstans have balancing mechanisms attached. The label $SX - Y$ in the figure legend should be interpreted as balancing mechanisms attached to coupled generalized coordinate ψ_X through ψ_Y. This may also be interpreted as using the $X'th$ to $Y'th$ rows of the matrix $\mathbf{S}$ and setting all other rows in the matrix to zero.

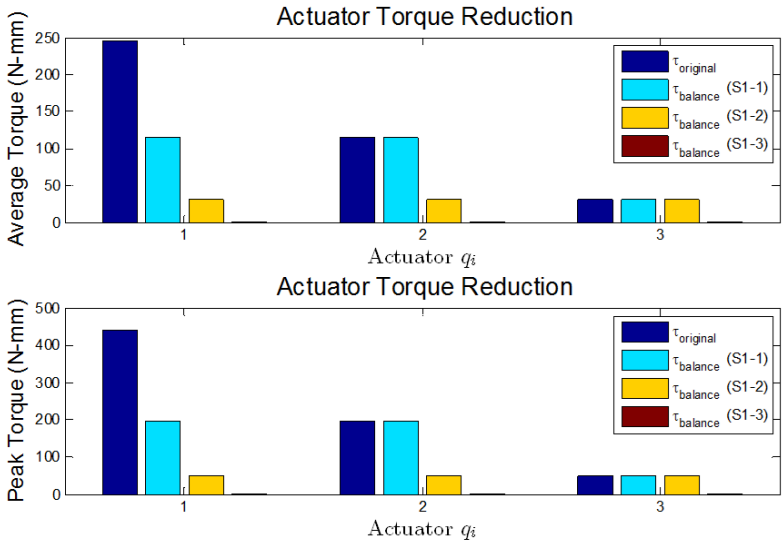

Figure IV.7: $3\bar{R}$ torque reduction. The top plot shows average torque reduction throughout the workspace and the bottom plot shows reduction in peak torque

What can be seen from Figure IV.2 is that torque in joint 1 continues to be reduced as each balancing mechanism is added because this joint carries the total load of the kinematic chain. Likewise, joint 3 sees no torque reduction until the third and final balancing mechanism is added. The torque reduction is perfect in theory, although the actuators would still need to compensate for friction and manufacturing tolerances in the balancing mechanism may introduce small amounts of residual torque in the actuators.

$3\bar{R}RR$ Balancing

The next example case presented is the $3\bar{R}RR$ planar parallel robot shown schematically in Figure IV.2. Unlike the serial $3\bar{R}$ robot, the workspace in this design was discretized in task space. Section B.2 of Appendix B provides details of the kinematics and differential kinematics of this mechanism.

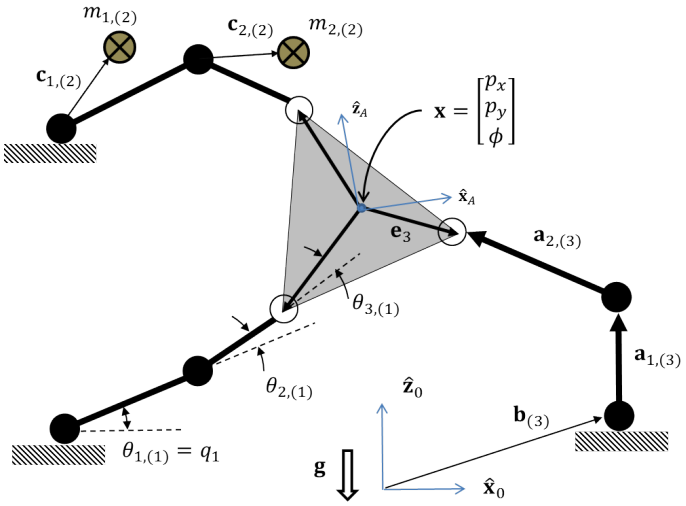

Figure IV.8: $3\bar{R}RR$ kinematic diagram.

The kinematic and mass parameters used in the analysis of the robot design are shown in Table IV.3. With three kinematic chains with three joints each the total permutations for the combination matrix $\hat{\mathbf{S}}$ is $p = 9841$ based on equation (IV.7).

This large dimension leads to poorly conditioned matrices for the identification of relevant energy functions as presented in equation (IV.13). What is required is a method for reducing the number of permutations.

Table IV.3: Parameters for $3\bar{R}RR$ Planar Parallel Robot

End Effector Properties			
Mass (kg)	10		
$\mathbf{g}$ (m/s^2)	$[0, 0, -9.81]^T$		
Kinematic Chain Properties			
Parameter	Chain $k = 1$	Chain $k = 2$	Chain $k = 3$
$\mathbf{e}_{(k)}$ (mm)	$[-86.6, -50, 0]^T$	$[0, 100, 0]^T$	$[86.6, -50, 0]^T$
$\mathbf{b}_{(k)}$ (mm)	$[-259.8, -150, 0]^T$	$[0, 300, 0]^T$	$[259.8, -150, 0]^T$
Mass $m_{1,(k)}$ (kg)	1	1	1
Mass $m_{2,(k)}$ (kg)	1	1	1
$\mathbf{a}_{1,(k)}$ (mm)	$[250, 0, 0]^T$	$[250, 0, 0]^T$	$[250, 0, 0]^T$
$\mathbf{a}_{2,(k)}$ (mm)	$[250, 0, 0]^T$	$[250, 0, 0]^T$	$[250, 0, 0]^T$
$\mathbf{c}_{1,(k)}$ (mm)	$[125, 0, 0]^T$	$[125, 0, 0]^T$	$[125, 0, 0]^T$
$\mathbf{c}_{2,(k)}$ (mm)	$[125, 0, 0]^T$	$[125, 0, 0]^T$	$[125, 0, 0]^T$
$\alpha_{1,(k)}$ (rad)	0	0	0
$\alpha_{2,(k)}$ (rad)	0	0	0
$\beta_{1,(k)}$ (rad)	0	0	0
$\beta_{2,(k)}$ (rad)	0	0	0

The method proposed in this work to reduce computational burden is to pre-assign the fraction of the wrench on the end effector that each kinematic chain is expected to support and design the balance mechanism independently for each chain. This results in a much smaller number of configurations to support with $p = 39$. In this analysis the end effector pose $\mathbf{x}$ is coincident with the center of mass of the end effector and each kinematic chain is expected to carry an equal fraction of the load. Three $3\bar{R}$ serial planar mechanisms are then balanced as previously presented. The first two links' parameters for each chain are taken directly from Table IV.3. For the third

link, the following values are used:

$$m_{3,(k)} = \frac{m_e}{3} \tag{IV.35a}$$

$${}^{3}\mathbf{a}_{3,(k)} = -{}^{A}\mathbf{e}_{(k)} \tag{IV.35b}$$

$${}^{3}\mathbf{c}_{3,(k)} = -{}^{A}\mathbf{e}_{(k)} \tag{IV.35c}$$

The results of the static balancing solution are shown in Figure IV.2. Like with the $3\bar{R}$ plots in Figure IV.2, the bar graphs show the torque reduction based on the number of balance mechanisms added. In this case, balance mechanism are added simultaneously to capstans controlling the same links in each kinematic chain. For example, the label $S1-1$ means that a balancing mechanism was added to each $\psi_{1,(k)}$ for $k = 1, 2, 3$.

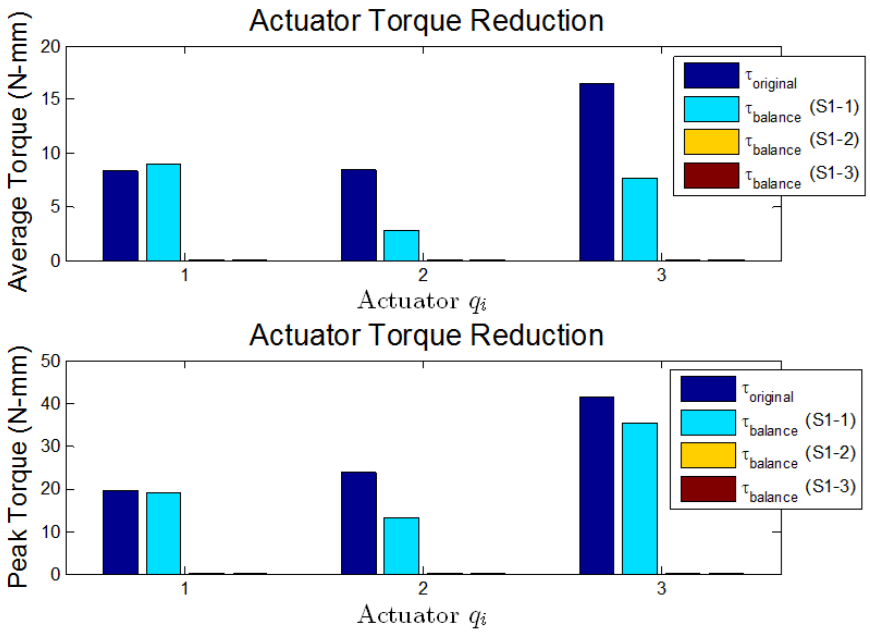

Figure IV.9: $3\bar{R}RR$ torque reduction. The top plot shows average torque reduction throughout the workspace and the bottom plot shows reduction in peak torque

An interesting result appears due to the symmetry of the design with the parameters from Table IV.3. The individual kinematic chains need 3 mechanisms to balance the three links and so nine mechanisms were added. However, when the chains are combined only the first two mechanisms in each link are necessary to balance the mechanism. This is not true in general and if the design is asymmetric then the nine balancing mechanisms are required.

$3\bar{R}S\bar{R}R$ Balancing

The final mechanism presented in this chapter is a $3\bar{R}S\bar{R}R$ parallel structure shown schematically in Figure IV.2. This a variation of the $3\bar{R}S\bar{P}R$ design studied by Simaan [96] which switches the prismatic actuated joint for a revolute joint. The kinematic and differential kinematic solutions are detailed in section B.3 of Appendix B. The actuated joints, expressed in the vector $\mathbf{q} \in \mathbb{R}^6$ have the following relationship with the generalized coordinates θ_i:

$$q_1 = \theta_{1,(1)}, \qquad q_2 = \theta_{4,(1)}, \qquad q_3 = \theta_{1,(2)}, \qquad q_4 = \theta_{4,(2)}, \qquad q_5 = \theta_{1,(3)}, \qquad q_6 = \theta_{4,(3)}$$

The parameters used for the analysis are summarized in Table IV.4. The spherical joint in this mechanism is created through three consecutive revolute joints on orthogonal axes that intersect at a common point. It can also be seen from Table IV.4 that the mechanism is designed so that the first two joints in each chain have their rotation axes parallel to $\hat{\mathbf{z}}_0$ and therefore do not have the weight of their links contribute to the actuator torque. This reduces the balancing problem to a set of three $4\bar{R}$ mechanisms.

When constructing the combination matrix $\hat{\mathbf{S}}$, the first two elements were force to zero to prevent any wire routing through the first two joints in each kinematic chain.

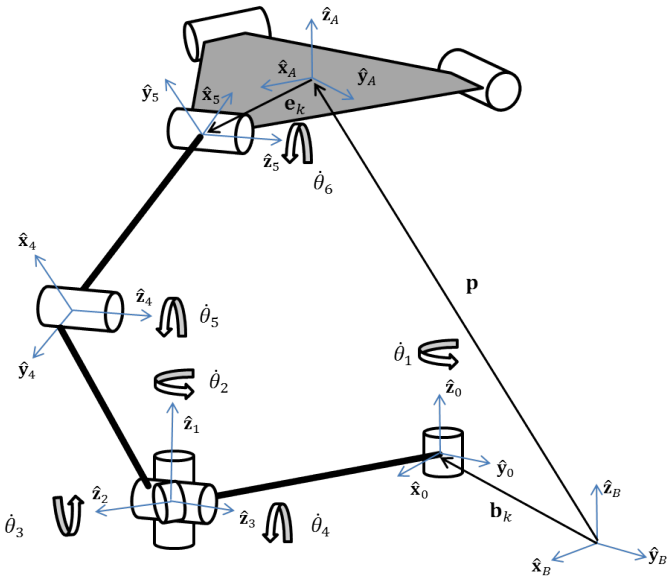

Figure IV.10: $3\bar{R}S\bar{R}R$ kinematic diagram.

The resulting structural matrix for each chain was:

$$\mathbf{S} = \begin{bmatrix} 0, & 0, & 1, & 1, & 0 & 0 \\ 0, & 0, & 1, & -1, & 0 & 0 \\ 0, & 0, & 1, & 1, & 1 & 0 \\ 0, & 0, & 1, & -1, & -1 & 0 \\ 0, & 0, & 1, & 1, & 1 & 1 \\ 0, & 0, & 1, & -1, & -1 & -1 \end{bmatrix}$$

which sets antagonistic pairs of balancing mechanisms in each kinematic chain. The balancing solution was tested in two cases, the first uses the parameters from Table IV.4 and the second uses the same parameters except that all links are considered massless. The torque reduction for the first case is shown in Figure IV.2 and the case with massless links is shown in Figure IV.2.

The assumption to exclude the first two joints put an artificial constraint on the

Table IV.4: Parameters for $3\bar{R}S\bar{R}R$ Spatial Parallel Robot

End Effector Properties			
Mass (kg)	10		
$\mathbf{g}$ (m/s^2)	$[0, 0, -9.81]^T$		
Kinematic Chain Properties			
Parameter	Chain $k = 1$	Chain $k = 2$	Chain $k = 3$
$\mathbf{e}_{(k)}$ (mm)	$[-259.8, -150, 0]^T$	$[0, 300, 0]^T$	$[259.8, -150, 0]^T$
$\mathbf{b}_{(k)}$ (mm)	$[-173.2, -100, 0]^T$	$[0, 200, 0]^T$	$[173.2, -100, 0]^T$
Mass $m_{4,5,(k)}$ (kg)	1	1	1
Mass $m_{1,2,3,6,(k)}$ (kg)	0	0	0
$\mathbf{a}_{1,(k)}$ (mm)	$[300, 0, 0]^T$	$[300, 0, 0]^T$	$[300, 0, 0]^T$
$\mathbf{a}_{2,3,(k)}$ (mm)	$[0, 0, 0]^T$	$[0, 0, 0]^T$	$[0, 0, 0]^T$
$\mathbf{a}_{4,(k)}$ (mm)	$[450, 0, 0]^T$	$[450, 0, 0]^T$	$[450, 0, 0]^T$
$\mathbf{a}_{5,(k)}$ (mm)	$[450, 0, 0]^T$	$[450, 0, 0]^T$	$[450, 0, 0]^T$
$\mathbf{a}_{6,(k)}$ (mm)	$[300, 0, 0]^T$	$[300, 0, 0]^T$	$[300, 0, 0]^T$
$\mathbf{c}_{1,2,3,(k)}$ (mm)	$[0, 0, 0]^T$	$[0, 0, 0]^T$	$[0, 0, 0]^T$
$\mathbf{c}_{4,(k)}$ (mm)	$[125, 0, 0]^T$	$[125, 0, 0]^T$	$[125, 0, 0]^T$
$\mathbf{c}_{5,(k)}$ (mm)	$[125, 0, 0]^T$	$[125, 0, 0]^T$	$[125, 0, 0]^T$
$\mathbf{c}_{6,(k)}$ (mm)	$[300, 0, 0]^T$	$[300, 0, 0]^T$	$[300, 0, 0]^T$
$\alpha_{3,(k)}$ (rad)	$-\pi/2$	$-\pi/2$	$-\pi/2$
$\alpha_{1,2,4,5,6,(k)}$ (rad)	0	0	0
$\beta_{2,(k)}$ (rad)	$-\pi/2$	$-\pi/2$	$-\pi/2$
$\beta_{1,3,4,5,6,(k)}$ (rad)	0	0	0

synthesis process to get a simpler mechanism design. As a result there is residual torque present throughout the workspace. Like with the $3\bar{R}RR$ mechanism, the addition of the counter torque mechanisms was not necessary once the links are assembled. The total actuator load reduction is approximately 75% throughout the workspace.

When the links are massless, the results seen in Figure IV.2 demonstrate perfect balancing. In situations where the payload of the end effector is the dominant load on the actuator, this balancing solution will be near ideal.

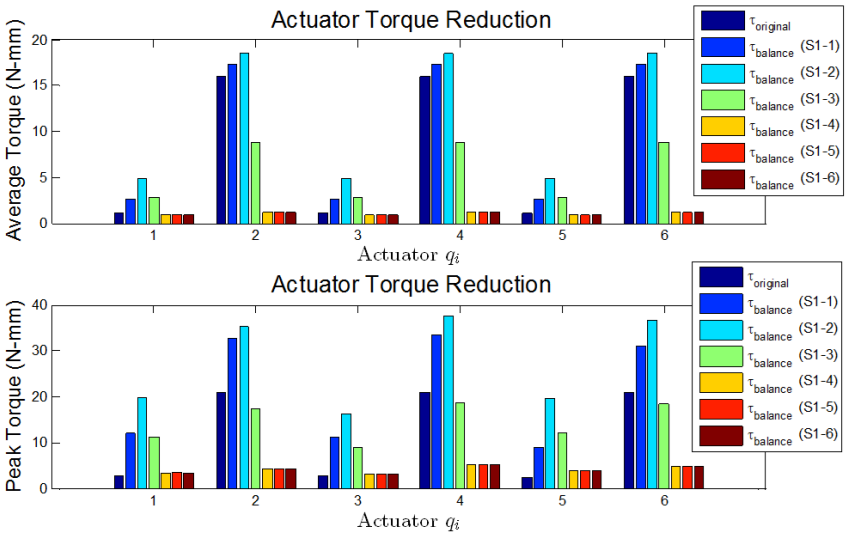

Figure IV.11: $3\bar{R}S\bar{R}R$ torque reduction. The top plot shows average torque reduction throughout the workspace and the bottom plot shows reduction in peak torque

IV.3 Conclusions

In this chapter an efficient method for the static balancing of wire actuated mechanisms with combinations of revolute links. The key principle of this method is to linearize the potential energy of a mechanism into a set of basis functions. The arguments into these basis functions are linear combinations of the mechanism's generalized coordinates. The realization of these combinations is through selective joint coupling with closed loop wire actuation. The work in the present literature has already addressed the different aspects of the problem but the synthesis methods are specific to the mechanism under discussion. The balancing solution presented by Kim [51, 52] is similar in result but the approach is tailored specifically to Approaching the problem from energy partitioning allows the same method to be employed for various mechanism designs.

There are several directions to continue developing this method to fully generalizable approach. The first is identifying basis functions that can capture prismatic

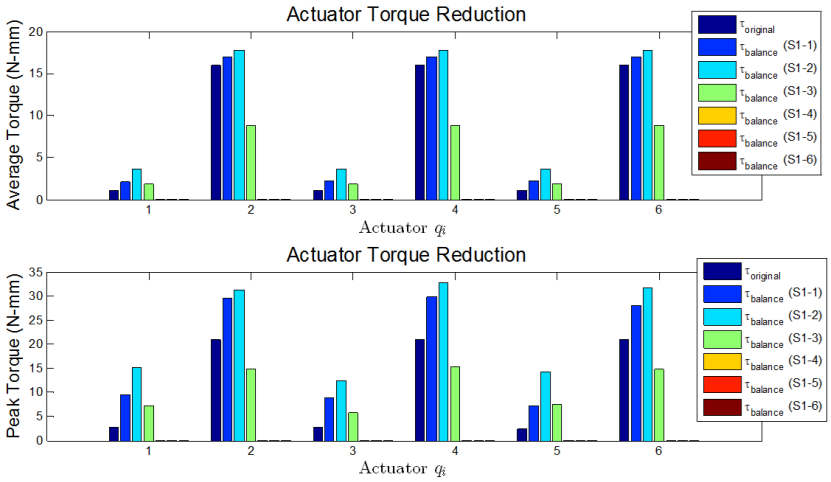

Figure IV.12: $3\bar{R}S\bar{R}R$ torque reduction with massless links. The top plot shows average torque reduction throughout the workspace and the bottom plot shows reduction in peak torque

actuation in rotating frames that preserves linearity when identifying basis functions for a given potential energy function. Inspection of specific mechanisms can lead to heuristic formulations but a general approach the requires no additional knowledge of the device than its generalized coordinates and potential energy would have a far greater utility. A second direction to explore in continuing research is in the design of the counter-balancing mechanism. The zero length spring design is a classic solution to sinusoidal torque functions but does not provide the capability of modulating stiffness. Antagonistic designs like the one proposed by Kilic [50] provide stiffness modulation at a price of feasible joint limit restrictions.

Lastly, in the balance of parallel mechanism's the approach proposed in this chapter divides the wrench from the end effector a priori to the individual kinematic chains. This was done so that the number of permutations in the combination matrix $\hat{\mathbf{S}}$ would remain manageable. For large numbers of generalized coordinates $n > 6$ a

more restricted combination algorithm may allow for efficient identification of coupling options between kinematic chains.

Chapter V

EXPERIMENTALLY DERIVED MODELS FOR NORMAL CI INSERTION FORCES

Insertion forces during CI implantation have been presented in the literature as a quantitative metric for insertion quality. The guiding assumption is that low insertion forces directly correlate with reduced intra cochlear trauma. Physical damage to the cochlea (trauma rating of 2 or higher of Eshraghi's scale [32]) requires mechanical force which in turn can be felt through the reaction loads on the PEA. The degree to which mechanical force correlates with trauma is a question still being explored but there are measured minimum thresholds for the rupture of the basilar membrane [44, 94]. Forces applied on the PEA throughout CI insertion are a primary extra-cochlear metric for measuring trauma. In live patients, histological and high energy radiological evaluations are not possible to evaluate the likelihood of intra-cochlea damage. Robotic insertion provides accurate measurement of both the insertion force imparted by the implant during insertion and the position of the electrode array throughout the insertion process.

The creation of baseline force models serves several objectives. The first is to quantify the variability and magnitude of insertion forces so that there exists a metric to evaluate the benefits of robotic control to CI insertion. Robot controlled insertion has the previously stated goal of reducing forces imparted on the cochlea during insertion and the insertion force measurements presented in this chapter form a baseline metric for comparison. A second goal is to use known force measurements to construct prediction of total insertion force during a new robotic insertion. If accurate predictions can be made then changing or stopping the insertion before excessive force is applied

is possible. The third objective of the baseline model is to serve as data for failure detection algorithms.

This chapter presents the initial experimental results of robotic CI insertion. It begins with a review of the insertion technique used both in phantom model and cadaveric specimens and a series of definitions on how the insertion data is collected and presented. Next, a collection of data on insertion forces in both phantom models and cadaveric specimens is presented with a fitted model for the data. The compilation of this insertion data leads to a set of baseline models for the expected insertion force as a function of insertion depth. The chapter conclude with using this data to create a predictive model of the insertion force.

Part of the work presented in this chapter has been previously published in [80].

V.1 Friction Forces During PEA Insertion

This section reviews the experiment protocol used for the insertion of PEA's into cochlea specimens. An identical protocol was used regardless of whether the specimen was a phantom model or a human cadaveric temporal bone specimen. There are several key measurements used to define the robotic insertion of a cochlear implant which will be defined here. The *pose* of the gripper is expressed as a 7 element vector $\mathbf{x}$ which consists of a three element position vector $\mathbf{p}$ followed by a unit quaternion $\hat{\mathbf{q}}$ to represent the orientation of the gripper frame with respect to the robot base frame $\{\mathbf{B}\}$. This notation is used for any insertion platform regardless of its degrees of freedom. The vector $\mathbf{x}_{des}$ denotes the desired pose position along an insertion trajectory. The vector $\mathbf{x}_{admit}$ denotes the adjusted gripper pose after corrections from the admittance control laws. The desired magnitude of stylet actuation before and after the admittance control law is referred to as q_s and $q_{s,admit}$ respectively. Refer to Figure III.16 to see how these signal move through the control architecture.

The forces measured by the robotic system are expressed in the force transducer frame, $\{\mathbf{F}\}$. The vector $\mathbf{f} \in \mathbb{R}^6$ is the force/moment wrench vector. A single letter subscript references a force along an axis in frame $\{\mathbf{F}\}$ while double letter subscripts refer to the moment about that axis. The force transducer is aligned to the gripper such that forces in f_z are the *insertion direction forces*. The magnitude of forces f_x and f_y are called the *lateral forces*. Moments f_{xx} and f_{yy} are called the *bending moments* and moment f_{zz} is the *twisting moment*.

Robot insertion requires registration between the cochlea insertion frame $\{\mathbf{C}\}$ and the robot base frame $\{\mathbf{B}\}$. This was accomplished through manual telemanipulation control to bring the end effector tip to the insertion point with an orientation dictated by anatomical restrictions and surgeon guidance. This pose, defined as $\mathbf{x}_{ref}$, defines the tool frame $\{\mathbf{A}\}$ in the robot base frame and the homogenous transform can be written as:

$$ {}^{B}\mathbf{T}_{A}\left(\mathbf{x}_{ref}\right) = \begin{bmatrix} {}^{B}\mathbf{R}_{A}\left(\hat{\mathbf{q}}_{ref}\right) & {}^{B}\mathbf{p}_{c} \\ \mathbf{0}_{[1\times 3]} & 1 \end{bmatrix} \tag{V.1} $$

where ${}^{B}\mathbf{p}_{c}$ is the position of the entry point and $\hat{\mathbf{q}}_{ref}$ is the quaternion orientation at the insertion point. Defining $\hat{\mathbf{k}} = [0, 0, 1]^{T}$, the insertion vector ${}^{B}\mathbf{v}$ is:

$$ {}^{B}\mathbf{v} = {}^{B}\,\mathbf{R}_{A}\left(\hat{\mathbf{q}}_{ref}\right)\hat{\mathbf{k}} \tag{V.2} $$

It can be seen that (V.2) is insufficient to define the frame $\{\mathbf{C}\}$. However, it is assumed that the axis $\hat{\mathbf{x}}_{A}$ is roughly parallel to $\hat{\mathbf{z}}_{C}$. Figure V.1 presents a rendering of the PEA and cochlea frames with the force moment components shown.

Once the robotic platform is registered to the cochlea, the end effector is retracted and a PEA is loaded into the gripper. The tip of the PEA is brought to the insertion

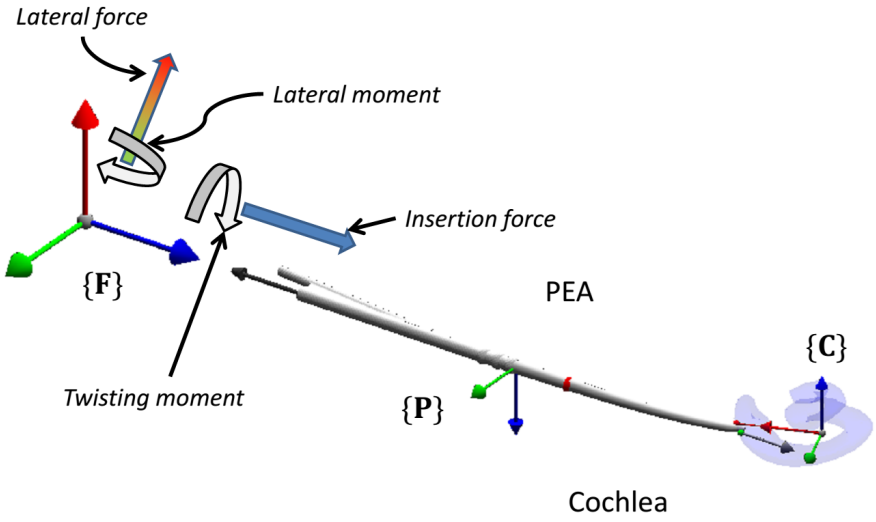

Figure V.1: Insertion force diagram.

point and an insertion trajectory is calculated as discussed in Chapter II. The insertion forces, moments and trajectory are output as a data file after the insertion has been completed.

All cadaveric specimens were prepared by trained surgeons with access to the cochlea provided by a traditional mastoidectomy and the drilling of the insertion point into the cochlea was either a cochleostomy or extended round window. In the case of cadaveric specimens, a lubricant would be injected into the cochlea and allowed to soak for at least one hour. Then directly before an insertion the lubricant was added to the cochlea again. For plastic phantom models, there was no need for the pre-soak phase and lubricant was added just prior to insertion. Some temporal bone specimen had other sections of bone excavated for camera and fiberscope access to view insertions in greater detail. These extra sections of removed bone did not alter the robotic tool's access to the cochlea and did not interfere with the insertion. The placement of the specimen with respect to the insertion system is shown in Figure V.2.

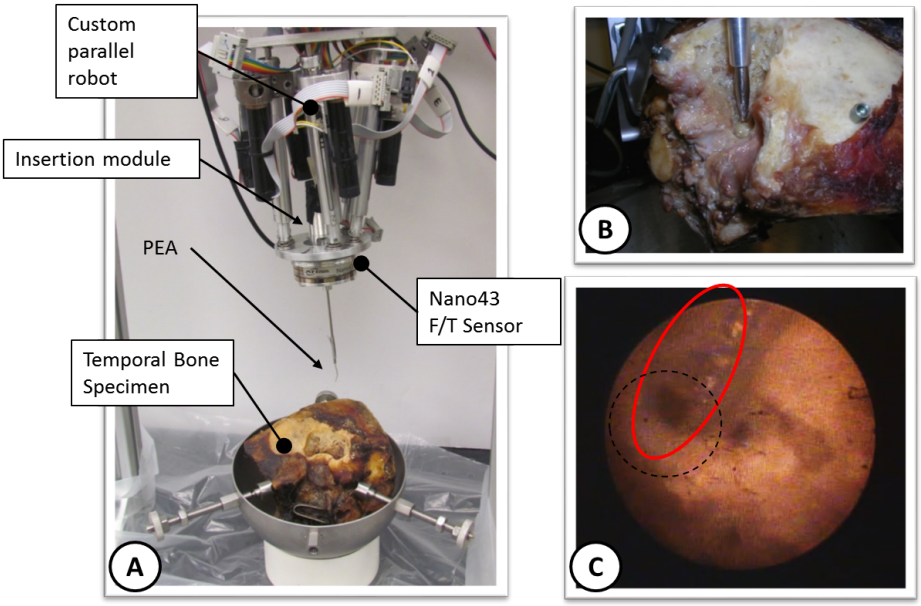

Figure V.2: Temporal Bone Insertion Experimental Setup. (A) 6 dof Stewart-Gough insertion system with a cadaveric temporal bone specimen. (B) Captured view from fiberscope placed near cochlea insertion point. (C) A specimen with non-essential structure removed to allow visualization of the entire insertion process.

During real CI procedures, there is perilymph fluid present in the cochlea which acts as both a conductive medium and lubrication. This natural lubrication is not present in preserved cadaveric specimens nor in plastic phantom models. There have been several methods of lubricating bones and phantoms prior to insertion. These methods include using soap solutions (as contained in training model kits from Cochlear Ltd.), glycol solution [86], or sodium hyaluronate (Healon) [62]. A study by Kontorinis et al.[54] compared insertion forces in a plastic phantom using these lubricants and distilled water. Their conclusion was that soap solutions had the lowest coefficient of friction with glycol and Healon solutions approximately equal. Distilled water had the highest coefficient of friction. For all experiments presented in this chapter, a glycol solution of equal parts distilled water and glycol was used as the lubricant.

The progress through an insertion is parameterized by the unit scalar $\lambda \in [0, 1]$ which corresponds to distance along the insertion trajectory parameterized by q. The insertable portion of the *Contour Advance* PEA is $15mm$ long and a full insertion should travel approximately that distance. However it is very common for the gripper tip to have contact with rigid bone structures in the final millimeter of insertion. This usually results in a sharp increase in forces which do not reflect true intra-cochlear forces. To mitigate corruption of force data, a full insertion is defined as an insertion depth of $q_{max} = 13.8mm$ which corresponds to $\lambda = 1$ through the function:

$$\lambda = \frac{q - q_{max}}{q_{max}} \tag{V.3}$$

Shown in Figure V.3 is an example of robotic insertion in the phantom model. The insertion depth and stylet actuation are shown with three snapshots of the insertion progress.

The entire wrench perceived by the system, $\mathbf{f}(\lambda \in [0, 1])$ is recorded although force acting in the insertion direction (f_z) is the most common measurement reported in the literature [86, 125, 127, 66, 53, 54, 92]. Each vector of force/moment information is then descretized into m points throughout the insertion (i.e. $f_z(\lambda) \rightarrow \mathbf{f}_z \in \mathbb{R}^m$).

Fitting Models

The raw data collected by the force transducer is sampled at a rate of 1kHz over a period of approximately 15 seconds. This results in a large amount of numerical data that makes dissemination of the information difficult. The goal of the work in this section is to identify a numerically lower order representation of the force / moment signals as a function of insertion depth. This representation must fit the densely sampled data within the accuracy of the force sensor. The benefit of such a representation is two fold; the first is that numerical data can be presented more

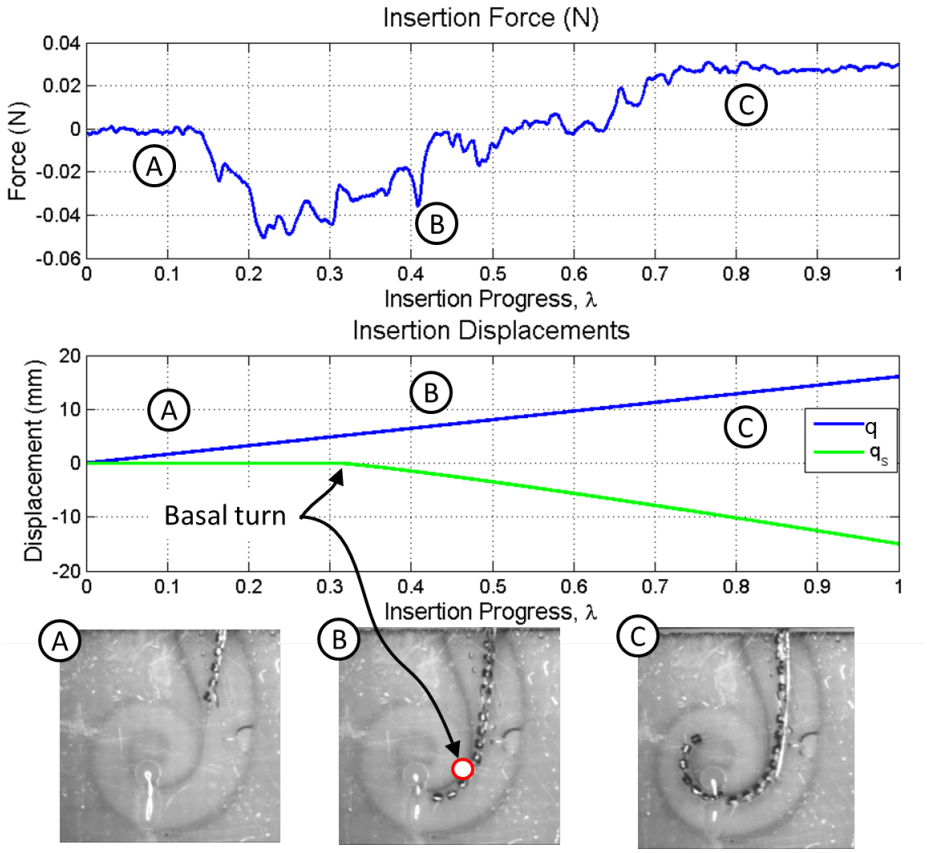

Figure V.3: Example of Robotic PEA Insertion. Measure insertion force f_z is shown in the top plot with the insertion displacement q and stylet actuation q_s shown in the middle plot. Three photos of the insertion progress in the phantom model are shown with matching labels in the plots to correlate the images with the data.

accurately in the literature as opposed to relying on graphical plots. Secondly, such models can be used in other processing algorithms with less computational load.

Force measurements in normal insertions can be modeled as continuous functions with at least C^1 differentiability. By normal insertion it is meant that there are no collision contacts and the reaction loads perceived are the sliding contact friction between the electrode array and the intra-cochlear anatomy. In this case, the quantity of raw measurement data can be captured accurately through regression fitting of some functional. A general basis of order n can be used to approximate a function

$f(x)$ by the sum:

$$f(x) = \sum_{0}^{n} c_i B_i(x) \tag{V.4}$$

where $B_i(x)$ are the basis terms as a function of the variable x. The coefficients c_i determine the unique function. If the domain of the input variable x is descretized into m elements such that $\mathbf{x} = [x_1, \ldots, x_m]^T$ and $\mathbf{f}(\mathbf{x}) = [f(x_1), \ldots, f(x_m)]^T$ then the basis matrix $\mathbf{B}$ can be written as:

$$\mathbf{B} = \begin{bmatrix} B_1(x_1), & \ldots, & B_n(x_1) \\ \vdots, & \ddots & \vdots \\ B_1(x_m), & \ldots, & B_n(x_m) \end{bmatrix} \tag{V.5}$$

satisfying the linear equation:

$$\mathbf{B}\left(\mathbf{x}\right)\mathbf{c} = \mathbf{f}\left(\mathbf{x}\right) \tag{V.6}$$

There are several types of basis functions which can be applied to the force / moment profiles seen during CI insertion. The first is the power polynomial basis with terms $B_i(x) = P_i(x)$ such that:

$$P_i(x) = x^n,\ n = 0, 1, 2, \ldots \tag{V.7}$$

A polynomial series of order n has $n + 1$ coefficients and is simple to compute. Unfortunately at higher orders (i.e. $n > 6$) this basis becomes poorly conditioned and can result in fittings highly sensitive to rounding errors in the coefficients [6].

To overcome the conditioning difficulties, Bernstein polynomials of the first kind may be used. In this work they are denoted as $B_i(x) = T_i(x)$ such that:

$$T_i(x) = \frac{n!}{i!(n-i)!}\left(x^i\left(1-x\right)^{n-i}\right),\ n = 0, 1, 2, \ldots \tag{V.8}$$

A key property of Bernstein polynomials is that regardless of their order, the sum of the basis terms is always 1 on the interval $x \in [0, 1]$ (i.e. a *barycentric combination*). This results in good conditioning at high orders while being able to exactly match any solution produced by the basic polynomial basis of equivalent order. Since $\lambda \in [0, 1]$ is the domain of all force measurements, Bernstein polynomials can be used without additional scaling. The number of the coefficients in a basis of order n is $n + 1$.

Another common basis is the Fourier series with basis terms $B_i(x) = F_i(x)$ such that:

$$F_i(x) = c_{i,1} \cos(i\pi x) + c_{i,2} \sin(i\pi x), \ \forall x \in [0, 1], i = 0, 1, 2, \ldots, n \tag{V.9}$$

This basis benefits from orthogonality properties and like the Bernstein polynomial, works well with domains that naturally scale to a unit interval. For an order n this basis requires $2n + 1$ coefficients.

The conditioning of the basis matrices is evaluated through the singular value decomposition of the basis matrix $\mathbf{B}$. For this evaluation, the domain was discretized into 50 equally spaced points resulting in $\mathbf{B} \in \mathbb{R}^{50 \times n+1}$ for elementary and Bernstein polynomials and $\mathbf{B} \in \mathbb{R}^{50 \times 2n+1}$ for the Fourier basis. The condition number is defined as the ratio between the maximum and minimum singular values with a domain ranging from zero to positive infinity. The inverse condition number is bounded between zero and one with values approaching one being better conditioned and less sensitive to small errors.

It can be seen in the Figure V.4 that the Bernstein polynomial basis has a significant advantage over elementary polynomials in this application. When comparing the Bernstein basis to the Fourier its important to note that the dimensionality of the two basis are different for the same order. For example, a 7'th degree Bernstein

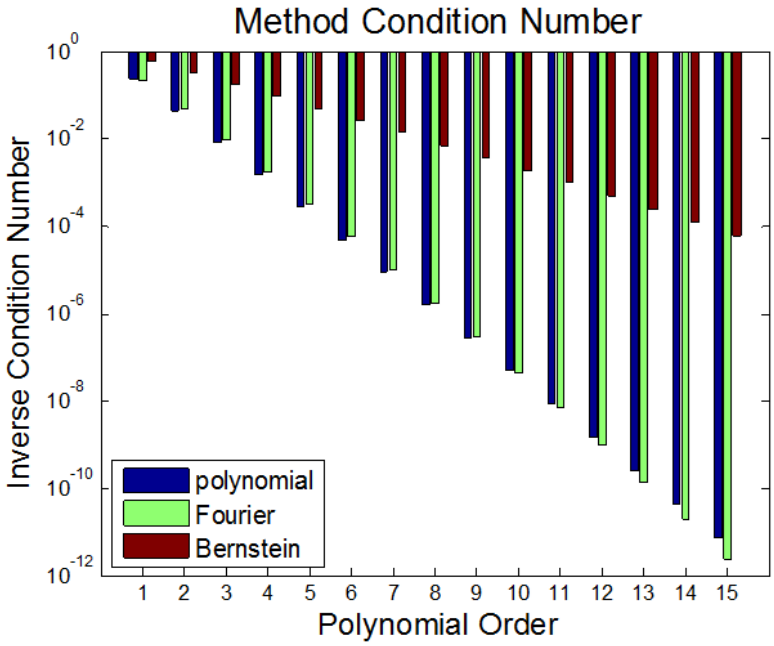

Figure V.4: Inverse condition numbers of basis matrices. Sets of bar plots are ordered left to right as polynomial, Bernstein polynomial, and Fourier series.

basis is dimensionally identical to a 3rd order Fourier. When comparing these basis in terms of matching dimensionality they have similar conditioning quality. Bernstein polynomials were finally selected as the representation basis for reason given in the following sections.

The following sections review the insertion force information collected by several robotic insertion systems in both temporal bones and in plastic phantom models with fittings from using these basis functions. The robotic system developed by Zhang et al. [128] is referred to as the *spatial* insertion platform and the system presented in Chapter III is called the *planar* insertion platform. Both are used in the collection of the data and are shown interchangeably in figures.

V.2 Baseline Insertion Forces in Bone

A series of 50 insertions in temporal bone were performed at four fixed rates of insertion; 0.5, 1, 2, and 3 mm/s. The distribution of bone insertions per speed group

Insertion Speed	Number of insertions
$0.5mm/s$	17
$1mm/s$	11
$2mm/s$	11
$3mm/s$	11

Table V.1: PEA Insertions in Temporal Bone Specimens Categorized by Speed

is presented in Table V.1. A total of 9 temporal bones were used across the 50 insertions. The purpose of varying insertion velocity was to determine if speed is a factor in resulting friction forces. A prior study by Zhang et al. [125] found a strong correlation between insertion speed and force using lateral wall electrodes in a plastic phantom. However Kontorinis et al. found a much weaker correlation using PEA's in a phantom model [53]. There is an open question in the literature as to whether the conclusions on force and insertion speed using PEA's translate to insertions in human specimens.

The average insertion force as a function of insertion depth is shown in Figure V.5 (A). There was no statistical difference between the groups of data when comparing insertion forces directly. However, when using an unpaired t-test on the work done through the insertion process, there was a significant difference between insertions at $0.5mm/s$ and those at $1mm/s$ and higher. This result suggests that stiction effects are only relevant at low insertion speeds. If insertion rates are maintained above $1mm/s$ a single model can be used to characterize the expected insertion force.

Figure V.5 (B) plots the average insertion force as a function of depth along with the standard deviation and the 95% confidence interval of the mean. In this case a third order polynomial was used to express the average function.

There is little evidence that perimodiolar insertion force can be modelled as a function of insertion speed. Rather the variability of access and variability of the

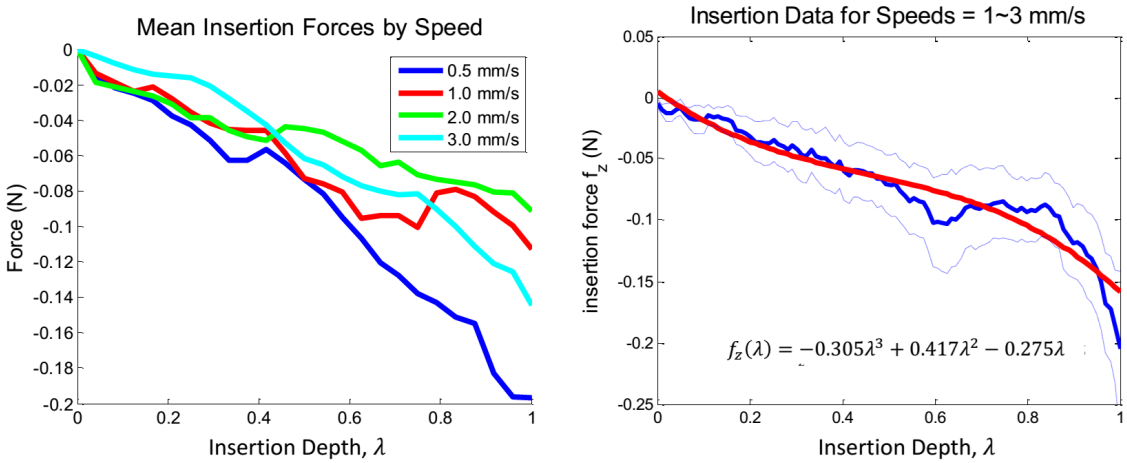

Figure V.5: Average Insertion Forces in Temporal Bone by Speed.

cochlea structure between specimens plays a dominant role. However, these insertions were performed with the same insertion trajectory. In the next chapter, an evaluation of force-based admittance control is used against this insertion data to investigate how a robotic system can *actively reduce* insertion forces.

Another result from this set of experiments is that insertion speeds greater than 1mm/s do not significantly change the magnitude of insertion force. Based on this result, the majority of the work presented in the following sections and chapters fixed insertion speed to a rate of 1mm/s. This rate allows for more time to calculate adjustments to control inputs while not increasing insertion forces on the cochlea. It may also be inferred from this work and that of Zhang et al. [125] that smooth, continuous insertion motions is a recommended technique for surgeons to help keep insertion force low.

V.3 Baseline Insertion Forces in Phantom Models

Insertions into a plastic phantom model were performed with two goals. The first was to examine if forces measured in the phantom were comparable to those in temporal bones. If this is true then the second objective would be to use insertions

in the phantom model to observe PEA behavior and develop methods to identify complications or failures in the insertion process. The setup for phantom model insertions is shown in Figure V.6

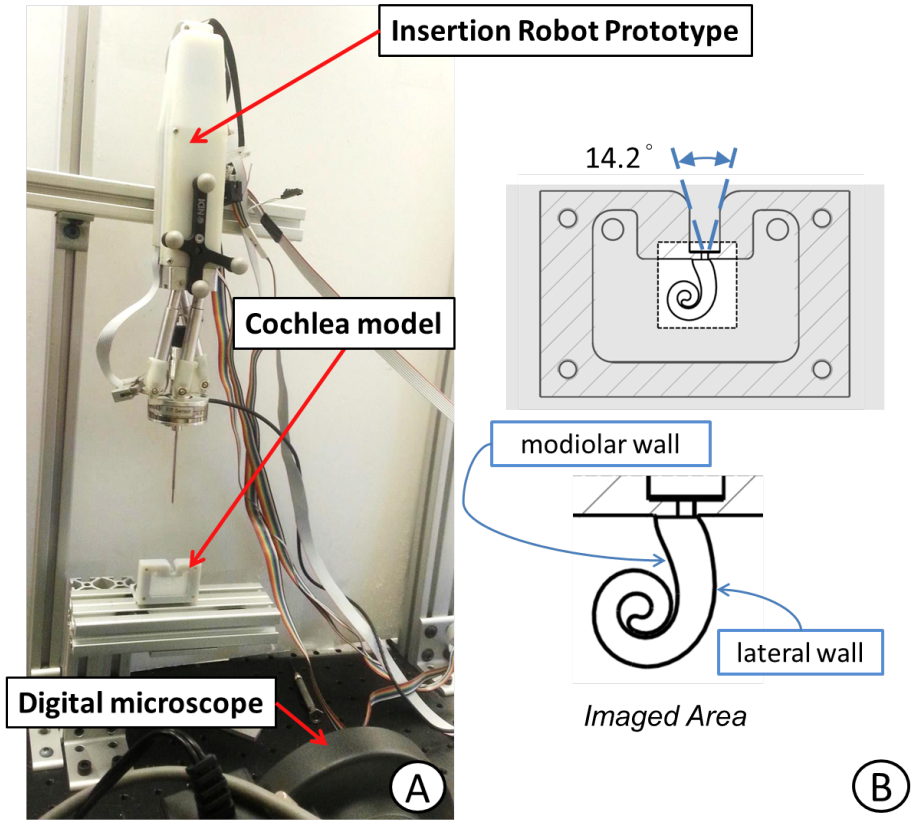

Figure V.6: Phantom Model Insertion Experimental Setup. (A) The prototype 4 DoF insertion system is shown with a phantom model provided by Cochlear Ltd. (B) The phantom is a planar model with access restrictions matching those in Chapter II

The cochlea model itself is from the insertion training phantom provided by Cochlear Ltd. It is generally a two dimensional path although there is narrowing of the scala tympani as depth into the cochlea increases. The model is cut from teflon and its top surface, corresponding to the basilar membrane in a real cochlea, is made of acrylic so that the insertion of the electrode array may be observed visually. Normally the model is housed in a model of the human temporal bone but for these

experiments the model is contained in a simplified holder as shown in Figure V.6 (B). This new holder enforces the same angular access restrictions to insertion as those found in real temporal bones. The purpose of this simplified holder was to allow access for a high resolution digital microscope to acquire images of the insertions.

A set of 51 insertions of perimodiolar electrode arrays in the phantom model were performed by the 6 dof spatial parallel insertion system. An additional 10 insertions were performed by the prototype planar insertion system. The force transducer and gripper module were shared between the two systems as can be seen in Figures V.2 and V.6

Figure V.7 shows the insertion forces for the 51 trials using the spatial insertion platform. Average insertion force is approximately 0.05N with a characteristic rise in the final portion of insertion.

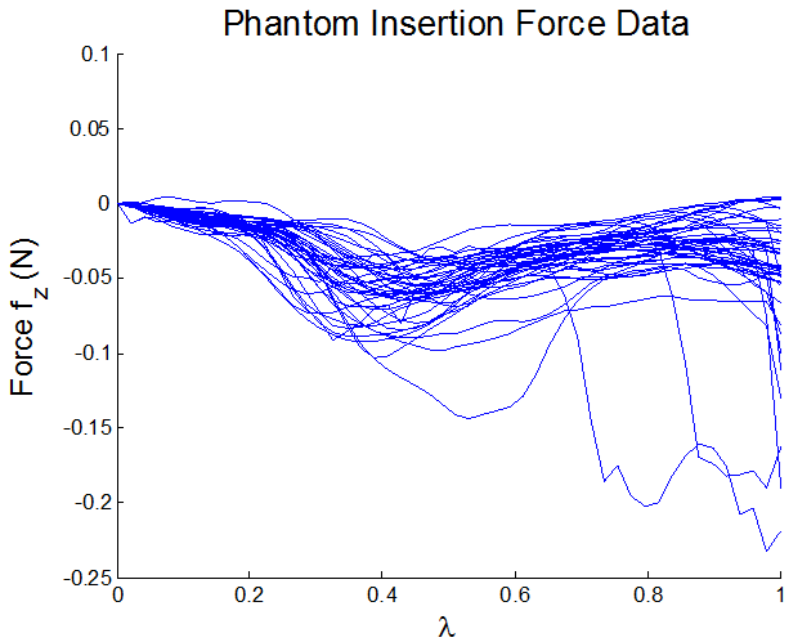

Figure V.7: Phantom model insertion forces using the spatial insertion platform.

Insertion forces using the planar insertion platform are shown in Figure V.8. This

system used slower insertion speeds of 0.5 and 0.3mm/s so that mechanism motion could be recorded and examined later if needed. The results show comparable insertion force magnitudes to those performed by the spatial insertion platform. The accuracy of the planar insertion system, although lower than its original target values, was sufficient for the insertion task.

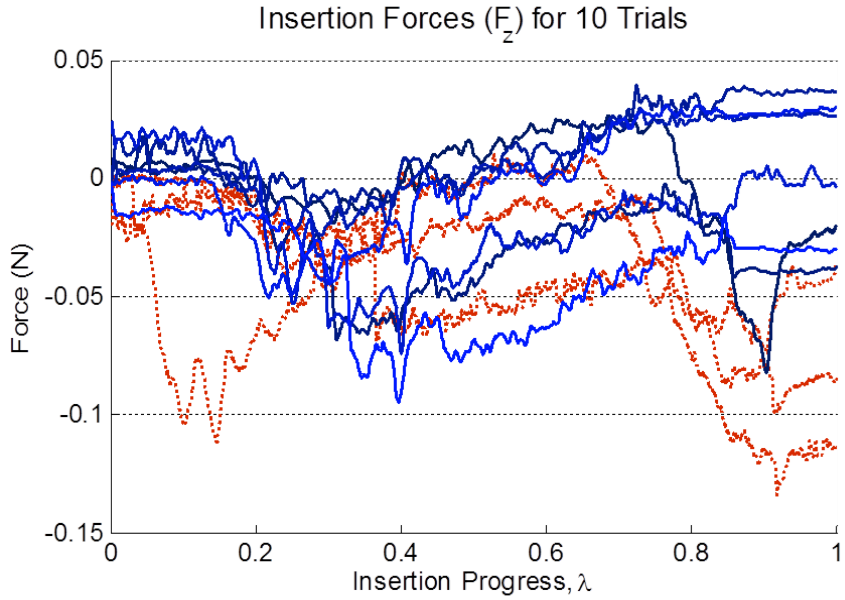

Figure V.8: Phantom model insertion forces using the planar insertion platform.

Lateral forces in the planar insertion system must be separated into two components. Force in the plane of motion of the mechanism are called the lateral forces and those in the null space of the design are called the out of plane forces. Figure V.9 shows these force components.

It can be seen that lateral forces within 0.05N in magnitude and through force based admittance control it is possible to adjust end effector motion to reduce the magnitude of lateral force. The out of plane forces are due to misalignment between the planar insertion system and the cochlea insertion point and with the planar insertion system they cannot be compensated for through control action. The large

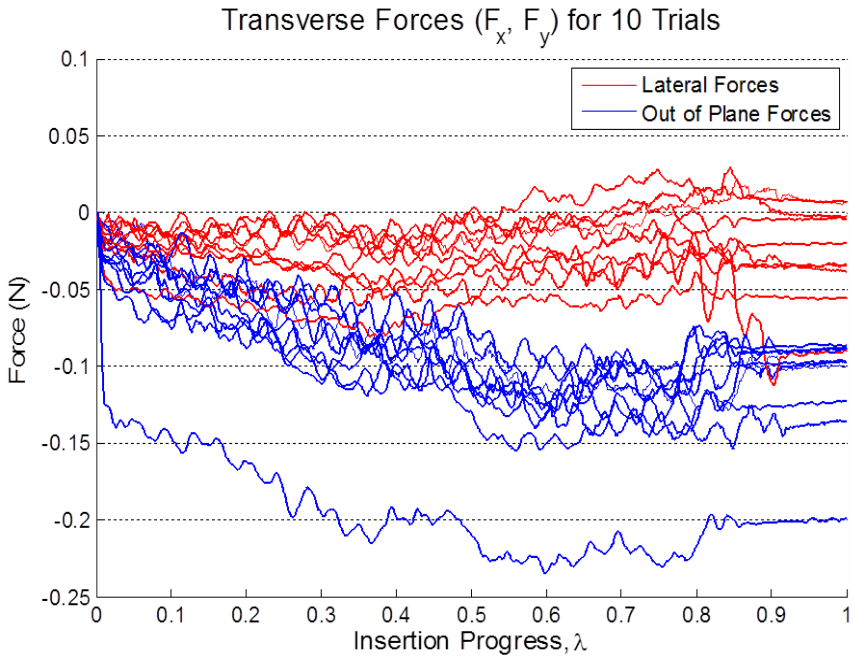

Figure V.9: Phantom model lateral forces using the planar insertion platform shown in Figure V.6.

increase in lateral force in one of the ten insertions, with a magnitude greater than 0.2N, did not adversely affect insertion force. This suggests that perceived lateral forces do not clearly correspond to the intra cochlear friction observed during insertion.

The total set of phantom model insertion force data was used to generate a general model of expected insertion force. The three sets of basis functions were compared for fitting accuracy as a function of order n. The fitting accuracy was defined by the root mean squared error of the fitting result which can be written as:

$$\epsilon_{RMS} = \left[\sum_{1}^{k} \frac{\left(\mathbf{f}(\lambda) - \hat{\mathbf{f}}(\lambda)\right)^T \left(\mathbf{f}(\lambda) - \hat{\mathbf{f}}(\lambda)\right)}{k\,m} \right]^{\frac{1}{2}} \tag{V.10}$$

where k is the number of insertions included in the evaluation, m is the number of

samples taken in an insertion and[1]:

$$\hat{\mathbf{f}}(\lambda) = \mathbf{B}(\lambda)\left(\mathbf{B}(\lambda)^{\dagger}\mathbf{f}\right) \tag{V.11}$$

Figure V.10 shows the fitting error for insertion forces and Figure V.11 shows the standard deviation of the errors for the three basis types based on order.

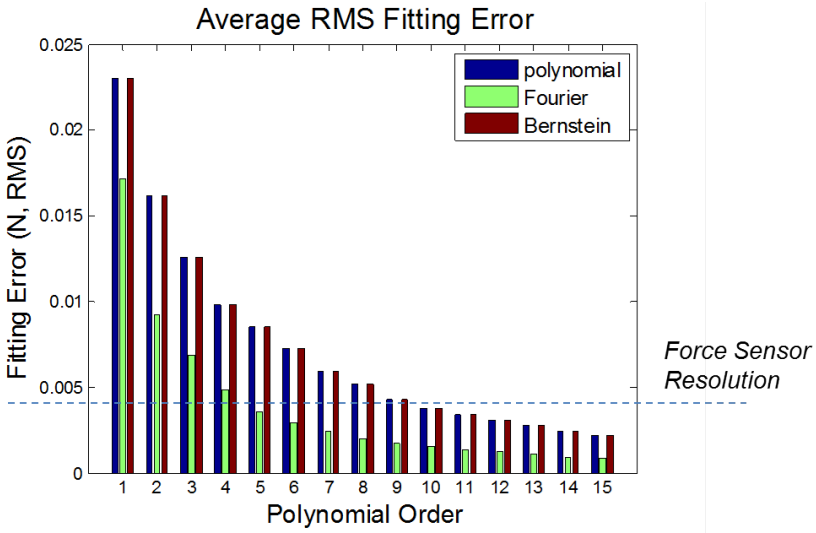

Figure V.10: RMS error of insertion force fitting. Sets of bar plots are ordered left to right as polynomial, Bernstein polynomial, and Fourier series.

From these results, both Bernstein and Fourier basis show comparable results when orders with matching dimensionality are compared. Bernstein polynomials were selected at this point due to their computational advantages over Fourier terms. Since the force measurements are not periodic, the Fourier series does not have an inherent advantage.

Using Bernstein polynomials, the force vector can be resized by changing the number of sample points in $\boldsymbol{\lambda}$. From the collection of measured normal insertion data, the average and variance as a function of insertion depth λ are denoted as $\bar{f}_m$

[1]the notation $\mathbf{A}^{\dagger}$ refers to the Moore-Penrose matrix pseudo inverse[77] of $\mathbf{A}$

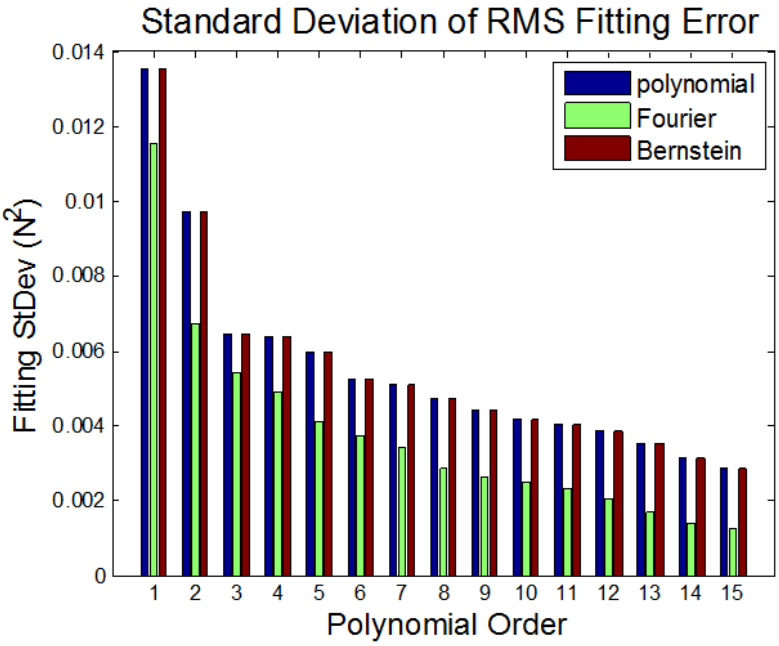

Figure V.11: Standard deviation of errors in insertion force fitting. Sets of bar plots are ordered left to right as polynomial, Bernstein polynomial, and Fourier series.

and σ_m respectively. A second subscript denotes the axis of the measurement (i.e. $\bar{f}_{m,z}$ is the average force for the z axis in the force sensor frame $\{\mathbf{F}\}$). Table V.2 presents the fitting coefficients for the averages and variances of the insertion forces and lateral moments from the set of phantom insertion data discussed in this section.

V.4 In-Vivo Prediction of Nominal Insertion Forces

During the insertion of a PEA it is useful for the control system to determine the likely trajectory that measurements will follow so as to avoid complications. There are many ways that such predictive models can be created. In linear systems, Markov state transition matrices can propagate a current state into the future. The key weakness to such models is the reliance on knowing all states that influence the progagation of the current state. Similarly, Kalman filters and other linear observers require knowledge of the system dynamics to propagate the current state. While the

Table V.2: Insertion Force Summary

Coefficients	$\bar{f}_{m,z}$	$\sigma_{m,z}$	$\bar{f}_{m,xx}$	$\sigma_{m,xx}$	$\bar{f}_{m,yy}$	$\sigma_{m,yy}$
c_0	-0.00368	0.00754	-0.02584	0.06385	0.01062	0.04616
c_1	0.00322	0.00454	-0.30809	-0.19397	-0.10120	-0.07260
c_2	-0.09043	-0.07346	1.67939	1.17943	0.67325	0.39600
c_3	0.27410	0.31662	-3.86249	-3.78169	-2.18398	-1.43339
c_4	-0.66837	-0.53801	2.56596	9.13224	4.65950	4.16891
c_5	0.48569	0.81025	3.16762	-5.35123	-6.10697	-3.64368
c_6	-0.32705	-0.77213	-4.02440	4.77472	2.50529	3.21728
c_7	0.08950	0.51994	3.20528	0.43311	-1.68914	-0.37063
c_8	-0.09196	-0.15782	0.00664	1.75574	-0.12048	0.87301
c_9	-0.02012	0.07319	-0.12767	1.35499	-0.69473	0.46814
c_{10}	-0.09988	0.11535	-0.41673	1.47611	-0.19172	1.06752

dynamics of the robot and elastic PEA can be modeled, the boundary conditions applied on to the PEA are not well known. Such boundary conditions include the exact location of the insertion point with respect to the Scala Tympani, the distribution of viscous fluid in the scala, and the geometry of the separating membranes (which cannot be seen directly in CT).

The approach presented in this work to predict insertion forces as the implantation is in progress relies on weighted fitting based on prior insertion data statistics. The predicted force vector as a function of insertion depth is expected to continually update until the insertion is complete. Refer to Figure V.12 throughout this section as the prediction process is detailed. At the k'th sample (where $1 \leq k \leq m$) the predicted force vector is denoted by $\tilde{\mathbf{f}}(\lambda_k)$. At each prediction update the estimated coefficient vector $\tilde{\mathbf{c}}(\lambda_k)$ is determined and then used in (V.12) to provide the latest estimation:

$$\tilde{\mathbf{f}}(\lambda_k) = \mathbf{B}(\boldsymbol{\lambda})\, \tilde{\mathbf{c}}(\lambda_k) \tag{V.12}$$

The coefficients in $\tilde{\mathbf{c}}(\lambda_k)$ converge to $\mathbf{c}$ from (V.6) at the final sample ($\tilde{\mathbf{c}}(\lambda_m) = \mathbf{c}$).

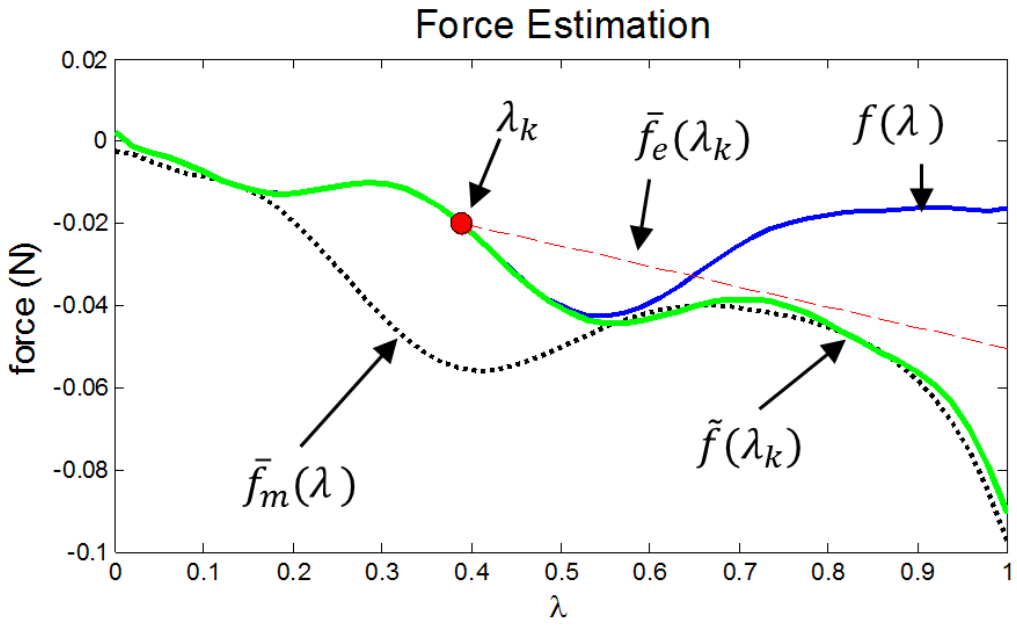

Figure V.12: Example of force prediction. The dashed line is the measured force average $\bar{f}_m(\lambda)$ from prior phantom model data. The thin solid line is the true final measurement $f(\lambda)$ for this insertion. The dot represents the current point of the insertion λ_k where the prediction is made. A linearly extrapolation $\bar{f}_e(\lambda_k)$ from the current measurement $f(\lambda_k)$ is made based on the average rate of change $\bar{f}'_m(\lambda_k)$. The thick solid line indicates the final prediction $\bar{f}(\lambda_k)$ based on a combination of $\bar{f}_m(\lambda_k)$ and $\bar{f}_e(\lambda_k)$.

The estimation of $\tilde{\mathbf{c}}(\lambda_k)$ is a weighted least squares solution of the form:

$$\tilde{\mathbf{c}}(\lambda_k) = \left(\mathbf{B}^T \mathbf{W}_k^{-1} \mathbf{B}\right)^{-1} \mathbf{B}^T \mathbf{W}_k^{-1} \mathbf{g}\left(\lambda_k\right) \tag{V.13}$$

where $\mathbf{W}_k$ is the weight matrix and $\mathbf{g}(\lambda_k)$ is the augmented force vector at the k'th sample. The vector $\mathbf{g}(\lambda_k)$ is a combination of measurements taken by the robot up to the present position λ_k and an estimated average force $\bar{\mathbf{f}}_k$ for future measurements:

$$\mathbf{g}\left(\lambda_k\right) = \begin{bmatrix} \mathbf{f}_k \\ \bar{\mathbf{f}}_k \end{bmatrix}, \; \mathbf{f}_k \triangleq \begin{bmatrix} f\left(\lambda_1\right) \\ \vdots \\ f\left(\lambda_k\right) \end{bmatrix}, \bar{\mathbf{f}}_k \triangleq \begin{bmatrix} \bar{f}\left(\lambda_{k+1}\right) \\ \vdots \\ \bar{f}\left(\lambda_m\right) \end{bmatrix} \tag{V.14}$$

The weight matrix $\mathbf{W}_k$ ensures that $\tilde{\mathbf{f}}(\lambda_k)$ agrees with the currently known data and passes through the estimated future force averages with weight proportional to an estimated variance. Typically the best weight matrix would be the covariance matrix of the data set [102] but this is unknown *a-priori* in practice. Instead, the m measurements are considered independent Gaussian distributions with a variance $\sigma^2(\lambda)$. The measured force data also has a degree of uncertainty based on sensor accuracy that is parameterized by β. For the ATI F/T sensor used in this work, $\beta = 0.004N$ for force and $\beta = 0.10N - mm$ for moment measurements. The weighting matrix is thus diagonal and of the form:

$$\mathbf{W}_k = \begin{bmatrix} \frac{1}{\beta}\mathbf{I}_{[k\times k]} & \mathbf{0}_{[m-k\times m-k]} \\ \mathbf{0}_{[m-k\times m-k]} & \mathbf{\Sigma}_k^{-1} \end{bmatrix} \tag{V.15}$$

given that:

$$\mathbf{\Sigma}_k = \begin{bmatrix} \sigma_m^2(\lambda_{k+1}) & \dots & 0 \\ \vdots & \ddots & \vdots \\ 0 & \dots & \sigma_m^2(\lambda_m) \end{bmatrix} \in \mathbb{R}^{m-k \times m-k} \tag{V.16}$$

When constructing the augmented force vector $\mathbf{g}(\lambda_k)$ the most naive future force input would be to use the previously measured averages and variance. In this case $\bar{f}(\lambda_k) = \bar{f}_m(\lambda_k)$ and $\sigma(\lambda_k) = \sigma_m(\lambda_k)$ from Table V.2. This method will cause the prediction to quickly match the experimental average and does not take into account the current magnitude of the insertion forces. To improve the prediction of $\bar{f}(\lambda)$ and $\sigma(\lambda)$, the average force distribution $\bar{f}_m(\lambda_k)$ and $\sigma_m(\lambda_k)$ are combined with an extrapolated distribution $\bar{f}_e(\lambda_k)$ and $\sigma_e(\lambda_k)$. The two distributions are combined using the method described in [15] such that:

$$\bar{f}(\lambda_j) = \frac{\bar{f}_m(\lambda_j)\sigma_e^2(\lambda_j) + \bar{f}_e(\lambda_j)\sigma_m^2(\lambda_j)}{\sigma_e^2(\lambda_j) + \sigma_m^2(\lambda_j)} \tag{V.17}$$

$$\sigma^2(\lambda_j) = \frac{\sigma_e^2(\lambda_j)\sigma_m^2(\lambda_j)}{\sigma_e^2(\lambda_j) + \sigma_m^2(\lambda_j)} \tag{V.18}$$

The extrapolated distribution is based on the current force measurement $f(\lambda_k)$ and the measured rate of change of insertion force $f'(\lambda_k) = \frac{df}{d\lambda}$ and its standard deviation as $\sigma'(\lambda_k)$. The extrapolation is first order and starting at the current sample k, the distance in normalized insertion space to the j'th predicted sample is defined as:

$$\Delta\lambda_{k,j} = \lambda_j - \lambda_k \;\; \forall k \leq j \leq m \tag{V.19}$$

This means that the average extrapolated force has mean $\bar{f}_e$ and is estimated by starting at the current measurement $f(\lambda_k)$ and linearly extrapolating based on the

fixed rate $\bar{f}'$ such that:

$$\bar{f}_e(\lambda_j) = f(\lambda_k) + \Delta\lambda_{k,j}\,\bar{f}'(\lambda_k) \quad \forall k \leq j \leq m \tag{V.20}$$

We assume a linear propagation of the uncertainty distribution with insertion depth. The uncertainty grows proportionally to σ' and the distance travelled $\Delta\lambda_{k,j}$. The extrapolated distribution standard deviation σ_e equal to:

$$\sigma_e(\lambda_j) = \Delta\lambda_{k,j}\,\sigma_d(\lambda_k)\;\forall k \leq j \leq m \tag{V.21}$$

This update procedure generates the elements in $\bar{\mathbf{f}}$ from (V.14) and the variance matrix $\mathbf{\Sigma}_k$ from (V.16). The steps in the predictive calculation are reviewed in Algorithm 1. After generating predictions for the wrench components using (V.12) the data is used in detecting the onset of insertion failures in a process detailed in the next chapter.

Algorithm 1 Generation of Estimated Force

Require: $\bar{\mathbf{f}}_m$, $\bar{\boldsymbol{\sigma}}_m$, $\bar{\mathbf{f}}'_m$, $\bar{\boldsymbol{\sigma}}'_m$
  for $j = k, \ldots, m$ **do**
    $\Delta\lambda_{k,j}$ from V.19
    Calculate $\bar{f}_e(\Delta\lambda_{k,j})$ from (V.20)
    Calculate $\sigma_e(\Delta\lambda_{k,j})$ from (V.21)
  end for
  Calculate $\bar{\mathbf{f}}$ from (V.17)
  Calculate $\boldsymbol{\sigma}$ from (V.18)
  Construct $\mathbf{g}(\lambda_k)$ from (V.14)
  Calculate $\tilde{\mathbf{c}}(\lambda_k)$ from (V.13)
  Calculate $\tilde{\mathbf{f}}(\lambda_k)$ from (V.12) **return** $\tilde{\mathbf{f}}(\lambda_k)$

Figure V.12 shows how the information is combined to form a prediction for insertion force at $\lambda_k = 0.4$. The current point in the insertion process for the shown

prediction is designated by a large dot. The average insertion force for a prior sample set of normal insertions is shown as a dashed line. The final insertion force for this particular insertion is shown in the fine solid line. A thick solid line is used to show the predicted force. The contribution of $\bar{f}_e$ and σ_e on the force prediction on the forecasted force signal is generally limited to the next few millimeters of insertion.

V.5 Conclusions

This chapter presented the method in which insertion force measurements were obtained and recorded. Measurements have been obtained in both phantom models and in human cadaveric specimens. Using a fixed insertion trajectory, the insertion forces were considerably higher on average in the temporal bones than in the phantom model. However prior work has suggested that in bone, insertion forces can be equivalent to those seen in the phantom model.

The Bernstein basis model proposed in this chapter is well suited to capture the insertion force signals as a function of insertion depth with only 11 coefficients. This reduction of data size greatly eases the difficulty in disseminating accurate insertion force measurements in the literature. Another benefit associated with this curve fitting approach is that force derivatives can be easily estimated with less influence from measurement noise.

What was missing in the cadaveric specimen experiments presented in this chapter is knowledge of the exact cochlea geometry and the point of insertion. While work in imaging can provide accurate models of geometry, the point of insertion is still unknown since drilling occurs after the imaging process. The next two chapters will address the issue of correcting the estimated point to initiate AOS in two different but complimentary ways. Using these adaptive insertion techniques it will be shown that the force models generated from these phantom model insertions is representative of

insertions performed in real cochlea so long as correct perimodiolar insertion technique is performed.

Chapter VI

FORCE-BASED GUIDANCE AND FAILURE DETECTION

This chapter presents an investigation of methods for using *in vivo* insertion force data for insertion guidance and and fault detection. The motivation for force feedback control and failure detection is twofold; minimizing dependance on exact registration of the robot to patient anatomy and minimizing intra-cochlear trauma.

Current approaches for robot-assisted or autonomous electrode array insertion [128, 59, 66] assume that the robot is fixed at an optimal pose relative to the cochlea. Generally, the optimal pose is established and insertion trajectory is generated a priori. This approach relies heavily on the availability of pre-operative imaging, use of fiducial markers, digitization and registration. All of these steps add significant cost to the surgical process, expose the patient to potentially unnecessary radiation and complicate the surgical deployment. Presented in this chapter are force-based control feedback methods for adjusting the rate of stylet actuation during AOS and the alignment of the electrode in order to minimize insertion forces.

The detection and classification of insertion failure modes are also investigated. Specifically, the failure modes investigated are the electrode tip folding and extra-cochlear buckling of the PEA. Metrics that may be used for detecting and classifying these failure modes are presented and evaluated.

A simple representation of the insertion domains to be monitored and controlled is shown in Figure VI.1. The insertion point into the cochlea separates the intra and extra-cochlear regions.

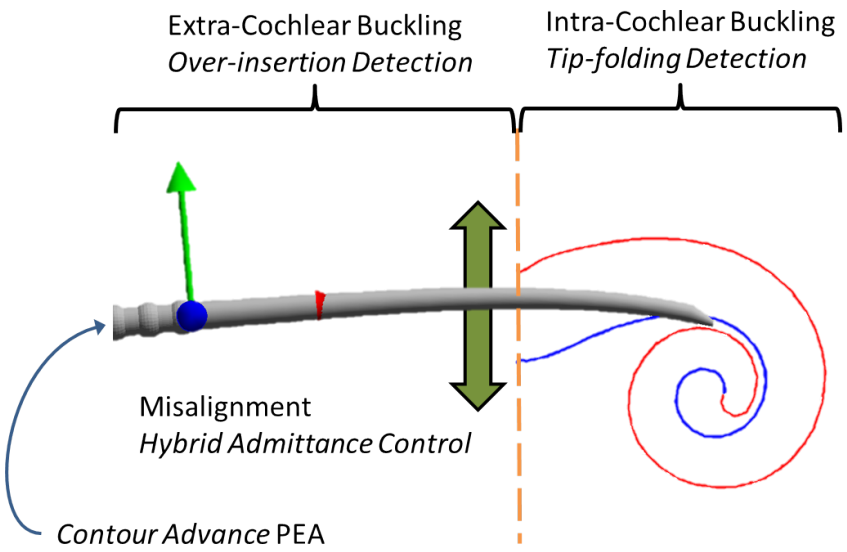

Figure VI.1: CI insertion domains.

The types of insertions considered in this work are categorized into three groups with examples of these three types of insertions are shown in Figure VI.2:

Normal: These insertions result in proper placement of the PEA, with electrodes contacting the modiolar wall.

Tip Folding: Tip folding is a case of intra-cochlear buckling of the PEA. If incorrectly deployed, the distal tip of the PEA folds over on itself while the stylet is actuated. This results in some electrode contacts being poorly positioned with respect to the modiolar wall.

Buckling: These are cases in which the portion of the PEA outside the cochlea buckles during insertion. In these cases the PEA must be removed and replaced. Although termed buckling, this is not a case of elastic instability but rather a condition where the loads on the PEA have caused permanent plastic deformation.

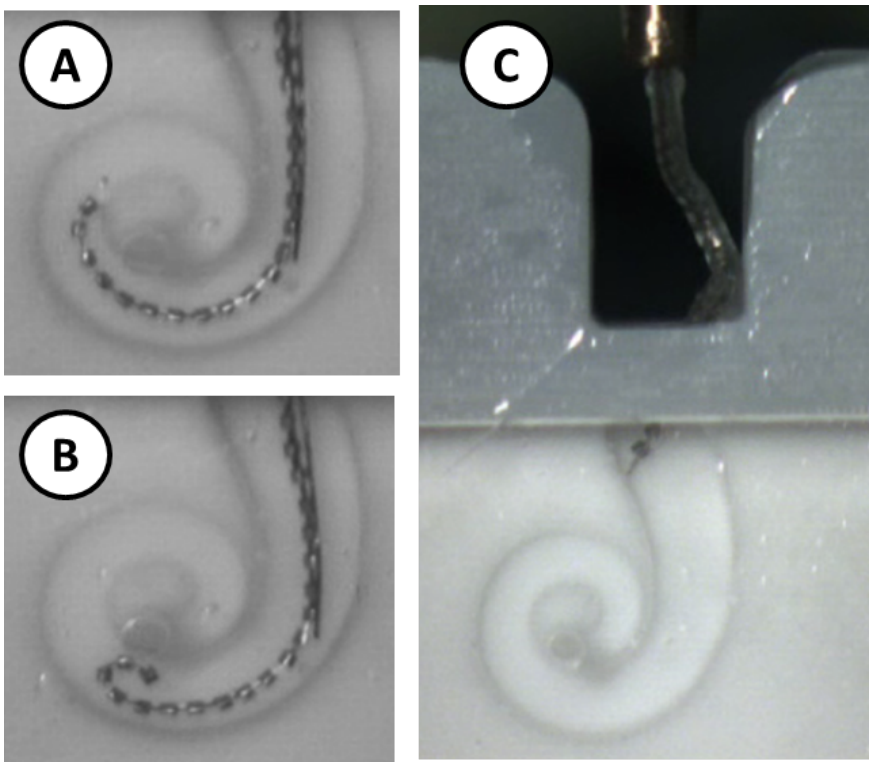

Figure VI.2: Types of CI insertions. (A) Normal insertions result in the PEA electrodes being in close contact with the modiolus. (B) Tip-folding results in the distal tip of the PEA bending over itself inside the cochlea. (C) Excessive force or improper alignment can result in mechanical buckling of the PEA outside of the cochlea.

A different strategy is presented to detect failures in the extra and intra-cochlear regions and to minimize intra-cochlear force. The first section will detail the implementation and performance of a hybrid position/admittance controller to correct for registration errors between the robotic insertion system and the cochlea. This is followed by a method to detect buckling danger by tracking the energy expended in the insertion process. Lastly, this chapter closes with the use of machine learning algorithms to detect intra-cochlear tip folding. In each of these cases, insertion pose data and insertion forces and moments are the only features used in detection and control. Table VI.1 shows the number of insertions conducted to test the detection algorithms.

Insertion Type	Number of insertions
Nominal	51
Tip-Folding	56
Buckling	10

Table VI.1: PEA Insertions in a Phantom Model Categorized by Type

In its entirety the work presented in this chapter presents steps to demonstrating intelligent, semi-autonomous deployment of CI devices. It is the first work, to the best of the author's knowledge, to apply control feedback in CI insertion based on intra operative measurements. The results of this work are hopefully present motivation for the continued development of intelligent tools for CI deployment that can eventually lead to lower registration requirements and increased likelihood of atraumatic insertion.

Part of the work presented in this chapter has been previously published in [80, 82].

VI.1 Hybrid Position / Force Admittance Control

This section proposes an approach to updating the insertion path plan by using hybrid position / force admittance control. This control adjusts motion in the lateral plane (perpendicular to the insertion direction) and adjusts the rate of stylet actuation during AOS execution. This controller design is based on the work of Yoshikawa [124] and applied within the context of CI insertion. A hybrid force / motion admittance controller adds motion compensation to task-specific degrees of freedom based on sensed reaction force at the end effector. These reaction forces are translated to velocities based on a proportional constant and these velocities are additively combined with the nominal trajectory. The purpose of adding this control law is to correct for registration errors between the robot and the cochlea actively during the insertion process.

Figure VI.3 shows a simplified block diagram of the implemented controller. The

original trajectory commanded from the High Level Controller (HLC see Figure III.16), $\mathbf{x}_{des}$, to which the force controller adds a corrective value $\Delta\mathbf{x}_{admit}$ and is then passed as the commanded position $\mathbf{x}_{admit}$ to the trajectory planner.

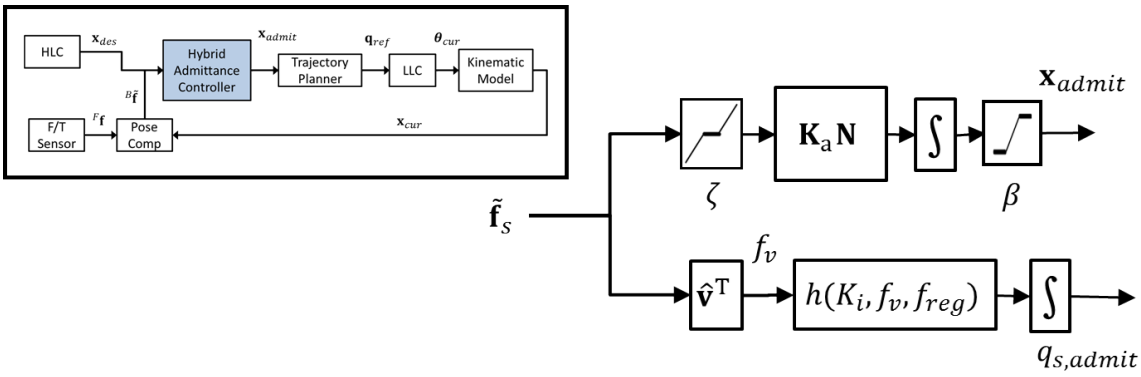

Figure VI.3: Hybrid Force/Position Admittance Controller. Forces acting in the space of $\mathbf{N}$, which defines the lateral plane, apply corrective displacement on the command position $\mathbf{x}_{des}$. The values ζ and β define the deadband and saturation boundaries respectively. Force acting along $\hat{\mathbf{v}}$ affects the rate of stylet actuation $\dot{q}_s$. The function $h(f_v,\ f_{reg})$ refers to (VI.7). The entire control loop to shown in the bordered sub-figure.

The admittance law is broken into two distinct parts; the first modifies motion in the plane normal to the insertion direction $\hat{\mathbf{v}}$ and is referred to as the lateral plane. The second part uses forces detected in the insertion direction to modify the preplanned actuation of the stylet $q_{s,des}$.

Given the insertion direction vector $\hat{\mathbf{v}}$, the lateral admittance control actively adjusts the end effector position in the lateral plane to minimize forces in the plane. The space of the lateral plane can be defined by a projection matrix $\mathbf{N}$ defined as:

$$\mathbf{N} = \mathbf{I} - \hat{\mathbf{v}}\hat{\mathbf{v}}^T \tag{VI.1}$$

Raw force measurements are corrected by a gravity compensation term as shown

in Figure III.16. The corrected measurement is denoted as $\tilde{\mathbf{f}}_s$. The gravity load compensation has a residual amount of force error depending on end effector orientation which should not be allowed to influence the controller. A norm deadband margin ζ is applied to the force reading $\tilde{\mathbf{f}}_s$ and the resulting signal is denoted as $\bar{\mathbf{f}}_s$. The admittance control law is a proportional gain $\mathbf{K}_a$ which applies corrective action $\dot{\mathbf{x}}_{admit}$ to the nominal insertion path $\mathbf{x}_{des}$.

$$\dot{\mathbf{x}}_{admit} = \mathbf{K}_a \mathbf{N} \bar{\mathbf{f}}_s \tag{VI.2}$$

The corrective action $\dot{\mathbf{x}}_{admit}$ is integrated to a displace $\Delta\mathbf{x}$ which is limited by a displacement saturation value β such that:

$$\left\| \int_0^t \dot{\mathbf{x}}_{admit} dt \right\| = \Delta\mathbf{x} \leq \beta \tag{VI.3}$$

This saturation limit acts as a safety against potential malfunctioning in the force transducer. If such a failure were to occur the manipulator could move unpredictably and with the only bound being the workspace of the mechanism.

The insertion direction force, f_v, can be found by:

$$f_v = \hat{\mathbf{v}}^T \tilde{\mathbf{f}}_s \tag{VI.4}$$

which is the component of the perceived force along the insertion direction. For example, in the previous baseline insertion experiments from Chapter V, f_v was identical to f_z.

During the PEA insertion, the rate of insertion is fixed at 1 mm/s but the actuation of the stylet is adjusted through an admittance law in an attempt to regulate force

in the insertion direction. The reference regulation value is denoted as f_{reg}, and the admittance law as $h\left(K_v, f_v, f_{reg}\right)$. The constant K_v is used to scale the strength of the admittance law with units of velocity per unit force. The resulting corrected action to the stylet actuation, $q_{s,admit}$, is defined as:

$$\dot{q}_{s,admit} = \dot{q}_{s,des} + h\left(K_v, f_v, f_{reg}\right) \tag{VI.5}$$

Insertion direction forces are primarily governed by proper execution of AOS technique. The actuation of the stylet is unidirectional ($\dot{q}_s \geq 0$). In an ideal PEA insertion, the electrode is inserted until the basal turn, at which point the surgeon holds the stylet fixed in space and continues to guide the rest of the electrode into the cochlea. If done correctly, the PEA maintains minimal sliding contact with the modiolar wall and does not touch the lateral wall as shown in the simulation in Figure II.12.

If the AOS techique is executed too late, the PEA will make contact with the lateral wall and the reaction force may be detected along the insertion vector. Actuation of the stylet moves the PEA toward the modiolar wall and in general establishes a relationship of the form[1]:

$$\dot{q}_s = g(q)\dot{f}_v, \ \forall \dot{q}_s \geq 0 \tag{VI.6}$$

The exact form of $g(q)$ depends on the internal geometry of the cochlea, the elastic properties of a specific PEA, and the lubrication in the cochlea. A simple approach for online applications is to take a look at the general mechanics of the insertion and attempt to use $\dot{q}_s$ to regulate insertion force $\tilde{f}_v$. No significant force can be imparted on the cochlea in the insertion direction $\hat{\mathbf{v}}$ by the PEA until the electrode has passed

[1] $\dot{x}$ denotes the time derivative of x. $\dot{x} = \frac{dx}{dt}$

the first turn. In some experiments [93, 86] it can be seen from the data that the PEA can reverse the direction of force and effectively pull itself into the cochlea. The proposed control law on stylet actuation is written as:

$$\dot{q}_{s,admit} = h\left(K_i, f_v, f_{reg}\right) = K_i \frac{\gamma(q)}{2}\left[f_{reg} - \tilde{f}_v + \|f_{reg} - \tilde{f}_v\|\right] \tag{VI.7}$$

where f_{reg} is a limit to the expected insertion force (a negative value for resistance to insertion), K_i is a proportional gain in units of mm/Ns, and $\gamma(q)$ controls when adjustment to AOS is used. The lower and upper bounds for insertion depth q that correspond to onset of AOS insertion technique are defined as γ_1 and γ_2 respectively. Using these definitions, $\gamma(q)$ is given by:

$$\gamma(q) = \begin{cases} 0, & q \leq \gamma_1 \\ \frac{q-\gamma_1}{\gamma_2-\gamma_1}, & \gamma_1 < q < \gamma_2 \\ 1, & q \geq \gamma_2 \end{cases} \tag{VI.8}$$

The control law results in no correcting action to the preplanned stylet actuation for forces less than f_{reg} and is a proportional adjustment for large resistive insertion forces. The total adjustment to the stylet actuation is $q_{s,admit}$ where:

$$q_{s,admit} = \int_0^t \dot{q}_{s,admit} dt \tag{VI.9}$$

and is applied to the original desired stylet actuation $q_{s,des}$ as shown in Figure VI.3. The total retraction of the stylet is limited to 15mm since displacement beyond this point no longer affects the shape of the PEA.

Table VI.2: Summary of Experiment Trials

Set	Model	N	K_a (mm/Ns)	K_i (mm/Ns)	$[\gamma_1, \gamma_2]$ (mm)
0	plastic	95	0	0	N/A
0b	cadaveric	8	0	0	N/A
1	plastic	5	20	0	N/A
2	plastic	5	50	0	N/A
3	plastic	5	50	50	$[4, 7]$
4	plastic	5	50	80	$[4, 7]$
5	cadaveric	5	50	80	$[4, 7]$

Evaluation of the Admittance Controller

The proposed insertion control law was validated through a series of insertions in both plastic phantom models and in human cadaveric temporal bone specimens. Insertions in plastic models provided a means of observing electrode behavior during insertion while temporal bone experiments determined whether benefits in force reduction translate to real patient anatomy.

Table VI.2 summarizes the experimental parameters. Data from prior insertions in Chapter V act as a baseline for comparison as they did not use force control and relied solely on pre-registration. The data sets "0" and "0b" designate plastic and bone baseline insertions respectively. The value of N indicates the number of separate insertions in the data set. Only lateral admittance control was applied to sets 1 and 2 at different proportional gains. Force-based adjustment of the AOS technique was then added in sets 3 and 4 with insertion in temporal bone occurring in set 5.

Experiments for unbiasing the force sensor according to (III.57) resulted in a residual force with magnitudes below $0.03N$. Accordingly, the deadband margin was set at $\zeta = 0.03N$. The saturation boundary for the lateral admittance controller was set to $\beta = 5mm$ as used in (VI.3). This saturation value was determined based on the facial recess limits identified in Chapter II

The insertion procedure for the plastic and cadaveric specimens were identical to one described in Chapter V.

Admittance Controller Evaluation

Table VI.3 provides a summary of the insertion force results across all sets of data. Force values are presented as averages with the standard deviation in parentheses. Figures VI.4 and VI.5 plot the average force in the insertion direction for the plastic and bone insertion cases respectively. The percentage of insertion completed based on distance travelled through the insertion is parameterized by λ.

Table VI.3: Force Results Between Admittance Controller Cases

Specimen Type	Plastic Phantom		
Set	0	1	2
Insertion Force (N)	0.042 (0.023)	0.052 (0.029)	0.062 (0.034)
t-test (p)	N/A	0.090	0.032
Post-AOS Ins. F. (N)	0.047 (0.028)	0.076 (0.042)	0.091 (0.041)
t-test (p)	N/A	0.085	0.008
Peak Ins. Force (N)	0.190	0.186	0.168
Lateral Force (N)	0.016 (0.016)	0.022 (0.014)	0.026 (0.013)
Specimen Type	Plastic Phantom		
Set	0	3	4
Insertion Force (N)	0.042 (0.023)	0.037 (0.018)	0.044 (0.021)
t-test (p)	N/A	0.325	0.722
Post-AOS Ins. F. (N)	0.047 (0.028)	0.050 (0.023)	0.056 (0.036)
t-test (p)	N/A	0.584	0.482
Peak Ins. Force (N)	0.190	0.124	0.134
Lateral Force (N)	0.016 (0.016)	0.018 (0.014)	0.024 (0.018)

Specimen Type	Cadaveric	
Set	0b	5
Insertion Force (N)	0.071 (0.033)	0.046 (0.005)
t-test (p)	N/A	0.033
Post-AOS Ins. Force (N)	0.110 (0.058)	0.051 (0.021)
t-test (p)	N/A	0.009
Peak Ins. Force (N)	0.284	0.143
Lateral Force (N)	0.026 (0.030)	0.031(0.023)

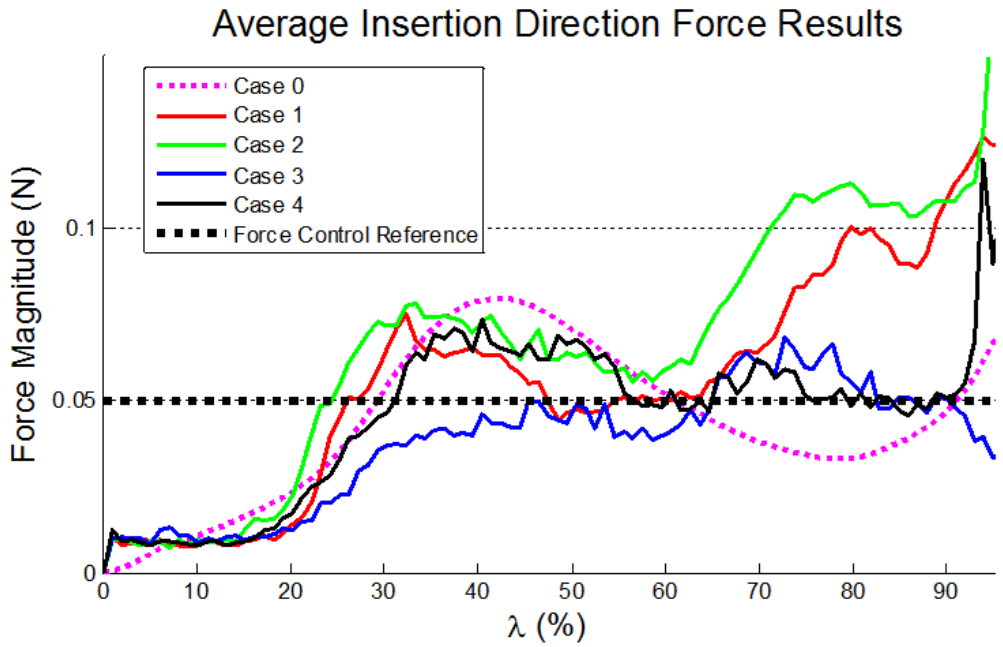

Figure VI.4: Average Insertion Force Data for Plastic Model Insertions

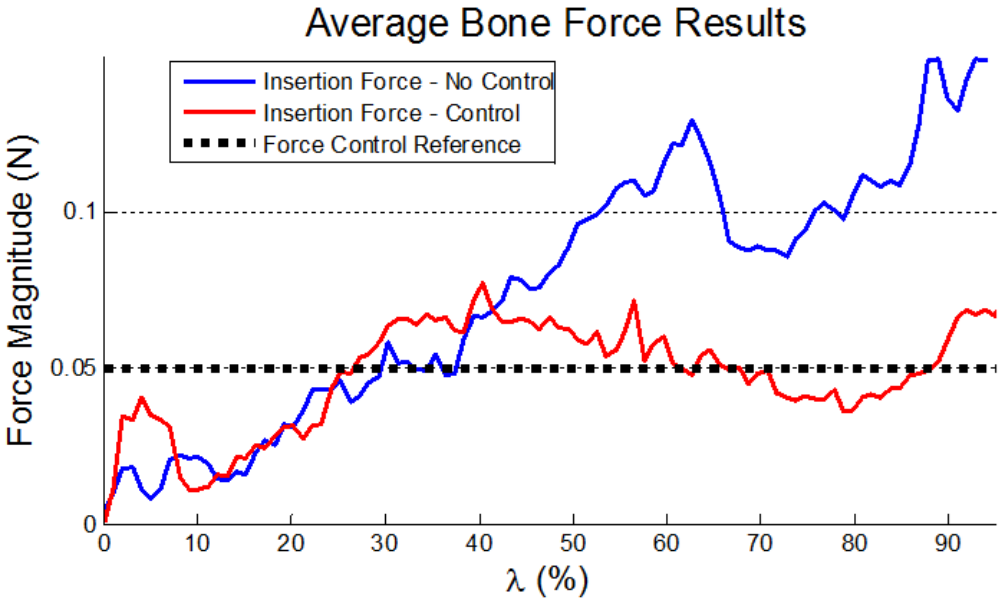

Figure VI.5: Average Bone Insertion Forces

Insertion forces were broken into two subsets; across the entire insertion and during the AOS portion of insertion. Admittance control applied in the lateral plane is active through the entire insertion while the stylet actuation admittance control can only affect the latter half of insertion. Set 0 and 0b act as the baseline for comparison for plastic and bone insertions respectively. A single sided t-test was used to compare the performance of the new insertion controller with reference sets 0 and 0b. Set 2 showed a statistically significant increase in average force compared to Set 0 ($p = 0.032$ for full insertion and $p = 0.008$ post-AOS). However in sets 3 and 4, which show enabled stylet admittance control data, there was no difference with the baseline set and peak forces were also reduced. The bone insertion data shows a statistical difference in post-AOS insertion force in the temporal bone insertions when using the admittance control law compared to non-force guided AOS from the baseline results ($p = 0.009$). There was no significant difference in lateral force between the sets. Little change in average pre-AOS insertion forces could be seen.

Figure VI.6 shows final corrections to insertion point location in the lateral plane at the end of insertion. In some cases, the initial robot alignment error was higher than one diameter of the PEA. The force controller sufficiently corrected the error without large changes in insertion force. The entrance into the cochlea requires passing through the facial recess and motion corrections much greater than $\pm 2mm$ are not generally possible due to anatomical restrictions.

These results reinforce the hypothesis from Chapter V that the higher insertion forces in cadaveric specimens were partly due to delayed initiation of proper AOS technique. The use of the baseline forces from the plastic phantom insertions, which had visible and repeatable registration, is also justified since the experiments with this controller resulted in insertion force signals comparable to the phantom model

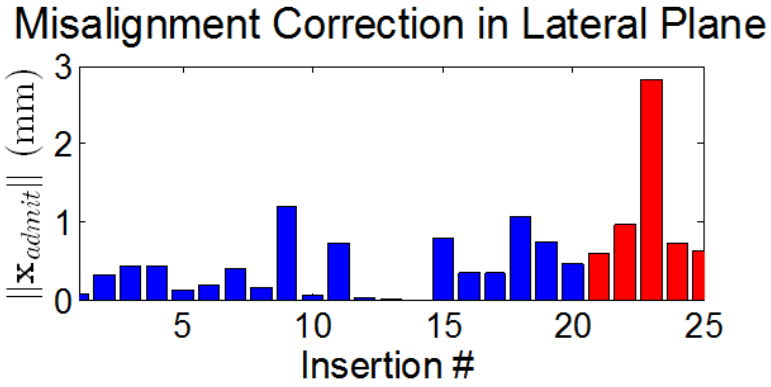

Figure VI.6: Correction to insertion point registration applied by hybrid force controller. Insertions 1 - 20 from plastic model sets and 21-25 are corrections in bone insertions.

in cadaveric specimens. The main weakness of this approach is that force guided actuation of the PEA requires that the distal tip of the PEA makes contact with the lateral wall. The work presented in the next chapter is intended to augment the stylet admittance law so that lateral wall contact is no longer necessary to modify stylet actuation.

VI.2 Detection of Extra-Cochlear PEA Buckling

There are very subtle variations in the relationship between sensed forces/moments and insertion depth when separating nominal insertions from tip-folding cases. The largest differences occur around the end of AOS and near full insertion depth. In the case of extra-cochlear buckling of the PEA, significantly larger forces are observed. The proposed method for detecting extra-cochlear buckling relies on using two features (denoted as ϕ_1 and ϕ_2) to define a region were PEA insertions are expected to be progressing into the cochlea. The features are defined as:

$$\phi_1 = \int f_z d\lambda \tag{VI.10}$$

$$\phi_2 = \int \sqrt{f_{xx}^2 + f_{yy}^2} d\lambda \tag{VI.11}$$

where f_z is the insertion force along $\hat{\mathbf{z}}_F$, f_{xx} is the insertion moment along $\hat{\mathbf{x}}_F$, and f_{yy} is the insertion moment along $\hat{\mathbf{y}}_F$ where frame $\{\mathbf{F}\}$ designates the frame of the force sensor.

The purpose of integrating force and moment information is to use energy as the metric to detect extra-cochlear bucking. Before a thin beam (like the PEA) will buckle, the structure stores elastic energy which will differentiate it from non-buckling cases. The integral also has the advantage of monotonically increasing during insertion. This increase is due to the fact that forces perceived during insertion dissipate energy either through sliding friction or through permanent mechanical deformation of the PEA.

Figure VI.7 shows the raw feature data for three types of insertions in the plastic phantom model. Blue traces represent cases of normal insertion while red represent tip folding cases and green represents extra-cochlear buckling cases. It can be seen clearly that nominal and tip-folding insertions dissipate a similar amount of energy during insertion. The buckling cases show a distinctly higher amount of energy stored through the insertion.

For any normalized insertion depth λ the is a corresponding average $\bar{\phi}_i(\lambda)$ and standard deviation $\bar{\phi}_{\sigma,i}(\lambda)$. These averages come from the measured normal insertions. A scale factor N is selected to define a new metric, $\phi'(\lambda)$, such that:

$$\phi'(\lambda) = \left|\phi_i(\lambda) - \bar{\phi}_i(\lambda)\right| - N\bar{\phi}_{\sigma,i}(\lambda), \;\; i = 1, 2 \tag{VI.12}$$

The value of N scales the number of standard deviations to include in the normal insertion region. A value of $N = 3$ was selected to use the 95% confident interval.

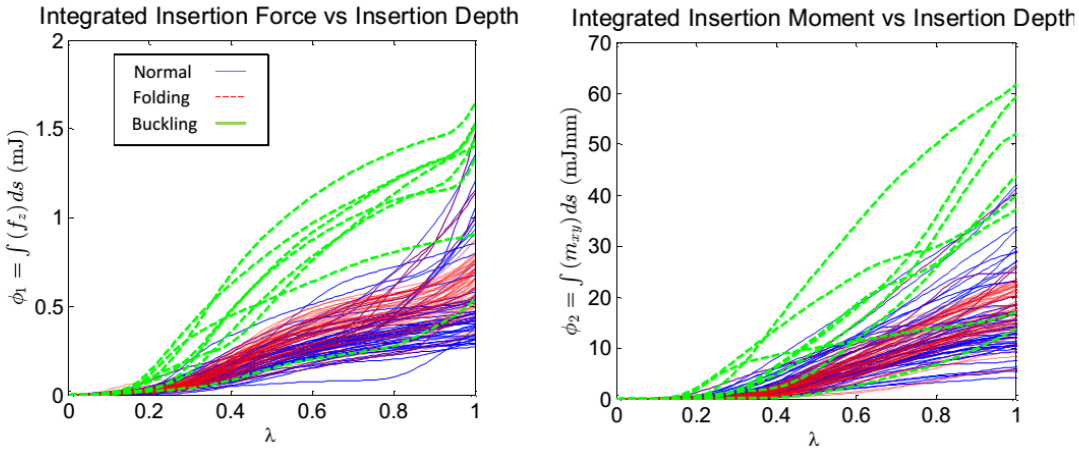

Figure VI.7: Insertion force and moment integrated over insertion depth.

If both of these conditions become positive, although not necessarily at the same time, the insertion is aborted and reports a failure. With this threshold, 9 of the 10 buckling cases could be detected and none of the normal and folding insertions are misclassified. In the case where buckling was not detected, the PEA failed near the end of the insertion process where there was insufficient insertion depth remaining for the integration of forces and moments to pass the detection threshold.

VI.3 Tip Folding Detection

The next two sections present a method for detecting intra-cochlear folding of the PEA called tip folding. The tip folding phenomenon was first described by Briggs et al. [12] in 2001 in a study evaluating the trauma reducing potential of PEA's. Other works since [13, 25] have also drawn attention to this possible complication. The onset of tip folding can occur when the stylet is retracted too early during the insertion process. This encourages the tip to bend before the basal turn and provides an opportunity for it to fold back on itself.

There is no estimate available in the current literature on the rate of tip-folding

in clinical implantations, suggesting that it is rare in procedures using hand tools. The motivation for detecting this particular type of complication stems from the fact that electrodes must be loaded into the mechanism. In this process, which was not part of the original PEA design, there is a risk of the user perturbing the stylet which the robotic system should be capable of identifying. Creating the complication is relatively simple since it involves incorrect actuation of the stylet. Just prior to insertion, the stylet was actuated by less than $0.5mm$. This intentionally induced error would repeatedly induce tip folding during insertion.

Detection of tip folding events is more difficult than buckling conditions since threshold techniques do not apply. Figure VI.8 compares the insertion force data from normal (blue traces) and tip folding (red traces) cases. While the magnitudes of insertion force are comparable, there is a noticeable difference in the shape of the two groups of traces.

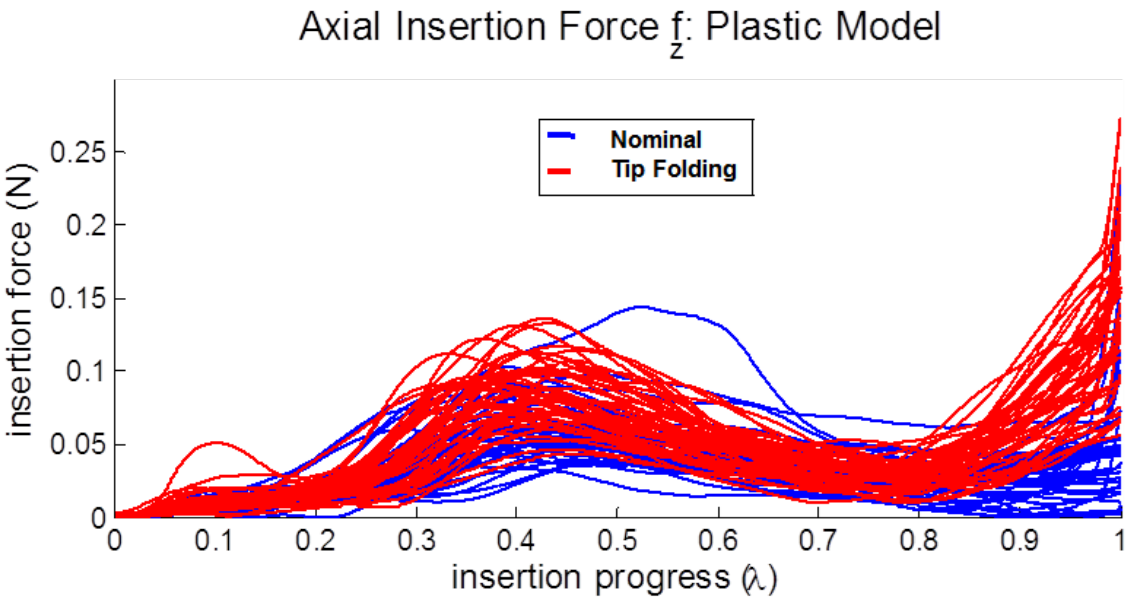

Figure VI.8: Normal and Tip Folding Insertion Forces.

To identify which sets of measurements belong to which group a type of machine learning algorithm called a support vector machine (SVM) is used. This type of algorithm belongs to the class of supervised learning methods - meaning that training data with ground truth must be provided to construct the classification model. The following section reviews the SVM algorithm, the selection of features for training, how to incorporate the predictive model from Chapter V and lastly, the expected performance of the classification scheme.

Support Vector Machine Classification

Support vector machines can be employed as classification and regression learning algorithms in a variety of problems [90]. The goal is to separate sets of data into one of two groups. Each sample contains a constant length vector $\mathbf{v} \in \mathbb{R}^{[m\times 1]}$ called the *feature space* representing attributes of the sample. A vector $\mathbf{y} \in \mathbb{R}^n$ has a value of -1 or 1 to distinguish which group the sample belongs to. Ideally, there would exist a hyperplane in $\mathbb{R}^n$ that separates the two groups. This hyperplane could be described by a vector $\mathbf{w}$ and bias b which results in the decision function:

$$f(\mathbf{v}) = \operatorname{sgn}\left((\mathbf{w}\cdot\mathbf{v}) + b\right) \tag{VI.13}$$

When utilizing SVM's the linear inputs $\mathbf{v}$ are substituted with a feature space $\boldsymbol{\phi}$ that maps non-linear parameters into a higher dimension linear space and casts the problem as a convex optimization [90]. Rather than compute the product $\mathbf{w}\cdot\mathbf{v}$ manually, a kernel function $k\langle\mathbf{v},\mathbf{v}_i\rangle$ may be used. The vectors $\mathbf{v}_i$ are taken from the training data and are called the *support vectors*. Each support vector is given a

weight α_i that is used in the decision function:

$$f(\mathbf{v}) = \sum_{i=1}^{l} \alpha_i k\langle \mathbf{v}, \mathbf{v}_i \rangle + b \tag{VI.14}$$

In the case of data that is not fully separable due to either measurement noise or the selection of non-distinct feature data, a trading penalty for data separation and the number of misclassifications in the training set is defined as $C > 0$. The conditions for finding the support vectors based on a set of training samples ($i = 1, \ldots, l$) is given by the following optimization problem [90]:

$$\begin{aligned} \text{maximize } W(\alpha) &= \sum_{i=1}^{l} \alpha_i - \frac{1}{2} \sum_{i,j=1}^{l} \alpha_i \alpha_j y_i y_j k\langle \mathbf{v}, \mathbf{v}_i \rangle \\ \text{subject to } \ 0 \leq \alpha_i \leq C \text{ and } &\sum_{i=1}^{l} \alpha_i y_i = 0 \end{aligned} \tag{VI.15}$$

The kernel functions used in SVM's are varied but the four most common kernels are the linear, polynomial, radial basis, and sigmoid. This work looked at employing the linear kernel and radial basis function (rbf). The linear kernel is a simple dot product operation:

$$k_{linear}\langle \mathbf{v}, \mathbf{v}_i \rangle = \mathbf{v}^T \mathbf{v}_i \tag{VI.16}$$

and the rbf is defined as:

$$k_{rbf}\langle \mathbf{v}, \mathbf{v}_i \rangle = \exp\left(\frac{-\|\mathbf{v} - \mathbf{v}_i\|}{2\sigma} \right) \tag{VI.17}$$

where σ is a tunable parameter governing the decay rate of the exponential.

A thorough review of SVM classifiers can be found in [90, 91] along with proofs for the solution conditions. In addition to selecting a kernel, a strategy must be adopted

for converting raw measurement data into a feature vector. The next section presents ways in which the insertion force data was processed into feature vectors for training the SVM classifier.

Effective Metrics for Tip Fold Over Detection

There is no single method for the selection of a feature space when using SVM methods. There are heuristic guides to the selection of features that also depend on the kernel to be used in the SVM [19]. In general, linear kernels benefit from large feature vectors while power and RBF kernels use smaller feature spaces to avoid over-fitting.

To reduce feature space size with RBF kernels the insertion domain was separated into four distinct regions as shown in Figure VI.9. This was done so that statistic features could be generated for each region and to keep the number of features small. The separation points between regions are denoted by normalized insertion depth λ. The depth at which AOS begins (λ_2) separates the early and latter portions of the insertion process. The depth values of λ_1 and λ_3 separate the portions equally based on insertion distance.

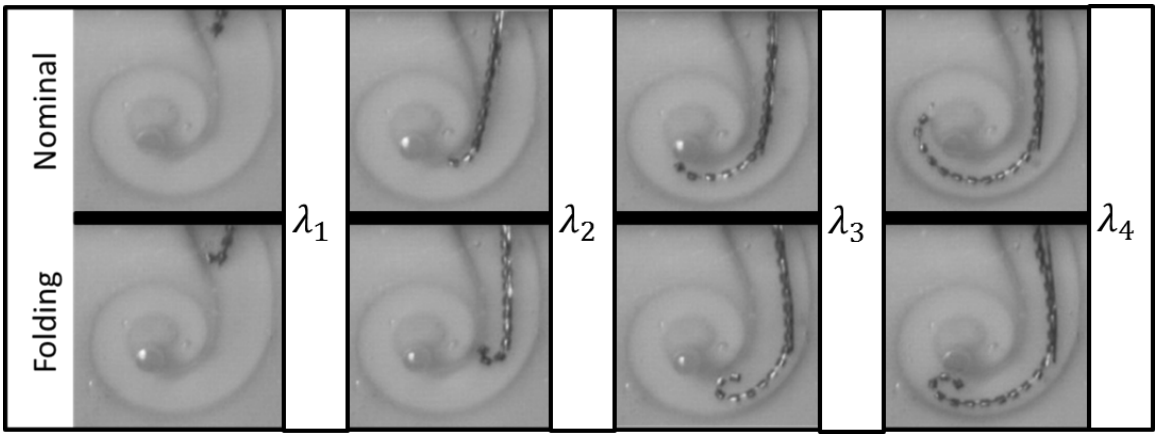

Figure VI.9: Insertion regions for feature extraction.

The feature space may include insertion depth λ, stylet actuation q_s, and perceived forces $\mathbf{f}(\lambda)$. Based on inspection from results in Figure VI.8 there is a distinguishable difference between nominal and tip folding in the final phase of insertion ($\lambda_3 < \lambda < \lambda_4$). A finite supply of electrodes resulted in a relatively sparse set of data (107 samples) and offers two distinct ways to analyze the data. The first method to sample the measured force signals at fixed insertion depth increments to create a large feature vector and use a linear kernel to process the data. This method essentially maps a high dimension pattern into a lower dimensional space. The second method is to generate a few distinct features based on statistical measures from sample sections of the signal and use a non-linear kernel to find decision boundaries in a higher dimensional space. This method was been used in process EEG and EKG signals to identify seizures [76] and arrthymias [46] respectively.

During the final phase of insertion ($\lambda \in [\lambda_3,\ \lambda_4]$) there is a significant rise in mean stiffness, and as a result, an increase in the energy required to push the folded electrode through the cochlea. Scaling is an important factor in generating feature sets to avoid biasing results to features with higher numerical ranges. In the case of stiffness, the scaling factor is $1/\rho$ where $\rho = 0.3N/mm$ was selected to safely bound non-buckling insertions in a range of $[-1, 1]$. The normalized mean stiffness κ_i refers to the i'th stage of the insertion process.

$$\kappa_i = \frac{1}{\rho} \frac{\int_{\lambda_{i-1}}^{\lambda_i} \frac{\partial \widetilde{\mathbf{f}}}{\partial \lambda} d\lambda}{\lambda_i - \lambda_{i-1}} \tag{VI.18}$$

Work done inserting the electrode was scaled by taking the proportion of work done

in the insertion phase of interest (η_i).

$$\eta_i = \frac{\int_{\lambda_{i-1}}^{\lambda_i} \widetilde{f}_z \, d\lambda}{\int_{\lambda_0}^{\lambda_4} \widetilde{f}_z \, d\lambda} \tag{VI.19}$$

Due to the fact that SVM's and other hyperplane classifiers are inherently geometric, they are sensitive to issues of scaling. If the domain of each feature is radically different then features with the largest domains will dominate the solution. This may be acceptable behavior in some cases but for the work presented here, preconditioning is applied before training the classifier. The vector $\mathbf{o} \in \mathbb{R}^m$ is an offset vector with each element equal to the mean of the same element in the the collection of feature vectors used in training the SVM. The matrix $\mathbf{S} \in \mathbb{R}^{m \times m}$ is a diagonal matrix with the diagonal elements equal to the standard deviation of the corresponding feature in the training data. A new preconditioned feature vector $\boldsymbol{\phi}$ is then defined as:

$$\boldsymbol{\phi}(\lambda_k) = \mathbf{S}^{-1} \left(\mathbf{v}(\lambda_k) - \mathbf{o} \right) \tag{VI.20}$$

which is substituted into (VI.14) in place of $\mathbf{v}_i$ and results in the decision function:

$$h(\boldsymbol{\phi}) = \sum_{i=1}^{l} \alpha_i k \langle \boldsymbol{\phi}_i, \boldsymbol{\phi}(\lambda_k) \rangle_{linear} + b \tag{VI.21}$$

When $h(\boldsymbol{\phi}) \geq 0$ the insertion is classified as normal, otherwise it is identified as a folding insertion.

This scaling method lets the SVC algorithm find a best fit separation hyperplane where each feature has zero mean and has a variance of unity. If the sample population from which the averages and variances are calculated is sufficiently large, then the scaling coefficients using this method should converge to constant values.

Verification of Tip Fold Over Detection

To evaluate the efficacy of different sets of features and avoid over fitting the model to the data, a k-fold sampling technique was used to generate 10 randomized training and testing sets from the pool of available data (51 normal and 56 folding). The objective function seeks to find the optimal training parameters (C and σ) to minimize test inaccuracies over the 10 sets. When using the linear kernel there is one adjustable parameter and two parameters when using the rbf kernel. Table VI.4 summarizes the kernel, feature vectors, and optimized SVM parameters for each classification strategy. In the case of the linear kernel methods, the length of the feature vector scale by the

Table VI.4: Classification method summary

Method	**kernel**	**SVM parameters**	**features**
1	linear	$C = 1.24$	$\widetilde{\mathbf{f}}_z$
2	linear	$C = 1.05$	$\widetilde{\mathbf{f}}_z(\boldsymbol{\lambda}),\ \widetilde{\mathbf{f}}_{xx}(\boldsymbol{\lambda}),\ \widetilde{\mathbf{f}}_{yy}(\boldsymbol{\lambda})$
3	rbf	$\sigma = 0.25,\ C = 1.23$	$\kappa_4,\ \eta_4$
4	rbf	$\sigma = 2.11,\ C = 2.63$	$\kappa_1, \ldots, \kappa_4,\ \eta_1, \ldots, \eta_4$

number of samples in the signal, n. There was no benefit for extending the signal segmentation beyond $n = 25$ samples in both linear methods.

Table VI.5: Results of SVM feature selection methods. Average accuracy of 500 randomized sets.

Method	**Average Accuracy**	**False Positive**	**False Negative**
Method 1 (25 Samples)	87%	6.3%	7.0%
Method 2 (3 x 25 Samples)	91%	5.3%	4.4%
Method 3	84%	6.7%	9.3%
Method 4	80%	7.5%	12%

After selecting optimal SVM parameters, each data set was randomized into 500 sets of training / testing groups and classification accuracy was evaluated. The final

results for the different sets of feature vectors are shown in Table VI.5. It can be seen that the linear kernel with a 75 element feature vector $\mathbf{v} = \left[\widetilde{\mathbf{f}}_z^T(\boldsymbol{\lambda}),\ \widetilde{\mathbf{f}}_{xx}^T(\boldsymbol{\lambda}),\ \widetilde{\mathbf{f}}_{yy}^T(\boldsymbol{\lambda})\right]^T$ with $\boldsymbol{\lambda} \in \mathbb{R}^{25}$ had the highest prediction accuracy.

Figure VI.10 shows the decision boundary results for the 500 randomized trials using Method 2. The decision boundary from (VI.14) is value $f(\mathbf{v}) = 0$. Normal insertions have a value greater than zero and folding insertion classifications are less than zero. Results with circle markers indicate that the insertion was properly classified and those marked with an x are incorrectly identified.

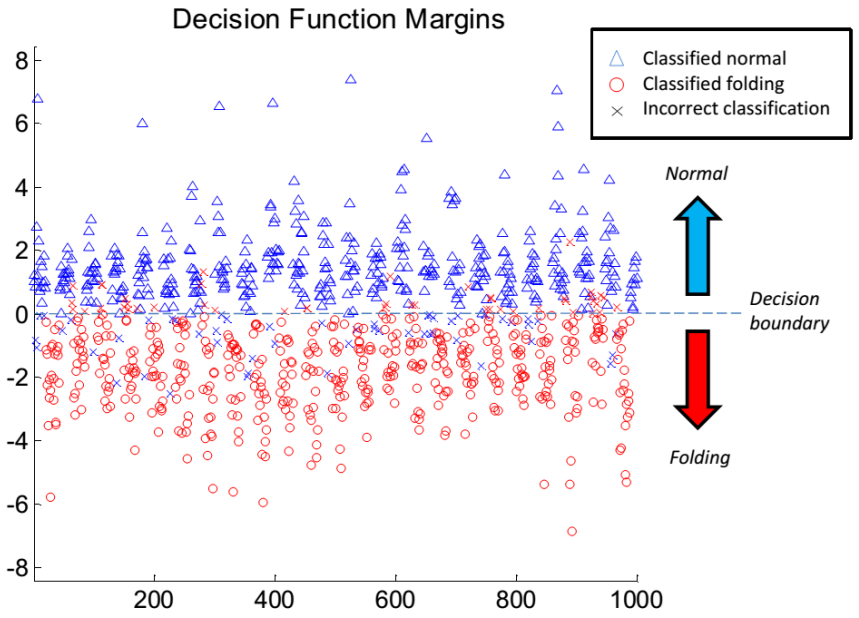

Figure VI.10: Decision function results.

Adjustment to the rate of false positives (positive being a folding detection) can be easily tuned using the same SVM model. In general, it is better to miss folding cases rather than reinsert a properly placed implant and the folding event could be identified with radiological imaging after surgery. Since reimplantations, although costly, have been shown to be safe for patients [41, 4]. From (VI.14) it can be seen

that the decision function has a trained bias term, b, that may be adjusted to shift the decision boundary. For example, by shifting b by -0.25 all normal insertions would be properly classified but more folding events would be classified as normal.

Onset of Folding

The key weakness with the classification method described above is that the entire insertion must be completed before a decision could be made. This is undesirable since the folded PEA will have been forced into the scala tympani thus increasing the risk of trauma. The approach for tip folding detection is presented in Figure VI.11. The wrench data is sampled at a high rate with m total measurements for any given insertion. The indexing subscript k references one measurement or prediction with $1 \leq k \leq m$. All data is expressed in terms of the normalized insertion depth vector $\boldsymbol{\lambda} \in \mathbb{R}^m$ with the use of λ_k indicating the k'th step of the insertion. The prediction model estimator is used to augment the current component wrench measurement $f_j(\lambda_k)$ with the experimental distribution $\bar{\mathbf{f}}_j(\boldsymbol{\lambda})$ to produce a prediction of the insertion wrench component $\tilde{\mathbf{f}}_j(\boldsymbol{\lambda})$. A subset of the predicted wrench components $\tilde{\mathbf{f}}_j(\boldsymbol{\lambda}),\ j \in [x, y, z, xx, yy, zz]$ are then used to generate a feature vector $\boldsymbol{\phi}(\lambda_k)$ which is used as an input to the SVC discussed in the previous section.

There is uncertainty in the predictive model's estimation that can be propagated into the decision function (VI.21). The estimated feature vector can then be written as:

$$\tilde{\mathbf{v}}(\lambda_k) = \mathbf{v} + \boldsymbol{\epsilon}(\lambda_k) \tag{VI.22}$$

where $\boldsymbol{\epsilon}(\lambda_k)$ is the error in the prediction estimation at step k. Substituting (VI.22) into (VI.20) and (VI.21) using a linear kernel and differentiating with respect to $\boldsymbol{\epsilon}$

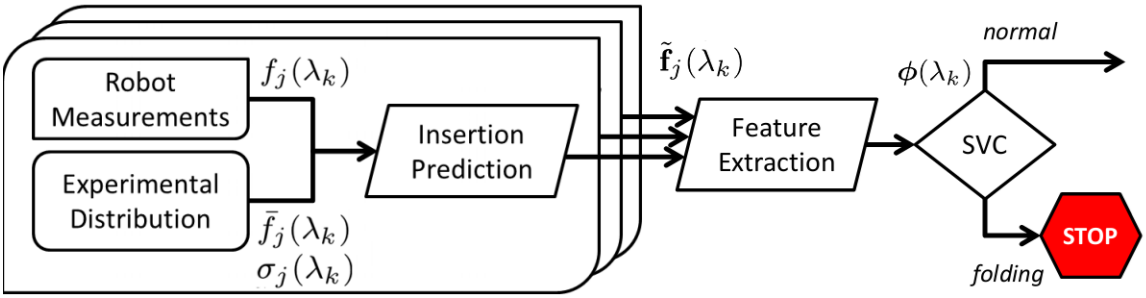

Figure VI.11: Tip folding detection process. The subscript j refers to one of the measured wrench components. As a force component measurement f_j is made at depth λ_k, is combined with a known population of normal insertion data with mean $\bar{f}_j$ and variance σ_j to generate an estimate of a likely complete insertion force vector $\mathbf{f}_j$. This estimate is then used to construct a feature vector $\boldsymbol{\phi}$ that is passed to a SVC decision function to decide whether a tip fold has occurred. In the case of tip folding, the robot is instructed to stop further insertion of the PEA into the cochlea.

yields:

$$\frac{dh}{d\boldsymbol{\epsilon}} = \sum_{i=1}^{l} \alpha_i \mathbf{S}^{-1} \mathbf{v}_i \tag{VI.23}$$

Individual elements of the vector $\boldsymbol{\epsilon}(\lambda_k)$ have their $i'th$ index denoted as $\epsilon_i(\lambda_k)$. It is assumed that only samples estimated beyond the current measurement have a significant effect on the decision function and therefore $\epsilon_i(\lambda_k) = 0, \forall\, i \leq k$. Since errors are not considered up to the $k'th$ out of m measurements, two auxilary vectors $\mathbf{a}_k$ and $\mathbf{b}_k$ are defined as:

$$\begin{aligned} \mathbf{a}_i(\lambda_k) &= [v_{i,k+1}, \ldots, v_{i,m}]^T \in \mathbb{R}^{m-k} \\ \mathbf{b}(\lambda_k) &= [\epsilon_{k+1}, \ldots, \epsilon_m]^T \in \mathbb{R}^{m-k} \end{aligned} \tag{VI.24}$$

which are substituted into (VI.23), replacing $\tilde{\mathbf{v}}(\lambda_i)$ and $\boldsymbol{\epsilon}$ respectively without loss of information.

$$\frac{dh}{d\mathbf{b}(\lambda_k)} = \sum_{i=k}^{l} \alpha_i \mathbf{S}^{-1} \mathbf{a}_i(\lambda_k) = \mathbf{z}(\lambda_k) \tag{VI.25}$$

The effect of $\mathbf{b}(\lambda_k)$ on the deviation of the decision function (parameterized as δh) is not known precisely but can be bounded using the Cauchy-Schwarz inequality:

$$\delta h(\lambda_k) \leq \|\mathbf{z}(\lambda_k)\|\|\mathbf{b}_k\| \tag{VI.26}$$

The value of $\mathbf{z}(\lambda_k)$ is easily calculated from the trained support vectors and $\|\mathbf{b}_k\|$ is estimated from evaluating the prediction model error as a function of λ as shown from the set of data used in training the SVC. The bound on the uncertainty from (VI.26) is highly conservative and can be tuned by introducing a scalar constant $\rho \in [0, 1]$. The final real time classification of folding event then becomes:

$$g(\lambda_k) = \begin{cases} -1 & \text{if } h(\tilde{\mathbf{v}}_k) + \rho\|\mathbf{z}(\lambda_k)\|\|\mathbf{b}(\lambda_k)\| \leq 0 \\ 1 & \text{otherwise} \end{cases} \tag{VI.27}$$

Since a negative value in (VI.27) indicates a tip folding event, this approach is intended to be conservative in declaring a tip folding event.

To test the onset detection method the original linear SVC (method 2 from Table VI.5) was used and the associated support vectors were removed from the testing data set. An additional 20 insertion experiments were added to the original set. Classification was treated as a one way process, once the algorithm returned a tip-folding event the insertion could not be classified as normal. A *false positive* is defined as identifying a normal insertion as a tip folding event. A *false negative* is defined as a tip folding insertion that the SVC identifies as normal. The *combined accuracy* is defined as the ratio of the correctly identified normal and folding insertions compared to the total number of insertions.

The primary goal of the predictive model is to identify tip folding events as soon

as possible. Figure VI.12 presents a histogram of onset detection with the insertion domain divided into 10 equal bins. Five values of ρ are shown to see the effect of the uncertainty margin on the point of onset detection. The vertical dashed line represents the point of initiation for *AOS* technique. Due to the mechanics of tip folding, the detection algorithm should not detect folding event until after *AOS* begins.

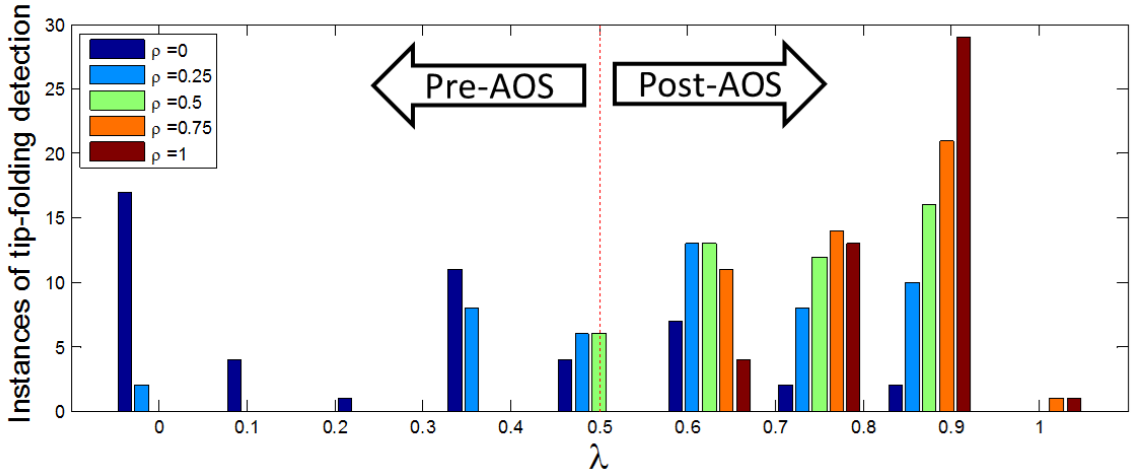

Figure VI.12: Tip Folding Onset Detection.

As the uncertain margin increases as ρ approaches 1, the tip-folding detection is delayed as the SVC decision function must have a stronger degree of confidence to declare a folding event early. With higher margins ($\rho > 0.5$) the accidental declaration of a folding event before AOS is eliminated. With no margin applied, there are cases of accidental folding detection early in the insertion process.

Table VI.6 shows the number of false positives and negatives for different values of ρ. Adjusting the uncertainty margin has little effect on the number of false negatives, with the most conservative bound ($\rho = 1$) allowing one additional tip folding event to be missed. Without the uncertainty margin ($\rho = 0$), the number of false positives increases drastically. Based on the results shown in Table VI.6 a value of $\rho = 0.75$ is recommended for the insertion system.

Table VI.6: Classification Errors

ρ	0	0.25	0.5	0.75	1
false positives (%)	42	19	19	14	14
false negatives (%)	7	10	10	10	10
combined accuracy (%)	74	85	85	88	88

As expected, from Table VI.6 we see that classification accuracy reaches a comparable value of 88% to the preliminary result using full insertion depth data shown in Table VI.5.

VI.4 Conclusion

This chapter has demonstrated several ways in which *in vivo* force sensing can be utilized during the insertion process so that the robotic system can actively reduce insertion forces and halt insertion in cases where the electrode may be experiencing abnormal behavior. The proposed hybrid force/position admittance controller is capable of correcting misalignments in registration within the expected workspace bounds of the CI procedure. Insertion direction forces are also useful in modifying the pre-planned stylet actuation so that insertion forces in temporal bones is equivalent to those measured in phantom models benefitting from well defined registration.

Insertion forces are also useful in fault detection and although the methods presented in this chapter do not have 100% accuracy they provide more insight into intra-cochlear electrode behavior than previously demonstrated without radiological imaging. By incorporating prior knowledge of normal CI insertion force progression during insertion, a classification algorithm was presented that could detect intra-cochlear tip folding before completion of the insertion. Such a detection method has potential to avoid excessive cochlea damage during insertion.

There are several ways that this work could continue. For the admittance control of the stylet actuation its primary weakness is that contact must occur before the

robot can react and adjust its insertion trajectory. The next chapter addresses this weakness through the introduction of a new sensor modality. Both the hybrid admittance controller and estimations of buckling conditions could benefit from elastic mechanics models. The gains in the admittance control law are conservative so as not to push against an unknown stability margin dictated by the compliance of the electrode. Also only a couple of CI complications were considered in this work but ideally a suite of simultaneously running functions should be used during insertion to access likelihood of inducing trauma, such as a perforation of the basilar membrane.

Chapter VII

ELECTRICAL IMPEDANCE FOR INSERTION GUIDANCE

The previous chapter explored the use of *in vivo* force sensing to adjust the rate of stylet actuation so as to help avoid lateral wall contact. The method was contingent on sensing excessive reaction loads in the electrode array insertion direction, which were assumed to be the result of lateral wall contact. While this assumption can be checked in phantom model insertions, it cannot be checked in real time during cadaveric insertions. Also, it is preferable to avoid *any* lateral wall contact during insertion and the force information is only available after contact.

There has been some prior development of methods to detect intra-cochlear position of a CI using sensors on the device. Wang et al. [117] proposed an electrode array design with integrate shape and contact sensing. More recently, Watanabe et al. [120] proposed a custom electrode array with a dense array of contacts. Proximity to the scala walls was estimated through scanning electrochemical microscopy. These technique are novel and can facilitate contact-less CI steering but require the development of drastically new electrode array designs with the associated time and expense to deploy clinically.

This chapter proposes a novel method of guiding the PEA during insertion without changing the electrode design. All CI implants rely on generating controlled electrical stimulation at specific frequencies to excite the auditory nerve. Electrical impedance is commonly used to evaluate the connectivity quality of the implant with respect to the auditory nerve. Measurements are categorized by where the ground for the conductive path is located. In *monopolar* impedance measurements, a current

source is generated in one electrode contact at a time which must flow to a common grounding element. With *bipolar* impedance, one electrode contact acts as the source and another as the ground.

There has been a large body of work in modelling the impedance of the cochlea with examples found in the following works [103, 47, 113, 23, 104, 104]. In most of these works, the theoretical challenge is in modelling the tissue and bone conductivity as the ultimate goal is to best model the electrical stimulation of the auditory nerve.

In monopolar stimulation modes, tissue conductivity is of critical importance since the common ground is located outside of the scala tympani. However, when measuring bipolar impedance, the conductive path is considerably shorter and contained entirely in the cochlea. In this work, it is hypothesized that the perilymph (fluid in the scala tympani) dominates the impedance measurement and, if true, this can be used as sensory information relating electrode proximity to the scala tympani walls. Recent work by Tan et al. [106] lends support to this premise as there was noticeable difference in bipolar impedance measurements between insertion techniques maintaining modiolar contact and lateral wall contact.

This chapter presents work on incorporating bipolar impedance feedback during CI insertion. The final goal is to use real time bipolar impedance measurements to guide stylet actuation so that modiolar contact is maintained and contact with the lateral wall is avoided. The following sections present a series of experiments to investigate the relation between bipolar impedance measurements and the proximity of the PEA electrode contacts to the modiolus. These experiments were first conducted in phantom cochlea and then in temporal bone to both confirm the findings of Tan et al. [106] and to determine if the phantom model is a suitable surrogate for a real cochlea.

Next, a numerical model is presented that can verify the experimentally derived measurements. Following this, an admittance control law for PEA stylet actuation based on impedance feedback is derived and evaluated in a set of experiments.

VII.1 Preliminary Investigation of Impedance Measurements

The first step in constructing an impedance guided control model was to perform experiments which could directly measure impedance and electrode position. This data was used to identify a reasonable function for the modiolar proximity / impedance relationship.

In the human cochlea, the scala tympani chamber is filled with perilymph. Work by Hibbert et al. [42] provides a detailed chemical composition for creating artificial perilymph solutions that mimic the electro-chemistry of real perilymph. However, the bulk of the artificial perilymph is a saline solution which defines the electrical conductivity properties. Since fluid conductivity is the characteristic of insert in this application, buffered saline solution is used in all experiments presented in this chapter. Work by Jolly et al. [47] measured conductivity using mono, bi, and quadropolar stimulation and used buffered saline as a surrogate as well.

Collection of realtime impedance data comes from the *Cochlear Impedance Measurement* (CIM) software developed by Cochlear Ltd. and featured in the work of Tan et al. [106]. The software package was designed to interface with Cochlear brand electrodes through the *Nucleus freedom* communication pod. When the program is connected to an implant it is possible to sample the monopolar or bipolar impedance of any combination of electrode contacts. The selection of electrodes must be made prior to sampling and cannot be changed while measurements are being taken. During collection the data is streamed while measuring individual electrodes sequentially. Current signal processing limits of the technology require a period of 0.07 seconds per

electrode sampled. This equates to a 1.40 second sample window to read all 20 bipolar impedance pairs once.

Through a research agreement with Cochlear Ltd., the source code was provided so that modifications could be made for communication with a robotic system. The change made was to send the sample time, electrode ID, and impedance measurement in a packet on the PC loopback network port using a User Datagram Protocol (UDP). With this approach, any program running on the same PC as the CIM has access to the impedance data by listening to the loopback address. A UDP relay program was used to send data to the xPC realtime target robot controller.

Electrical impedance is usually expressed as a complex value characterizing the resistance and reactance. The output of the CIM measurements is a scalar quantity representing the impedance magnitude. Excitation current and frequency are fixed for all measurements. The current delivered is $75\mu A$ in biphasic pulses with a $25\mu s$ pulse width [106].

Initial experiments measured electrode position and bipolar impedance in the phantom model. A separate four DoF robot was used to control electrode insertion for these experiments so that modifications to the prototype insertion tool could be made in parallel. However this robot was fitted with the same force sensor and gripper module as the parallel and planar insertion systems as shown in Figure VII.1 (A). The phantom model was observed with a DinoLite digital microscope. A custom software application called *impCap* was developed to save snapshots of the insertion timed with impedance measurements received from the CIM software through UDP. The *impCap* interface is shown in Figure VII.1 (B).

Rather than execute a preplanned insertion trajectory, the robot was controlled directly by the user through a telemanipulation control mode. The purpose for this

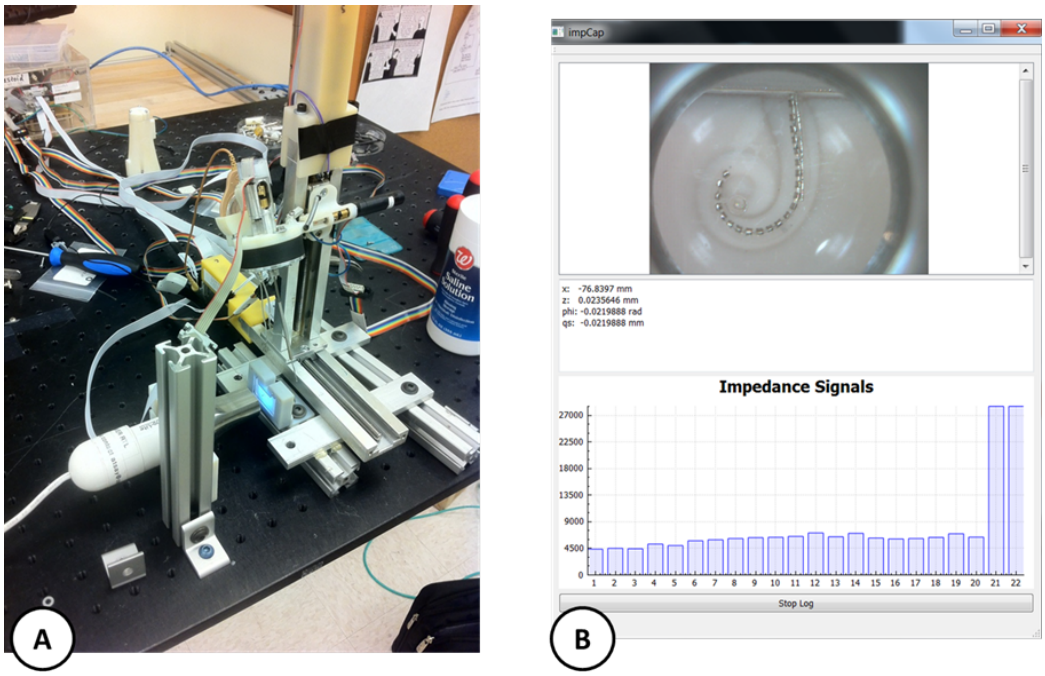

Figure VII.1: Preliminary impedance testing. (A) A four DoF robot was used to control and monitor electrode placement (insertion robot was being modified at the time of the experiment). *Dinolite* camera and Teflon cochlea model provided by Cochlear Ltd. were used. (B) Custom data logging software saves snapshots of the camera feed when impedance signals from the CIM software are received. The robot controller also provides position updates to this GUI.

was to move the PEA throughout the volume of the scala tympani model to collect a rich set of impedance and electrode position data.

The data analysis began with the digitization of individual electrodes from the collected snapshots taken with each impedance measurement. The CAD model of the Teflon cochlea was used to generate a template image to register to the photographs. This template also sets the scaling of the snapshot images.

For a single impedance measurement, the pair of electrode being measured for impedance were marked and their distances to the nearest points on the modiolar wall was automatically calculated. The distance was calculated by a closest point distance minimization to the registered modiolar curve. The average of these distances

is called the *distance metric*. The four points for the closest distance lines on adjacent electrodes (two on the electrode array and two on the modiolar wall) also defines a 2D quadrilateral shape whose area was also recorded as an estimate of the fluid volume between the electrodes. This area is termed the *area metric*. An example of this processing is shown in Figure VII.1

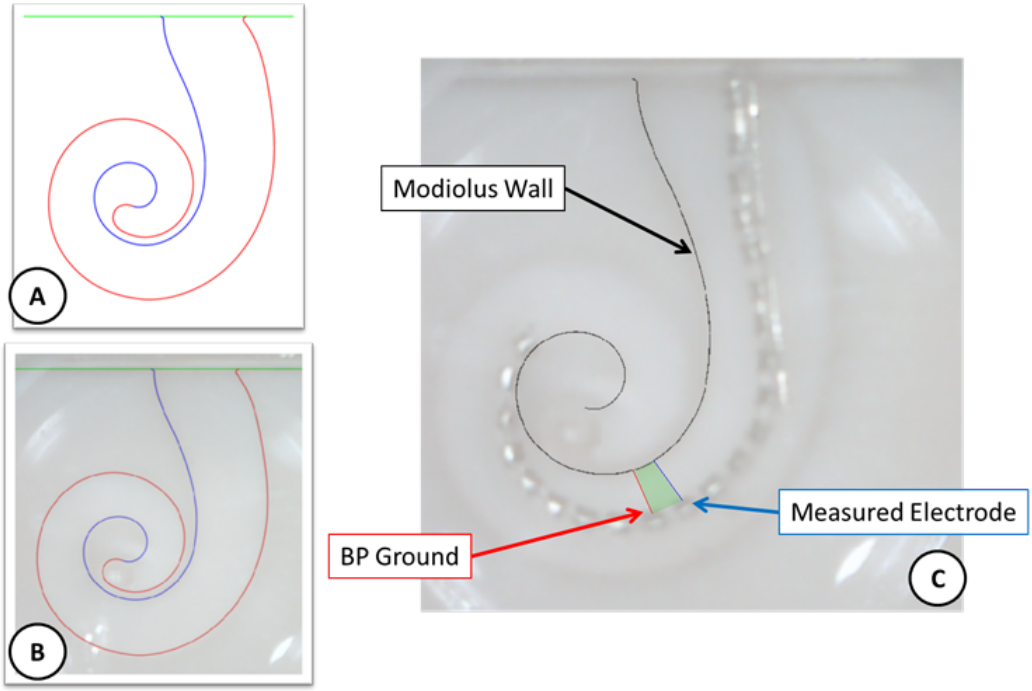

Figure VII.2: Example of electrode segmentation. The modiolar wall dimensions (black line) were taken directly from the CAD model (A) and registered to the sample photographs(B). (C) The blue line shows the distance from the measured electrode to the modiolar wall while the red line corresponds to the ground electrode for the current sample. The green area is proportional to the volume of fluid trapped between the modiolar wall and the sampling electrodes.

Figure VII.3 shows the measurement results for electrode 20 in BP negative polarity sampling using distance and area metrics. Several fitting models for the data were attempted (polynomial, exponential, trigonometric, and power) with power law fittings of the form

$$f(x) = ax^b + c \tag{VII.1}$$

having the best result in terms of R^2 values. The fits are not very strong in best cases (between 0.75 and 0.8) with several electrodes having unacceptable fits due to lack of contact with the modiolar wall. The electrodes must be within about 0.2mm of the wall before significant changes in impedance can be seen. This observation is comparable to results by Jolly et al. [47] with bipolar measurements using electrode arrays from Advanced Bionics.

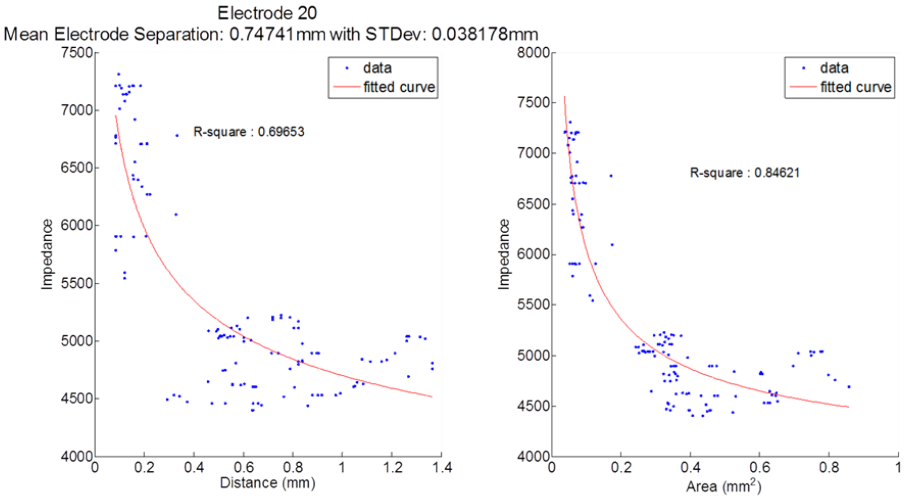

Figure VII.3: Measured bipolar impedance as a function of modiolar proximity.

A summary of the fitting performance in terms of R^2 values is shown in Figure VII.4. Several electrodes (11, and 15-18) show poor fitting results and when inspecting there individual plots it can be seen that little or no measurements were taken with the electrode in close proximity to the modiolar wall. An interesting point seen in Figure VII.4 is that the area measurement metric consistently has an equal or better fit than distance alone. The true conductivity is expected to be a volumetric function but due to the small variation of out of plane depth through the scala tympani, the area metric is used as an approximate model.

The end result from this initial investigation is a basic model that relates bipolar

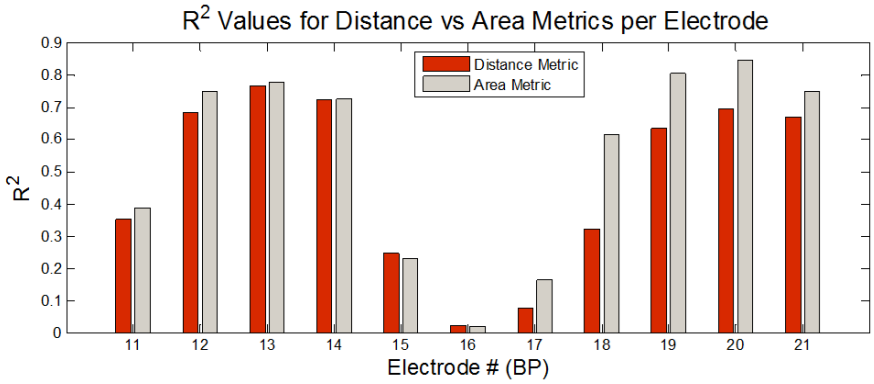

Figure VII.4: R^2 fitting per electrode. Several electrode (11,15-18) had unacceptable level of error in the fitting require more sampling of impedances closer to the modiolar wall. The area metric consistently had a better fit compared to linear distance.

impedance measurements to a proximity metric. Based on these results the model equation is:

$$z(A_k) = aA_k^b + c \tag{VII.2}$$

where the index k denotes the electrode pair, A_k is the area enclosed by the k'th electrode pair and the modiolar wall in millimeters, and the coefficients a, b, c are the model constants. The impedance value is stated in Ohms in this work. This simple model will be used in deriving the stylet admittance law governed by impedance measurements.

VII.2 Bipolar Impedances in Human Specimens

Before continuing with control experiments, a series of insertions were performed in cadaveric bone specimens to test whether the impedance measurements would be useful in real human cochlea. This question was explored by Tan et al. [106] but was verified independently through the small study presented in this section.

The goal of this study was to determine if bipolar impedance measurements change with modiolar proximity. Imaging was not available for this study and would not provide adequate resolution to segment and measure electrode contact distance from

the modiolus. Instead, the experiment was designed so that PEA's would be inserted using two different techniques; the recommended AOS technique and the Standard Insertion Technique (SIT).

While AOS involves the coordinated movement of inserting the PEA and removing the stylet, in SIT the PEA is inserted completely with the stylet still in the PEA. After insertion is completed to full depth, the stylet is removed and the electrodes curls toward the modiolus. In effect, when using the SIT, a PEA behaves like a stiff lateral wall implant.

For this experiment, a total of 22 insertions were performed across 4 different bones, and used 6 different PEA's. The experimental matrix is shown in Table VII.1. The organization of the experiments was designed so that each bone would have at least two different PEA's inserted and each PEA would have insertions with AOS and SIT technique.

Table VII.1: Experimental Matrix for Impedance Measurements in Cadaveric Specimens

Trial	Bone	PEA	Technique	Trial	Bone	PEA	Technique
1	1	4	AOS	12	3	3	SIT
2	1	4	SIT	13	3	3	AOS
3	1	1	SIT	14	3	4	AOS
4	1	1	AOS	15	3	4	SIT
5	2	1	SIT	16	3	4	SIT
6	2	1	AOS	17	4	5	SIT
7	2	2	AOS	18	4	5	AOS
8	2	2	AOS	19	4	5	SIT
9	2	2	SIT	20	4	6	SIT
10	2	2	SIT	21	4	6	AOS
11	3	3	AOS	22	4	6	AOS

Using the experimental setup is shown in Figure VII.5, experienced clinicians performed the insertions with standard tools in a laboratory setting. The cochleas were

soaked in buffered saline solution prior to insertion and data was captured continuously throughout the insertion process. At the end of an insertion, the clinician held the PEA still at its final depth so that a stable set of impedance samples could be collected. In the case of SIT insertions, measurements were taken before the stylet was removed from the PEA.

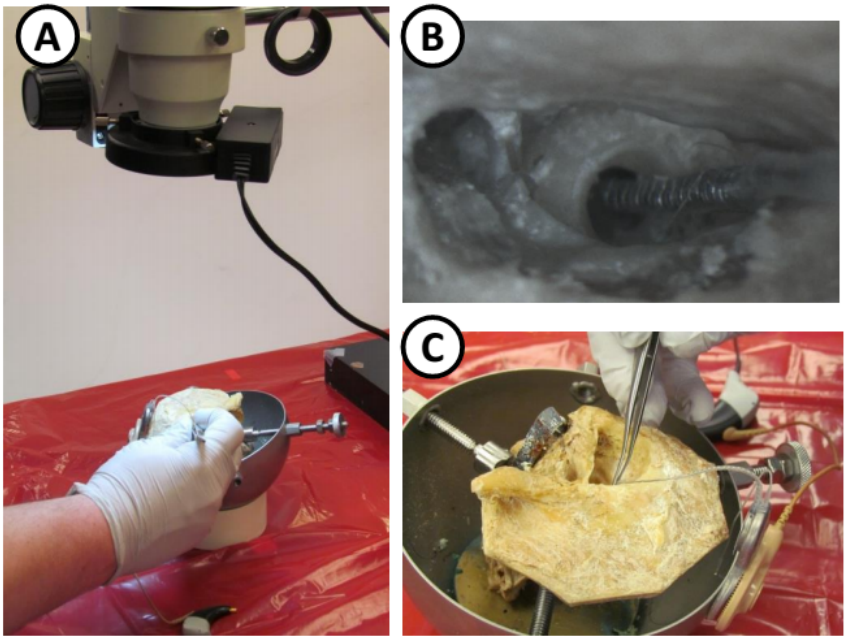

Figure VII.5: Impedance measurements in cadaveric specimens. (A) Insertions were conducted manually by experienced clinicians using insertion forceps and a stereo microscope. (B) View of the implantation from the microscope perspective taken by attached microscope camera. (C) The CI communication hardware attached to the temporal bone holder.

An example of one of the sets of raw experiment data is shown in Figure VII.6. All 21 bipolar pairs are shown in the plot. The point of final placement is clearly observable in the plot and it is this region of data that was used from each experiment.

A preprocessing step was required before beginning analysis to capture two measurement issues that would corrupt our results. The first case of data removal occurred

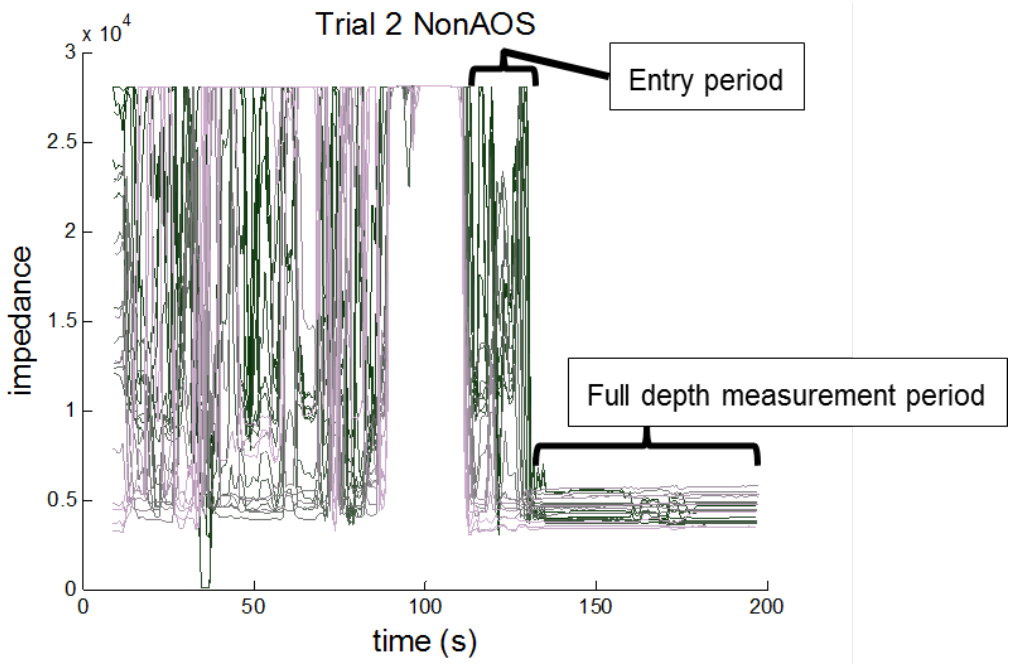

Figure VII.6: Recording on impedance signals in temporal bone insertion.

when a measurement failure on a particular channel was unresponsive. When not submerged in a conductive medium, the impedance measurements report open circuits at $28.8k\Omega$. In some insertions, air pockets could be trapped temporarily in the ST, preventing proper conduction. If a signal remained above $20k\Omega$ at final placement, that electrode pair for the particular trial was removed from the data set.

The second case for preprocessing removal of an electrode channel was in the presence of unusually high noise. The standard deviation of the impedance signal at final placement is typically on the order of several hundred ohms. If during a trial a particular channel had a standard variation greater than 800Ω at final placement, it was removed from the data set. Unstable measurements could be due to a variety of factors outside the scope of this work. We note that we have reused each electrode for multiple insertions therefore possibly causing damage to internal wiring.

A total of 73 electrode channels out of 462 through 22 insertions were removed

from the total data set before processing results. Out of the 73 filtered channels, only 5 were due to high standard deviations of the measurement. Figures VII.7 and VII.8 plot the magnitude of signals and the standard deviations respectively. Included in the plots are the values before and after filtering the data set. The dashed horizontal lines show the respective thresholds on magnitude and standard deviation.

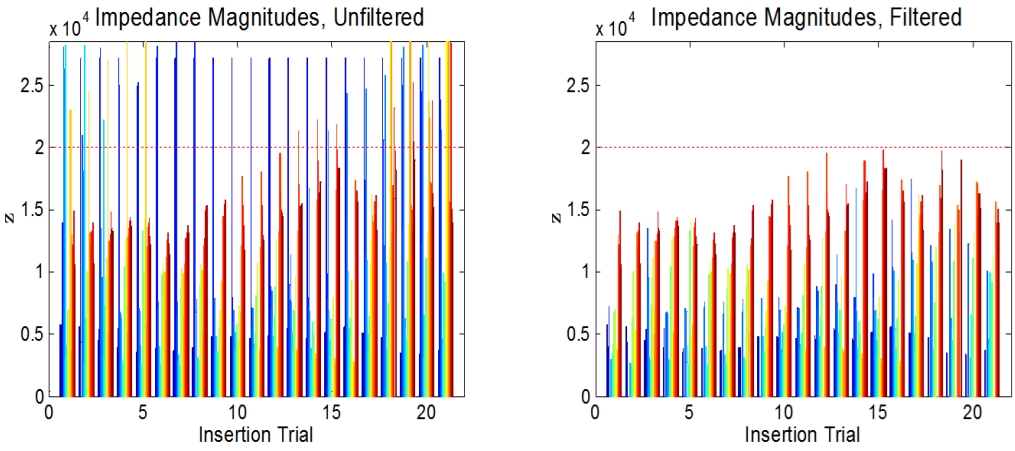

Figure VII.7: Impedance averages in cadaveric specimens. Bins are organized by electrode channel. Each bin contains a set of bar plots covering values through all 22 experiments

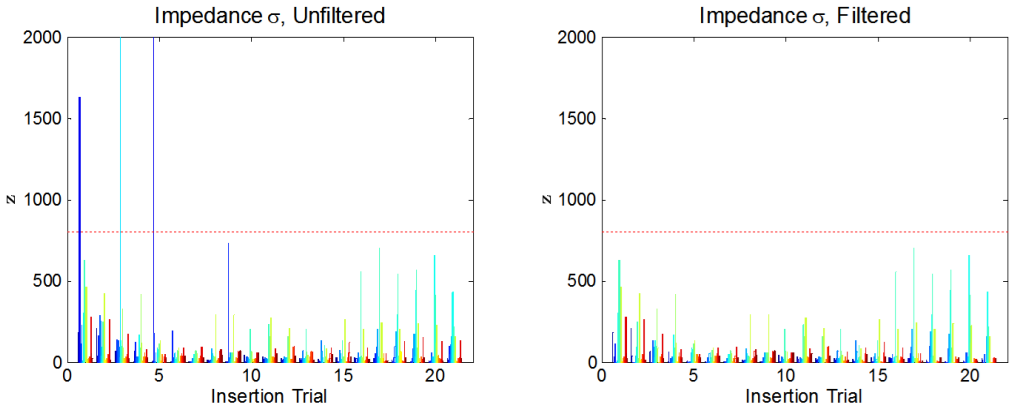

Figure VII.8: Impedance standard deviations in cadaveric specimens. Bins are organized by electrode channel. Each bin contains a set of bar plots covering values through all 22 experiments

Removal of outlying signals eliminated almost 20% of the measurements and without elimination of these measurement faults, results can be significantly altered. The electrode channels removed from each trial were not consistent and suggest that unaccounted factors in the process could be responsible rather than a systemic fault in the device. The vast majority of the filtered signals (68/73) were from open circuit measurements. A likely cause could be the presence of air in the ST which would raise impedances to open circuit magnitudes in an unrepeatable way between insertion trials.

A 3-way, two sided ANOVA test was applied to the filtered data set, evaluating significance of the PEA used, bone specimen, and insertion technique employed. Differences from each factor were considered significant with $\rho < 0.025$. While the differences are significant, ANOVA does not provide insight of factors which lead to discernment of electrode position.

The next processing step was to normalize the differences on a per electrode pair basis among the three factors (bone, PEA, and technique used). We denote a particular pair of electrode contacts by the index $k = 1, ..., 21$. The average of impedance measurements across all experiments for the kth channel is denoted as $\bar{z}_k$ based on the filtered data set. The corrected impedance from a measurement z_k is defined as $\tilde{z}_k$ and removes the average impedance value from each channels measurements. It is calculated by the equation:

$$\tilde{z}_k = z_k - \bar{z}_k \tag{VII.3}$$

Figures VII.9, VII.10, and VII.11 show the corrected impedances separated by either electrode ID, bone specimen ID, or technique used. It can be seen in Figure VII.11 that there is a consistent separation between SIT and AOS techniques with

the AOS (closer modiolar proximity) impedance consistently higher than the SIT cases. When considering bone and the particular electrode used, the separation is not consistent.

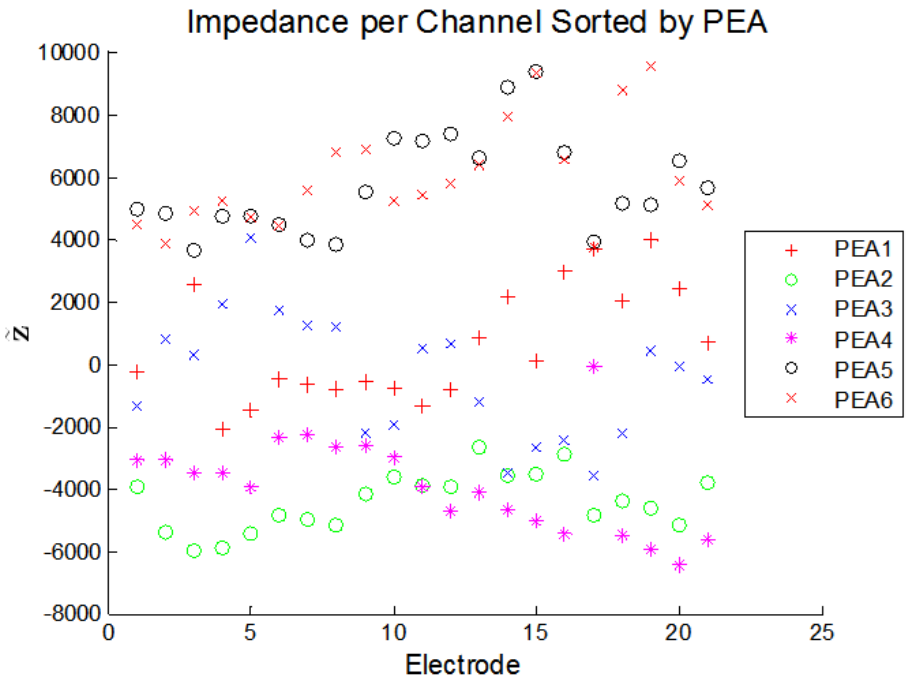

Figure VII.9: Separation of impedance readings based on PEA used.

It can be observed from Figure VII.10 that one cadaveric specimen (bone 4) had consistently higher impedances that the other three specimens. A definitive explanation of the higher impedances cannot be made from the data collected but higher baseline impedance does not bias the comparisons based on the PEA or technique used since equal number of insertions were performed on this bone across groups.

Figure VII.9 shows the separation of impedances by PEA used. There is no clear separation between PEAs across all electrodes. PEAs 5 and 6 have higher impedances due to their use in bone 4 but also show no clear difference between each other. While the electrode array selected can influence the magnitude of impedance, it does not appear to be a differentiating factor.

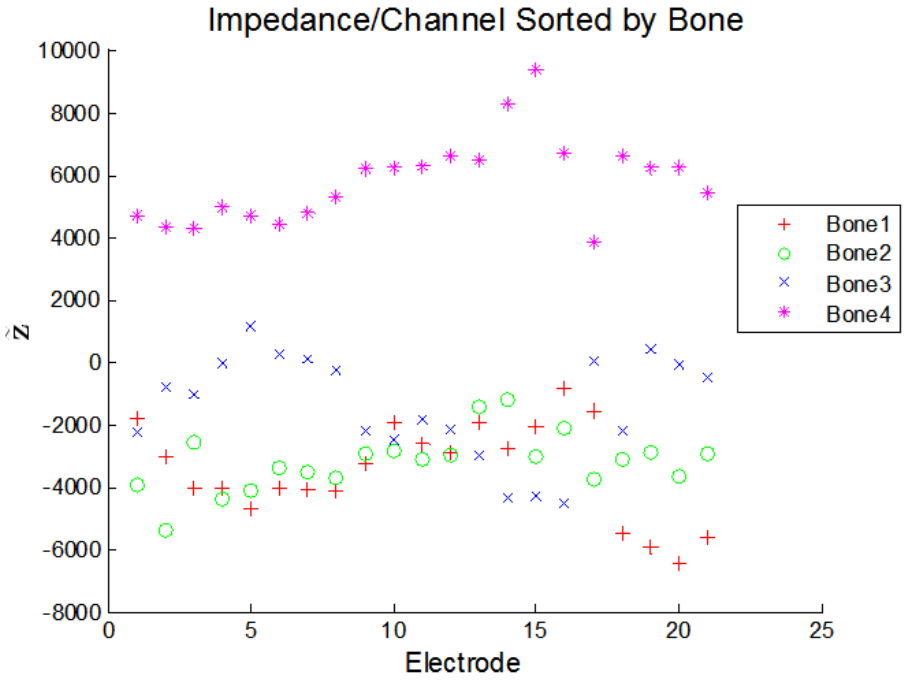

Figure VII.10: Separation of impedance readings based on bone used.

When impedance measurements are separated by technique used, there is a strong separation of the groups about the average. The use of AOS technique, which should result in closer modiolar placement, has consistently higher impedance than the SIT technique across the majority of the electrode contacts. Since the PEA electrode contacts are half banded, there is a large conductive fluid path between contact and therefore less impedance. The two most proximal electrode contacts (1 and 2) do not show clear separation. Since they are the closest to the entrance into the ST, their placement is governed more by the placement of the cochleostomy than the technique used during insertion. The most distal electrode contacts show the largest separation which may be attributed to their location in the ST far past the basal turn. Also, the magnitude of separation is over $2k\Omega$ at the distal channels which provides good discrimination with per channel standard deviations typically below 200Ω as seen in Figure VII.8.

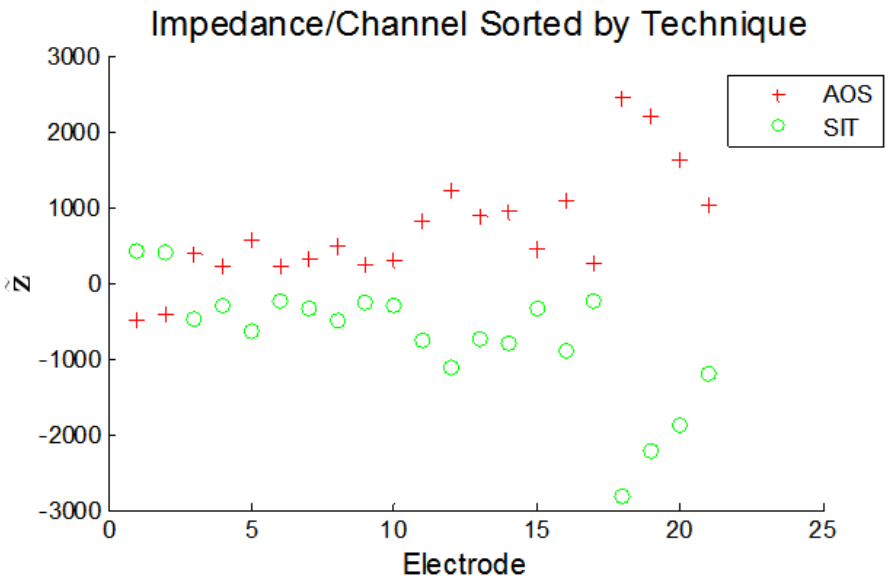

Figure VII.11: Separation of impedance readings based on technique used.

The conclusion drawn from this experiment is that bipolar impedance measurements in bone behave similarly to what was seen in the phantom model. As electrode contact pairs are drawn toward the modiolus the impedance measurement rises. Since the goal of proper PEA insertion is to maintain close modiolar contact, the impedance readings can be used as a proximity sensor to help coordinate the actuation of the stylet. Before developing the admittance control law, these findings were compared against a computational model of the impedance conductive path that is presented in the next section.

VII.3 Numerical Model for Bipolar Impedance

The experiments presented in the previous sections provide empirical evidence that bipolar impedance can be used to detect changes in modiolar proximity in a PEA. However, the measurement methods in the phantom model introduce considerable measurement noise (from photo registration and digitization errors) on top of an impedance measurement that also has variations. Before developing a control law, a

more reliable model of the conductive behavior is necessary. The problem is stated as the following; find the electrical impedance between two electrode contacts separated by a conductive fluid medium of known conductivity.

Electrical impedance through fluid volume can be treated as a quasistatic problem for human hearing frequency ranges [47, 83]. As such the electric field potential can be modelled using the Poisson equation:

$$\nabla^2\phi = \frac{i}{\sigma} \tag{VII.4}$$

where ϕ is the field potential, i is the charge density, and σ is the conductivity of the fluid. This form of the electrostatic solution assumes an isotropic and homogeneous fluid. If there is no free charge in the fluid ($i = 0$)then (VII.4) reduces to the Laplace equation.

$$\nabla^2\phi = 0 \tag{VII.5}$$

The domain of the problem is illustrated in Figure VII.12 in a two dimensional representation. This 2D assumption has worked in the preliminary empirical model and greatly reduces the computational burden. The domain is enclosed by a continuous curve $C = C_1 \bigcup C_2 \bigcup C_3 \bigcup C_4 \bigcup C_5 \bigcup C_6$ and contains adjacent electrode contact surfaces (C_1 and C_3), the silicone body between contacts (C_2), tangent lines to the modiolus (C_4 and C_6), and the modiolar wall (C_5). The volume of conductive fluid is considered irregular trapezoidal based on the measurements taken from the phantom model experiments. Local curvature between adjacent electrode contacts is not significant to the shape of the domain for the PEA used. The parameter h is the shorter electrode to modilous distance and the angle α specifies the shape of the trapezoid.

Along the boundary, either the potential or the flux can be specified but not both.

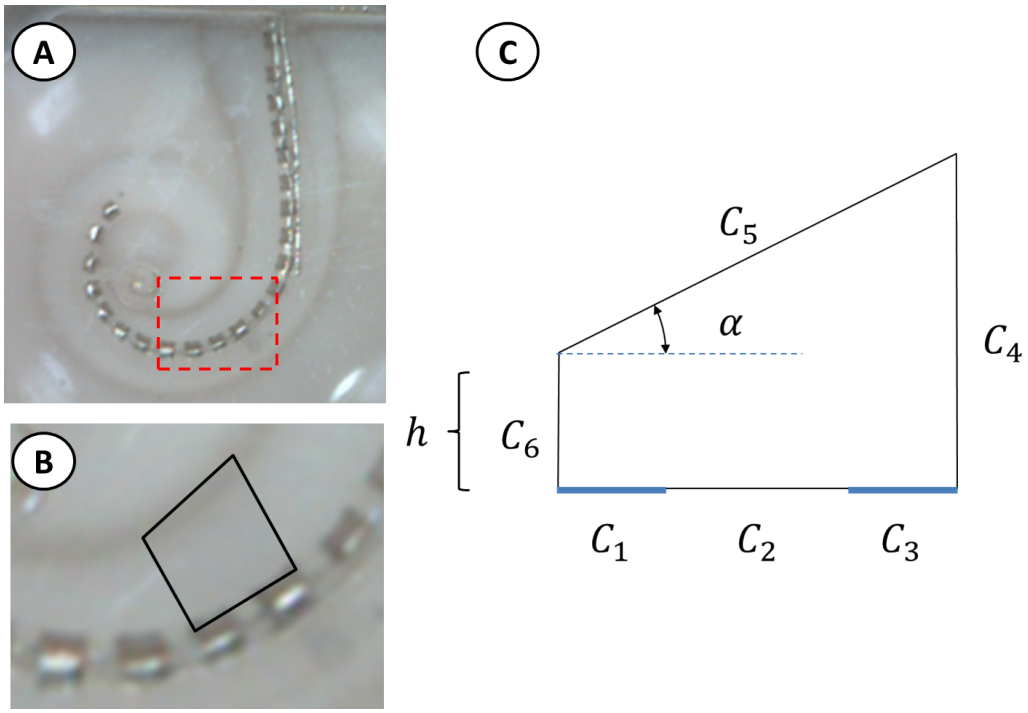

Figure VII.12: Two dimensional impedance domain. (A) Microscope image of PEA inserted in a phantom model. (B) Example of the irregular trapezoid area for the impedance domain between to adjacent electrode contacts. (C) The domain model parameterized by h and α.

In order for numerical solutions to converge properly at least one boundary must be Dirichlet and specify potential. In this problem, the boundary C_1 is treated as a current source and the boundary C_3 is a constant potential sink. All other surfaces prescribe no net current flux through their boundaries. These boundary conditions (BC's) are summarized in the following equations:

$$\begin{aligned} \frac{d\phi}{dn}|_{C_1} &= \frac{J}{\sigma} \\ \phi|_{C_3} &= 0 \\ \frac{d\phi}{dn}|_{C_i} &= 0, \quad i = 2, 4, 5, 6 \end{aligned} \tag{VII.6}$$

where σ is the fluid conductivity and J is the current density through the boundary.

The derivative $\frac{d\phi}{dn}$ is the change in potential normal to the surface. Current density is a function of the total current i_k through the k'th boundary divided by the arc length L_k of the k'th boundary. To compute the impedance Z, Ohm's law may be applied along the source electrode electrode curve:

$$z = \frac{\int_{C_1} \phi ds}{i_1 L_1} \tag{VII.7}$$

where $i_1 = 75\mu A$ is the total current, L_1 is the length of the curve C_1 and $s \in [0, L_1]$ is the arc length parameterization of the curve.

There are several methods of solving (VII.5) given the BC's in (VII.6). Finite difference and finite element solutions are possible candidates but even in 2D they require meshing of the interior of the domain which results in thousands of evaluation nodes. The potential field inside the domain is not needed to compute the impedance between the electrode contacts. The Boundary Element Method (BEM) is a numerical approximation method that can provide the required information without evaluating the PDE inside the domain during the solution process.

The Boundary Element Method

The BEM is a modelling technique to solve a PDE as a line integral on the domain boundary, from which the solution inside the domain can be extrapolated. An introductory text by Ang [5] details the formulation of the BEM for a variety of problems. Critical equations in the computation are reviewed here with the details of the derivations left to Ang's book. Also, Zhou provided solutions for electric and magnetic static BEM problems with anisotropic and isotropic material conditions [131].

The major advantage of BEM's is the reduction of computation time. Only the perimeter of the domain must be descretized which greatly reduces the time required

to mesh the domain in comparison to finite element or finite difference solutions. Also, the solution to the 2D Laplace equation can be obtained through a direct linear solution [5] removing costly iterative steps used in PDE solutions like the shooting method. However, if the goal is to compute solutions within the domain, the computational advantage of the BEM is quickly lost.

Where BEM's have the greatest difficulty is in problems where the material contained within the domain is not homogeneous. This is not a concern in this particular application as the saline solution is assumed to have a constant conductivity property.

To begin constructing the solution to (VII.5) we begin by a change of coordinates to a polar representation where $x = r\cos(\theta)$ and $y = \sin(\theta)$ and $\phi(x, y)$ becomes $\psi(r, \theta)$. The fundamental solution to the Laplace equation can then be written as:

$$\psi(r) = A\ln(r) + B \tag{VII.8}$$

and the cartesian solution through substitution becomes:

$$\phi\left(x, y\right) = A\ln\sqrt{x^2 + y^2} + B \text{ for}(x, y) \neq (0, 0) \tag{VII.9}$$

To remove the constants A and B a shift of coordinates to the origin by (ζ, η) yields the final form of the fundamental solution:

$$\Phi\left(x, y; \zeta, \eta\right) = \frac{1}{4\pi}\ln\sqrt{\left(x - \zeta\right)^2 + \left(y - \eta\right)^2} \text{ for}(x, y) \neq (\zeta, \eta) \tag{VII.10}$$

Assuming that a region R is encircled by the curve C, the reciprocal relation is used to convert the solution throughout the domain R into a line integral along C. The reciprocal relation states that if ϕ_1 and ϕ_2 are both solutions to the PDE over R

then the following holds true:

$$\int_C \left(\phi_2 \frac{\partial \phi_1}{\partial n} - \phi_1 \frac{\partial \phi_2}{\partial n} \right) ds(x,y) = 0 \tag{VII.11}$$

where n is the curve normal.

To find the BEM solution integral, equation (VII.10) is used in (VII.11) to calculate $\phi(x,y)$ along the domain boundary C. The final integral solution becomes:

$$\lambda(\zeta,\eta)\phi(\zeta,\eta) = \int_C \left[\phi \frac{\partial}{\partial n} \left(\Phi(x,y;\zeta,\eta) \right) - \Phi(x,y;\zeta,\eta) \frac{\partial}{\partial n} \left(\phi(x,y) \right) \right] ds(x,y) \tag{VII.12}$$

where

$$\lambda(\zeta,\eta) = \begin{cases} 0 & \text{if } (\zeta,\eta) \notin R \bigcup C, \\ 1/2 & \text{if } (\zeta,\eta) \text{ lies on smooth part of } C, \\ 1 & \text{if } (\zeta,\eta) \in R \end{cases} \tag{VII.13}$$

The next step is to discretize the curve C into segements, along each segment solution of (VII.12) is found. An example of the discretization is shown in Figure VII.13. Each curve segement C_i is broken into smaller elements with index k and expressed as $C_{i(k)}$. The index k does not reset on each sub curve and the model has a total of M elements (i.e. $k = 1, ..., M$). Each element has a normal unit vector $\hat{\mathbf{n}}_{(k)}$, length $L_{(k)}$, start point $\mathbf{x}_{0,(k)} = \left[x_{0,(k)}, y_{0,(k)} \right]^T$, and end point $\mathbf{x}_{1,(k)} \left[x_{1,(k)}, y_{1,(k)} \right]^T$. The potential and flux are considered constant across the element and evaluated at the midpoint $\mathbf{x}_{m,(k)} \left[x_{m,(k)}, y_{m,(k)} \right]^T$ of each element.

Using the constant value elements, the approximate solution to the PDE can be

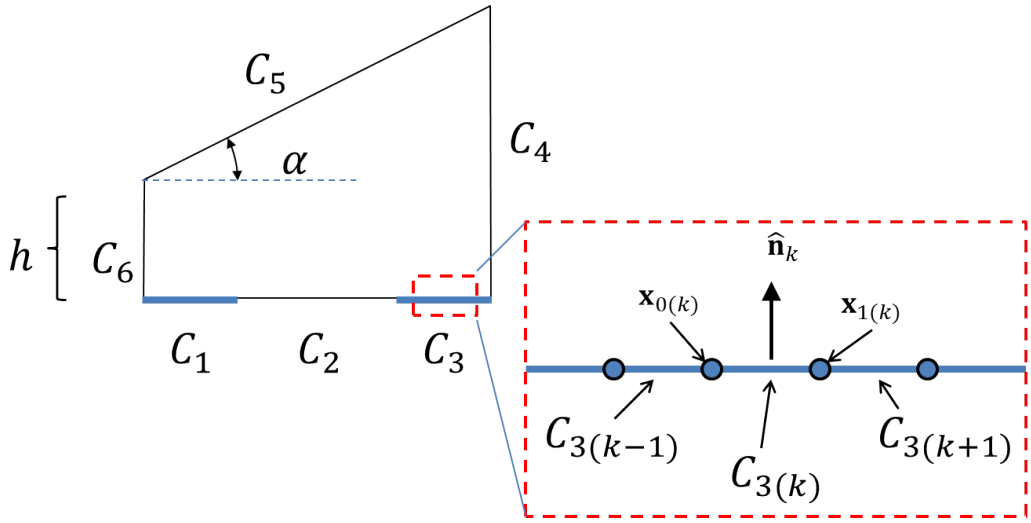

Figure VII.13: BEM element descretization.

found by solving the linear equation:

$$\mathbf{Au} = \mathbf{r} \tag{VII.14}$$

where $\mathbf{A} \in \mathbb{R}^{M\times M}$ is the integral coefficient matrix, $\mathbf{r} \in \mathbb{R}^{M\times 1}$ is a vector of the specified BC values and $\mathbf{u} \in \mathbb{R}^{M\times 1}$ is a vector of the unknown compliment boundary values to the BC's. To compute the coefficients of (VII.14) the following functions must be evaluated sequentially for each element with the final goal of having the

terms $F_{1,(k)}$ and $F_{2,(k)}$ known for each element:

$$A_{(k)} = {L_{(k)}}^2 \tag{VII.15a}$$

$$B_{(k)}(\zeta,\eta) = 2L_{(k)}\left(-n_{y,(k)}\left(x_{0,(k)}-\zeta\right)+n_{x,(k)}\left(y_{0,(k)}-\eta\right)\right) \tag{VII.15b}$$

$$E_{(k)}(\zeta,\eta) = \left(x_{0,(k)}-\zeta\right)^2+\left(y_{0,(k)}-\eta\right)^2 \tag{VII.15c}$$

$$T_{(k)} = 4A_{(k)}\,E_{(k)}(\zeta,\eta) - B_{(k)}(\zeta,\eta)^2 \tag{VII.15d}$$

$$Q_{(k)} = \begin{cases} 0, & \text{if } T \le 0 \\ \sqrt{T}, & \text{otherwise} \end{cases} \tag{VII.15e}$$

$$W_{(k)} = \begin{cases} 0, & \text{if } T \le 0 \\ \arctan\frac{2A_{(k)}+B_{(k)}}{Q_{(k)}} - \arctan\frac{B_{(k)}}{Q_{(k)}}, & \text{otherwise} \end{cases} \tag{VII.15f}$$

$$F_{2,(k)} = \begin{cases} 0, & \text{if } T \le 0 \\ W_{(k)}L_{(k)}\left(\frac{n_{x,(k)}*\left(x_{0,(k)}-\zeta\right)+n_{y,(k)}*\left(y_{0,(k)}-\eta\right)}{\pi Q_{(k)}}\right), & \text{otherwise} \end{cases} \tag{VII.15g}$$

$$\begin{aligned} F_{1,(k)} = \frac{L_{(k)}}{4\pi}\Bigg[&2\left(\ln L_{(k)}-1\right) - \frac{B_{(k)}}{2A_{(k)}}\ln\left|\frac{E_{(k)}}{A_{(k)}}\right| \\ &+\left(1+\frac{B_{(k)}}{2A_{(k)}}\right)\ln\left|1+\frac{B_{(k)}}{A_{(k)}}+\frac{E_{(k)}}{A_{(k)}}\right| + \frac{Q_{(k)}W_{(k)}}{A_{(k)}}\Bigg] \end{aligned} \tag{VII.15h}$$

In the case of constant elements, the series of calculations above use the inputs $\zeta = x_{m,(k)}$ and $\eta = y_{m,(k)}$. For each element, the average potential is denoted as $\bar{\phi}_{(k)}$ and the average flux as $\bar{p}_{(k)}$. The next step is the calculation of the elements in

(VII.14):

$$\mathbf{A}_{(j,k)} = \begin{cases} -F_{1,(k)}(x_{m,(j)}, y_{m,(j)}) & \text{if } \phi \text{ is specified over } C_{(k)} \\ F_{2,(k)}(x_{m,(j)}, y_{m,(j)}) - \frac{1}{2}\delta_{j,k} & \text{if } \partial\phi/\partial \text{ is specified over } C_{(k)} \end{cases} \tag{VII.16a}$$

$$\mathbf{r}_{(}j) = \sum_{k=1}^{M} b_{j,k} \tag{VII.16b}$$

$$b_{j,k} = \begin{cases} \bar{\phi}_{(k)} \left(-F_{2,(k)}(x_{m,(j)}, y_{m,(j)}) + \frac{1}{2}\delta_{j,k}\right) & \text{if } \phi \text{ is specified over } C_{(k)} \\ \bar{p}_{(k)} F_{1,(k)}(x_{m,(j)}, y_{m,(j)}) & \text{if } \partial\phi/\partial n \text{ is specified over } C_{(k)} \end{cases} \tag{VII.16c}$$

$$\delta_{j,k} = \begin{cases} 0 & \text{if } j \neq k \\ 1 & \text{if } j = k \end{cases} \tag{VII.16d}$$

$$u_{(k)} = \begin{cases} \bar{p}_{(k)} & \text{if } \phi \text{ is specified over } C_{(k)} \\ \bar{\phi}_{(k)} & \text{if } \partial\phi/\partial n \text{ is specified over } C_{(k)} \end{cases} \tag{VII.16e}$$

The solution for the vector $\mathbf{u}$ is linear and can be solved with a single inversion of the matrix $\mathbf{A}$. To determine the value of $\phi(x, y) \in R$ the values of $F_{1,(k)}(x, y)$ and $F_{2,(k)}(x, y)$ and compute the following:

$$\phi(x, y) = \sum_{k=1}^{M} q_{(k)} \tag{VII.17a}$$

$$q_{(k)} = \begin{cases} \bar{\phi}_{(k)} F_{2,(k)}(x, y) - u_{(k)} F_{1,(k)}(x, y) & \text{if } \phi \text{ is specified over element } k \\ u_{(k)} F_{2,(k)}(x, y) - \bar{\phi}_{(k)} F_{1,(k)}(x, y) & \text{if } \partial\phi/\partial n \text{ is specified over element } k \end{cases} \tag{VII.17b}$$

With the model complete, the next step was to verify the conductive model.

BEM Impedance Model Results

The space of parameters input into the BEM model are listed in Table VII.2. The goal was to determine if impedance as a function of fluid volume was a suitable model and to determine if the power law from equation (VII.1) empirically derived from phantom insertions captures the realistic physics.

Table VII.2: BEM Model Input Parameters

Parameter	Value	Units
h	$[0.1, 1]$	mm
α	$[0, 1]$	radians
σ	16	S/cm
i	75	μA
L_1	0.2	mm
L_2	0.42	mm
L_3	0.2	mm
L_4	$h + 0.82 \tan \alpha$	mm
L_5	$0.82/\cos \alpha$	mm
L_6	h	mm

Due to the constant element assumption used in the model formulation, the accuracy of the model is a function of the elements in a segment and is denoted as $N_{resolution}$. Curve C_1 is the baseline reference for the number of elements in each curve. Table VII.3 shows the relative element ratio compared to curve C_1. The convergence test repeated the impedance model solution with the parameters $h = 1$ and $\alpha = 0$ for C_1 element counts ranging from $N_{resolution} = 20$ to 80. The convergence of the solution is shown in Figure VII.14. It can be seen that after 25 elements the change in the expected value is less the 0.4%. A final value of $N_{resolution} = 30$ elements for curve C_1 was selected for the model. As can be inferred from Table VII.3, the total number of elements in the model was 270.

Once the number of elements was selected the model was calculated as a function

Table VII.3: Element count ratio

Curve	C_1	C_2	C_3	C_4	C_5	C_6
Ratio	1	2	1	1	3	1

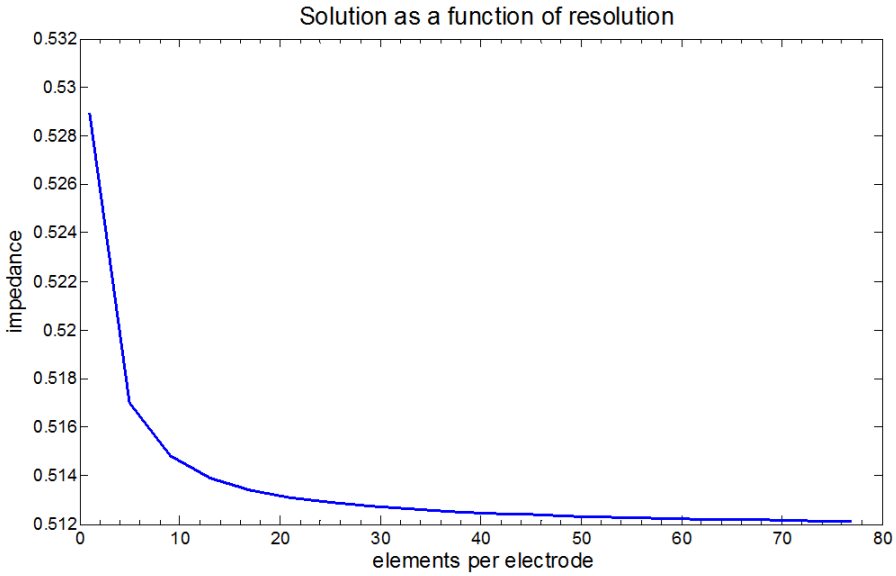

Figure VII.14: Convergence of BEM solution.

of h and α. Equation (VII.7) specifies that impedance is evaluated as the average potential divided by the total current through the boundary C_1 and follow Ohm's Law. From the BEM solution this defines the impedance z as:

$$z = \frac{\frac{1}{N_{resolution}} \sum_{k=1}^{N_{resolution}} \bar{\phi}_{(k)}}{i} \tag{VII.18}$$

Figure VII.15 presents a plot of these results using a 3D contour. There is a noticeable effect of α on the impedance z but its effect is most prominent at small values of h.

The original curve fitting for the impedance from observations applied a power law fitting based on the enclose area (or volume assuming uniform depth) of conductive fluid. The results shown in Figure VII.15 were compressed into a 2D feature space

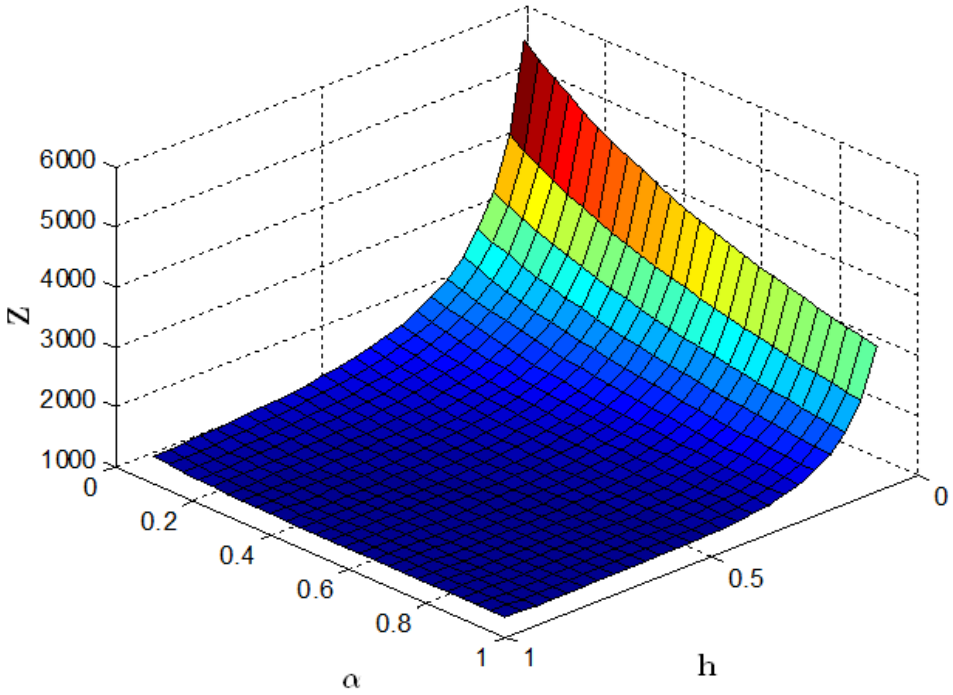

Figure VII.15: Impedance based on h and α.

based on the domain area A_R as a function of both h and α. The resulting 2D plot of impedance versus domain area is shown in Figure VII.16.

The individual impedances based on h and α are shown as a scatter plot with the solid line showing the model fitting. Again several models were fit to the data with the power law providing the best fit with a correlation coefficient of $R^2 = 0.9964$. The root mean square error for the fitting was 46Ω. Table VII.4 shows the coefficients used in the power law and includes the 95% confidence interval for the fit.

Table VII.4: Model Based Impedance Parameters
Model: $z(A_R) = a\,(A_R)^b + c$

Parameter	Nominal Value	Range (95% Confidence)
a	83.2	$[79.84, 86.57]$
b	-1.317	$[-1.331, -1.302]$
c	1149	$[1139, 1159]$

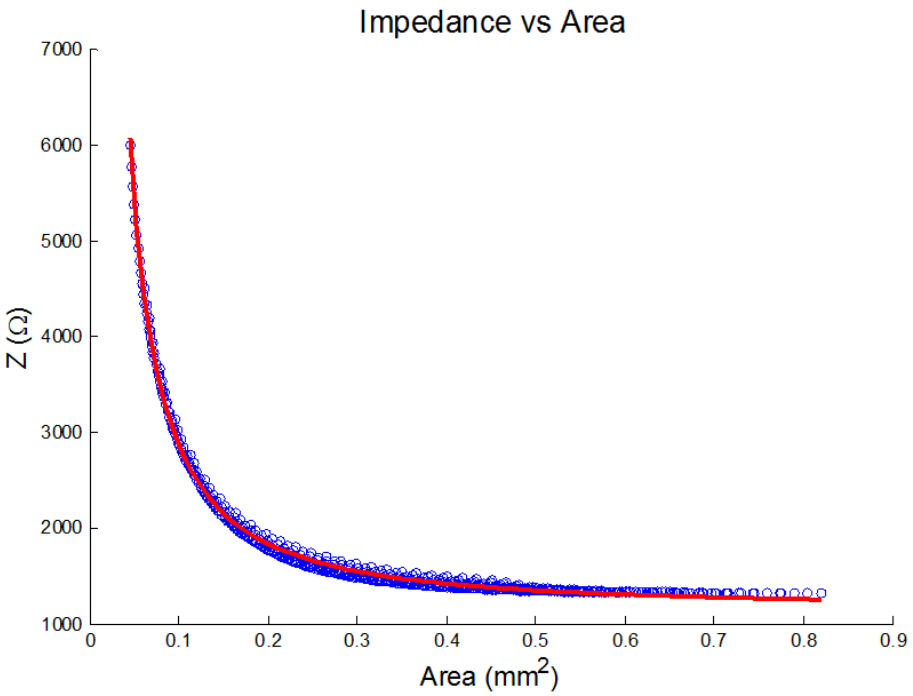

Figure VII.16: Modeled impedance based vs area.

Based on the small distribution range of the fitting and an RMS error below the expected measurement noise, this model with the nominal coefficients from Table VII.4 are used in the control law to be presented in the next section. The final impedance model is then written as:

$$z(A_R) = a\,(A_R)^b + c \tag{VII.19}$$

The coefficient values found from the phantom model experiments tended to have a lower exponent magnitude and the value of the coefficient a was higher than the values computed from the BEM model. When the fitting as shown in Figure VII.16 is compared to the fitting shown in Figure VII.3 there are similar key characteristics. Both fittings have a measurable impedance range of approximately $2k\Omega$ between areas of 0.1 and $0.4mm^2$. The fits also see little change for areas greater than $0.4mm^2$. Since

the model matches the behavior of real insertion data, equation (VII.19) provides a fast method based on a computational model to estimate impedance to proximity behavior.

VII.4 Impedance Guidance for Electrode Steering

In this section an admittance law for stylet actuation is proposed and tested utilizing real time measurements of bipolar impedances from the PEA. Based on the results presented in the previous sections of this chapter the strategy for the bipolar impedance control law was to use knowledge of the PEA kinematics presented in Chapter II to guide the rate at which the stylet is adjusted based on the rate of impedance change.

The impedance measurements are defined in the vector $\mathbf{z} \in \mathbb{R}^p$, where $1 \leq p \leq 21$ is the number of electrode pairs used to guide insertion. If a series of electrodes are adjacent to each other without skipping contacts, then the total number of electrodes used in the measurement is $p + 1$.

The actual impedance measurement taken by the CIM software includes a constant measurement bias based on internal resistances in the PEA's electronic assembly. For each electrode channel, this bias is different and expressed by the vector $\mathbf{r} \in \mathbb{R}^p$. If the raw measurement taken from the CIM is denoted as $\tilde{\mathbf{z}} \in \mathbb{R}^p$ then the true inter-electrode impedance is:

$$\mathbf{z} = \tilde{\mathbf{z}} - \mathbf{r} \tag{VII.20}$$

Fortunately the values in the vector $\mathbf{r}$ can be easily calibrated by immersing the electrode array in saline and sampling impedances. So long as a minimum distance of a couple of millimeters from any surface and the electrode contacts is maintained

during calibration, the result should obey the relationship:

$$\tilde{\mathbf{z}}_i - \mathbf{r}_i = c, \qquad \forall i = 1, ..., p \tag{VII.21}$$

where c is the impedance model constant from Table VII.4 and the index i is used to denote the i'th elements in vectors $\tilde{\mathbf{z}}$ and $\mathbf{r}$.

The first step in designing the admittance law was to formulate the relationship between the rate of change in stylet actuation $\dot{q}_s$ and the rate of change in the set of bipolar impedances $\dot{\mathbf{z}}$. Once this relationship is known it is inverted so that a change in impedance leads to a recommended change in velocity.

From the discussions in the previous sections it was determined that impedance can be modelled as a function of the 2D projected area of fluid volume between the electrode contacts. Figure VII.17 presents a sketch of the domain for a single pair of electrodes. The electrodes are separated by a constant pitch defined as Δs and the k'th electrode is at a distance d_k from the modiolus. A trapezoid approximation is assumed to define the area:

$$A_k = \frac{1}{2}\left(d_k + d_{k+1}\right)\Delta s \tag{VII.22}$$

This assumption is valid so long as curvature between the adjacent electrodes is small and the distance from the modiolus is not excessively large. Since the scala tympani is a constricted path with moderate curvature, these assumptions were considered valid for a control model.

The k'th electrode contact has a position ${}^{E}\mathbf{p}_e$ and instantaneous velocity ${}^{E}\dot{\mathbf{p}}_e$, expressed in PEA frame $\{\mathbf{E}\}$ through a Jacobian $\mathbf{J}_{pq_s}$ defined previously in equation

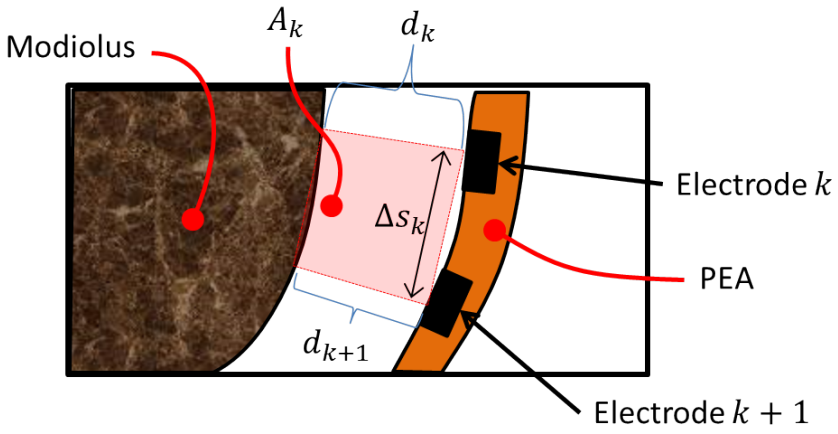

Figure VII.17: Model of impedance domain for control.

(II.8) such that:

$$^{E}\dot{\mathbf{p}}_{e,k} = \mathbf{J}_{pq_s}\dot{q}_s \tag{VII.23}$$

where $\{\mathbf{E}\}$ is the PEA frame as shown in Figure II.4 and $\dot{\mathbf{p}}_{e,k}$ is the velocity of the PEA curve at the k'th electrode contact.

At each electrode contact a normal vector $\hat{\mathbf{n}}_k$ is defined with its direction locally perpendicular to the PEA curve and pointing toward the modiolus:

$$\hat{\mathbf{n}}_k = [\sin(\theta_k), -\cos(\theta_k), 0]^T \tag{VII.24}$$

This implies that with the assumptions in (VII.22) that the rate of change in area A_k can be written as:

$$\frac{dA_k}{dq_s} = \frac{\Delta s}{2}\frac{d}{dq_s}(d_k + d_{k+1}) = \frac{\Delta s}{2}\left(\hat{\mathbf{n}}_k^T\mathbf{J}_{pq_s}(s_k) + \hat{\mathbf{n}}_{k+1}^T\mathbf{J}_{pq_s}(s_{k+1})\right) \tag{VII.25}$$

With a relationship between the stylet actuation and change in the fluid domain established, the next step is to derive a relationship between the change in the fluid

domain and impedance. When differentiating (VII.2) with respect to time the following result is achieved:

$$\dot{z}_k = \left(abA_k^{b-1}\right) \frac{dA_k}{dq_s} \dot{q}_s \tag{VII.26}$$

The area A_k must be estimated by the impedance measurements. Rewriting (VII.19) to find area as a function of impedance results in:

$$A_k = \left(\frac{z_k - c}{a}\right)^{-b} \tag{VII.27}$$

and when substituted into (VII.26) yields the final impedance Jacobian denoted as $\mathbf{J}_{zq_s} \in \mathbb{R}^{p\times 1}$. The k'th element of $\mathbf{J}_{zq_s}$ is denoted as $\mathbf{J}_{zq_s(k)}$and is defined as:

$$\mathbf{J}_{zq_s(k)} = ab\left(A_k\right)^{b-1} \frac{dA_k}{dq_s} = ab\left(\frac{z_k - c}{a}\right)^{b-b^2} \frac{dA_k}{dq_s} \in \mathbb{R}^{p\times 1} \tag{VII.28}$$

The final expression relating $\dot{\mathbf{z}}$ to $\dot{q}_s$ is then written as:

$$\dot{\mathbf{z}} = \mathbf{J}_{zq_s} \dot{q}_s \tag{VII.29}$$

What can be seen from (VII.29) is that the inverse Jacobian $\mathbf{J}_{zq_s}^{-1}$ acts as a weighted average of the change in impedance measurements to the change in stylet actuation.

In addition to the differential relationship of equation (VII.29) there are additional restrictions on the corrective action allowed to be applied on the stylet. The first is that the value of $\dot{q}_s$ must be positive; the stylet is not allowed to be inserted back into the electrode. If the value of $\dot{q}_s$ is calculated to be less than zero it is set to zero. The second restriction is on when the control law takes effect as a function of insertion depth q. This restriction is identical to the one implemented with the force based impedance law (VI.8) and will be covered again here. The final adjustment of

the stylet is denoted as $q_{s,admit}$:

$$q_{s,admit} = -\gamma(q)\mathbf{J}_{zq_s}^{-1}\dot{\mathbf{z}} \tag{VII.30}$$

and the function $\gamma(q)$ is defined by a range of $[\gamma_1, \gamma_2]$ such that:

$$\gamma(q) = \begin{cases} 0, & d \leq \gamma_1 \\ \frac{q-\gamma_1}{\gamma_2-\gamma_1}, & \gamma_1 < q < \gamma_2 \\ 1, & q \geq \gamma_2 \end{cases} \tag{VII.31}$$

The parameters γ_1 and γ_2 set the range for where the impedance control law starts in the same manner as the force based admittance law. This new admittance control law replaces the one presented in Chapter VI as shown in Figure VII.18. Force admittance is still applied to correct lateral misalignment but stylet adjustment is driven completely by bipolar impedance measurements.

The following section presents a set of preliminary experiments to evaluate the control law.

Evaluation of Bipolar Impedance Admittance Controller

All insertion experiments were performed using the spatial insertion system as shown in Figure VII.19 (A). The insertion system had an attachment added to support the connection of the Contour Advance electrode array to the Freedom Nucleus system and is shown in Figure VII.19 (B).

A new cochlea phantom was fabricated for these experiments as shown in a CAD rendering in Figure VII.19 (C). The geometry of the scala tympani chamber was taken directly from the Cochlear training phantom (left side temporal bone) so that results would be comparable to other phantom model experiments. The purpose of

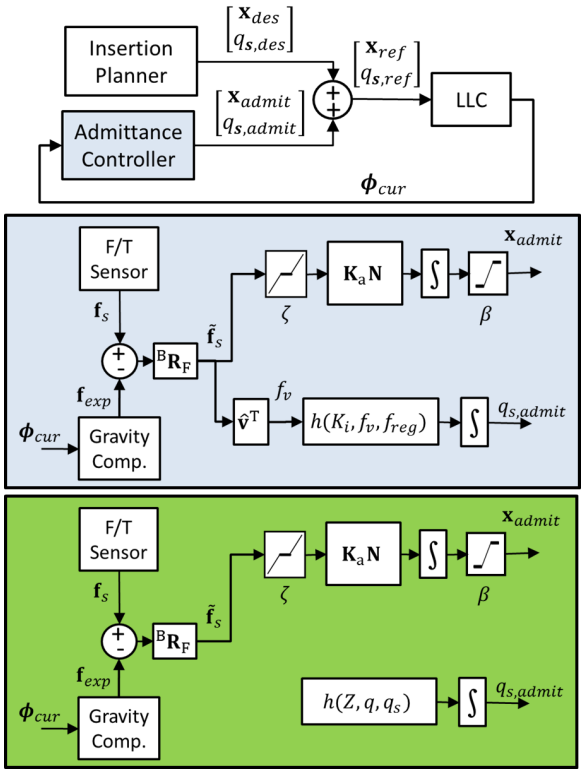

Figure VII.18: Impedance hybrid admittance controller. Variants of the admittance controller are shown in the blue and green boxes. The blue box shows the original force-based admittance controller. Adjustment to the actuation of the stylet is no longer dependent on insertion force and uses impedance measurements as shown in the green box.

remaking the phantom model was so that fluid would not leak out of the model during experimentation. The other benefit of the new model is that it is easier to register the model to the image due to its high contrast with the aluminum frame.

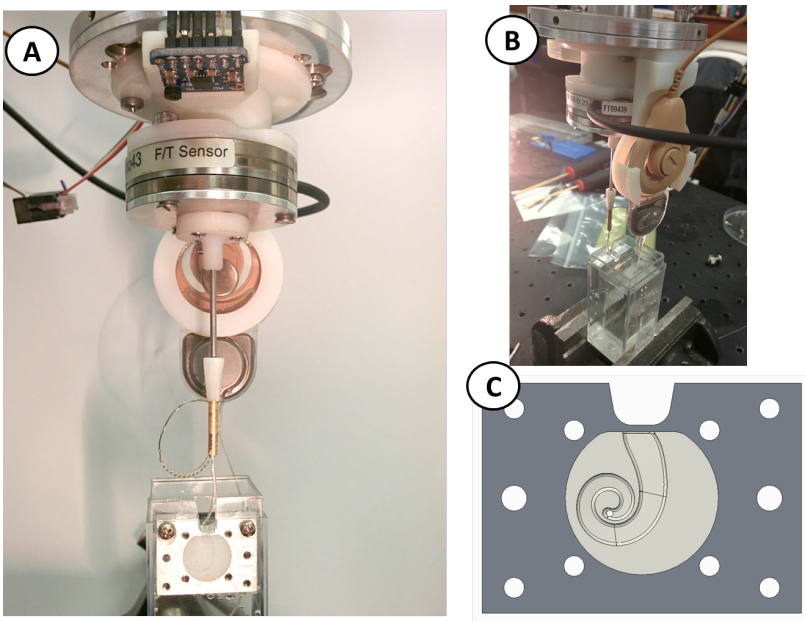

Figure VII.19: Experimental setup for bipolar impedance guidance. (A) Spatial insertion system set over cochlea phantom submerged in saline. (B) Attachment for supporting the connection between the *Contour Advance* PEA and the *Nucleus freedom* communication hardware. (C) CAD rendering of new cochlea phantom model.

The insertion tests were broken into two parts to test the control law. In the first set of experiments, the insertion was paused in 1mm increments so that data could be checked and recorded and the corrective action on stylet actuation could be applied. These experiments are referred to as the *discontinuous insertions*. The purpose of this incremental stepping was to preserve the electrodes for as many insertions as possible. If there was an error in the untested process it could be stopped before damaging the electrode. A secondary reason for pausing the insertions was to allow for higher quality images to be recorded.

Each discontinuous insertion experiment was conducted in the following manner.

The robot gripper was registered to the cochleostomy site and a PEA was then loaded into the gripper. Once the robot guided the tip of the electrode to the cochleostomy, an estimation of the PEA calibration matrix $\mathbf{A}$ was made and the insertion trajectory was calculated. At each incremental pause during the insertion, the current depth, impedance signal and stylet actuation were recorded. Based on this data, the control law output the desired corrective action to stylet actuation. After the correction was applied, a new measurement was taken and the insertion continued. Corrections would only be applied once for any insertion depth q.

A total set of 5 experiments were performed for this evaluation. Processing the results of the completed insertions began with looking at the modified control input during insertion. Figure VII.20 shows the pre-computed AOS actuation of the stylet (q_s) with respect to the depth of insertion (q). The solid blue line is the planned trajectory and the dashed traces show the corrected actuation based on the control law for each insertion. Vertical jumps in the traces are due to the fact that the insertion was paused in 1mm increments. It can be seen that the largest corrections are around the basal turn ($q = 6mm$ to $q = 8mm$) but that small corrections occur throughout the rest of the insertion.

The second set of experiments performed the insertions without stopping, denoted as *continuous insertion* in the following figures. This method is identical to the insertion procedure from the previous chapters. In this case the impedance guided insertion control law was updated at discrete steps in the insertion. At insertion intervals of $\Delta q = 0.5mm$ the admittance law was computed against the previous impedance measurements. The admittance evaluation using the sample index j is written as:

$$\delta q_{s,admittance,(j)} = \mathbf{J}^{-1}_{zq_s,(j)} \left[\mathbf{z}_{(j)} - \mathbf{z}_{(j-1)}\right] \tag{VII.32}$$

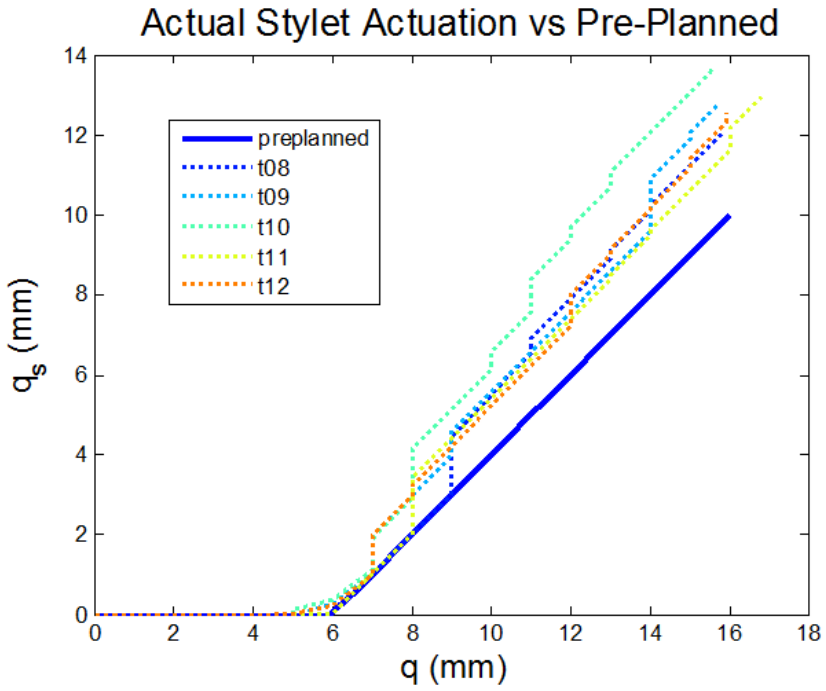

Figure VII.20: Adjustment to stylet actuation based on discontinuous impedance control law.

A plot of the stylet control action is shown in Figure VII.21. Corrections to the stylet actuation rate were fast in this mode although their was no visible seen in the resulting insertion forces. The majority of the corrective actions took place near the basal turn as expected.

To evaluate electrode placement, the geometry of the cochlea was first registered to the photo and then the electrode contact were segmented manually. The closest distance to the modiolar wall was also calculated. Examples of the segmentation are shown in Figure VII.22.

After segmenting all of the insertion data, a plots of all electrode contacts throughout the insertions was generated and is shown in Figure VII.23. From the set of 10 completed insertions it was clear that the robot inserted the PEAs without any contact to the lateral wall. In the continuous insertions, placement of the electrodes

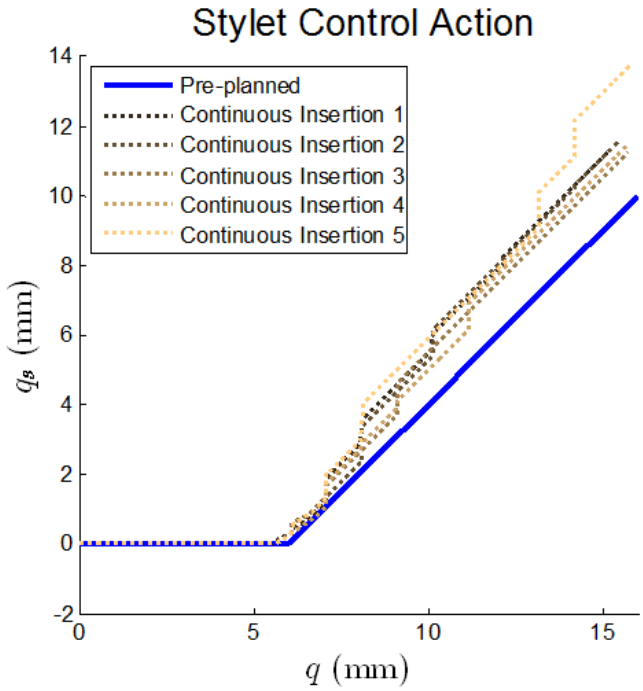

Figure VII.21: Adjustment to stylet actuation based on continuous impedance control law.

remained closer to the modiolus due to the more frequent updates of the impedance guided admittance control law.

The controller achieved the desired result, maintaining close modiolar proximity without relying on contact pressure against the lateral wall. There was one event in each set of experiments that warrant special attention. In the second discontinuous insertion there was one measurement in which the control law specified a corrective actuation of the stylet greater than $2mm$. The correction for that step was limited to $1mm$. The reason for this error comes from the inversion of Equation (VII.19) to estimate the fluid area. When the impedance approaches the far field conductivity levels, the power law generates a flat curve that is highly sensitive to small changes in impedance. Fortunately, there are practical limitations to the estimate of fluid volume. The work by Zrunek [133, 132] measured the width of the scala tympani

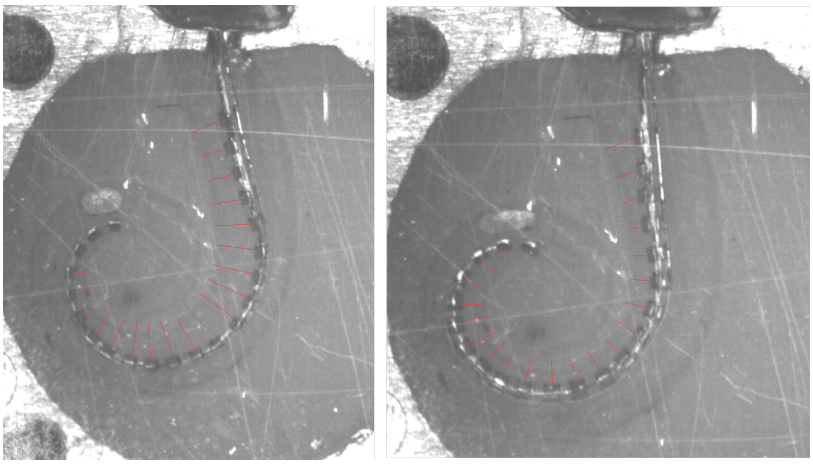

Figure VII.22: PEA placement during impedance guided insertion. The left figure shows electrode positions with discontinuous insertion. The right figure shows placement results with continuous motion throughout the insertion.

and given a PEA diameter of approximately $0.8mm$, the maximum expected fluid area has an estimated upper bound of $0.8mm^2$. This upper bound was applied to the continuous insertions when using Equation (VII.27).

Applying this area estimate bound was useful in the fifth continuous insertion experiment. During the insertion process the most distal electrode contact (electrode number 22) separated from the PEA body and folding back on its adjacent electrode (electrode number 21). As a result, the impedance on electrode channel 21 dropped below the baseline constant c from Equation (VII.19). Normally this would result in an exceptionally large area estimate from Equation (VII.27). Since the estimate was bounded, the admittance control was able to function using only three working channels. The failure of the distal electrode contract was not indicative of a fault in the PEA but rather continuous reinsertions (a total of 7) that is outside the allowable use of the CI in a clinical setting.

This particular fault during insertion highlights the utility of using changes in impedance, rather than raw values, to guide insertion. Once the contact shorted,

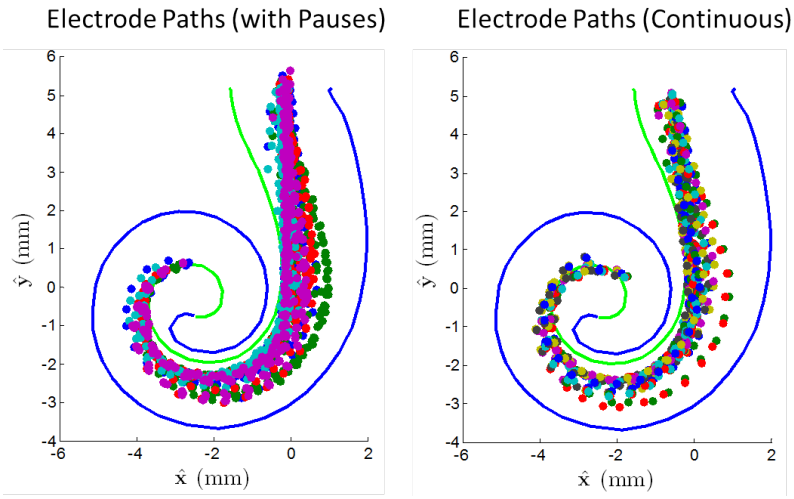

Figure VII.23: Locations of electrode contacts throughout insertions. The left side figure shows placement in insertions with discrete pauses. The right figure shows electrode placement for continuous insertion experiments

the change in impedance was negligible and could no longer influence the control law. If the admittance law had been based on absolute difference between current impedance and a target value, the controller would have continued to apply additional stylet actuation throughout the entire insertion.

VII.5 Conclusions

The work presented in this chapter has demonstrated strong evidence that bipolar impedance measurement sampled directly from the cochlear implant during insertion can be effectively used to guide insertion. Proper AOS technique is critical in taking advantage of the perimodiolar design but is difficult to execute perfectly in practice. The major contribution of this method of electrode guidance is that it does not require large and highly expensive capital equipment to be used like in works proposing magnetic, CT, or OCT guidance. The sensor modality is part of the implant's intrinsic function and does not add cost to the procedure. The guidance technique proposed in this chapter can be easily applied to non-robotic tools as well.

As a feedback modality, bipolar impedance can be useful in estimating electrode array placement before verification with radiological imaging. In monopolar stimulation, the bone and tissue properties play a role in the measured impedances which may degrade signal to noise performance. With bipolar measurements across adjacent electrodes, the fluid medium plays a dominant role and improves the ability to discern changes in placement.

The use of bipolar impedance for proximity feedback has a couple of limitations that must be addressed. The first is that it depends on the presence of a relatively conductively homogenous fluid medium. Without fluid immersion the impedance measurements are too high to be useful. Secondly, in our experiments electrode channels could become unstable or lose reading during insertion. This occurs due to disruption in the conductive path which is beyond the control of the surgeon. A larger series of studies across multiple electrode array designs would be required to determine reliability of acquiring meaningful measurements.

These problems are relatively minor and at worst could create situations where conclusions inferred from impedance information may not be clear. However, this work has shown that a CI device not specifically tuned to provide the proposed functionality still had sufficient resolution and bandwidth to make real time guidance using impedance measurements possible. An exciting future direction would be to add the capability of changing stimulation parameters during insertion and confirming electrode placement though quadrapolar stimulation modes. It should also be noted that although the BEM model was not used in realtime to estimate fluid volume it is sufficiently fast to do so and may be useful in future real time control models where multiple stimulation modes are simultaneously measured or where excitation frequencies make the electrostatic assumption no longer valid.

Chapter VIII

CONCLUSIONS

VIII.1 Summary of Findings

This dissertation has presented a body of work aimed at advancing the concepts of robot-assisted cochlear implant insertion. The organization of the dissertation follows a classical design approach beginning with quantitative task specification, moving to the development of physical hardware, and lastly implementing layers of control and error detection into the system.

The process of designing an implantation system began with the identification of quantitative specifications and performance metrics. Some of these metrics, such as desired insertion speeds and force, were available from the available literature. A contribution of this dissertation was in the measurement of additional metrics such as facial recess restrictions that have not been presented in prior works in a way useful for the development of new tools for CI insertion. A study of the perimodiolar electrode array kinematics also presented a compact method for modeling the kinematic behavior of a commercially available steerable implant. This modelling framework was also shown to be useful for estimating the kinematic behavior of PEA's without detailed calibration. Together with the access restrictions to the cochlea, a set of viable insertion trajectories were simulated to create a workspace specification for an automated CI insertion system.

Robotic insertion tool synthesis was derived from the task workspace and performance criterion. Prior works have developed systems with full spatial degrees of freedom for CI insertion or minimal degrees of freedom. Proposed in this work is a

system that bridges the complexity gap with a multidegree of freedom system that moves in the main insertion plane. Part of this mechanism's design is the inclusion of closed loop wire actuation to serve as the transmission between motor output and mechanism motion. The advantage of such a design comes from the benefit of being able to remotize the location of sensitive hardware from the area of the robot requiring harsh sterilization treatment. Using this transmission concept introduces kinematic coupling between parallel kinematic chains that affect stiffness and calibration of the mechanism to which solutions to these problems have been presented. Also explored in this work is how wire actuation can be used to construct compact and practical static balancing mechanisms.

In the present literature the proposed uses of robotics in the CI surgical procedure have relied heavily on preoperative imaging and rigid motion plan execution of electrode array insertion. This is not how surgeons approach the task and the work presented here developed a robotic insertion platform capable of adapting to uncertainties based on intraoperative real time measurements. All studies to the author's knowledge which use force measurements in CI insertion do so only as an evaluation metric for quality of insertion. The work presented here is the first to demonstrate the utility of force feedback as a viable method to make adjustments to CI insertions in real time. The proposed control architecture greatly reduces the burden of preoperative registration requirements with the added benefit of reducing time to deployment in a clinical setting.

In addition to demonstrating the utility of force feedback in guiding CI insertion, this work has presented a novel method of using bi-polar impedance feedback to facilitate corrections to electrode array steering. The control method takes advantage of the electrical conductivity of perilymph fluid found within the cochlea to act as a

range sensing modality for determining relative proximity of the electrode contacts to the modiolus. In this particular electrode array design, the goal is to maintain close proximity to the modiolus at all times throughout the insertion and bi-polar impedance measurements provide feedback at sufficient rates and accuracy to accomplish this task. The significant benefit of this approach is that corrections to electrode array actuation can be applied before the implant makes contact with intra cochlear structure and thus reduces risk of trauma. Force based methods can only attempt to mitigate the effect of undesirable electrode array contact after it has already begun.

VIII.2 Future Directions

There are numerous ways that the work presented in this dissertation can be expanded. In regards to wire actuated parallel robots there are several additional questions that need to be addressed. It was found that the idler pulley radii have a direct influence on end effector stiffness. The layout of the kinematic chains is the other factor that affects mechanism stiffness. Algorithmic investigation of how to optimize wire routing to achieve specific compliance characteristics could be very useful in specific applications. For example, it may be desirable for a device to be compliant in some directions but have high stiffness in others. A wire actuated parallel mechanism could achieve this in its structure rather than in feedback control.

The planar device proposed evaluated in this work may not be the conceptually optimal design for the CI insertion task. Out of plane insertion forces can be significant and the planar 3RPR design cannot compensate for this. A manipulator with three Cartesian degrees of freedom and one orientation degree of freedom in the insertion plane may be a superior design that takes full advantage of the hybrid force / position admittance controller discussed in this dissertation.

A large amount of work remains to develop intelligent tools for the insertion of

flexible implants, not limited to those used in CI surgery. An elastic mechanics model for the flexible implant was not needed for the control systems demonstrated in this work but may be needed for other implant designs. In the detection of insertion failures, there is a large amount of experimentation, including cadaveric studies, required to improve the robustness of the detection methods demonstrated in this work.

Lastly, impedance feedback for electrode navigation is an exciting new field to explore in the development of CI insertion systems. A single stimulation mode at a fixed frequency was used in this work but there is possibly new and useful information in other stimulation modes that can facilitate in electrode array placement. It may also be possible to measure CI placement completely through impedance and eliminate the use of radiological imaging in many cases. If a tool is tracking electrode array insertion progression externally, impedance feedback may be employed to locate the implant's location through probabilistic algorithms.

Appendix A

CALIBRATION OF FORCE / MOMENT TRANSDUCER UNDER GRAVITY LOADS

The insertion module carried by the F/T sensor exerts a wrench on the sensor that needs to be determined and subtracted from all readings so that the true wrench acting on the tool from the outside environment may be known. This initially unknown wrench is assumed to be composed of two components; the wrench from gravity acting on the center of gravity of the live load and a constant bias force. This bias wrench is partly due to the initial taring (unbiasing) of the F/T sensor and partly from the strain relief of connecting motor wires from the live load. Let the true wrench from gravity be $\mathbf{w} = \left[\mathbf{f}^T, \mathbf{m}^T\right]^T$ in the wolrd frame $\{O\}$, the observed wrench from the sensor be $\tilde{\mathbf{w}}$ in the sensor frame $\{F\}$ and the bias $\mathbf{b} = [b_x, b_y, b_z, b_{xx}, b_{yy}, b_{zz}]^T$ in the sensor frame $\{F\}$ such that:

$$^F\tilde{\mathbf{w}} = ^F\mathbf{w} + ^F\mathbf{b} \tag{A.1}$$

The orientation of the sensor with respect to the world frame will be designated $^O\mathbf{R}_F$ and the coordinates of the c.g. in FT sensor frame as $^F\mathbf{r}$. At any given point, assuming the end effector is at steady state, the sensor will measure a wrench from the mass of the payload under gravitational acceleration with a nominal value of:

$$^F\tilde{\mathbf{w}} = \begin{bmatrix} ^F\mathbf{f} \\ \\ ^F\mathbf{r} \times ^F\mathbf{f} \end{bmatrix} + ^F\mathbf{b} = \begin{bmatrix} \tilde{\mathbf{f}} \\ \\ \tilde{\mathbf{m}} \end{bmatrix} \tag{A.2}$$

The calibration is broken into two parts; the first uses the force data to find the mass of the live load and the force biases. Then this data is used to find the moment biases and the center of mass.

The solution is based on fitting spheres to point cloud data but in this case the sphere is a set of forces of constant magnitude rotated by ${}^{O}\mathbf{R}_{F}$. Assuming a mass m and a gravitational acceleration of magnitude g in the direction $\hat{\mathbf{n}} = [n_x, n_y, n_z]^T$, then the following linear relation holds:

$$a\,{}^{F}\tilde{f}_x^2 + b\,{}^{F}\tilde{f}_y^2 + c\,{}^{F}\tilde{f}_z^2 + d = -{}^{F}\tilde{f}_x^2 - {}^{F}\tilde{f}_y^2 - {}^{F}\tilde{f}_z^2 \tag{A.3}$$

where a, b, c, and d are coefficients to be determined. After collecting N unique pose measurements with the index $k = [1, ..., N]$, the linear solution is summarized in the following equations:

$$\mathbf{A}\mathbf{x} = \mathbf{y} \tag{A.4a}$$

$$\mathbf{A} = \begin{bmatrix} \mathbf{A}_{(1)}^T, & \ldots, & \mathbf{A}_{(k)}^T, & \ldots, & \mathbf{A}_{(N)}^T \end{bmatrix}^T \tag{A.4b}$$

$$\mathbf{y} = \begin{bmatrix} y_{(1)}, & \ldots, & y_{(N)} \end{bmatrix}^T \tag{A.4c}$$

$$\mathbf{A}_{(k)} = \begin{bmatrix} f_{x,(k)}, f_{y,(k)}, f_{z,(k)}, 1 \end{bmatrix} \tag{A.4d}$$

$$y_{(k)} = -\left(f_{x,(k)}^2 + f_{y,(k)}^2 + f_{z,(k)}^2\right) \tag{A.4e}$$

$$\mathbf{x} = [a, b, c, d]^T \tag{A.4f}$$

Solving for $\mathbf{x}$ through least squares fitting determines the geometry of the force

sphere in frame $\{F\}$. The biases are the offsets of the sphere are defined as:

$$b_x = -a/2 \tag{A.5a}$$

$$b_y = -b/2 \tag{A.5b}$$

$$b_z = -c/2 \tag{A.5c}$$

and the force magnitude is the radius of the fitting with the result:

$$m\,g = \sqrt{\frac{a^2 + b^2 + c^2}{4} - d} \tag{A.6}$$

The direction of gravity in the world frame is estimated by rotating all force measurements into the world frame:

$$\hat{\mathbf{n}} = \frac{\frac{1}{N}\sum_{i=1}^{N} {}^{O}\mathbf{R}_{F}\,{}^{F}\mathbf{f}_i}{\|\frac{1}{N}\sum_{i=1}^{N} {}^{O}\mathbf{R}_{F}\,{}^{F}\mathbf{f}_i\|} \tag{A.7}$$

Once the mass m is known the center of gravity vector $\mathbf{r}$ is found through a set of linear relationships. The estimated moment is the load vector written in the sensor frame $\{F\}$ is denoted as $\tilde{\mathbf{m}}$

$$\tilde{\mathbf{m}}_{(k)} = {}^{F}\mathbf{r} \times m\,g\,{}^{F}\tilde{\mathbf{n}} = [\tilde{m}_x, \tilde{m}_y, \tilde{m}_z]^T \tag{A.8}$$

The following set of equations must be computed to solve for the vector $\mathbf{u} = [r_x, r_y, r_z, b_{xx}, b_{yy}, b_{zz}]^T$ which are the remaining unknown biases and center of gravity.

$$\mathbf{B}\mathbf{u} = \mathbf{z} \tag{A.9a}$$

$$\mathbf{B} = \begin{bmatrix} \mathbf{B}_{(1)}^T & \dots & \mathbf{B}_{(k)}^T & \dots & \mathbf{B}_{(N)}^T \end{bmatrix}^T \tag{A.9b}$$

$$\mathbf{z} = \begin{bmatrix} z_{(1)}^T, & \dots, & z_{(N)}^T \end{bmatrix}^T \tag{A.9c}$$

$$\mathbf{B}_{(k)} = \begin{bmatrix} 0 & \tilde{m}_{z,(k)} & -\tilde{m}_{y,(k)} & 1 & 0 & 0 \\ -\tilde{m}_{z,(k)} & 0 & \tilde{m}_{x,(k)} & 0 & 1 & 0 \\ \tilde{m}_{y,(k)} & -\tilde{m}_{x,(k)} & 0 & 0 & 0 & 1 \end{bmatrix} \tag{A.9d}$$

$$z_{(k)} = \left[\tilde{m}_{x,(k)}, \tilde{m}_{y,(k)}, \tilde{m}_{z,(k)}\right]^T \tag{A.9e}$$

$$\mathbf{u} = [r_x, r_y, r_z, b_{xx}, b_{yy}, b_{zz}]^T \tag{A.9f}$$

After the mass and center of mass have been determined, they can be applied as a feed forward term to measure wrenches applied from external sources. If the compensated wrench is denoted as $\bar{\mathbf{w}}$, then after calibration its value is:

$${}^F\bar{\mathbf{w}} = {}^F\tilde{\mathbf{w}} - {}^F\mathbf{b} - \begin{bmatrix} m\,g\,{}^F\hat{\mathbf{n}} \\ m\,g\,{}^F\mathbf{r} \times {}^F\hat{\mathbf{n}} \end{bmatrix} \tag{A.10}$$

After calibration the magnitude of ${}^F\bar{\mathbf{w}}$ should remain near zero in any end effector pose so long as gravity is the only source of acceleration applied on the end effector.

Appendix B

KINEMATIC MODELS FOR BALANCED MECHANISMS

Included in this appendix are the kinematic derivations for three robot architectures discussed in Chapter IV. For the serial mechanism, the forward kinematic model is provided and for parallel mechanisms the direct inverse kinematic model is presented. The Jacobians $\mathbf{J}_{qx}$, $\mathbf{J}_{\theta x}$, and $\mathbf{J}_{cx,(i)}$ are required for the static balancing analysis and are derived for each mechanism. The architecture covered in this chapter are the $3\bar{R}$ planar serial robot, the $3\bar{R}RR$ planar parallel robot, and the $3\bar{R}S\bar{R}R$ spatial parallel robot.

Several conventions are common to the derivations in this chapter. The world reference frame is $\{\mathbf{0}\}$ with the basis vectors $\{\hat{\mathbf{x}}_0, \hat{\mathbf{y}}_0, \hat{\mathbf{z}}_0\}$ defined as:

$$\hat{\mathbf{x}}_0 = [1,0,0]^T, \qquad \hat{\mathbf{y}}_0 = [0,1,0]^T, \qquad \hat{\mathbf{z}}_0 = [0,0,1]^T \tag{B.1}$$

In planar mechanisms, translational motion is restricted to the world frame x-y plane $\{\hat{\mathbf{x}}_0, \hat{\mathbf{y}}_0\}$ and all revolute joint axes are parallel to $\hat{\mathbf{z}}_0$. The task space in $\mathbb{R}^3$ is denoted by $\mathbf{x} = [p_x, p_y, \phi_z]^T$. In spatial mechanisms, the task space is denoted by its position and the Euler angles ϕ_x, ϕ_y, and ϕ_z such the $\mathbf{x} = [p_x, p_y, p_z, \phi_x, \phi_y, \phi_z]^T$. The Euler angle rotation sequence is:

$${}^0\mathbf{R}_{xyz} = \mathbf{R}_x(\phi_x)\,\mathbf{R}_y(\phi_y)\,\mathbf{R}_z(\phi_z) \tag{B.2}$$

where $\mathbf{R}_x$, $\mathbf{R}_y$, and $\mathbf{R}_z$ are rotations about the axes $\hat{\mathbf{x}}$, $\hat{\mathbf{y}}$, and $\hat{\mathbf{z}}$ respectively. Similarly, the homogeneous transform for the $i'th$ link with respect to the $i-1$ link is written

as:

$$ {}^{i-1}\mathbf{T}_i = \begin{bmatrix} \mathbf{R}_z(\theta_i)\,\mathbf{R}_y(\beta_i)\,\mathbf{R}_x(\alpha_i), & \mathbf{R}_z(\theta_i)^i\mathbf{a}_i \\ \mathbf{0}, & 1 \end{bmatrix} \tag{B.3} $$

where α_i and β_i are link parameter constants. When homogeneous transforms are written in the base frame, the vector $\mathbf{o}$ is introduced to denote the location of a joint. It's location in the transformation is:

$$ {}^{0}\mathbf{T}_i = \begin{bmatrix} {}^{0}\mathbf{R}_i, & \mathbf{o}_i \\ \mathbf{0}, & 1 \end{bmatrix} \tag{B.4} $$

In parallel mechanisms, an index is added in parenthesis to indicate what kinematic chain is being reference. For example, ${}^k\mathbf{a}_{i,(j)}$ is read as the vector $\mathbf{a}$ of the $i'th$ link in the $j'th$ kinematic chain as expressed in frame k. The following three sections detail the kinematics of each mechanism. When the frame definition in the left superscript is omitted, the reader may assume that the vector is in the base frame $\{\mathbf{0}\}$.

B.1 $3\bar{R}$ Kinematics

The $3\bar{R}$ planer serial robot is shown in Figure B.1 (a duplication of Figure IV.1 for the purpose of easy reference). The joint parameters are also the active joint parameters (i.e. $\boldsymbol{\theta} = \mathbf{q} \in \mathbb{R}^q$).

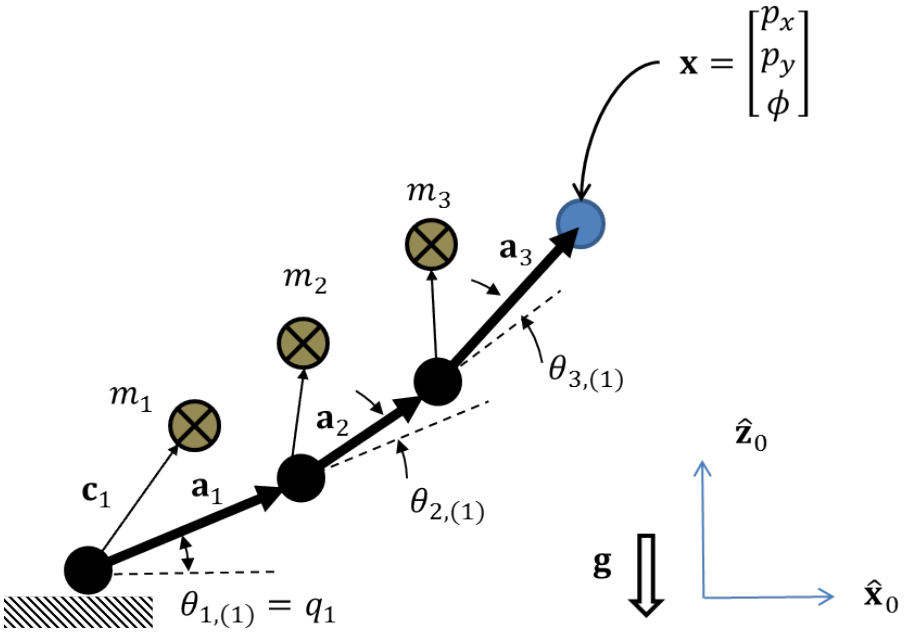

Figure B.1: $3\bar{R}$ kinematic diagram.

The pose of the robot is calculated through forward kinematics with:

$$p_x = \hat{\mathbf{x}}_o^T \left(\sum_{i=1}^{3} \mathbf{a}_i \right) \tag{B.5a}$$

$$p_y = \hat{\mathbf{y}}_o^T \left(\sum_{i=1}^{3} \mathbf{a}_i \right) \tag{B.5b}$$

$$\phi_z = \sum_{i=1}^{3} \theta_i \tag{B.5c}$$

The center of mass for the $i'th$ link are calculated by:

$$\begin{bmatrix} {}^0\mathbf{c}_i \\ 1 \end{bmatrix} = {}^0\mathbf{T}_{i-1} \begin{bmatrix} R_z(\theta_i) {}^i\mathbf{c}_i \\ 1 \end{bmatrix} \tag{B.6}$$

The Jacobian $\mathbf{J}_{qx}$ is used in equation (IV.33) although typically for serial chain the

inverse Jacobian $\mathbf{J}_{xq} = \mathbf{J}_{qx}^{-1}$ is calculated:

$$\mathbf{J}_{xq} = \begin{bmatrix} \hat{\mathbf{x}}_0^T (\mathbf{o}_3 - \mathbf{o}_0), & \hat{\mathbf{x}}_0^T (\mathbf{o}_3 - \mathbf{o}_1), & \hat{\mathbf{x}}_0^T (\mathbf{o}_3 - \mathbf{o}_2) \\ \hat{\mathbf{y}}_0^T (\mathbf{o}_3 - \mathbf{o}_0), & \hat{\mathbf{y}}_0^T (\mathbf{o}_3 - \mathbf{o}_1), & \hat{\mathbf{y}}_0^T (\mathbf{o}_3 - \mathbf{o}_2) \\ 1, & 1, & 1 \end{bmatrix} \tag{B.7}$$

The actuated joints are the same as the generalized coordinates and therefore $\mathbf{J}_{qx} = \mathbf{J}_{\theta x}$ and $\mathbf{J}_{q\theta} = \mathbf{I} \in \mathbb{R}^3$. The velocity of the $i'th$ center of mass is calculated as:

$$\dot{\mathbf{c}}_i = \sum_{j=1}^{i-1} \dot{\theta}_j \left[\hat{\mathbf{z}}_0 \times (\mathbf{o}_{i-1} - \mathbf{o}_{j-1} + \mathbf{c}_i) \right] + \dot{\theta}_i (\hat{\mathbf{z}}_0 \times \mathbf{c}_i) \tag{B.8}$$

In the above equation, in cases where $j > i$ the result is interpreted as a zeros vector $\mathbf{0} \in \mathbb{R}^3$ which leads to the final Jacobians:

$$\mathbf{J}_{cq,1} = \mathbf{J}_{c\theta,1} = \begin{bmatrix} \hat{\mathbf{z}}_0 \times \mathbf{c}_1, & \mathbf{0}, & \mathbf{0} \end{bmatrix} \tag{B.9}$$

$$\mathbf{J}_{cq,2} = \mathbf{J}_{c\theta,2} = \begin{bmatrix} \hat{\mathbf{z}}_0 \times (\mathbf{o}_1 - \mathbf{o}_0 + \mathbf{c}_2), & \hat{\mathbf{z}}_0 \times \mathbf{c}_2, & \mathbf{0} \end{bmatrix} \tag{B.10}$$

$$\mathbf{J}_{cq,3} = \mathbf{J}_{c\theta,3} = \begin{bmatrix} \hat{\mathbf{z}}_0 \times (\mathbf{o}_2 - \mathbf{o}_0 + \mathbf{c}_3), & \hat{\mathbf{z}}_0 \times (\mathbf{o}_2 - \mathbf{o}_1 + \mathbf{c}_3), & \hat{\mathbf{z}}_0 \times \mathbf{c}_3 \end{bmatrix} \tag{B.11}$$

B.2 $3\bar{R}RR$ Kinematics

The $3\bar{R}RR$ planer parallel robot is shown in Figure B.2 (a duplication of Figure IV.2 for the purpose of easy reference).

In the parallel mechanism, the inverse kinematics are computed directly through loop closure. The inverse kinematic solution for the $3\bar{R}RR$ is virtually identical to the $3R\bar{P}R$ presented in Chapter III and is not repeated here for brevity. The designer will have a choice of configuration in each chain is 'elbow up' or 'elbow down'. In

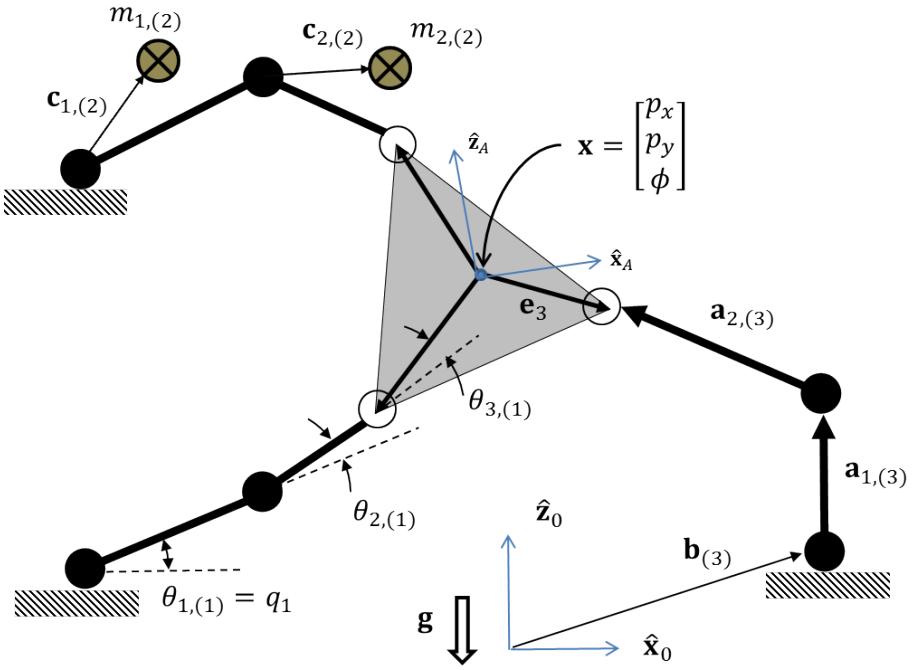

Figure B.2: $3\bar{R}RR$ kinematic diagram.

this work, the links were configured so that $\hat{\mathbf{z}}_0^T \left(\mathbf{a}_{2,(k)} \times \mathbf{a}_{1,(k)}\right) \geq 0$. What follow is the derivation of the instantaneous kinematics.

In this derivation, the generalized coordinates $\boldsymbol{\theta}$ are defined as:

$$\boldsymbol{\theta} = \left[\theta_{1,(1)}, \theta_{1,(2)}, \theta_{1,(3)}, \theta_{2,(1)}, \theta_{2,(2)}, \theta_{2,(3)}, \theta_{3,(1)}, \theta_{3,(2)}, \theta_{3,(3)}\right]^T \tag{B.12}$$

with the task to joint space Jacobian $\mathbf{J}_{\theta x} \in \mathbb{R}^{9\times 3}$ split into several sub-Jacobians with the following definition:

$$\dot{\boldsymbol{\theta}} = \mathbf{J}_{\theta x}\dot{\mathbf{x}} = \begin{bmatrix} \mathbf{J}_{qx} \\ \mathbf{J}_{\theta_1 x} \\ \mathbf{J}_{\theta_2 x} \end{bmatrix} \tag{B.13}$$

The first sub-Jacobian to solve is $\mathbf{J}_{qx}$ for the actuated generalized coordinates. For

the $k'th$ kinematic chain the loop closure equation is:

$$\mathbf{b}_i + \mathbf{a}_{1,(k)} + \mathbf{a}_{2,(k)} = \mathbf{p} + \mathbf{e}_i \tag{B.14}$$

Differentiating (B.14) with respect to time yields:

$$\dot{\theta}_{1,(k)} \left(\hat{\mathbf{z}}_0 \times \mathbf{a}_{1,(k)} \right) + \left(\dot{\theta}_{1,(k)} + \dot{\theta}_{2,(k)} \right) \left(\hat{\mathbf{z}}_0 \times \mathbf{a}_{2,(k)} \right) = \dot{\mathbf{p}} + \dot{\phi}_z \left(\hat{\mathbf{z}}_0 \times \mathbf{e}_i \right) \tag{B.15}$$

The active joints are $q_k = \theta_{1,(k)}$ so multiplying (B.15) by ${\mathbf{a}_{2,(k)}}^T$ and applying triple product rules eliminates the passive joint angle and results in:

$$\dot{\theta}_{1,(k)} {\mathbf{a}_{2,(k)}}^T \left(\hat{\mathbf{z}}_0 \times \mathbf{a}_{1,(k)} \right) = {\mathbf{a}_{2,(k)}}^T \dot{\mathbf{p}} + \dot{\phi}_z {\mathbf{a}_{2,(k)}}^T \left(\hat{\mathbf{z}}_0 \times \mathbf{e}_i \right) \tag{B.16}$$

From (B.16) the equations are reordered to produce the Jacobian $\mathbf{J}_{qx}$:

$$\mathbf{J}_{qx} = {\mathbf{J}_q}^{-1} \mathbf{J}_x \tag{B.17}$$

where:

$$\mathbf{J}_q = \begin{bmatrix} \hat{\mathbf{z}}_0^T \left(\hat{\mathbf{a}}_{1,(1)} \times \mathbf{a}_{2,(1)} \right), & 0, & 0 \\ 0, & \hat{\mathbf{z}}_0^T \left(\hat{\mathbf{a}}_{1,(2)} \times \mathbf{a}_{2,(2)} \right), & 0 \\ 0, & 0, & \hat{\mathbf{z}}_0^T \left(\hat{\mathbf{a}}_{1,(3)} \times \mathbf{a}_{2,(3)} \right) \end{bmatrix} \tag{B.18a}$$

$$\mathbf{J}_q = \begin{bmatrix} {\mathbf{a}_{2,(1)}}^T \hat{\mathbf{x}}_0, & {\mathbf{a}_{2,(1)}}^T \hat{\mathbf{y}}_0, & \hat{\mathbf{z}}_0^T \left(\hat{\mathbf{e}}_1 \times \mathbf{a}_{2,(1)} \right) \\ {\mathbf{a}_{2,(2)}}^T \hat{\mathbf{x}}_0, & {\mathbf{a}_{2,(2)}}^T \hat{\mathbf{y}}_0, & \hat{\mathbf{z}}_0^T \left(\hat{\mathbf{e}}_2 \times \mathbf{a}_{2,(2)} \right) \\ {\mathbf{a}_{2,(3)}}^T \hat{\mathbf{x}}_0, & {\mathbf{a}_{2,(3)}}^T \hat{\mathbf{y}}_0, & \hat{\mathbf{z}}_0^T \left(\hat{\mathbf{e}}_3 \times \mathbf{a}_{2,(3)} \right) \end{bmatrix} \tag{B.18b}$$

The Jacobian $\mathbf{J}_{\theta x}$ is a collection of sub-Jacobians following the relationship:

$$\begin{bmatrix} \dot{\mathbf{q}} \\ \dot{\theta}_{2,(1)} \\ \dot{\theta}_{2,(2)} \\ \dot{\theta}_{2,(3)} \\ \dot{\theta}_{3,(1)} \\ \dot{\theta}_{3,(1)} \\ \dot{\theta}_{3,(1)} \end{bmatrix} = \mathbf{J}_{\theta x}\dot{\mathbf{x}} = \begin{bmatrix} \mathbf{J}_{qx} \\ \mathbf{J}_{\theta_1 x} \\ \mathbf{J}_{\theta_2 x} \end{bmatrix} \dot{\mathbf{x}} \tag{B.19}$$

To find the $\mathbf{J}_{\theta_1 x}$ we begin by defining the following vector substitutions for readability:

$$\mathbf{u}_k = \hat{\mathbf{z}}_0 \times \mathbf{a}_{1,(k)} \tag{B.20a}$$

$$\mathbf{v}_k = \hat{\mathbf{z}}_0 \times \mathbf{a}_{2,(k)} \tag{B.20b}$$

$$\mathbf{w}_k = \hat{\mathbf{z}}_0 \times \mathbf{e}_k \tag{B.20c}$$

$$\tag{B.20d}$$

Next multiply (B.15) by $\frac{\mathbf{u}_k^T}{\mathbf{u}_k^T \mathbf{u}_k}$ to get the following equation:

$$\dot{\theta}_{1,(k)} + \left(\dot{\theta}_{1,(k)} + \dot{\theta}_{2,(k)}\right) \frac{\mathbf{u}_k^T \mathbf{v}_k}{\mathbf{u}_k^T \mathbf{u}_k} = \left[\frac{\mathbf{u}_k^T \hat{\mathbf{x}}_0}{\mathbf{u}_k^T \mathbf{u}_k}, \frac{\mathbf{u}_k^T \hat{\mathbf{y}}_0}{\mathbf{u}_k^T \mathbf{u}_k}, \frac{\mathbf{u}_k^T \mathbf{w}_k}{\mathbf{u}_k^T \mathbf{u}_k}\right] \dot{\mathbf{x}} \tag{B.21}$$

The sub-Jacobian can then be written as:

$$\mathbf{J}_{\theta_1 x} = \mathbf{J}_2^{-1} \left(\mathbf{J}_3 - \mathbf{J}_1 \mathbf{J}_{qx}\right) \tag{B.22}$$

where:

$$\mathbf{J}_1 = \begin{bmatrix} 1 + \frac{\mathbf{u}_1^T \mathbf{v}_1}{\mathbf{u}_1^T \mathbf{u}_1}, & 0, & 0 \\ 0, & 1 + \frac{\mathbf{u}_2^T \mathbf{v}_2}{\mathbf{u}_2^T \mathbf{u}_2}, & 0 \\ 0, & 0, & 1 + \frac{\mathbf{u}_3^T \mathbf{v}_3}{\mathbf{u}_3^T \mathbf{u}_3} \end{bmatrix} \tag{B.23a}$$

$$\mathbf{J}_2 = \begin{bmatrix} \frac{\mathbf{u}_1^T \mathbf{v}_1}{\mathbf{u}_1^T \mathbf{u}_1}, & 0, & 0 \\ 0, & \frac{\mathbf{u}_2^T \mathbf{v}_2}{\mathbf{u}_2^T \mathbf{u}_2}, & 0 \\ 0, & 0, & \frac{\mathbf{u}_3^T \mathbf{v}_3}{\mathbf{u}_3^T \mathbf{u}_3} \end{bmatrix} \tag{B.23b}$$

(B.23c)

$$\mathbf{J}_3 = \begin{bmatrix} \frac{\mathbf{u}_1^T \hat{\mathbf{x}}_0}{\mathbf{u}_1^T \mathbf{u}_1}, & \frac{\mathbf{u}_1^T \hat{\mathbf{y}}_0}{\mathbf{u}_1^T \mathbf{u}_1}, & \frac{\mathbf{u}_1^T \mathbf{w}_1}{\mathbf{u}_1^T \mathbf{u}_1} \\ \frac{\mathbf{u}_2^T \hat{\mathbf{x}}_0}{\mathbf{u}_2^T \mathbf{u}_2}, & \frac{\mathbf{u}_2^T \hat{\mathbf{y}}_0}{\mathbf{u}_2^T \mathbf{u}_2}, & \frac{\mathbf{u}_2^T \mathbf{w}_2}{\mathbf{u}_2^T \mathbf{u}_2} \\ \frac{\mathbf{u}_3^T \hat{\mathbf{x}}_0}{\mathbf{u}_3^T \mathbf{u}_3}, & \frac{\mathbf{u}_3^T \hat{\mathbf{y}}_0}{\mathbf{u}_3^T \mathbf{u}_3}, & \frac{\mathbf{u}_3^T \mathbf{w}_3}{\mathbf{u}_3^T \mathbf{u}_3} \end{bmatrix} \tag{B.23d}$$

The last sub-Jacobian is simple to compute. The joint velocities $\dot{\theta}_{3,(k)}$ do not appear explicitly in the loop closure equations but follow the relationship:

$$\dot{\theta}_{1,(k)} + \dot{\theta}_{2,(k)} + \dot{\theta}_{3,(k)} = \dot{\phi}_z \tag{B.24}$$

which leads to the following Jacobian:

$$\mathbf{J}_{\theta_1 x} = \begin{bmatrix} 0, & 0, & 1 \\ 0, & 0, & 1 \\ 0, & 0, & 1 \end{bmatrix} - \mathbf{J}_{qx} - \mathbf{J}_{\theta_1 x} \tag{B.25}$$

Once $\mathbf{J}_{\theta x}$ is constructed, the last Jacobians required are $\mathbf{J}_{c\theta,i,(k)} \forall i, k = 1, 2, 3$. The individual kinematic chains are identical to the $3\bar{R}$ planar serial robot and derived in

the same manner. The third kinematic link for the $k'th$ chain is defined as ${}^{k}\mathbf{a}_{3,(k)} = [\|\mathbf{e}_k\|, 0, 0]^T$ and the center of mass for the third link is ${}^{3}\mathbf{c}_{3,(k)} = {}^{k}\mathbf{a}_{3,(k)}$.

B.3 $3\bar{R}S\bar{R}R$ Kinematics

The $3\bar{R}S\bar{R}R$ mechanism is shown schematically in Figure B.3. Only one of the three kinematic chains are shown in the figure for clarity. Since the joints are all revolute, this mechanism may be considered a special case of the $3\bar{R}RRR\bar{R}R$ configuration where the axes of the second, third, and fourth joints intersect at a common point. The kinematic solution details will focus on one kinematic chain with index k and omit the second subscript in parenthesis for clarity. Also, all vectors are assumed to be expressed in the base frame unless explicitly stated.

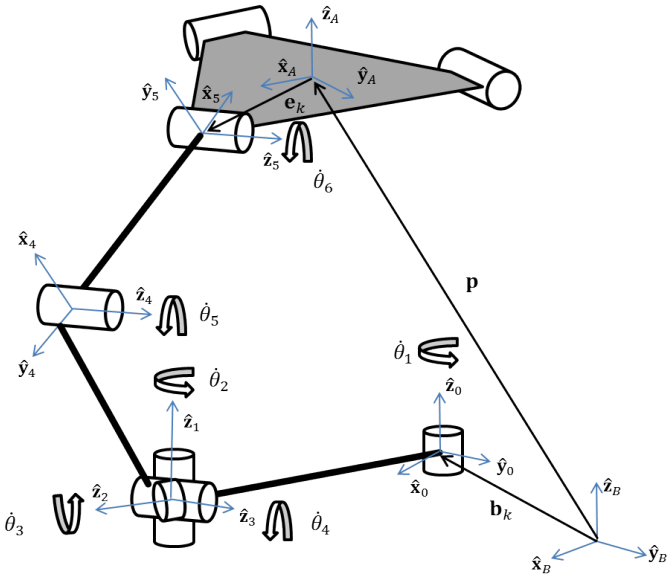

Figure B.3: $3\bar{R}S\bar{R}R$ kinematic diagram.

There are some baseline assumptions made in the configuration of the individual links. Table B.1 shows the assumed parameters in the design, leaving variability in the lengths of the various links.

The kinematic derivation begins with specification of the end effector pose $\mathbf{x} =$

Table B.1: Basic Parameters for $3\bar{R}S\bar{R}R$ Spatial Parallel Robot

Link	α	β	${}^{i}\mathbf{a}_i$
1	0	0	$[l_1, 0, 0]^T$
2	0	$-\pi/2$	$[0, 0, 0]^T$
3	$-\pi/2$	0	$[0, 0, 0]^T$
4	0	0	$[l_4, 0, 0]^T$
5	0	0	$[l_5, 0, 0]^T$
6	0	0	$-{}^{A}\mathbf{e}_k$

$\left[\mathbf{p}^T, \boldsymbol{\phi}^T\right]^T$. The orientation of 6'th link's frame can then be determined:

$$\hat{\mathbf{x}}_6 = -\frac{\mathbf{e}_k}{\|\mathbf{e}_k\|}, \qquad \hat{\mathbf{y}}_6 = \hat{\mathbf{z}}_A, \qquad \hat{\mathbf{z}}_6 = \hat{\mathbf{x}}_6 \times \hat{\mathbf{y}}_6 \tag{B.26}$$

Next, the location of point were the $k'th$ kinematic chain connects to the end effector platform is given by:

$$\mathbf{o}_5 = \mathbf{p} + \mathbf{e}_k \tag{B.27}$$

The joint values are computed sequentially in a chain, beginning with θ_1 and ending with θ_6. To find θ_1, begin by projecting the point $\mathbf{o}_5$ along the direction $\hat{\mathbf{z}}_A$ onto the plane defined by $\{\hat{\mathbf{x}}_0, \hat{\mathbf{y}}_0\}$. This projected point is specified by the vector $\mathbf{f}$:

$$\mathbf{f} = \mathbf{o}_5 + \left(\left[\mathbf{o}_0 - \mathbf{o}_5\right]^T \hat{\mathbf{z}}_A\right) \hat{\mathbf{z}}_A \tag{B.28}$$

The line intersecting with the first link is along the unit vector $\hat{\mathbf{s}}$ at point $\mathbf{f}$. The direction of $\hat{\mathbf{s}}$ is the projection of the unit vector $\hat{\mathbf{x}}_6$ onto the plane $\{\hat{\mathbf{x}}_0, \hat{\mathbf{y}}_0\}$:

$$\hat{\mathbf{s}} = \frac{\hat{\mathbf{x}}_6 - \hat{\mathbf{x}}_6^T \hat{\mathbf{z}}_0}{\|\hat{\mathbf{x}}_6 - \hat{\mathbf{x}}_6^T \hat{\mathbf{z}}_0\|} \tag{B.29}$$

In the plane $\{\hat{\mathbf{x}}_0, \hat{\mathbf{y}}_0\}$ the coordinates r_x and r_y specify to location of $\mathbf{f}$ from $\mathbf{o}_0$ in

the plane $\{\hat{\mathbf{x}}_0, \hat{\mathbf{y}}_0\}$. The scalar λ is the distance along $\hat{\mathbf{s}}$ from point $\mathbf{f}$ where the end of link one (point $\mathbf{o}_1$) intersects. Set $r_x = (\mathbf{f} - \mathbf{o}_0)^T \hat{\mathbf{x}}$ and $r_y = (\mathbf{f} - \mathbf{o}_0)^T \hat{\mathbf{y}}$ and the following equations must be satisfied:

$$\lambda \hat{s}_x + r_x = l_1 \cos\theta_1 \tag{B.30a}$$

$$\lambda \hat{s}_y + r_y = l_1 \sin\theta_1 \tag{B.30b}$$

Taking the sum of squares of these two equations eliminates θ_1 and provides an equation that is quadratic with respect to λ:

$$\lambda^2 \left(\hat{s}_x^2 + \hat{s}_y^2\right) + 2\left(\hat{s}_x r_x + \hat{s}_y r_y\right)\lambda + \left(r_x^2 + r_y^2 - 2l_1^2\right) = 0 \tag{B.31}$$

There are two solutions to this equation using the quadratic solution, the one assumed in this work is the smaller value, which corresponds with the link pointing away from the center of the parallel mechanism:

$$\lambda = \frac{-\left(\hat{s}_x r_x + \hat{s}_y r_y\right) - \sqrt{\left(\hat{s}_x r_x + \hat{s}_y r_y\right)^2 - \left(\hat{s}_x^2 + \hat{s}_y^2\right)\left(r_x^2 + r_y^2 - 2l_1^2\right)}}{\left(\hat{s}_x^2 + \hat{s}_y^2\right)} \tag{B.32}$$

Once λ is known, θ_1 is calculated as:

$$\theta_1 = \arctan\left(\frac{\lambda \hat{s}_y + r_y}{\lambda \hat{s}_x + r_x}\right) \tag{B.33}$$

Once θ_1 is known, then frame $\{1\} = \{\hat{\mathbf{x}}_1, \hat{\mathbf{y}}_1, \hat{\mathbf{z}}_1\}$ is defined. The next three joint angles represent the spherical joint and are found by sequentially aligning the axes according to Figure B.3. There are many ways that the order of these three joints could be calculated and one solution is presented here. The joint angle θ_2 is calculated

as:

$$\theta_2 = \arctan\left(\frac{-\hat{\mathbf{x}}_1^T\hat{\mathbf{z}}_2'}{-\hat{\mathbf{y}}_1^T\hat{\mathbf{z}}_2'}\right) \tag{B.34}$$

where

$$\hat{\mathbf{z}}_2' = \frac{\hat{\mathbf{z}}_5 - \left(\hat{\mathbf{z}}_5^T\hat{\mathbf{z}}_1\right)\hat{\mathbf{z}}_1}{\|\hat{\mathbf{z}}_5 - \left(\hat{\mathbf{z}}_5^T\hat{\mathbf{z}}_1\right)\hat{\mathbf{z}}_1\|} \tag{B.35}$$

Next, the frame $\{2\} = \{\hat{\mathbf{x}}_2, \hat{\mathbf{y}}_2, \hat{\mathbf{z}}_2\}$ is computed through forward kinematics and the joint value θ_3 is calculated as:

$$\theta_3 = \arctan\left(\frac{-\hat{\mathbf{x}}_2^T\hat{\mathbf{z}}_3'}{-\hat{\mathbf{y}}_2^T\hat{\mathbf{z}}_3'}\right) \tag{B.36}$$

where

$$\hat{\mathbf{z}}_3' = \frac{\hat{\mathbf{z}}_5 - \left(\hat{\mathbf{z}}_5^T\hat{\mathbf{z}}_2\right)\hat{\mathbf{z}}_2}{\|\hat{\mathbf{z}}_5 - \left(\hat{\mathbf{z}}_5^T\hat{\mathbf{z}}_2\right)\hat{\mathbf{z}}_2\|} \tag{B.37}$$

The last axes of the spherical joint is parallel to the rotation axes of joints θ_5 and θ_6, creating a planar $3R$ mechanism. Finding the values of θ_4, θ_5 and θ_6 is similar to the solution used in the $3\bar{R}RR$ inverse kinematic solution. Start by defining the vector $\mathbf{d}$:

$$\mathbf{d} = \mathbf{o}_5 - \mathbf{o}_3 \tag{B.38}$$

and define the magnitude of this vector as $d = \|\mathbf{d}\|$. The values of θ_4 and θ_5 are found by looking at the triangle created by links 4 and 5 and the vector $\mathbf{d}$ and applying the law of cosines. This results in the solution:

$$\theta_4 = -\arccos\left(\frac{\mathbf{d}^T\hat{\mathbf{x}}_3}{d}\right) + \arccos\left(\frac{l_4^2 + d^2 - l_5^2}{2l_4 d}\right) \tag{B.39}$$

and

$$\theta_5 = -\pi + \arccos\left(\frac{l_4^2 + l_5^2 - d^2}{2l_4 l_5}\right) \tag{B.40}$$

Using forward kinematics, the orientation of frame $\{5\} = \{\hat{\mathbf{x}}_5, \hat{\mathbf{y}}_5, \hat{\mathbf{z}}_5\}$ is now known and the final joint angle θ_6 can be calculated as:

$$\theta_6 = \arccos\left(\frac{-\hat{\mathbf{x}}_5^T \mathbf{e}_k}{\|\mathbf{e}_k\|}\right) \tag{B.41}$$

Once the inverse kinematics of the mechanism have been calculated, it is possible to derive the instantaneous kinematics relating an end effector twist $\dot{\mathbf{x}} = \left[\dot{\mathbf{p}}^T, \omega^T\right]^T$ to the actuated joint velocities $\dot{\mathbf{q}}$. The derivation begins with the velocity loop closure equation for a kinematic chain:

$$\dot{q}_1\left(\hat{\mathbf{z}}_0 \times (\mathbf{o}_5 - \mathbf{o}_0)\right) + \dot{\theta}_2\left(\hat{\mathbf{z}}_1 \times \mathbf{d}\right) + \dot{\theta}_3\left(\hat{\mathbf{z}}_2 \times \mathbf{d}\right) + \dot{\theta}_4\left(\hat{\mathbf{z}}_3 \times \mathbf{d}\right) + \dot{q}_2\left(\hat{\mathbf{z}}_4 \times (\mathbf{o}_5 - \mathbf{o}_4)\right) = \dot{\mathbf{p}} + \boldsymbol{\omega} \times \mathbf{e}_{(k)} \tag{B.42}$$

Applying $\mathbf{d}^T$ to equation (B.42) will eliminate the passive joint variables and results in the following equation:

$$\dot{q}_1 \mathbf{d}^T\left(\hat{\mathbf{z}}_0 \times (\mathbf{o}_5 - \mathbf{o}_0)\right) + \dot{q}_2 \mathbf{d}^T\left(\hat{\mathbf{z}}_4 \times (\mathbf{o}_5 - \mathbf{o}_4)\right) = \mathbf{d}^T + \left(\mathbf{e}_{(k)} \times \mathbf{d}^T\right)^T \boldsymbol{\omega} \tag{B.43}$$

Each kinematic chain has two active joints and therefore two equations are needed per kinematic chain. The loop velocity closure equation can also be written from the perspective of the spherical joint. This results in the following equation:

$$\dot{q}_1\left(\hat{\mathbf{z}}_0 \times (\mathbf{o}_5 - \mathbf{o}_0)\right) = \dot{\mathbf{p}} + \boldsymbol{\omega} \times (\mathbf{o}_2 - \mathbf{p}) + \dot{\theta}_2\left(\hat{\mathbf{z}}_1 \times -\mathbf{d}\right) + \dot{q}_2\left(\hat{\mathbf{z}}_4 \times (\mathbf{o}_3 - \mathbf{o}_4)\right) \tag{B.44}$$

A special characteristic of this design is the the rotation axes of links 4,5 and 6 are parallel. This means that $\hat{\mathbf{z}}_4 = \hat{\mathbf{z}}_5$. Using this fact and multiplying $\hat{\mathbf{z}}_5^T$ into (B.44)

results in the second required equation:

$$\dot{q}_1 \hat{\mathbf{z}}_5^T \left(\hat{\mathbf{z}}_0 \times (\mathbf{o}_5 - \mathbf{o}_0) \right) = \hat{\mathbf{z}}_5^T \dot{\mathbf{p}} + \left((\mathbf{o}_2 - \mathbf{p}) \times \hat{\mathbf{z}}_5 \right)^T \boldsymbol{\omega} \tag{B.45}$$

This process can be repeated for each kinematic chain. The final Jacobian $\mathbf{J}_{qx}$ is then calculated as:

$$\mathbf{J}_{qx} = \mathbf{J}_q^{-1} \mathbf{J}_x \tag{B.46}$$

where

$$\mathbf{J}_q = \begin{bmatrix} J_{1,1}, & J_{1,2}, & 0, & 0, & 0, & 0 \\ J_{2,1}, & 0, & 0, & 0, & 0, 0 & \\ 0, & 0, & J_{3,3}, & J_{3,4}, & 0, & 0 \\ 0, & 0, & J_{4,3}, & 0, & 0, & 0 \\ 0, & 0, & 0, & 0, & J_{5,5}, & J_{5,6} \\ 0, & 0, & 0, & 0, & J_{6,5}, & 0 \end{bmatrix} \tag{B.47}$$

with

$$
\begin{aligned}
J_{1,1} &= \mathbf{d}_{(1)}^T \left(\hat{\mathbf{z}}_{0,(1)} \times (\mathbf{o}_{5,(1)} - \mathbf{o}_{0,(1)}) \right) \\
J_{1,2} &= \mathbf{d}_{(1)}^T \left(\hat{\mathbf{z}}_{4,(1)} \times (\mathbf{o}_{5,(1)} - \mathbf{o}_{4,(1)}) \right) \\
J_{2,1} &= \hat{\mathbf{z}}_{5,(1)}^T \left(\hat{\mathbf{z}}_{0,(1)} \times (\mathbf{o}_{5,(1)} - \mathbf{o}_{0,(1)}) \right) \\
J_{3,3} &= \mathbf{d}_{(2)}^T \left(\hat{\mathbf{z}}_{0,(2)} \times (\mathbf{o}_{5,(2)} - \mathbf{o}_{0,(2)}) \right) \\
J_{3,4} &= \mathbf{d}_{(2)}^T \left(\hat{\mathbf{z}}_{4,(2)} \times (\mathbf{o}_{5,(2)} - \mathbf{o}_{4,(2)}) \right) \\
J_{4,3} &= \hat{\mathbf{z}}_{5,(2)}^T \left(\hat{\mathbf{z}}_{0,(2)} \times (\mathbf{o}_{5,(2)} - \mathbf{o}_{0,(2)}) \right) \\
J_{5,5} &= \mathbf{d}_{(3)}^T \left(\hat{\mathbf{z}}_{0,(3)} \times (\mathbf{o}_{5,(3)} - \mathbf{o}_{0,(3)}) \right) \\
J_{5,6} &= \mathbf{d}_{(3)}^T \left(\hat{\mathbf{z}}_{4,(3)} \times (\mathbf{o}_{5,(3)} - \mathbf{o}_{4,(3)}) \right) \\
J_{6,5} &= \hat{\mathbf{z}}_{5,(3)}^T \left(\hat{\mathbf{z}}_{0,(3)} \times (\mathbf{o}_{5,(3)} - \mathbf{o}_{0,(3)}) \right)
\end{aligned}
$$

and

$$
\mathbf{J}_x = \begin{bmatrix}
\mathbf{d}_{(1)}^T, & \left(\mathbf{e}_{(1)} \times \mathbf{d}_{(1)}^T \right)^T \\
\hat{\mathbf{z}}_{5,(1)}^T, & \left((\mathbf{o}_{2,(1)} - \mathbf{p}) \times \hat{\mathbf{z}}_{5,(1)} \right)^T \\
\mathbf{d}_{(2)}^T, & \left(\mathbf{e}_{(2)} \times \mathbf{d}_{(2)}^T \right)^T \\
\hat{\mathbf{z}}_{5,(2)}^T, & \left((\mathbf{o}_{2,(2)} - \mathbf{p}) \times \hat{\mathbf{z}}_{5,(2)} \right)^T \\
\mathbf{d}_{(3)}^T, & \left(\mathbf{e}_{(3)} \times \mathbf{d}_{(3)}^T \right)^T \\
\hat{\mathbf{z}}_{5,(3)}^T, & \left((\mathbf{o}_{2,(3)} - \mathbf{p}) \times \hat{\mathbf{z}}_{5,(3)} \right)^T
\end{bmatrix} \tag{B.48}
$$

The Jacobian $\mathbf{J}_{\theta x}$ could not be computed in the manner used for the $3\bar{R}RR$ due

to the spherical joint. The Euler angle parameterizations result in gimbal lock conditions. Instead, the forward kinematic Jacobian for each chain is computed independently and inverted to create the matrix:

$$\mathbf{J}_{\theta x} = \begin{bmatrix} \mathbf{J}^{-1}_{x\theta(1)} \\ \mathbf{J}^{-1}_{x\theta(2)} \\ \mathbf{J}^{-1}_{x\theta(3)} \end{bmatrix} \tag{B.49}$$

where, given the definition $\mathbf{u}_{i,(k)} = \mathbf{z}_{i-1,(k)} \left(\mathbf{p} - \mathbf{o}_{i-1,(k)} \right)$, the Jacobian $\mathbf{J}_{x\theta(k)}$ is defined as:

$$\mathbf{J}_{x\theta(k)} = \begin{bmatrix} \mathbf{u}_{1,(k)}, & \mathbf{u}_{2,(k)}, & \mathbf{u}_{3,(k)}, & \mathbf{u}_{4,(k)}, & \mathbf{u}_{5,(k)}, & \mathbf{u}_{6,(k)} \\ \mathbf{z}_{0,(k)}, & \mathbf{z}_{1,(k)}, & \mathbf{z}_{2,(k)}, & \mathbf{z}_{3,(k)}, & \mathbf{z}_{4,(k)}, & \mathbf{z}_{5,(k)} \end{bmatrix} \tag{B.50}$$

The final set of Jacobians required to evaluate the static balancing of this mechanism, $\mathbf{J}_{c\theta,i,(k)}$ which are expressed by:

$$\mathbf{J}_{c\theta,i,(k)} = \begin{bmatrix} \mathbf{v}_{i,1,(k)}, & \mathbf{v}_{i,2,(k)}, & \mathbf{v}_{i,3,(k)}, & \mathbf{v}_{i,4,(k)}, & \mathbf{v}_{i,5,(k)}, & \mathbf{v}_{i,6,(k)} \end{bmatrix} \tag{B.51}$$

where

$$\mathbf{v}_{i,j,(k)} = \begin{cases} \mathbf{z}_{i-1,(k)} \times \left({}^{0}\mathbf{c}_{i,(k)} + \mathbf{o}_{i-1,(k)} - \mathbf{o}_{j-1,(k)} \right), & \text{if } i \geq j \\ [0,0,0]^{T}, & \text{otherwise} \end{cases} \tag{B.52}$$

Bibliography

[1] Adunka, O., Unkelbach, M. H., Mack, M., Hambek, M., Gstoettner, W., and Kiefer, J. Cochlear implantation via the round window membrane minimizes trauma to cochlear structures: a histologically controlled insertion study. *Acta oto-laryngologica 124*, 7 (Sept. 2004), 807–12.

[2] Agrawal, A., and Agrawal, S. K. Design of gravity balancing leg orthosis using non-zero free length springs. *Mechanism and Machine Theory 40*, 6 (June 2005), 693–709.

[3] Agrawal, S. K., and Fattah, A. Gravity-balancing of spatial robotic manipulators. *Mechanism and Machine Theory 39*, 12 (Dec. 2004), 1331–1344.

[4] Alexiades, G., Roland, J. T., Fishman, A. J., Shapiro, W., Waltzman, S. B., and Cohen, N. L. Cochlear reimplantation: surgical techniques and functional results. *The Laryngoscope 111*, 9 (Sept. 2001), 1608–13.

[5] Ang, W.-T. *A Beginners Course in Boundary Element Methods*. Universal Publishers, Boca Raton, 2007.

[6] Angeles, J., and Lopez-Cajun, C. *Optimization of cam mechanisms*. Springer, 1991.

[7] Arsenault, M., and Gosselin, C. M. Static Balancing of Tensegrity Mechanisms. *Journal of Mechanical Design 129*, 3 (2007), 295.

[8] Barber, C. B., Dobkin, D. P., and Huhdanpaa, H. The quickhull algorithm for convex hulls. *ACM Transactions on Mathematical Software 22*, 4 (Dec. 1996), 469–483.

[9] Baron, S., Eilers, H., Munske, B., Toennies, J. L., Balachandran, R., Labadie, R. F., Ortmaier, T., and Webster, R. J. Percutaneous inner-ear access via an image-guided industrial robot system. *Proceedings of the Institution of Mechanical Engineers, Part H: Journal of Engineering in Medicine 224*, 5 (May 2010), 633–649.

[10] Bosscher, P., Riechel, A., and Ebert-Uphoff, I. Wrench-feasible workspace generation for cable-driven robots. *IEEE Transactions on Robotics 22*, 5 (Oct. 2006), 890–902.

[11] Bostelman, R., Albus, J., and Dagalakis, N. RoboCrane Project: An Advanced Concept for Large Scale Manufacturing. In *Proceedings of the AUVSI Conference* (1996).

[12] Briggs, R. J., Tykocinski, M., Saunders, E., Hellier, W., Dahm, M., Pyman, B., and Clark, G. M. Surgical implications of perimodiolar cochlear implant electrode design: avoiding intracochlear damage and scala vestibuli insertion. *Cochlear implants international 2*, 2 (Sept. 2001), 135–49.

[13] Briggs, R. J. S., Tykocinski, M., Lazsig, R., Aschendorff, A., Lenarz, T., Stöver, T., Fraysse, B., Marx, M., Roland, J. T., Roland, P. S., Wright, C. G., Gantz, B. J., Patrick, J. F., and Risi, F. Development and evaluation of the modiolar research array–multi-centre collaborative study in human temporal bones. *Cochlear implants international 12*, 3 (Aug. 2011), 129–39.

[14] Briggs, R. J. S., Tykocinski, M., Stidham, K., and Roberson, J. B. Cochleostomy site: Implications for electrode placement and hearing preservation. *Acta Oto-laryngologica 125*, 8 (Jan. 2005), 870–876.

[15] Bromiley, P. A. Products and Convolutions of Gaussian Distributions. Tech. rep., Medical School, Univ. Manchester, Manchester, UK, Tech. Rep 3, Manchester, UK, 2003.

[16] Brown, R. F., Hullar, T. E., Cadieux, J. H., and Chole, R. a. Residual hearing preservation after pediatric cochlear implantation. *Otology & neurotology : official publication of the American Otological Society, American Neurotology Society [and] European Academy of Otology and Neurotology 31*, 8 (Oct. 2010), 1221–6.

[17] Carlson, M. L., Driscoll, C. L. W., Gifford, R. H., Service, G. J., Tombers, N. M., Hughes-Borst, B. J., Neff, B. a., and Beatty, C. W. Implications of minimizing trauma during conventional cochlear implantation. *Otology & neurotology : official publication of the American Otological Society, American Neurotology Society [and] European Academy of Otology and Neurotology 32*, 6 (Aug. 2011), 962–8.

[18] Carricato, M., and Gosselin, C. A Statically Balanced Gough/Stewart-Type Platform: Conception, Design, and Simulation. *Journal of Mechanisms and Robotics 1*, 3 (2009), 031005.

[19] Chang, Chih-Chung and Lin, C.-J. LIBSVM: A library for support vector machines. *ACM Transactions on Intelligent Systems and Technology 2*, 3 (2011), 27:1—-27:27.

[20] Chen, I.-M., Angeles, J., Theingi, and Chuan Li. The management of parallel-manipulator singularities using joint-coupling. In *2003 IEEE International Conference on Robotics and Automation* (2003), vol. 1, Ieee, pp. 773–778.

[21] Chiacchio, P., Chiaverini, S., Sciavicco, L., and Siciliano, B. Global task space manipulability ellipsoids for multiple-arm systems. *IEEE Transactions on Robotics and Automation 7*, 5 (1991), 678–685.

[22] Chirikjian, G., and Burdick, J. A modal approach to hyper-redundant manipulator kinematics. *IEEE Transactions on Robotics and Automation 10*, 3 (June 1994), 343–354.

[23] Choi, C. A novel approach to compute the impedance matrix of a cochlear implant system incorporating an electrode-tissue interface based on finite element method. *IEEE Transactions on Magnetics 42*, 4 (Apr. 2006), 1375–1378.

[24] Choudhury, B., Adunka, O. F., Demason, C. E., Ahmad, F. I., Buchman, C. a., and Fitzpatrick, D. C. Detection of intracochlear damage with cochlear implantation in a gerbil model of hearing loss. *Otology & neurotology : official publication of the American Otological Society, American Neurotology Society [and] European Academy of Otology and Neurotology 32*, 8 (Oct. 2011), 1370–8.

[25] Clark, J. R. *Toward Improved Cochlear Implant Insertion Using Magnetic Guidance*. M.s., University of Utah, 2011.

[26] Cohen, L. T., Xu, J., Xu, S. A., and Clark, G. M. Improved and simplified methods for specifying positions of the electrode bands of a cochlear implant array. *The American journal of otology 17*, 6 (Nov. 1996), 859–65.

[27] Cohen, N. L., Roland, J. T., and Fishman, A. Surgical technique for the Nucleus Contour cochlear implant. *Ear and hearing 23*, 1 Suppl (Feb. 2002), 59S–66S.

[28] Cosetti, M., and Roland Jr, J. T. Cochlear implant electrode insertion. *Operative Techniques in Otolaryngology, head & neck surgery 21*, 4 (Dec. 2010), 223–232.

[29] Cosetti, M. K., Friedmann, D. R., Zhu, B. Z., Heman-Ackah, S. E., Fang, Y., Keller, R. G., Shapiro, W. H., Roland, J. T., and Waltzman, S. B. The Effects of Residual Hearing in Traditional Cochlear Implant Candidates After Implantation With a Conventional Electrode. *Otology & neurotology : official publication of the American Otological Society, American Neurotology Society [and] European Academy of Otology and Neurotology* (Feb. 2013), 0–5.

[30] Deepak, S. R., and Ananthasuresh, G. K. Perfect Static Balance of Linkages by Addition of Springs But Not Auxiliary Bodies. *Journal of Mechanisms and Robotics 4*, 2 (2012), 021014.

[31] Erixon, E., Högstorp, H., Wadin, K., and Rask-Andersen, H. Variational anatomy of the human cochlea: implications for cochlear implantation. *Otology & neurotology : official publication of the American Otological Society, American Neurotology Society [and] European Academy of Otology and Neurotology 30*, 1 (Jan. 2009), 14–22.

[32] Eshraghi, A., Yang, N., and Balkany, T. Comparative Study of Cochlear Damage with Three Perimodiolar Electride Designs. *The Laryngeoscope 113* (2003), 415–419.

[33] Fattah, a., and Agrawal, S. Gravity-balancing of classes of industrial robots. *Proceedings 2006 IEEE International Conference on Robotics and Automation, 2006. ICRA 2006.*, May (2006), 2872–2877.

[34] Fishman, A. J., Roland, J. T., Alexiades, G., Mierzwinski, J., and Cohen, N. L. Fluoroscopically assisted cochlear implantation. *Otology & neurotology : official publication of the American Otological Society, American Neurotology Society [and] European Academy of Otology and Neurotology 24*, 6 (Nov. 2003), 882–6.

[35] Fraysse, B., Macías, A. R., Sterkers, O., Burdo, S., Ramsden, R., Deguine, O., Klenzner, T., Lenarz, T., Rodriguez, M. M., Von Wallenberg, E., and James, C. Residual hearing conservation and electroacoustic stimulation with the nucleus 24 contour advance cochlear implant. *Otology & neurotology : official publication of the American Otological Society, American Neurotology Society [and] European Academy of Otology and Neurotology 27*, 5 (Aug. 2006), 624–33.

[36] Frisoli, a., Prisco, M., Salsedo, F., and Bergamasco, M. A two degrees-of-freedom planar haptic interface with high kinematic isotropy. In *8th IEEE International Workshop on Robot and Human Interaction. RO-MAN '99 (Cat. No.99TH8483)* (1999), no. September, Ieee, pp. 297–302.

[37] Gosselin, C. M. Static Balancing of Spherical 3-DOF Parallel Mechanisms and Manipulators. *The International Journal of Robotics Research 18*, 8 (Aug. 1999), 819–829.

[38] Gouttefarde, M., and Gosselin, C. Analysis of the wrench-closure workspace of planar parallel cable-driven mechanisms. *IEEE Transactions on Robotics 22*, 3 (June 2006), 434–445.

[39] Graham, A. *Kronecker products and matrix calculus : with applications* . Halsted Press,, New York, 1981.

[40] Guthart, G., and Salisbury, J. The Intuitive/sup TM/ telesurgery system: overview and application. In *Proceedings 2000 ICRA. Millennium Conference. IEEE International Conference on Robotics and Automation. Symposia Proceedings (Cat. No.00CH37065)* (2000), vol. 1, IEEE, pp. 618–621.

[41] Helbig, S., Rajan, G. P., Stöver, T., Lockley, M., Kuthubutheen, J., and Green, K. M. Hearing preservation after cochlear reimplantation. *Otology & neurotology : official publication of the American Otological Society, American Neurotology Society [and] European Academy of Otology and Neurotology 34*, 1 (Jan. 2013), 61–5.

[42] Hibbert, D. B., Weitzner, K., and Carter, P. Voltammetry of Platinum in Artificial Perilymph Solution. *Journal of The Electrochemical Society 148*, 1 (2001), E1.

[43] Ibrahim, H. N., Helbig, S., Bossard, D., and Truy, E. Surgical trauma after sequential insertion of intracochlear catheters and electrode arrays (a histologic study). *Otology & neurotology : official publication of the American Otological Society, American Neurotology Society [and] European Academy of Otology and Neurotology 32*, 9 (Dec. 2011), 1448–54.

[44] Ishii, T., Takayama, M., and Takahashi, Y. Mechanical properties of human round window, basilar and Reissner's membranes. *Acta oto-laryngologica. Supplementum 519* (Jan. 1995), 78–82.

[45] ISI. Intuitive Surgical Inc.

[46] Ivan Fanany, M., Jatmiko, W., and Basaruddin, T. A comparative study on Daubechies Wavelet Transformation, Kernel PCA and PCA as feature extractors for arrhythmia detection using SVM. In *TENCON 2011 - 2011 IEEE Region 10 Conference* (Nov. 2011), IEEE, pp. 5–9.

[47] Jolly, C. N., Member, S., Spelman, F. A., and Clopton, B. M. Quadrupolar Stimulation for Cochlear Prostheses : Modeling and ExDerimental Data. *Transactions on Biomedical Engineering 43*, 8 (1996), 857–865.

[48] Kazanzides, P., Mittelstadt, B., Musits, B., Bargar, W., Zuhars, J., Williamson, B., Cain, P., and Carbone, E. An integrated system for cementless hip replacement. *IEEE Engineering in Medicine and Biology Magazine 14*, 3 (1995), 307–313.

[49] Kazanzides, P., Zuhars, J., Mittelstadt, B., Williamson, B., Cain, P., Smith, F., Rose, L., and Musits, B. Architecture of a surgical robot. *[Proceedings] 1992 IEEE International Conference on Systems, Man, and Cybernetics*, 1624–1629.

[50] Kilic, M., Yazicioglu, Y., and Kurtulus, D. F. Synthesis of a torsional spring mechanism with mechanically adjustable stiffness using wrapping cams. *Mechanism and Machine Theory 57* (Nov. 2012), 27–39.

[51] Kim, H.-s., and Song, J.-b. Low-cost Robot Arm with 3-DOF Counterbalance Mechanism. In *IEEE International Conference on Robotics and Automation* (2013), pp. 4168–4173.

[52] Kim, H.-s., and Song, J.-b. Multi-DOF Counterbalance Mechanism for a Service Robot Arm. *IEEE/ASME Transactions on Mechatronics 19*, 6 (2014), 1756–1763.

[53] Kontorinis, G., Lenarz, T., Stöver, T., and Paasche, G. Impact of the insertion speed of cochlear implant electrodes on the insertion forces. *Otology & neurotology : official publication of the American Otological Society, American Neurotology Society [and] European Academy of Otology and Neurotology 32*, 4 (June 2011), 565–70.

[54] Kontorinis, G., Paasche, G., Lenarz, T., and Stöver, T. The effect of different lubricants on cochlear implant electrode insertion forces. *Otology & neurotology : official publication of the American Otological Society, American Neurotology Society [and] European Academy of Otology and Neurotology 32*, 7 (Sept. 2011), 1050–6.

[55] Koser, K. A cam mechanism for gravity-balancing. *Mechanics Research Communications 36*, 4 (June 2009), 523–530.

[56] Kratchman, L. B., Blachon, G. S., Withrow, T. J., Balachandran, R., Labadie, R. F., and Webster, R. J. Design of a bone-attached parallel robot for percutaneous cochlear implantation. *IEEE transactions on bio-medical engineering 58*, 10 (Oct. 2011), 2904–10.

[57] Kratchman, L. B., Schurzig, D., McRackan, T. R., Balachandran, R., Noble, J. H., Webster, R. J., and Labadie, R. F. A manually operated, advance off-stylet insertion tool for minimally invasive cochlear implantation surgery. *IEEE transactions on bio-medical engineering 59*, 10 (Oct. 2012), 2792–800.

[58] Kurtz, R., and Hayward, V. Dexterity measure for tendon actuated parallel mechanisms. *Fifth International Conference on Advanced Robotics 'Robots in Unstructured Environments* (1991), 1141–1146 vol.2.

[59] Labadie, R. F., Balachandran, R., Mitchell, J. E., Noble, J. H., Majdani, O., Haynes, D. S., Bennett, M. L., Dawant, B. M., and Fitzpatrick, J. M. Clinical validation study of percutaneous cochlear access

using patient-customized microstereotactic frames. *Otology & neurotology : official publication of the American Otological Society, American Neurotology Society [and] European Academy of Otology and Neurotology 31*, 1 (Jan. 2010), 94–9.

[60] Labadie, R. F., Chodhury, P., Cetinkaya, E., Balachandran, R., Haynes, D. S., Fenlon, M. R., Jusczyzck, A. S., and Fitzpatrick, J. M. Minimally invasive, image-guided, facial-recess approach to the middle ear: demonstration of the concept of percutaneous cochlear access in vitro. *Otology & neurotology : official publication of the American Otological Society, American Neurotology Society [and] European Academy of Otology and Neurotology 26*, 4 (July 2005), 557–62.

[61] Laliberte, T., Gosselin, C., and Jean, M. Static balancing of 3-DOF planar parallel mechanisms. *IEEE/ASME Transactions on Mechatronics 4*, 4 (1999), 363–377.

[62] Lehnhardt, E. Intracochlear electrode placement facilitated by Healon. *Advances in oto-rhino-laryngology 48* (Jan. 1993), 62–4.

[63] Lessard, S., Bigras, P., and Bonev, I. a. A New Medical Parallel Robot and Its Static Balancing Optimization. *Journal of Medical Devices 1*, 4 (2007), 272.

[64] Lim, H., Han, J.-M., Hong, J., Yi, B.-J., Lee, S. H., Jeong, J. H., Matsumoto, N., Oka, M., Komune, S., and Hashizume, M. Image-guided robotic mastoidectomy using human-robot collaboration control. *2011 IEEE International Conference on Mechatronics and Automation* (Aug. 2011), 549–554.

[65] Maier, T., Strauss, G., Hofer, M., Kraus, T., Runge, A., Stenzel, R., Gumprecht, J., Berger, T., Dietz, A., and Lueth, T. C. A new Micromanipulator System for middle ear surgery. In *2010 IEEE International Conference on Robotics and Automation* (May 2010), IEEE, pp. 1568–1573.

[66] Majdani, O., Schurzig, D., Hussong, A., Rau, T., Wittkopf, J., Lenarz, T., and Labadie, R. F. Force measurement of insertion of cochlear implant electrode arrays in vitro: comparison of surgeon to automated insertion tool. *Acta oto-laryngologica 130*, 1 (Jan. 2010), 31–6.

[67] Mako. Mako Surgical Corporation.

[68] Maruyama, N., Liu, L., Akahane, K., and Sato, M. A proposal of two-handed multi-finger haptic interface with rotary frame. In *Artificial Reality and*

Telexistence (ICAT), 2013 23rd International Conference on (Tokyo, Japan, 2013), vol. 1, pp. 40–45.

[69] Massie, T. H., and Salisbury, J. K. PHANToM haptic interface: a device for probing virtual objects. In *Proceedings of the 1994 International Mechanical Engineering Congress and Exposition* (Chicago, IL, 1994), vol. 55, ASME, pp. 295–299.

[70] Miroir, M., Nguyen, Y., Kazmitcheff, G., Ferrary, E., Sterkers, O., and Grayeli, A. B. Friction force measurement during cochlear implant insertion: application to a force-controlled insertion tool design. *Otology & neurotology : official publication of the American Otological Society, American Neurotology Society [and] European Academy of Otology and Neurotology 33*, 6 (Aug. 2012), 1092–100.

[71] Mustafa, S. K., and Agrawal, S. K. Reciprocal Screw-Based Force-Closure of Cable-Driven Closed Chains. In *Volume 6: 35th Mechanisms and Robotics Conference, Parts A and B* (2011), vol. 1, ASME, pp. 1243–1251.

[72] NIH Publication No. 11-4798. Cochlear Implants. Tech. rep., National Institute of Health, 2011.

[73] Noble, J. H., and Dawant, B. M. An atlas-navigated optimal medial axis and deformable model algorithm (NOMAD) for the segmentation of the optic nerves and chiasm in MR and CT images. *Medical image analysis 15*, 6 (Dec. 2011), 877–84.

[74] Noble, J. H., Dawant, B. M., Warren, F. M., and Labadie, R. F. Automatic identification and 3D rendering of temporal bone anatomy. *Otology & neurotology : official publication of the American Otological Society, American Neurotology Society [and] European Academy of Otology and Neurotology 30*, 4 (June 2009), 436–42.

[75] Noble, J. H., Labadie, R. F., Majdani, O., and Dawant, B. M. Automatic segmentation of intracochlear anatomy in conventional CT. *IEEE transactions on bio-medical engineering 58*, 9 (Sept. 2011), 2625–32.

[76] Pan, Y., Ge, S. S., Mamun, A. A., and Tang, F. R. Detection of seizures in EEG signal using weighted locally linear embedding and SVM classifier. In *2008 IEEE Conference on Cybernetics and Intelligent Systems* (Sept. 2008), IEEE, pp. 358–363.

[77] Penrose, R., and Todd, J. a. On best approximate solutions of linear matrix equations. *Mathematical Proceedings of the Cambridge Philosophical Society 52*, 01 (Oct. 1956), 17.

[78] Pierrot, F., Fournier, A., and Dauchex, P. Towards a fully-parallel 6 DOF robot for high-speed applications. In *Proceedings. 1991 IEEE International Conference on Robotics and Automation* (1991), no. April, IEEE Comput. Soc. Press, pp. 1288–1293.

[79] Pile, J., Cheung, M. Y., Zhang, J., and Simaan, N. Algorithms and design considerations for robot assisted insertion of Perimodiolar Electrode Arrays. In *2011 IEEE International Conference on Robotics and Automation* (May 2011), IEEE, pp. 2898–2904.

[80] Pile, J., and Simaan, N. Characterization of friction and speed effects and methods for detection of cochlear implant electrode tip fold-over. In *2013 IEEE International Conference on Robotics and Automation* (May 2013), Ieee, pp. 4409–4414.

[81] Pile, J., and Simaan, N. Modeling, Design, and Evaluation of a Parallel Robot for Cochlear Implant Surgery. *IEEE/ASME Transactions on Mechatronics* (2014), 1–10.

[82] Pile, J., Wanna, G. B., and Simaan, N. Force-Based Flexible Path Plans for Robotic Electrode Insertion. In *2014 IEEE International Conference on Robotics and Automation* (Hong Kong, 2014), IEEE, pp. 297–303.

[83] Plonsey, R., and Barr, R. C. *Bioelectricity: a quantitative approach*, 3rd ed. ed. Springer, New York, 2007.

[84] Raibert, M. H., and Craig, J. J. Hybrid Position/Force Control of Manipulators. *Journal of Dynamic Systems, Measurement, and Control 103*, 2 (1981), 126.

[85] Rau, T. S., Hussong, A., Leinung, M., Lenarz, T., and Majdani, O. Automated insertion of preformed cochlear implant electrodes: evaluation of curling behaviour and insertion forces on an artificial cochlear model. *International journal of computer assisted radiology and surgery 5*, 2 (Mar. 2010), 173–81.

[86] Roland, J. T. A model for cochlear implant electrode insertion and force evaluation: results with a new electrode design and insertion technique. *The Laryngoscope 115*, 8 (Aug. 2005), 1325–39.

[87] Russo, a., Sinatra, R., and Xi, F. Static balancing of parallel robots. *Mechanism and Machine Theory 40*, 2 (Feb. 2005), 191–202.

[88] Salisbury, K., Townsend, W., Ebrman, B., and DiPietro, D. Preliminary design of a whole-arm manipulation system (WAMS). In *Proceedings.*

1988 IEEE International Conference on Robotics and Automation (1988), IEEE Comput. Soc. Press, pp. 254–260.

[89] Saravanan, R., Ramabalan, S., and Dinesh Babu, P. Optimum static balancing of an industrial robot mechanism. *Engineering Applications of Artificial Intelligence 21*, 6 (Sept. 2008), 824–834.

[90] Scholkopf, B., Burges, C., and Smola, A., Eds. *Advances in kernel methods: support vector learning*. MIT Press, Cambridge, 1999.

[91] Schölkopf, B., and Smola, A. New support vector algorithms. *Neural computation 1245*, x (2000), 1207–1245.

[92] Schurzig, D., Labadie, R. F., Hussong, A., Rau, T. S., and Webster, R. J. A force sensing Automated Insertion Tool for cochlear electrode implantation. In *IEEE International Conference on Robotics and Automation* (Anchorage, Alaska, 2010), pp. 3674–3679.

[93] Schurzig, D., Webster, R. J., Dietrich, M. S., and Labadie, R. F. Force of cochlear implant electrode insertion performed by a robotic insertion tool: comparison of traditional versus Advance Off-Stylet techniques. *Otology & neurotology : official publication of the American Otological Society, American Neurotology Society [and] European Academy of Otology and Neurotology 31*, 8 (Oct. 2010), 1207–10.

[94] Schuster, D., Kratchman, L. B., and Labadie, R. F. Characterization of Intracochlear Rupture Forces in Fresh Human Cadaveric Cochleae. *Otology & neurotology : official publication of the American Otological Society, American Neurotology Society [and] European Academy of Otology and Neurotology* (2014), 1–5.

[95] Shepherd, R., Verhoeven, K., Xu, J., Risi, F., Fallon, J., and Wise, A. An improved cochlear implant electrode array for use in experimental studies. *Hearing research 277*, 1-2 (July 2011), 20–7.

[96] Sima'an, N., Glozman, D., and Shoham, M. Design considerations of new six degrees-of-freedom parallel robots. In *Proceedings. 1998 IEEE International Conference on Robotics and Automation (Cat. No.98CH36146)* (Leuven, Belgium, 1998), vol. 2, IEEE, pp. 1327–1333.

[97] Simaan, N., and Shoham, M. Robot Construction for Surgical Applications. In *Second Israeli Symposium on Computer-Aided Surgery, Medical Robotics, and Medical Imaging* (1999).

[98] Simionescu, I. The static balancing of the industrial robot arms Part I: Discrete balancing. *Mechanism and Machine Theory 35*, 9 (Sept. 2000), 1287–1298.

[99] Skarzyski, H., Lorens, A., Piotrowska, A., and Podskarbi-Fayette, R. Results of partial deafness cochlear implantation using various electrode designs. *Audiology & neuro-otology 14 Suppl 1* (Jan. 2009), 39–45.

[100] Stewart, D. A platform with six degrees of freedom. *ARCHIVE: Proceedings of the Institution of Mechanical Engineers 1847-1982 (vols 1-196) 180*, 1965 (June 1965), 371–386.

[101] Stöver, T., Issing, P., Graurock, G., Erfurt, P., ElBeltagy, Y., Paasche, G., and Lenarz, T. Evaluation of the advance off-stylet insertion technique and the cochlear insertion tool in temporal bones. *Otology & neurotology : official publication of the American Otological Society, American Neurotology Society [and] European Academy of Otology and Neurotology 26*, 6 (Nov. 2005), 1161–70.

[102] Strang, G. *Computational Science and Engineering*. Wellesley Cambridge Press, 2007.

[103] Suessennan, M. F., Ieee, M., and Spelman, F. A. Lumped-Parameter Model for In Vivo Cochlear Stimulation. *IEEE transactions on bio-medical engineering 40*, 3 (1993), 237–245.

[104] Suesserrnan, M. F. Quantitative In Vivo Measurements of Inner Ear Tissue Resistivities : I . In Vitro Characterization. *IEEE transactions on bio-medical engineering 40*, October (1993).

[105] Sutherland, G. R., Latour, I., and Greer, A. D. Integrating an image-guided robot with intraoperative MRI: a review of the design and construction of neuroArm. *IEEE engineering in medicine and biology magazine : the quarterly magazine of the Engineering in Medicine & Biology Society 27*, 3 (2008), 59–65.

[106] Tan, C.-T., Svirsky, M., Anwar, A., Kumar, S., Caessens, B., Carter, P., Treaba, C., and Roland, J. T. Real-time measurement of electrode impedance during intracochlear electrode insertion. *The Laryngoscope 123*, 4 (Apr. 2013), 1028–32.

[107] Taylor, R., and Stoianovici, D. Medical robotics in computer-integrated surgery. *IEEE Transactions on Robotics and Automation 19*, 5 (Oct. 2003), 765–781.

[108] Teszler, C. B., Ruimi, D., Bar-Meir, E., and Luntz, M. Width of the extended facial recess: a numerical study of ultrahigh-resolution computed tomography and its implications in minimally invasive otologic surgery. *Otology & neurotology : official publication of the American Otological Society, American Neurotology Society [and] European Academy of Otology and Neurotology 26*, 4 (July 2005), 782–9.

[109] Teymouri, J., Hullar, T. E., Holden, T. a., and Chole, R. a. Verification of computed tomographic estimates of cochlear implant array position: a micro-CT and histologic analysis. *Otology & neurotology : official publication of the American Otological Society, American Neurotology Society [and] European Academy of Otology and Neurotology 32*, 6 (Aug. 2011), 980–6.

[110] Todd, C. a., Naghdy, F., and Svehla, M. J. Force application during cochlear implant insertion: an analysis for improvement of surgeon technique. *IEEE transactions on bio-medical engineering 54*, 7 (July 2007), 1247–55.

[111] Tsai, L.-W. *Robot Analysis: The Mechanics of Serial and Parallel Manipulators*. John Wiley and Sons Inc., New York, NY, USA, 1999.

[112] Tykocinski, M., Saunders, E., Cohen, L. T., Treaba, C., Briggs, R. J. S., Gibson, P., Clark, G. M., and Cowan, R. S. C. The Contour Electrode Array: Safety Study and Initial Patient Trials of a New Perimodiolar Design. *Otology & Neurotology 22*, 1 (Jan. 2001), 33–41.

[113] Vanpoucke, F. J., Zarowski, A. J., and Peeters, S. A. Identification of the impedance model of an implanted cochlear prosthesis from intracochlear potential measurements. *IEEE transactions on bio-medical engineering 51*, 12 (Dec. 2004), 2174–83.

[114] Verbist, B. M., Skinner, M. W., Cohen, L. T., Leake, P. a., James, C., Boëx, C., Holden, T. a., Finley, C. C., Roland, P. S., Roland, J. T., Haller, M., Patrick, J. F., Jolly, C. N., Faltys, M. a., Briaire, J. J., and Frijns, J. H. M. Consensus panel on a cochlear coordinate system applicable in histologic, physiologic, and radiologic studies of the human cochlea. *Otology & neurotology : official publication of the American Otological Society, American Neurotology Society [and] European Academy of Otology and Neurotology 31*, 5 (July 2010), 722–30.

[115] Vermeulen, M., and Wisse, M. Intrinsically Safe Robot Arm: Adjustable Static Balancing andLow Power Actuation. *International Journal of Social Robotics 2*, 3 (Mar. 2010), 275–288.

[116] Waltzman, S. B., and Roland, J. T. J. *Cochlear Implants*, 2nd editio ed. Thieme Medical Publishers, New York, NY, 2006.

[117] Wang, J., and Wise, K. D. A Thin-Film Cochlear Electrode Array With Integrated Position Sensing. *Journal of Microelectromechanical Systems 18*, 2 (Apr. 2009), 385–395.

[118] Wardrop, P., Whinney, D., Rebscher, S. J., Luxford, W., and Leake, P. A temporal bone study of insertion trauma and intracochlear position of cochlear implant electrodes. II: Comparison of Spiral Clarion and HiFocus II electrodes. *Hearing research 203*, 1-2 (May 2005), 68–79.

[119] Wardrop, P., Whinney, D., Rebscher, S. J., Roland, J. T., Luxford, W., and Leake, P. a. A temporal bone study of insertion trauma and intracochlear position of cochlear implant electrodes. I: Comparison of Nucleus banded and Nucleus Contour electrodes. *Hearing research 203*, 1-2 (May 2005), 54–67.

[120] Watanabe, H., Velmurugan, J., Mirkin, M. V., Svirsky, M. a., Lalwani, a. K., and Llinas, R. R. Scanning electrochemical microscopy as a novel proximity sensor for atraumatic cochlear implant insertion. *IEEE Transactions on Biomedical Engineering 61*, 6 (2014), 1822–1832.

[121] Whiting, B. R., Bae, K. T., and Skinner, M. W. Cochlear implants: three-dimensional localization by means of coregistration of CT and conventional radiographs. *Radiology 221*, 2 (Nov. 2001), 543–9.

[122] Whitney, D. Resolved Motion Rate Control of Manipulators and Human Prostheses. *IEEE Transactions on Man Machine Systems 10*, 2 (June 1969), 47–53.

[123] Yokoi, K., Tanie, K., Inamura, N., Kawai, T., and Agou, K. Design and control of a seven-degrees-of-freedom manipulator actuated by a coupled tendon-driven system. *Proceedings IROS '91:IEEE/RSJ International Workshop on Intelligent Robots and Systems '91*, 91 (1991), 737–742.

[124] Yoshikawa, T. Dynamic hybrid position/force control of robot manipulators–Description of hand constraints and calculation of joint driving force. *IEEE Journal on Robotics and Automation 3*, 5 (Oct. 1987), 386–392.

[125] Zhang, J., Bhattacharyya, S., and Simaan, N. Model and parameter identification of friction during robotic insertion of cochlear-implant electrode arrays. *2009 IEEE International Conference on Robotics and Automation* (May 2009), 3859–3864.

[126] Zhang, J., J.T., R., Manolidis, S., and Simaan, N. Optimal Design of Under-actuated Steerable Electrode Arrays for Optimal Insertions. *ASME*

Journal of Mechanisms and Robotics, (2011), conditionally accepted 5/3/2011, under review.

[127] Zhang, J., Roland, J. T., Manolidis, S., and Simaan, N. Optimal Path Planning for Robotic Insertion of Steerable Electrode Arrays in Cochlear Implant Surgery. *Journal of Medical Devices 3*, 1 (2009), 011001.

[128] Zhang, J., Wei, W., Ding, J., Roland, J. T., Manolidis, S., and Simaan, N. Inroads Toward Robot-Assisted Cochlear Implant Surgery Using Steerable Electrode Arrays. *Otology & Neurotology* (June 2010), 1.

[129] Zhang, J., Wei, W., Manolidis, S., Roland, J. T., and Simaan, N. Path planning and workspace determination for robot-assisted insertion of steerable electrode arrays for cochlear implant surgery. *Medical image computing and computer-assisted intervention : MICCAI ... International Conference on Medical Image Computing and Computer-Assisted Intervention 11*, Pt 2 (Jan. 2008), 692–700.

[130] Zhang, J., Xu, K., Simaan, N., and Manolidis, S. A pilot study of robot-assisted cochlear implant surgery using steerable electrode arrays. *Medical image computing and computer-assisted intervention : MICCAI ... International Conference on Medical Image Computing and Computer-Assisted Intervention 9*, Pt 1 (Jan. 2006), 33–40.

[131] Zhou, H., and van Oosterom, A. Application of the boundary element method to the solution of anisotropic electromagnetic problems. *Medical and Biological Engineering and Computing 32*, 4 (July 1994), 399–405.

[132] Zrunek, M., and Lischka, M. Dimensions of the scala vestibuli and sectional areas of both scales. *Archives of Oto-Rhino-Laryngology 233*, 1 (Oct. 1981), 99–104.

[133] Zrunek, M., Lischka, M., Hochmair-Desoyer, I., and Burian, K. Dimensions of the scala tympani in relation to the diameters of multichannel electrodes. *Archives of oto-rhino-laryngology 229*, 3-4 (Jan. 1980), 159–65.